Cardiff
Catalysis Institute

Sefydliad Catalysis
Caerdydd

In situ Study of Au/C Catalysts for the Hydrochlorination of Acetylene

Thesis submitted in accordance with the requirements of Cardiff University for the degree of doctor of philosophy by

Grazia Malta

School of Chemistry

Cardiff University

2018

Supervisor

Prof. Graham Hutchings

DECLARATION

This work has not been submitted in substance for any other degree or award at this or any other university or place of learning, nor is being submitted concurrently in candidature for any degree or other award.

Signed …… (candidate) Date ……

STATEMENT 1

This thesis is being submitted in partial fulfillment of the requirements for the degree of ……(insert MCh, MD, MPhil, PhD etc, as appropriate)

Signed …… (candidate) Date ……

STATEMENT 2

This thesis is the result of my own independent work/investigation, except where otherwise stated, and the thesis has not been edited by a third party beyond what is permitted by Cardiff University's Policy on the Use of Third Party Editors by Research Degree Students. Other sources are acknowledged by explicit references. The views expressed are my own.

Signed …… (candidate) Date ……

STATEMENT 3

I hereby give consent for my thesis, if accepted, to be available online in the University's Open Access repository and for inter-library loan, and for the title and summary to be made available to outside organisations.

Signed …… (candidate) Date ……

STATEMENT 4: PREVIOUSLY APPROVED BAR ON ACCESS

I hereby give consent for my thesis, if accepted, to be available online in the University's Open Access repository and for inter-library loans **after expiry of a bar on access previously approved by the Academic Standards & Quality Committee.**

Signed …… (candidate) Date ……

Abstract

Very few commercial processes employ Au catalysts for the production of fine or commodity chemicals. The recent validation of Au/C catalysts to produce vinyl chloride monomer (VCM) via the acetylene hydrochlorination reaction, as a replacement of the traditionally used highly volatile and toxic mercuric chloride catalyst, represents a notable exception. However, the active form of the catalyst and the reaction mechanism are still not fully understood. The work presented in this thesis aims to provide detailed information about the nature of the catalyst's active species and the possible reaction pathway, combining commonly used characterisation techniques with more challenging *in situ* experiments.

The first part of this thesis (Chapter 3) aims to understand the influence of the choice of solvent and metal precursor during the catalyst preparation in the activity of the final material in order to identify the active state of Au during catalysis and to propose a reaction mechanism (Chapter 3). This investigation was carried out via a *in situ* X-ray absorption fine structure (XAFS) spectroscopy experiment. This study led to the conclusion that under reaction conditions highly active catalysts comprise single-site cationic Au species whose activity correlates with the ratio of Au(I)/Au(III) present, providing a new insight to the structure-function relationship of this reaction, while the mechanism has been hypothesised to proceed through the oxidative addition of HCl to Au chloride, followed by the insertion of acetylene and reductive elimination of VCM.

The deactivation of gold on carbon catalysts during acetylene hydrochlorination has been attributed to two possible deactivation mechanisms: the formation of oligomers on the catalyst surface blocking the active site and the reduction of active cationic gold to inactive metallic Au. These two deactivation pathways have been shown to be influenced by both reaction temperature used and the detrimental effect of acetylene rich feeds. The second part of this thesis (Chapter 4) investigates the role of each reactant on the catalyst composition to further elucidate both the reaction and deactivation mechanism via an *in situ* gas switching experiment while recording the XAS spectra at the Au L_3-edge. This study led to the hypothesis that the oxidative addition of HCl across the Au(I) chloride species requires the concerted addition with C_2H_2, in partial modification of the reaction mechanism proposed in chapter 3. An inelastic neutron scattering (INS) study of the catalyst exposed to C_2H_2 showed the formation of oligomeric acetylene species on the catalyst surface, which, upon re-introduction of both reactants, led to significant catalyst deactivation associated with the formation of metallic Au nanoparticles. The formation of Au(0) has been directly correlated with a decrease in VCM productivity when under reaction conditions also using an higher Au loading catalyst.

The recently validated Au/C catalyst by Johnson Matthey, prepared by using a sulphur containing Au complex, under industrial conditions, is more active and stable than the traditional Au/C catalyst made using hard donor ligands such as Cl. Clearly the choice of the ligand plays a major role in the final activity and stability of those catalysts. Chapter 5 reports *in situ* ligand K-edge XAS characterisation of gold on carbon catalyst for the hydrochlorination of acetylene to understand chlorine and sulphur speciation in the catalysts under operating conditions. In both catalytic systems, Cl is bounded directly to the gold and is directly involved in the reaction mechanism, re-affirming that $AuCl_x$ speciation are active site for the acetylene hydrochlorination reaction.

Acknowledgements

First of all, I would to express my sincere gratitude to Prof. Graham Hutchings for allowing me to undertake this project and for all the opportunities that have followed, it has been an honour.

Special thanks to Dr Simon Freakley for his supervision and guidance, from the beginning until the very end of my PhD (even if you are always overloaded of work you have always found time for me and for this I will always be grateful). And to Dr Simon Kondrat for all the help, support and 'XAFS Friday afternoon classes' and for being an exceptional teacher (this place is not the same without you!). Thank you guys for everything you have done for me, without you I would not be in this position.

I would like to thank Emma Gibson and Peter Wells for their help in XAFS acquisition and interpretation. They have been really supportive during all the beam times and those are moments I will never forget. I would also like to thank Prof Chris Kiely and Dr Li Lu for the amazing STEM images.

Many thanks to everybody from the workshop (especially Steve Morris: you are an absolute hero!), with your expertise and knowledge you have been essential. Thanks for your patience!

I would like to thank the Maxnet team and all of the PhDs and post docs who have shared with me all the good and bad moment of this PhD, especially Ricci, Rich, Chrissy, Marky, Sammy and King Beac. And the crossword team, thanks for teaching me how to spell words.

A very special thanks to Dr Nikolaos Dimitratos (Nikos), you have been not only a supervisor but also a friend for me. Thank you for the all your precious advices!

Many thanks to Nishtha for the IT service and English lessons and especially for her friendship and her support!

Finally, a special thanks to Dany for the past six years (maybe more?), he has supported and tolerated me as a friend, a labmate and a flatmate through happy and sad times (even if in his own way). To Marghe, thanks for our dinners, the glasses of wine and everything else. We started this together and we went through a lot, it's been a long way but we've finally (almost) made it. To Ricci, for he always made me feel at home away from home. You are my family guys!

Heartfelt thanks to Roby for being next to me during this stressful moments of writing this thesis and his support and patience for all this time.

Most importantly I would like to thank (maybe thank you is not enough!) mami and papi for all their encouragement and support all the way through my university life until this last step.

Table of contents

Chapter 3 – Investigation into the nature of the active site in gold catalysts for acetylene hydrochlorination

Chapter 4 – *In situ* study of the deactivation of Au/C-Aqua Regia catalysts for the acetylene hydrochlorination reaction

Chapter 1

Introduction

In this chapter a brief introduction to catalysis will be provided along with the state-of-the-art regarding the catalytic system discussed and investigated in this thesis.

1.1 – Catalysis

For a chemical reaction to take place, it is necessary to break the bonds holding together the atoms in the reacting molecules and form new bonds to generate the products. The breaking of a chemical bond is a process that necessitates energy, the minimum energy required for a chemical reaction to proceed is called activation energy ($E_a > 0$); only molecules that collide with an energy at least equal to the E_a can react with each other to form products. The speed at which reactants are converted into products is defined by the rate of reaction. The rate of many reactions could be zero even under conditions where the reaction is thermodynamically favourable. Thus, particularly in the chemical industry, increasing this reaction rate is extremely beneficial. In general, an increase in temperature can accelerate reactions because it brings more molecules to the energy level necessary to overcome the energy barrier; an alternative way to accelerate a process is to lower the activation barrier, and this can be achieved by adding a catalyst (Figure 1.1). According to the IUPAC definition, a catalyst is "a substance that increases the rate of a reaction without affecting the overall change in standard Gibbs energy of the reaction".[1] While, the word "catalysis" is Greek in origin and means "to break or to

dissolve" and it was first introduced by Berzelius in 1836 to identify a new entity proficient in promoting a chemical reaction by a "catalytic contact".[2] Consequently, catalysis can be described as the chemical phenomenon by which the rate of a chemical reaction undergoes modification through the intervention of a catalyst.

Figure 1.1 represents a hypothetical energy level diagram for a generic reaction (A + BC to give product C) with and without catalyst present. The un-catalysed process occurs in a single stage characterised by a high-energy activation barrier, while the same catalysed process might occur in several steps, each of which has a lower activation barrier than the un-catalysed process; the reaction can in this way reach equilibrium at a faster rate. It is important to note that, in presence of a catalyst, the Gibb's Free Energy (ΔG) from reactants to products is unchanged, thus, the overall thermodynamics remain the same, it is only the rate of reaction that increases in presence of a catalyst. Therefore, the effect of the catalysis is of kinetic nature not thermodynamic; the action of a catalyst modifies the intermediate states of a reaction, but it does not change the final state (or final states). Since a catalyst is not consumed during the process, and does not take part as a reactant, it can be recycled for repeated use. For this reason, only small amounts relative to the reactants are required to increase the rate of reaction.

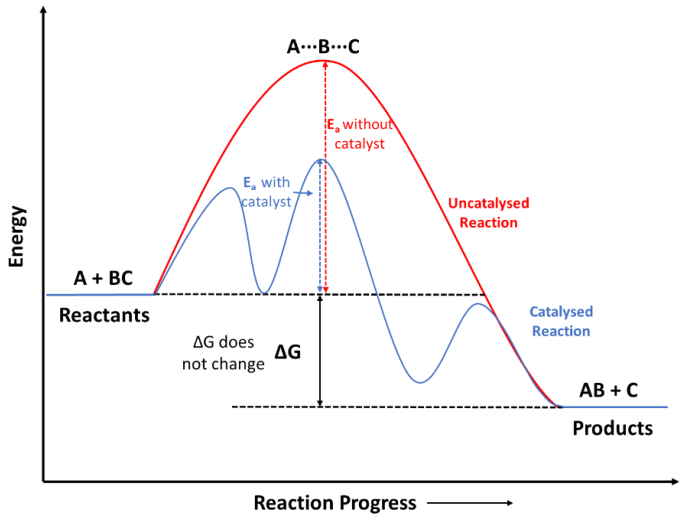

Figure 1.1 – Energy level diagram for a reaction A + BC to give product C with and without catalyst present. Where E_a = activation energy ΔG = overall Gibbs free energy

In general, a catalyst combines with one or more reactants weakening their bonds, making them easier to transform into a reaction intermediate, which proceeds to form the product. In particular, the overall catalytic process can typically be divided into the following elementary steps:

- adsorption of the reactants onto the catalyst surface.
- the breaking or weakening of the reactant bonds.
- the reaction to form the product through the interaction with the catalyst active site.

- the desorption of the products from the catalyst surface, freeing up the catalyst active sites for a repeat of the process.

  Substances that are permanently adsorbed on the active sites of a catalyst, rendering them unusable for catalysis, are called poisons.

Based on the state of matter of the catalyst and reactants it is possible to define two main class of catalysis: homogeneous and heterogeneous. In homogeneous catalysis the catalyst is in the same phase as the reactants, typically metal complexes in liquid reactions, and in heterogeneous catalysis the catalyst and reactant are in different phases.

The major advantage of heterogeneous catalysis over homogeneous catalysis is the ease in the product recovery after reaction, thus most of the catalysed industrial processes use heterogeneous catalysts.

1.2 – Vinyl Chloride Monomer Production

Vinyl chloride monomer (VCM) is an extremely important chemical intermediate. In 2016, over 99% of the VCM production was used for the manufacture of polyvinylchloride (PVC) (Reaction Scheme 1.1).[3] The commercial production of PVC started in the first half of the 20th century [4,5] and today, PVC is one of the top selling polymers, used word-wide in many applications.[6,7,8] Over 40 million tonnes of PVC were consumed in 2016, corresponding to the 16% of the total global plastic demand.[9]

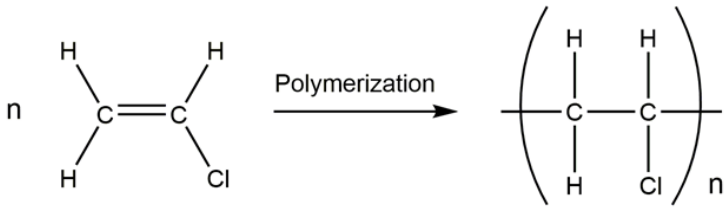

Scheme 1.1 – Vinyl Chloride Monomer (VCM) is polymerised to polyvinylchloride (PVC).

There are two main routes by which VCM is produced industrially depending on the starting materials. The traditional route is the direct hydrochlorination of acetylene (or ethyne – C_2H_2), which is a coal-derived starting material, catalysed by carbon-supported mercuric chloride ($HgCl_2$/C). As time progressed, the increase in PVC demand and the availability of oil led to the development of an alternative industrial process to produce VCM. This process is known as the "balanced process" and it is a combination of chlorination and oxychlorination reactions of ethylene (or ethene - C_2H_4). The balanced process is based on low cost oil-derived feedstocks, ethylene is in fact a by-product of petroleum refining that can also be isolated from natural gas. In this process ethene is converted to ethylene dichloride (or 1,2-dichloroethane - EDC) via oxychlorination (equation 1) and chlorination

(equation 2) reactions, catalysed by $CuCl_2$ and $FeCl_3$ respectively, subsequently the EDC is thermally cracked to VCM,[10] as it is shown in the equations below:

$CH_2=CH_2 + 2HCl + ½O_2 \rightarrow CH_2Cl\text{-}CH_2Cl + H_2O$ (Equation 1 – Oxychlorination)

$CH_2=CH_2 + Cl_2 \rightarrow CH_2Cl\text{-}CH_2Cl$ (Equation 2 – Chlorination)

$CH_2Cl\text{-}CH_2Cl \rightarrow CH_2=CHCl + HCl$ (Equation 3 – Cracking)

$2C_2H_4 + Cl_2 + ½O_2 - 2C_2H_3Cl + H_2O$ (Overall reaction)

In the recent decades, this multi-step process became the primary method for the VCM production, mainly within Europe and America, as the increased availability of oil made ethene a widely accessible feedstock. However, in countries such as China, where coal-derived feedstocks are still more readily available resources, over 13 million tonnes per year of VCM are manufactured *via* direct hydrochlorination of acetylene (Reaction Scheme 1.2). This process accounts now for a major part of VCM synthesis.

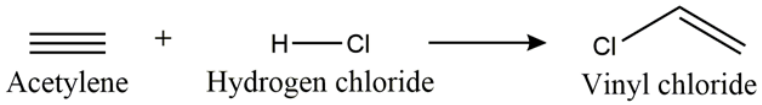

Scheme 1.2 – Direct hydrochlorination of acetylene to produce VCM.

1.3 – Hydrochlorination of Acetylene

1.3.1 – Mercury Chloride on Activated Carbon

Direct acetylene hydrochlorination is an exothermic reaction ($\Delta H° = -99$ kJ mol^{-1}) usually performed at a pressure of *ca*. 1-2 bar and a temperature in the range 100-200 °C [11] and represents the original industrial process to produce VCM. Traditionally, the industrial catalyst used consists of a high metal loaded mercuric chloride ($\approx 10_{wt}\%$ $HgCl_2$) deposited on high surface area activated carbon (1000−2000 $m^2\ g^{-1}$) by adsorption from an aqueous solution.[12] High surface area activated carbon was chosen because of its high stability at high temperature in the presence of HCl and its efficiency in adsorbing the $HgCl_2$. At the present time, more than the 60% of the annual mercury production is used for the manufacture of this catalysts and in China, over 10 000 ton/year of mercury-based catalyst are used for monomer production.

This class of catalysts is still employed to the present day despite there being several disadvantages associated with its use,[13,14,15,16] among which the loss of mercury from the catalyst represents the main

issue.[13,14] At reaction temperature (180-220 °C) mercuric chloride becomes extremely volatile and sublimes from the carbon support resulting in a high loss of mercury from the catalyst, leading to a very short catalyst lifetime, requiring frequent changes of the catalyst[13,14]. Moreover, mercury-based catalysts can also catalyse the secondary addition of HCl to vinyl chloride causing a loss in selectivity towards the desired product, VCM. The final result of this is the escape of Hg from the production units, which has not proved possible to trap effectively: *ca*. 0.6 kg of mercury is lost from the catalyst per ton of VCM produced.[17] Clearly this is an unsustainable situation, particularly due to the toxic nature of mercury.

For this reason, researchers are studying different approaches to improve the thermal stability of the mercury-based catalysts for the hydrochlorination of acetylene; for example, using additives, such as potassium halides, in the catalyst preparation to decrease the sublimation rates.[18] However, this is still a crucial problem that needs to be overcome. In China, VCM production *via* acetylene hydrochlorination does not show signs of diminishing, rather production capacity is increasing. Therefore, the need to produce a new mercury free catalyst for this process is more urgent than ever before. This need was accelerated in 2013, due to the Minamata Convention on Mercury. Taking its name from a neurological syndrome caused by mercury poisoning (Minamata disease), ‘‘the Minamata Convention on Mercury is a global treaty to protect human health and the environment from the adverse effects of mercury’’.[19] This treaty includes a clause which states that new VCM plants will not be allowed to use a mercury catalyst after 2017 and all VCM plants must be mercury free after 2022 if a suitable alternative is found.

1.3.2 – The Introduction of Gold

In the 1930s, a study was reported about the use of a small selection of metal chlorides supported on carbon or silica as catalysts for the acetylene hydrochlorination reaction.[20] After that, during the 1960s, detailed kinetic studies of the acetylene hydrochlorination reaction were carried out. [21,22,23] These studies identified the addition of HCl to absorbed C_2H_2 to produce vinyl chloride monomer as the rate-determining step of the reaction. These findings were fundamental to lead the research in looking at metallic salts that could lead to both stable metal-acetylene and metal-hydrochloric acid complexes. Considering the stability acetylide species as a crucial parameter to control activity, an initial attempt to correlate the activity of the catalyst with the electron affinity of the metal was made.[24] This study was then taken up and expanded by Shinoda,[25] who investigated the activity of over 30 metal chlorides supported on activated carbon for acetylene hydrochlorination and correlated the activity with the electron affinity of the metal cation, divided by the metal valence as a correction factor. However, the data do not statistically correlate with this parameter, as it is shown in Figure 1.2.

The correlation consisted of two straight lines, in which is possible to identify two distinct classes of metal chlorides; the higher part of the plot are the metal species able to form the most stable acetylides, and those are: Pd^{2+}, Hg^{2+}, Cu^{2+} and Ag^{+}; whereas the lower set includes metal cations that can form stable complex with HCl and act as Friedel-Craft catalysts. Moreover, if we consider for example three metal cations investigated, namely Zn^{2+}, Cd^{2+}, and Hg^{2+}, despite having similar electron affinities they show completely different activities, going from the least active to the most active. To conclude, the data as presented in Figure 1.2 could not be used in a predictive manner.

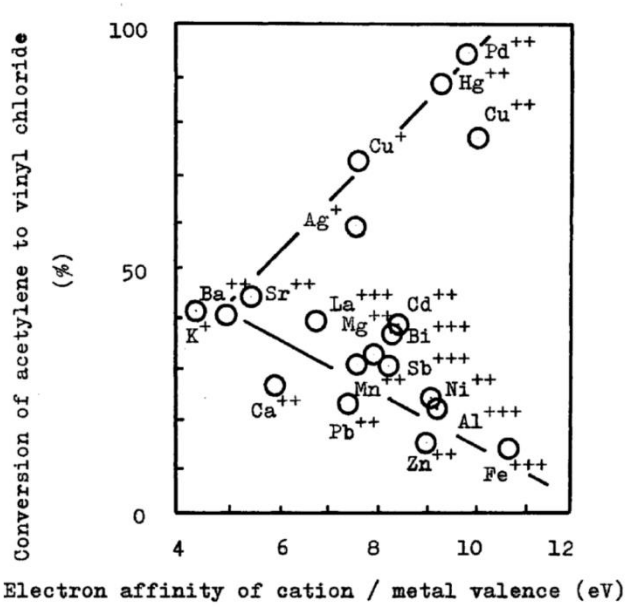

Figure 1.2 – Correlation of the hydrochlorination activities of metal chlorides supported on activated carbon and the electron affinities of metal cations divided by the corresponding metal valences (200 °C, Gas Hourly Space Velocity (GHSV) 150 h^{-1}).[25]

In addition, Shinoda's approach has another strong limitation: the correlation parameter used is the electron affinity, which considers only a single electron process, whereas, *ex situ* FTIR study performed by Smith *et al.*[24] suggested the hydrochlorination reaction to initially involve the oxidative addition of acetylene to metal centres, a 2-electron process. For this reason, in 1985, Hutchings re-plotted the data for the divalent cations reported by Shinoda against the standard electrode potential.[26] In this case, a single correlation curve is obtained, which could be used as a predictive model. As shown in Figure 1.3, the activity of the metal chlorides increases with increasing standard electrode potential, indicating that catalysts with high standard electrode potentials would be the most effective for the acetylene hydrochlorination reaction. Using this trend predictively it was determined that gold could have been the most active catalyst for this reaction. This evidence also suggested that the redox properties of the cations were important to the activity of the catalysts and was suggestive of a redox mechanism.

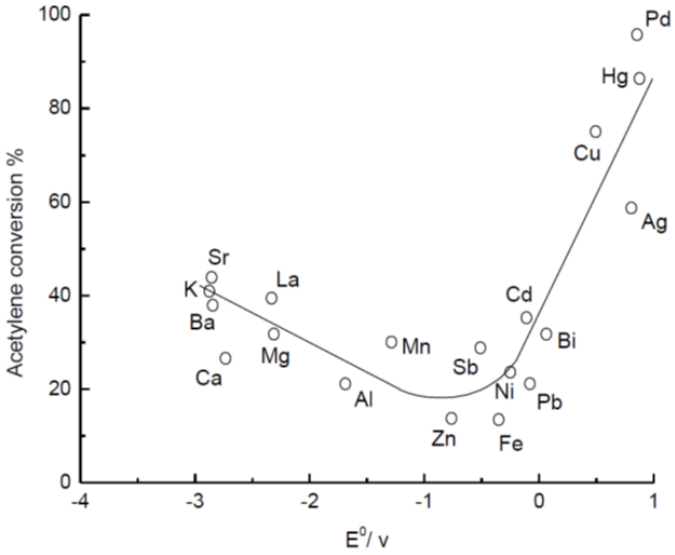

Figure 1.3 – Correlation of hydrochlorination activity of different metal chlorides supported on carbon (T = 200 °C, Gas Hourly Space Velocity (GHSV) = 150 h^{-1}), with the standard reduction potential of the metal, $M^{n+} + e^- \rightarrow M^{(n-1)+}$.[26] (conversion values after ref [25]).

It was subsequently confirmed experimentally that gold was indeed a very effective catalyst for the hydrochlorination of acetylene using supported Au(III) catalysts (Figure 1.4).[27,28,29] The data shown in Figure 1.4 confirm the correlation with the standard electrode potential (E°) and are based on initial activity, determined as an integrated rate over the catalyst bed, since the catalysts were generally affected of a rapid deactivation.

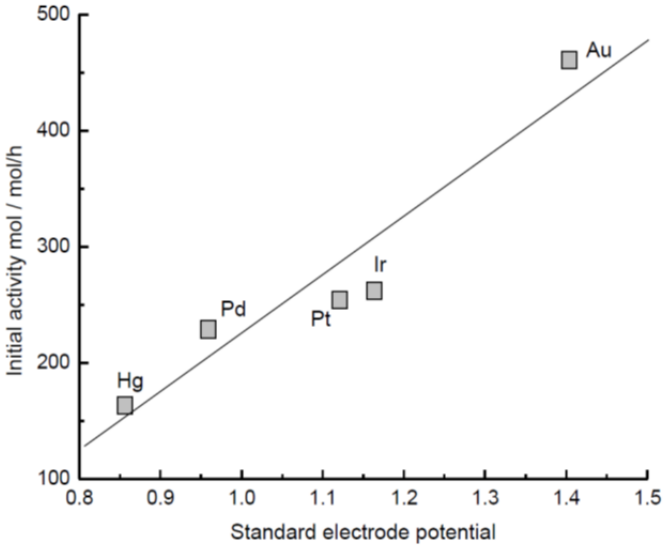

Figure 1.4 – Correlation of hydrochlorination activity of metal chlorides supported on carbon (180 °C, Gas Hourly Space Velocity (GHSV) 1140 h^{-1}) with the standard electrode potential (E°). Catalyst

contain 0.0005 mol metal/100 g catalyst. (it should be noted that in this series, Pt is obtained from a Pt^{2+} precursor).[28]

The correlation of E° with activity has been then further investigated by Conte *et al.*[30] using other platinum group metals, Figure 1.5, where the standard electrode potential of the metal chloride salt was used. In this study, all the catalysts were prepared via a wetness impregnation method using aqua regia as a solvent. The precursor salts were: $HAuCl_4$, $PdCl_2$, H_2PtCl_6, $RhCl_3{\cdot}3H_2O$, $IrCl_3{\cdot}3H_2O$ and $RuCl_3{\cdot}3H_2O$. This trend confirms the previous findings for this reaction, that is, the higher is the standard electrode potential, the higher is the activity[26,31] with the following order of initial activity: Au>Ru≈Ir>Pd>Pt≈Rh. In this correlation Pt represents an anomalous point. In fact, while in the original set Pt^{2+} was used,[26,28] in this case Pt^{4+} data were used, and in particular the reduction $Pt^{4+}\rightarrow Pt^{2+}$, whereas all the other metals had initial oxidation state II or III and the reduction for M^{n+} to M^0 was considered.[32] The reason of this anomaly can be explained considering that this catalyst deactivates very quickly and displays dehydrochlorination properties.[31] Furthermore, Pt^{4+} usually does not form stable complex with unsaturated species, and it is often considered inert towards alkyne complex formation.[33]

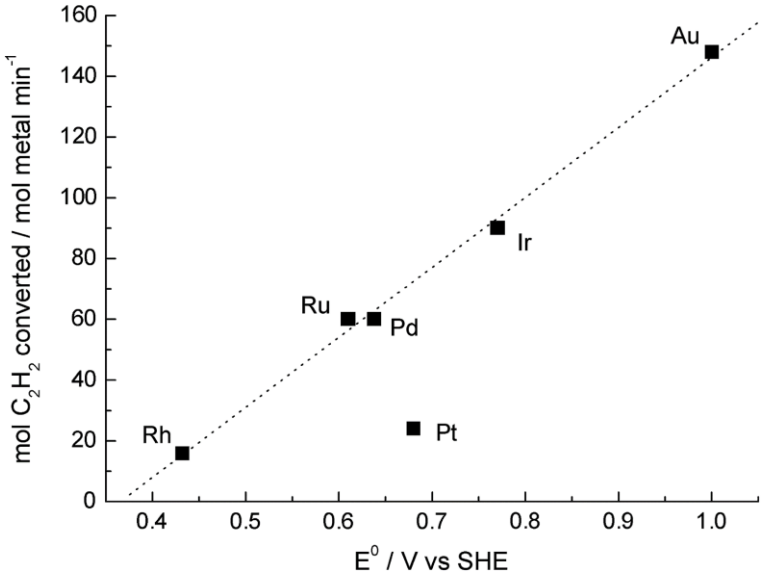

Figure 1.5 – Correlation between initial acetylene conversion and standard electron potential of platinum group metals. Potential were obtained from the reduction of the following chlorides salts: $RhCl_6^{3-}$, $RuCl_5^{2-}$, $PdCl_2$, $PtCl_6^{2-}$, $IrCl_6^{3-}$, and $AuCl_4^-$. The reaction was carried out at 180 °C, Gas Hourly Space Velocity (GHSV) 870 h^{-1}.[32]

More recently L. Lu *et al.*[34] investigated the active species in carbon-supported gold catalysts for acetylene hydrochlorination, using X-ray photoelectron spectroscopy (XPS) and transmission electron microscopy (TEM), where it was shown that fresh catalysts prepared by the impregnation of chloroauric acid dissolved in *aqua regia* comprises of a Au(III) surface film which on reaction with acetylene and

HCl transforms to a mixture of Au(I)/Au(III). Consequently, they have re-plotted the original data[30] using the appropriate chloride standard electrode potentials using the data for an Au(I)/Au(III) chloride couple.[35] The re-plotted data (Figure 1.6) confirms that a linear correlation is obtained. Further details about this work and the investigation of the active site for the acetylene hydrochlorination reaction will be reported later in this chapter.

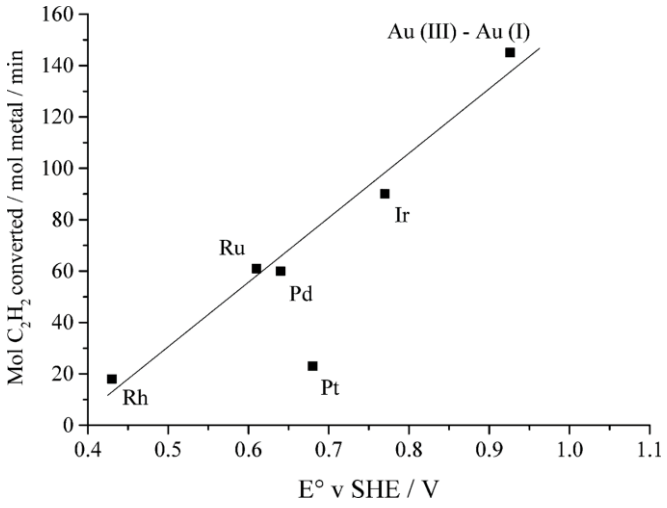

Figure 1.6 – Correlation between activity for acetylene hydrochlorination and the standard electrode potential. Potentials are obtained from the reduction potentials of the following chloride salts $(RhCl_6)^{3-}$, $(RuCl_5)^{2-}$, $PdCl_2$, $(PtCl_6)^{2-}$, $(IrCl_6)^{3-}$ (data re-plotted from reference 36, all potentials for a 2 e^- reduction). $(AuCl_4)^-$ to $(AuCl_2)^-$ potential taken from reference 37.

Importantly, Hutchings' prediction that Au would be an effective catalyst for the acetylene hydrochlorination reaction, contemporaneously with the work of Haruta *et al.*[38,39] in which they demonstrated that gold nanoparticles supported on transition metal oxides are active for the catalytic oxidation of CO at low-temperatures, led to an exponential increase in research into gold catalysis.[40,41,42,43]

1.3.3 – Deactivation/reactivation

During the acetylene hydrochlorination reaction, both the mercury and the gold catalysts deactivate with time, but the gold catalysts are much more stable at extended reaction times.[28,44] In particular, while the leaching of the metal chloride from the support seems to be the main reason of the loss of activity for most of the catalysts considered (Figure 1.7),[13] this was not the case for gold catalysts. The deactivation of gold on carbon catalyst was investigated by Nkosi *et al.*[28] by studying the effect of reaction temperature on the deactivation rate. In this study two main deactivation mechanism were identified and also it was observed that the minimum deactivation rate occurred at 100 °C, Figure 1.8.

Although this suggests that 100 °C may be the optimum reaction temperature, the activity at this temperature is too low for industrial applications and so a temperature of around 180 °C (or higher: ~200-220 °C) continues to be used for catalyst testing.[44] The deactivation observed at a temperature range between 120–180 °C was attributed to the reduction of Au(III) to metallic Au. In fact, X-ray photoelectron spectroscopy (XPS) and Mössbauer spectroscopy studies have shown that while the fresh catalyst was mainly comprised of Au(III), the deactivated catalysts was mostly Au(0).[28,29] On the other hand, at temperatures of 100–120 °C (Figure 1.8) the deactivation was found to be due to significant build-up of carbonaceous residues on the catalyst surface.

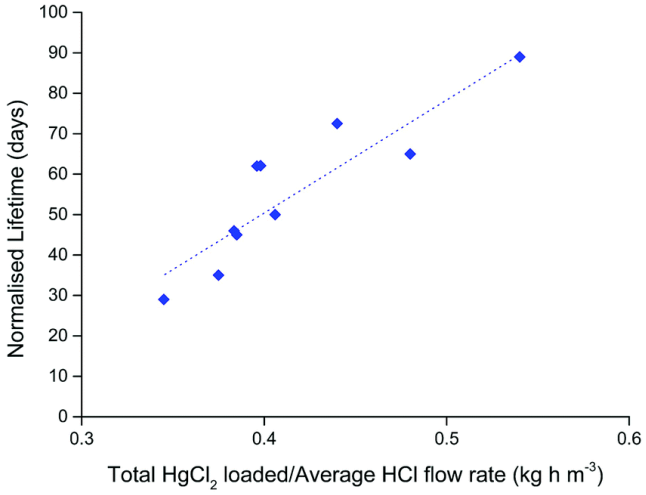

Figure 1.7 – Catalyst lifetime of mercuric chloride catalysts showing the relationship with [$HgCl_2$] and reactant flow rate.[13,45]

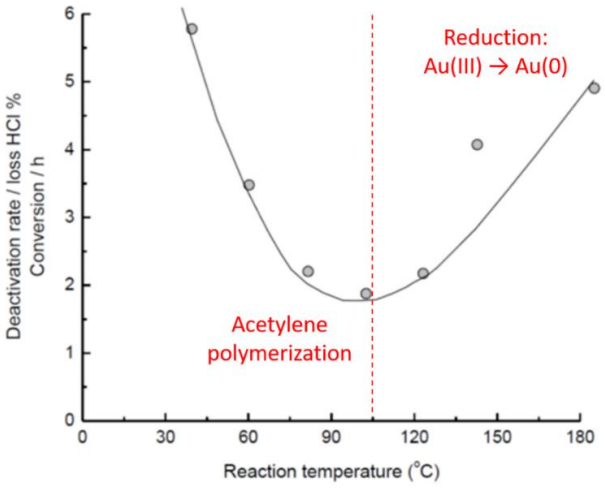

Figure 1.8 – Effect of temperature on rate of deactivation of Au/C catalysts for the acetylene hydrochlorination (loss of HCl, conversion per hour, averaged over the initial 3h). Reaction conditions: C_2H_2 : HCl = 1:1.1.[11,44]

In the recent work of P. Johnston *et al*.[12] a transmission electron microscopy (TEM) analysis of a Au/C catalyst that had been operated for several months, Figure 1.9 was reported. Both the low and the high magnification pictures clearly show the formation of significant amount of carbonaceous polymer and carbon-containing nanotubes on the catalyst surface presumably formed from gold nanoparticles, which are found at the tip of those carbon nanotubes. Analysis of the composition of those nanotubes indicated that these were arising from the acetylene polymerisation and their formation resulted from acid catalysed polymerisation reactions at strong acid sites introduced from the preparation using *aqua regia* as a medium for the dissolution/deposition of the metal precursor onto the activated carbon.[46]

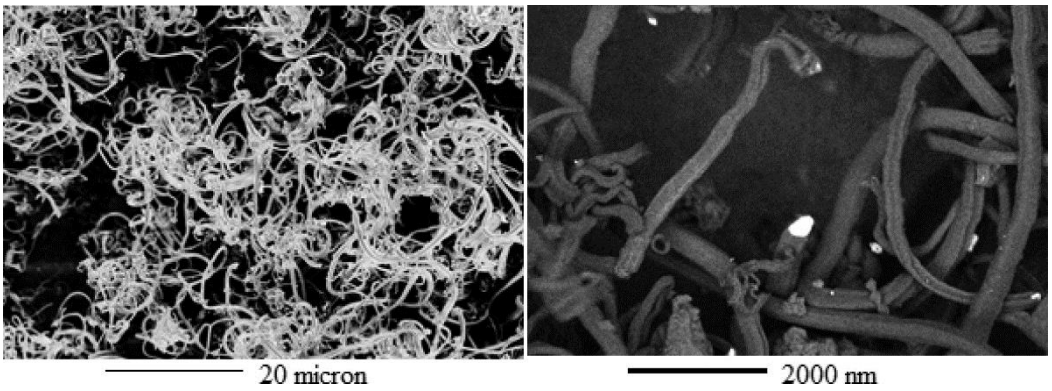

Figure 1.9 – TEM analysis of a used 1_{wt}% Au/C catalyst prepared used *aqua regia* after use for 24 days. (left) low magnification showing the extent of carbon nanofibers formed on the catalyst. (right) high magnification showing the gold nanoparticle at the tip of the carbon nanofiber.[12]

To summarise, two main routes are responsible for the deactivation of Au/C catalysts: (i) the reduction of Au(III) to metallic Au and (ii) the formation of oligomers on the catalyst surface with consequent site blocking. Although the oligomer formation can be minimised, e.g. choosing a suitable reaction temperature, the deactivation pathway due to the Au reduction is inevitable. Whilst the reactivation of mercury catalysts has not been found to be feasible, principally because the active component of the catalyst has been lost into the vapor phase, gold catalysts can be reactivated by treatment with Cl_2, NO and NO_2 at reaction temperature, with the most marked effect being displayed by NO,44 which allows full recovery of catalytic activity and slower decay of activity after the catalyst was regenerated, or by treatment with HCl.[29,44] More recently Conte *et al*.,[47] demonstrated that Au catalysts can be also be reactivated by treatment with boiling *aqua regia*[47] for a short time without changing the metal loading.

In all of these reactivation treatments it is the oxidation state of Au that is changed from the inactive form of Au(0) to Au(III) on the catalyst surface. Consequently, a correlation between the amount of cationic gold present in the unused and regenerated catalyst and their activity could be made, giving information about the active site of gold on carbon catalysts for this reaction, as it will describe in more details in the following section.

1.3.4 – Active Site of Au/C: "State-of-the-art"

Although over 30 years have passed since Hutchings' prediction that gold could be an active catalyst for the hydrochlorination of acetylene to produce VCM,[26] the nature of the active form of the catalyst is yet to be fully understood. However, general consensuses found in the literature is that the high catalytic activity of Au/C catalysts can be associated to the presence of dispersed oxidised gold species in the final material. Experimental data has not been yet conclusive about the identification of the active site. This is mainly due to two reasons: first, the observed presence of metallic Au in conjunction with cationic gold from most characterisation techniques; second, the absence of *in situ* or *operando* characterisations, mainly due to the highly corrosive nature of the reaction mixture involving roughly a 1:1 mixture of acetylene and HCl at 180−220 °C. Nkosi *et al.*,[28] performed a Mössbauer spectroscopy characterisation of a 2_{wt}% $HAuCl_4$/C catalyst, prepared using an *aqua regia* solution, providing some of the earliest evidence for cationic Au being the catalytically active species (Figure 1.10).

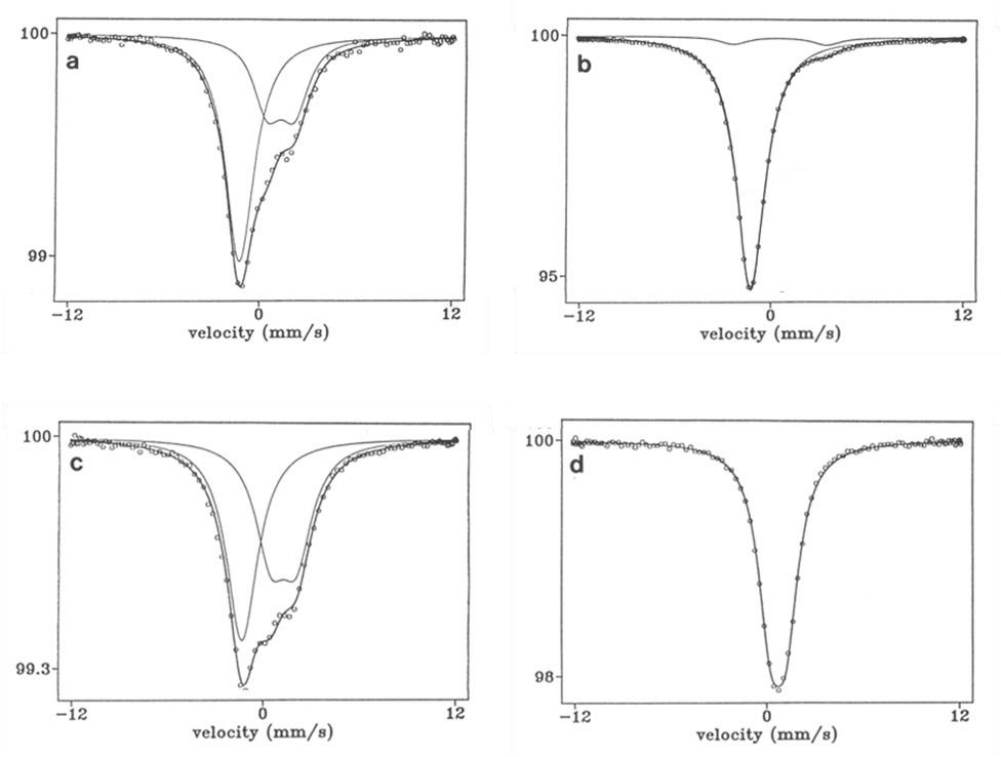

Figure 1.10 – ^{197}Au Mössbauer spectra of (a) 2% $HAuCl_4$/C - absorbed on activated carbon from aqua regia solution; (b) the same catalyst after deactivation at 180 °C for 6 h (Gas Hourly Space Velocity (GHSV) 1140 h^{-1}, C_2H_2:HCl 1:1.1); (c) a sample of the same type after reactivation by boiling in aqua regia; (d) crystalline $HAuCl_4 \cdot H_2O$.[28]

In this important experiment, the fresh catalyst (Fig. 1.10 (**a**)) was found to be comprise of both metallic Au and another species identified as adsorbed $AuCl_4^-$, due to its close similarity to the spectrum of crystalline $HAuCl_4$ (Fig. 1.10 (**d**)). Nkosi and collaborators also attempted to quantify the amount of

these different gold species observed and it was determined that, in the unused catalyst, the mass of Au metal is approximately 16 wt.% while the remaining 84 wt.% of the gold was attributed to $Au(III)Cl_4^-$ species. Conversely, the catalyst collected after reaction (Fig. 1.10 (**b**)), was almost completely comprised of metallic Au, but with an additional, even if weak, absorption line at +3.49 mm s^{-1}, hypothesised to be associated with a Au(I) species. The catalysts reactivated after reaction (Fig. 1.10 (**c**)) resulted in a recovery of the $Au(III)Cl_4^-$ species and therefore these where concluded to be associated with the active site.

In this work by Nkosi *et al*.[28] performed in 1991, not only the importance of cationic gold in the catalysts activity was highlighted, but the importance of the presence of gold in both oxidation state (Au(III) and Au(I)) and the potential relevance of the redox couple had also been speculated in the catalytic process. After that, other works have suggested the presence of cationic gold is important for high activity to be observed, but mainly as a Au(III), and the evidence have been provided by several characterisation techniques: X-ray photoelectron spectroscopy (XPS)[48,49,50], temperature programmed reduction (TPR)[51,52,53] and transmission electron microscopy (TEM) studies.[32,34 ,54] For example, recent work by Chao *et al*.[55] supports the idea that the Au(III) species are important and provides evidence that Au(III) located at the $AuCl_3$/C interface is the active site, together with the functional group of the activated carbon support. However, most of these techniques showed the co-occurrence of metallic Au in the analysed materials. The observed presence of metallic gold has also resulted in a range of postulated active species, from Au(0) clusters or nanoparticles [48,49,56] to cationic Au species at the surface of the gold nanoparticle and/or at the metal nanoparticle/carbon support interface.[51,57] In a more recent work by Zhou *et al.*,[58] the addition of a second metal to the catalyst formulation, i.e. bismuth, seems to stabilise the gold(I) which is claimed to be the active catalytic site.

Building on the pioneering work of Nkosi and collaborators in 2016 the possible role of the redox couple in the reaction mechanism has been taken into consideration again.[34] In this study a detailed analysis of the unused and the used catalyst at different times-on-stream, *via* a combination of X-ray photoelectron spectroscopy and electron microscopy, was performed. *Ex situ* XPS of the fresh sample prepared from the dissolution of the metal precursor with *aqua regia* (Au/C-AR) (Figure 1.11), initially showed significant concentrations of Au (0), Au(I) and Au(III) species (XPS Quantitative Data: 66.7%, 13.5% and 19.8%, respectively). Conventionally, TEM analysis of gold on carbon catalyst for the acetylene hydrochlorination reaction have predominantly showed the presence of metal nanoparticles.[59] In this case, thanks to the advances in both instrument resolution and the control of beam damage, high angle annular dark field (HAADF)-STEM imaging of the freshly prepared sample showed to be comprised mainly of atomically dispersed Au distributed all over the carbon support (Figure 1.12).

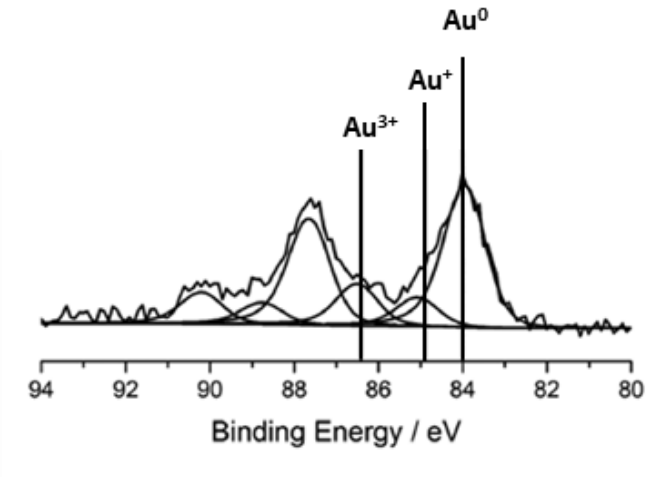

Figure 1.11 – *Ex situ* recorded X-ray Photoelectron Au(4f) spectrum for aqua regia prepared Au/C catalyst freshly prepared; XPS Quantitative Data: Au (0) 66.7%, Au(I) 13.5% and Au(III) 19.8%, respectively (data reproduced from reference 34).

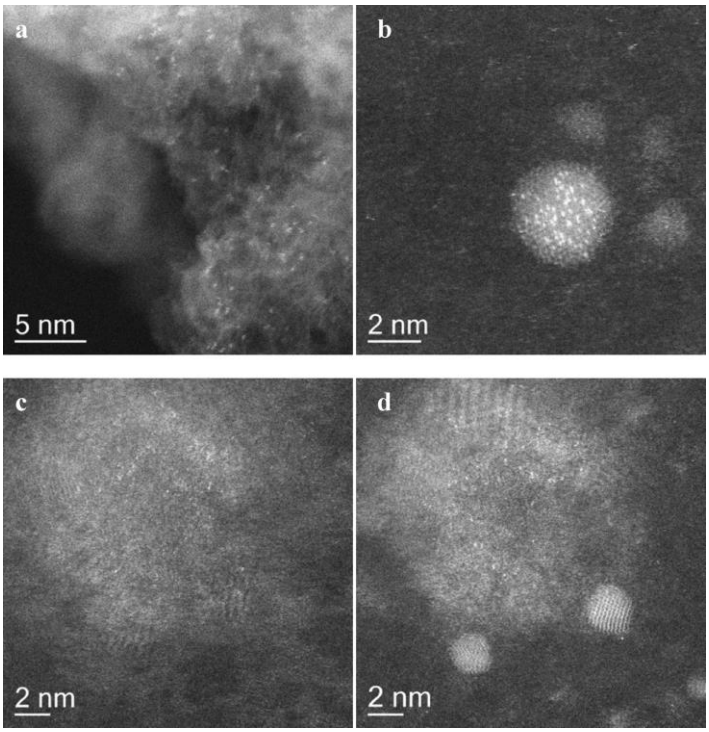

Figure 1.12 – Representative HAADF-STEM images of the as-prepared unused *aqua regia* treated Au/C sample showing: (a) dispersed Au atoms over the support; (b) discrete nanoparticles containing Au and Cl; and (c) unstable Au containing thin films which decompose to form Au nanoparticles (d) upon extended electron beam irradiation (data reproduced from reference 34).

In this important work the use of different solvents other than *aqua regia*, i.e. HNO_3, HCl and H_2O, has been investigated in terms of effect in both dispersion and the nature of the Au species present in the

final material. Interestingly the active catalysts were initially inactive and characterised by a pronounced induction period (Figure 1.13), which was hypothesised to be related with development of the active gold species during the reaction upon interaction with acetylene and hydrogen chloride at the reaction temperature.

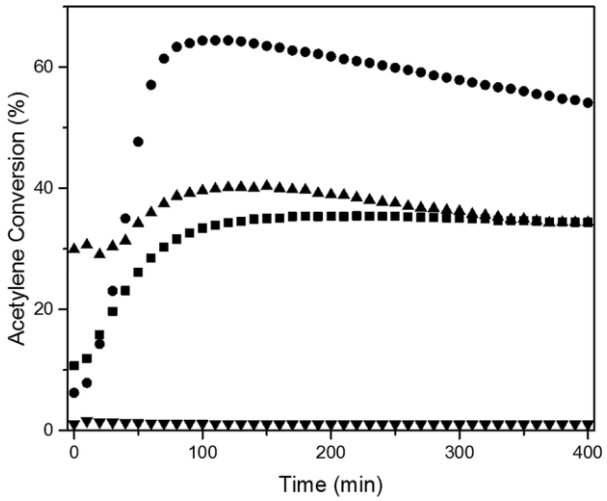

Figure 1.13 – Catalytic performance of the supported gold catalysts as a function of reaction time, the carbon supported gold catalysts prepared from water, HCl, HNO_3 and *aqua regia*, are labelled as Au/C-H_2O (▼), Au/C-HCl (▲), Au /C–HNO_3 (■) and Au /C–AR (●), respectively. All catalytic tests were conducted under identical reaction conditions: 150 mg catalyst, 5 mL min^{-1} C_2H_2, 6 mL min^{-1} HCl and 10 mL min^{-1} N_2, 185 °C.[34]

Figure 1.14 shown the XPS spectra of the evolution of the gold composition in the Au/C-AR catalysts during the induction period, first 60 min of reaction, until 300 minutes of reaction. During the time-on-line, the Au(I) concentration increases with a related decrease in the Au(III) concentration (Table 1.1), meaning that, while Au(III) is important in the initial phase, Au(I) has to be present for high activity to be observed. Moreover, the observation of high and constant Au(0) content in catalysts from XPS led to the conclusion that while cationic Au is very likely to be the active site, it must exist in association with metal gold nanoparticles and in particular metallic nanoparticles partially oxidised at the surface.

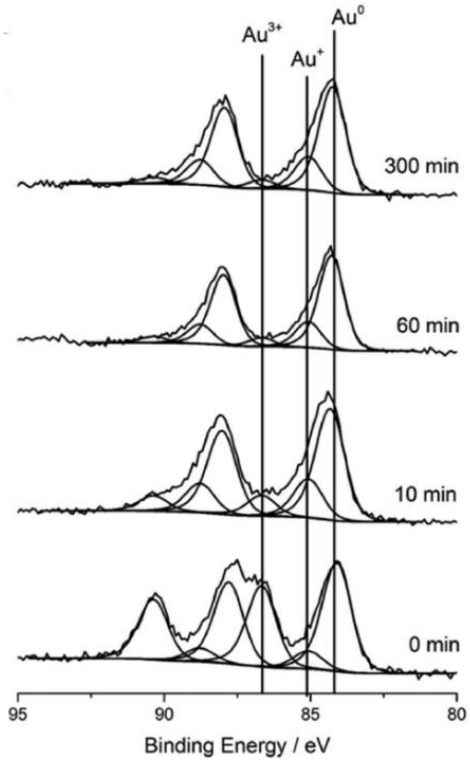

Figure 1.14 – *Ex situ* recorded X-ray Photoelectron Au(4f) spectra for *aqua regia* prepared Au/C catalyst taken from the reactor at different times-on-line.[34]

	Area % Au(0)	***Area % Au(I)***	***Area % Au(III)***
0 min	52.4	8.6	39.0
10 min	72.9	16.3	10.8
60 min	78.4	15.6	6.0
300 min	77.7	17.5	4.8

Table 1.1 – Quantitative XPS data for figure 1.13.[34]

Figure 1.15 shown HAADF-STEM imaging of the sample acquired after 60 min of reaction, in which it is possible to observe the presence of an atomically disperse gold speciation together with Au nanoparticles. However, given the predominant presence of metallic gold in the XPS one should have expected to observe more discrete gold nanoparticles in the STEM. Indeed, it very likely that the presence of metallic gold nanoparticles could have been over represented due to photo-reduction in XPS analysis. In the literature is possible to find several works where it is demonstrated that $AuCl_4^-$

salts can easily undergo photo-reduction to metallic Au, [60,61,62,63] as shown in Figure 1.16.[60] Although the quantitative analysis is clearly affected by this issue the qualitative results showed in Liu's work can be considered valid. However, for this reason, in this thesis has been decided not to rely on XPS to characterise any of the sample prepared and studied.

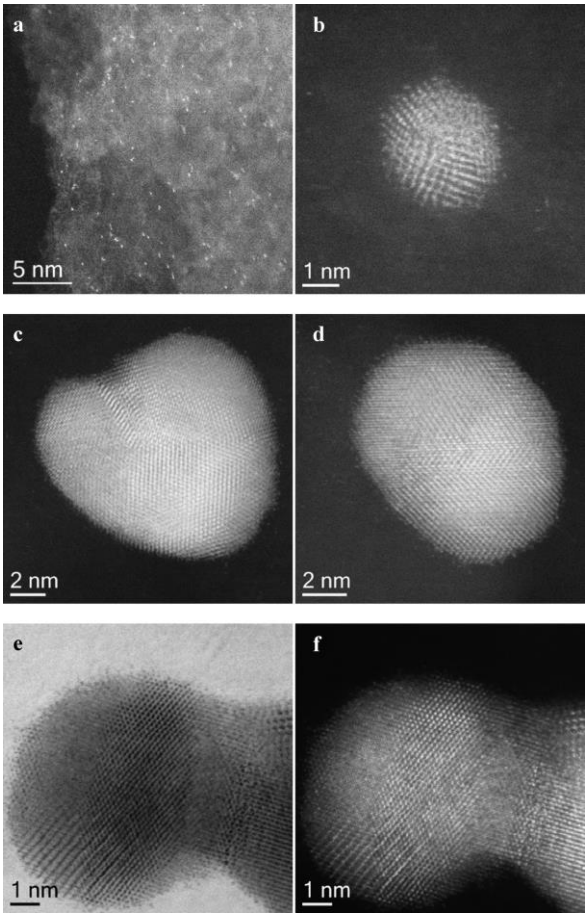

Figure 1.15 – The *aqua regia* treated Au/C sample after 60 minutes of use: (a) HAADF-STEM image showing discrete Au atoms decorating the support; (b) HAADF-STEM image of a discrete Au nanoparticle; (c) and (d) HAADF-STEM images of sintered agglomerates of Au nanoparticles; (e) and (f) complimentary BF- and HAADF-STEM image pair of a sintered Au agglomerate. Note that images (c)–(f) show evidence of an unidentified debris decorating the particle surface.[34]

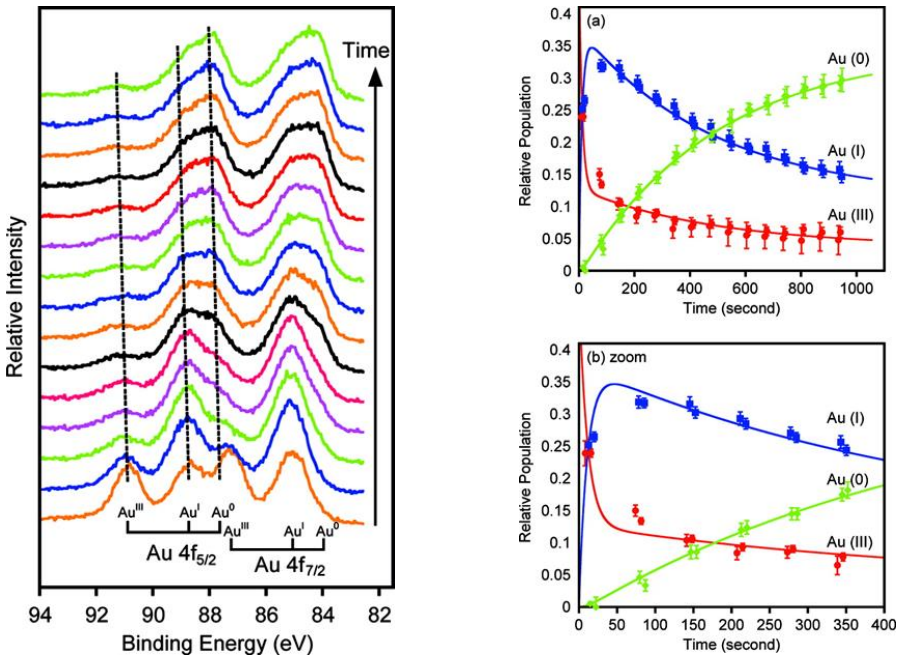

Figure 1.16 – (left) XPS spectra of sodium tetrachloroaurate ($NaAuCl_4$) as a function of time under synchrotron X-ray exposure. The dotted lines represent the peak position of the $4f_{5/2}$ peaks of each gold species. (right) (a) Population of the different gold species as a function of synchrotron exposure time. (b) The same data recorded within the first 400 s of exposure. The data points represent the relative population of each oxidation state. The lines represent best fits to the data. The error bars represent three standard deviations as determined by the least-squares fitting procedure.[60]

Sample damage during characterisation or lack of instrument resolution has limited the capability of understanding the detailed nature of these cationic species for the acetylene hydrochlorination reaction. Moreover, removing the sample from the reaction environment in order to perform *ex situ* characterisation may have led to misinterpretation due to the highly dynamic structure of these heterogeneous catalysts. For this reason, *in situ* or *operando* characterisation of catalysts under reaction conditions are now increasing.[64,65,66]

1.3.4.1 – Application of Cationic Gold in Homogeneous Catalysis

The role of cationic gold in the field of both heterogeneous and homogeneous catalysis has been previously reported extensively, in which the importance of gold(I) and gold(III) in the conversion of alkynes has been already documented.[67,68,69]Around the same time of Hutchings' and Haruta's discoveries in the field of heterogeneous catalysis,[26,38] Ito *et al.*[70] reported the first example of a gold(I) catalysed asymmetric aldol reaction. A common feature between heterogeneous and homogeneous catalysis by gold is the possibility to perform reactions under mild conditions maintaining high selectivity; in particular, very high selectivity of gold towards reaction of alkynes[71], which are the most

popular substrates in the field of homogeneous catalysis by gold.[72] The reason for the high reactivity of the alkynes, typically more reactive than the corresponding alkenes, arise from their electronic structure[73]. Typically, these substrates react with electrophilic reagents (E), i.e. halogens in organic synthesis, or electrophilic metal centres, i.e. gold (I or III) in the field of transition metal catalysis.[74,75] In the interaction with a metal centre, both the π-orbital in the plane of metal coordination and the π-orbital perpendicular to it can interact with the d-orbitals of the metal. This coordination withdraws electron density from the alkyne that becomes more electrophilic, enabling the attack of even weak nucleophile (Figure 1.17). [72]

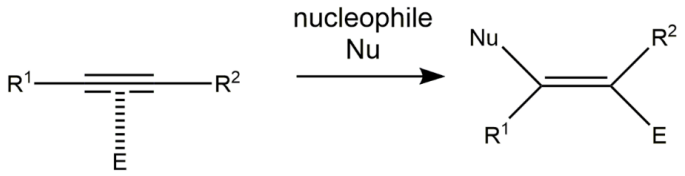

Figure 1. 17 – Nucleophilic-electrophilic interaction between the Au centre and the triple bond via π-coordination, where E is the metal centre.[72]

In the case of terminal alkynes[75] and acetylene itself, a second mode of interaction is possible, especially with gold(I)-complexes. The gold replaces a terminal hydrogen atom of alkyne, in the presence of a base which, taking up the hydrogen atom as a proton, can form gold(I)-alkynyl complexes (Figure 1.18).[76]

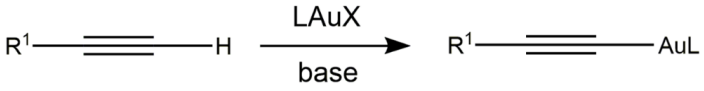

Figure 1.18 – σ-coordination between Au(I) and terminal alkynes via exchange reaction, with formation of. Formation of the Au(I)-alkynyl complex.[76]

Occasionally both the π-coordination and a gold-alkynyl-σ-bond can be found (Figure 1.X).[77]

Figure 1.19 – Contemporaneous presence of π- and σ-coordination of a terminal alkyne on two different Au centres (E).[77]

An important achievement in homogeneous catalysis was the addition of nucleophiles to alkynes. The first example is the work of Fukuda and Utimoto,[78] in which they investigated the addition of alcohols, water, and amines to alkynes. However, the most important result was obtained by Teles *et al*.[79] in 1998; in this work it was demonstrated that cationic gold(I) species gave great turnover numbers (TONs) and turnover frequencies (TOFs) for the addition of alcohols to alkynes. This result still represents one of

the most important examples of gold(I) in homogeneous catalysis. Following up from this work, in 2000, Hashmi *et al*. [80] extended the nucleophilic additions from alkynes to olefins for both the intramolecular additions of alcohols and the intermolecular addition of arenes. Since then, homogeneous gold catalysts have been used for numerous reactions of alkynes, e.g. hydrogenations, hydrations and hydrohalogenations. [81,82,83,84] In particular, it is reported that gold(III) can be superior to mercury(II) in activating alkynes for the addition of nucleophiles like H_2O or Cl.[83,85] García-Mota *et al*., [86] performed experimental and theoretical studies to analyse the selective activation of alkenes and alkynes and or enyne compounds of gold catalysts, in the form of nanoparticles, in both homogeneous and heterogeneous catalysis. They conclude that the selectivity is controlled by different mechanisms in homo- and heterogeneous gold catalysts. For heterogeneous catalysis, differential reactant adsorption is the key, leading to bonded, active species that give rise to fast hydrogenation or hydration reactions. Thus, the origin of the selectivity is in this case thermodynamic. While, for homogeneous catalysts, the alkynophilicity is not related to the relative strength of the bonding of the active alkyne species, but to its activation for a desired reaction. Thus, the origin of this high selectivity is kinetic in homogeneous catalysis.

1.3.5 – Role of the Individual Reactants

As mentioned previously, the work of Liu and collaborators underlined that the pronounced induction period observed in the active catalyst during the reaction could be associated with development of the active gold species during the reaction upon interaction with both reactant at the reaction temperature.[34] Previously Conte *et al.*[57] performed a detailed investigation into the mechanism of the reaction, including the study of the effects of the individual reactants on the catalyst. The results are showed in Figure 1.20 and the four sets of experiments were conducted as follows:

- Experiment A: C_2H_2/HCl (2 h) → He/HCl (2 h) → C_2H_2/HCl (2 h)
- Experiment B: He/HCl (2 h) →C_2H_2/HCl (2 h) →He/HCl (2 h)
- Experiment C: C_2H_2/HCl (2 h) → C_2H_2/He (2 h) → C_2H_2/HCl (2 h)
- Experiment D: C_2H_2/He (2 h) → C_2H_2/HCl (2 h) → C_2H_2/He (2 h)

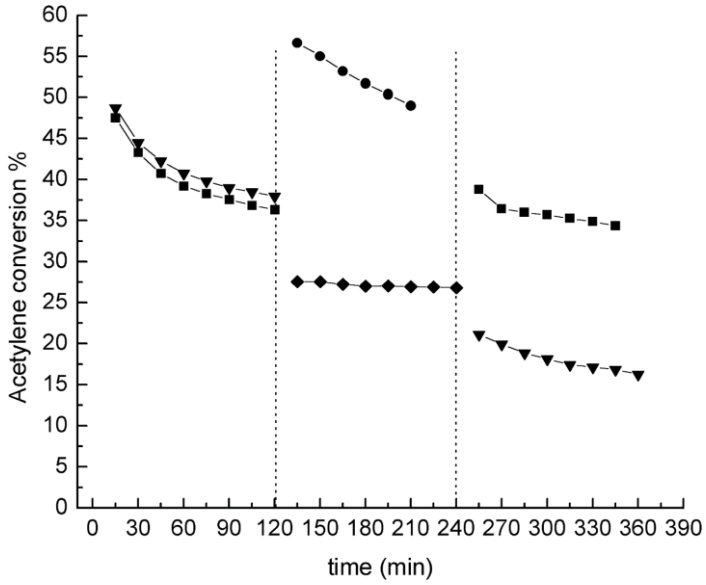

Figure 1.20 – Sequential flow experiments to evaluate the effect of each reactant for the hydrochlorination reaction of acetylene over Au/C catalyst. (Experiment A: ■) C_2H_2/HCl (2 h) → He/HCl (2 h) → C_2H_2/HCl (2 h); (experiment B: ●) He/HCl (2 h) → C_2H_2/HCl (2 h) → He/HCl (2 h); (experiment C: ▼) C_2H_2/HCl (2 h) → C_2H_2/He (2 h) → C_2H_2/HCl (2 h); and (experiment D: ▼) C_2H_2/He (2 h) → C_2H_2/HCl (2 h) → C_2H_2/He (2 h).[57]

From these experiments it is possible to observe that both C_2H_2 and HCl are able to modify the final performance of the catalyst, but in opposing ways.[57] In particular, the detrimental role of acetylene is demonstrated in this work. In fact, even when no reaction occurs initially, the catalyst is deactivated by exposure to C_2H_2, and when the reaction is brought on line again, the conversion to vinyl chloride is markedly lower compared with a standard reaction without interruption of the reactants, thus proving the detrimental role of C_2H_2. On the other hand, if HCl is used in excess, the catalyst can recover its initial activity, while this does not happen if HCl is used in a less than a stoichiometric amount.[57] Despite the importance of these experiments, this does not yet provide details of the reaction mechanism but provides an important support for the theoretical work described in the next section.

1.3.6 – Proposed Reaction Mechanism

Preliminary kinetic studies over Au/C catalysts determined that the reaction is first order with respect to both reactants, acetylene and HCl,[44] and formation of an activated C_2H_2-Au-HCl complex has been suggested as a reaction intermediate.[87] This results is peculiar of the reaction over Au/C; in fact, kinetic studies performed over $HgCl_2$/C catalysts indicated that in this case the rate-determining step of the reaction involves addition of HCl to a C_2H_2-Hg complex in an Eley-Rideal fashion instead

of a Langmuir-Hinshelwood mechanism (Figure 1.21). Detailed information about this will be provided in this section.

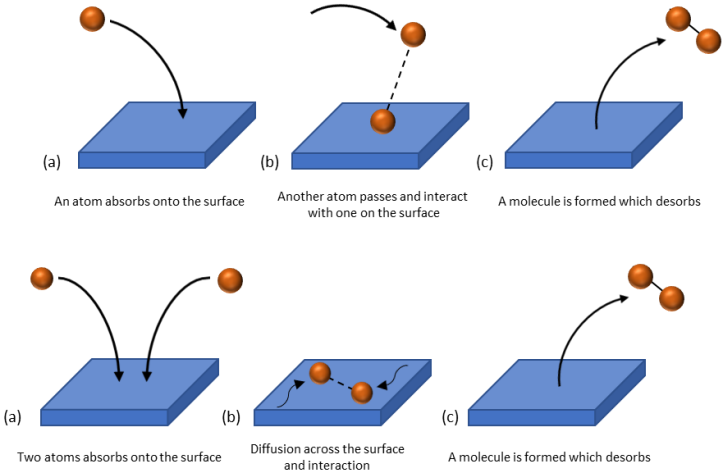

Figure 1.21 – (top) general scheme for the Eley-Rideal mechanism and (bottom) the Langmuir-Hinshelwood mechanism.

Another important difference between the two classes of catalysts is that the reaction over Au/C presents a selectivity towards VCM of ~ 100%,[26,32] whereas the reaction over $HgCl_2$ leads to a significant amount of 1,2-dichloroethane.[13,14] When considering reactions in the presence of double or triple bonds there are two different ways in which two substituents can be added: syn-addition (two substituents to the same side of a double bond or triple bond) and anti-addition (two substituents are added to opposite sides of a double bond or triple bond). Moreover, if we consider the addition of hydrogen halides to alkenes, or alkynes as in the hydrochlorination of acetylene, the product obtained can be Markovnikov or anti-Markovnikov. This is an empirical rule based on Markovnikov's experimental observations which states that: "*when an unsymmetrical alkene reacts with a hydrogen halide to give an alkyl halide, the hydrogen adds to the carbon of the alkene that has the greater number of hydrogen substituents, and the halogen to the carbon of the alkene with the fewer number of hydrogen substituents.*".

As already mentioned earlier in this chapter, the reactivity of cationic gold towards alkynes is usually explained in two ways: a nucleophilic-electrophilic interaction between the Au centre and the triple bond via π-coordination (Figure 1.17), the formation of σ-coordination complex in presence of a base (Figure 1.18) or the contemporaneous presence of π- and σ-coordination of a terminal alkyne on two different Au centres (Figure 1.19).
Unfortunately, being a symmetrical molecule, the reaction of acetylene does not provide mechanistic data since only one product is possible. For this reason, experiments with substituted alkynes were performed previously by Conte *et al.*,[57] The substrates used are shown in Figure 1.22.

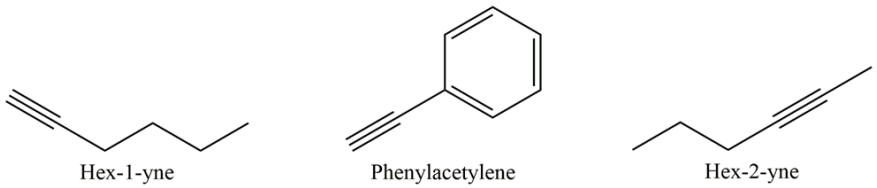

Figure 1.22 – Substituted alkyne substrates used to investigate the mechanism of addition of HCl across the alkyne bond.

Hydrochlorination of hex-1-yne can lead to four different products (Figure 1.23). ^{1}H NMR spectroscopy showed that the product distribution consists of 96% Markovnikov products (**1** and **2**) and the remaining 4% is constituted by the anti-Markovnikov product with anti HCl addition (**4**). These results are extremely important, in fact from this a pure nucleophilic electrophilic interaction over Au(III)centres (or a pure Eley-Rideal mechanism if a surface is considered) can be excluded, because it would lead to a syn-addition product. On the other hand, the anti HCl addition to the acetylene triple bond can be only obtained if the existence of C_2H_2-Au-HCl complex is taken into consideration.

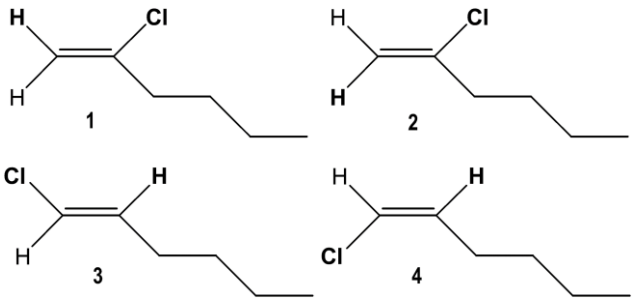

Figure 1.23 – Possible regioselectivity and stereochemistry of the addition of HCl to hex-1-yne: 1, Markovnikov with syn HCl addition; 2, Markovnikov with anti HCl addition; 3, anti-Markovnikov with syn HCl addition; and 4, anti-Markovnikov with anti HCl addition.[57]

Phenylacetylene was found to be slightly less active than hex-1-yne, this lower activity can be attributed to the aromatic ring conjugation with the triple bond. Also in this case there are four possible products (Figure 1.24). The major products were determined to be the Markovnikov products **5** and **6** (>99%) with traces of the product for the anti-addition of HCl **8** (<1%). Reported in Table 1.2 are the differences in observed activity for these substrate, together with acetylene, which can be attributed to the steric hindrance of the substrates.[57]

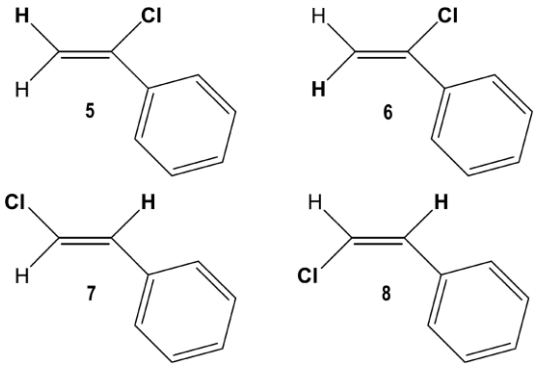

Figure 1.24 – Possible regioselectivity and stereochemistry of the addition of HCl to phenyl-acetylene: 5, Markovnikov with syn HCl addition; 6, Markovnikov with anti HCl addition; 7, anti-Markovnikov with syn HCl addition; and 8, anti-Markovnikov with anti HCl addition.[57]

Substrate	***Conversion (%)***
Acetylene	25-50
Hex-1-yne	10
Phenylacetylene	7
Hex-2-yne	<2

Table 1.2 – Average hydrochlorination conversions for different alkynes as substrates.

These results support the hypothesis of the formation of a C_2H_2-Au-HCl complex (Figure 1.24), which can be represented as a distorted six membered ring between Au(III) centre, Cl and RC≡CH with chloride as the counter ion (Figure 1.25). In view of this, it is reasonable to propose the reaction scheme shown in Scheme 1.3.

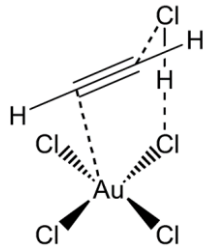

Figure 1.25 – Formation of a C_2H_2-Au-HCl complex is assumed to explain the acetylene hydrochlorination with the formation of a six-membered ring.[57]

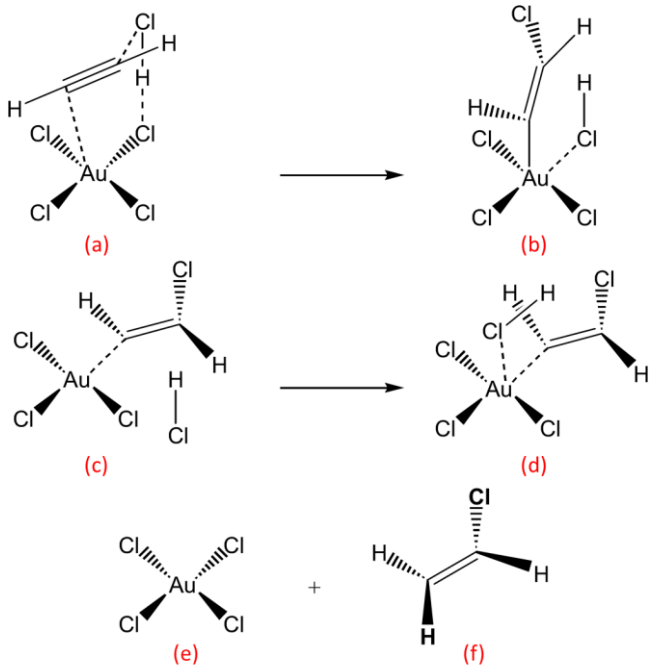

Scheme 1.3 – Proposed model for the hydrochlorination of acetylene over Au/C catalyst, assuming C_2H_2-Au-HCl complex formation.[57]

In this model, starting from the initial six-membered ring (a) the subsequent cleavage of HCl giving H transfer to an adjacent chloride (b) is observed. This results in a penta-coordinated complex. This pent-coordinated complex can be considered to be unstable, for this reason HCl is removed from the system(c). To obtain the final product and regenerate the catalyst the addition of HCl is required (d), with the H that gives the final organic substrate (e), and the Cl atom that regenerates the catalyst (f). Once again it is very important to underline that the final product, which results from an anti-addition of HCl, can only be obtained via the C_2H_2-Au-Cl complex, and not *via* a Eley-Rideal model. Most importantly this proposed mechanism is complementary with the results obtained regarding the hydrochlorination of higher alkynes and experimental evidence showed in the previous section. In particular and the regeneration effect of HCl (d),[29,57] and the deleterious effect of C_2H_2 and can also explain polymerisation that could lead to catalyst deactivation.[44]

1.3.6.1 – Density Functional Theory Calculations

To obtain a deeper insight to the reaction mechanism, Conte *et al.*[57] also performed a detailed molecular modelling study applying density functional theory (DFT) calculations. In this case, the active species considered was $AuCl_3$ instead of $AuCl_4^-$ for two main reasons: firstly, the use of $AuCl_4^-$ in molecular modelling investigations could lead to some complications owing to the presence of a negative charge and secondly despite the central role of Au(III) centres, it seems more realistic to take

into account to some extent the effect of the support. Considering the latter motive if a supported species is considered, it is more realistic to propose the existence of $AuCl_3$ rather than $AuCl_4^-$, as $AuCl_3$ would lead to a square-planar coordination with the alkyne. $AuCl_3$-alkyne complexes have also been calculated recently at a fully relativistic level and compared with corresponding isoelectronic Pt(II) complexes,[88] showing that a Markovnikov-type attack on the alkynes is the most probable mechanism.

The first step in the development of the molecular modelling requires the determination of the $AuCl_3$ geometry. The 3 chloride ligands do not have an equispaced arrangement at 120 ° each; rather, the $AuCl_3$ has a T-shape with the largest Cl-Au-Cl angle of 169 °C. it is between these two chloride atoms that the lowest unoccupied molecular orbital (LUMO) is localised. This is consistent with the electrophilic nature of Au(III) and it is within this Cl-Au-Cl angle that a ligand can be placed to achieve a square-planar geometry.[57] (Figure 1.26)

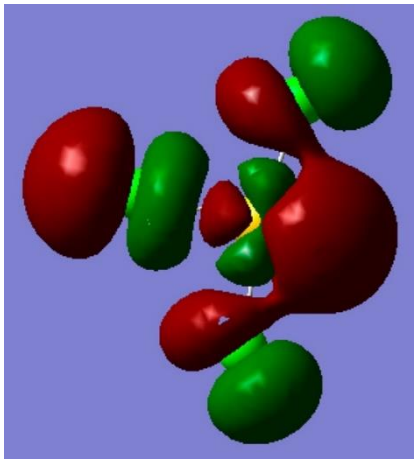

Figure 1.26 – Calculated LUMO state for $AuCl_3$ at the BH and H/6-31(d,p) level. The AuCl3 structure geometry optimisation gave a T-shaped complex with a largest Cl–Au–Cl angle of 169°. The lowest unoccupied molecular orbital (LUMO) of this structure has a large lobe in the plane of the complex between the two trans Cl ligands. This is consistent with the well-known electrophilic nature of Au(III) and would suggest complexation of a nucleophilic reactant in a square planar geometry.[12,57]

Thus, DFT calculations were carried out using C_2H_2, HCl and $AuCl_3$ as the active site.[89,90] The reaction pathway is shown in Scheme 1.4.[12,57] With respect to the reference state **1**, the coordination of HCl results in a calculated coordination energy of −105 kJ mol^{-1} **2**, while coordination of C_2H_2 with $AuCl_3$ results in a relative energy of −168 kJ mol^{-1} **3**. Although C_2H_2 gives the lower coordination energy, both reactants could independently coordinate with the Au centre. However, the coordination of acetylene to **2** does not seem to be possible, while coordination of HCl over a pre-existing 3 complex can lead to an C_2H_2-Au-HCl complex **6,** with a coordination energy of -180 kJ mol^{-1}, which is more stable that the single coordination of C_2H_2 to $AuCl_3$ **4**. This is to be considered the key step of the

hydrochlorination reaction of acetylene over Au/C catalysts, leading to the activated complex **7**, characterised by a distorted symmetry with the two hydrogen atoms of the acetylene molecule on the opposite sides on the newly forming alkene, as a consequence of a sigma interaction of Au with acetylene. The next step consists in the HCl cleavage to add Cl directly to the alkyne and H to one of the chloride atoms of $AuCl_3$. Finally, an H atom migrates to replace the Au centre to the alkyne **8**.

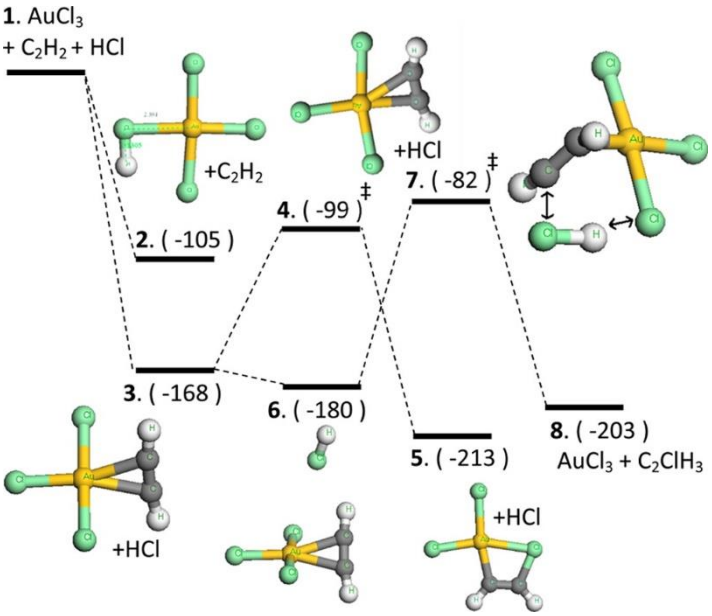

Scheme 1.4 – Reaction energy profile for hydrochlorination of acetylene. All energies in kJ mol^{-1}, transition states marked with ‡. Key: Au, yellow; Cl, green; C, grey; H, white.[12,57]

The mechanism proposed with theoretical study is in agreement with the experimental results however it does not consider in any case the presence of Au(I). Thus, the evidence obtained by the characterisation of Au/C for the acetylene hydrochlorination reaction and theoretical results are not consistent at the moment.

1.3.7 – Alternative Preparation and Commercialisation

For all the reasons mentioned in section 1.3.1 of this chapter, during the last decade, the amount of research focused on finding a suitable replace to mercury-based catalysts for the acetylene hydrochlorination reaction has increased significantly. Although the performance of other monometallic systems has been investigated, i.e. Ag,[27] mechanically activated Pt[91] and Pd[92] chloride salts, Pd,[32] Rh,[27] Ir[44] and Cu[93] chlorides, they all show significantly reduced activity and stability compared to Au. However, while gold catalysts are demonstrated to be most active and selective for the reaction, their stability is still considered an issue. To increase the stability of these catalysts, the

reduction of cationic gold to metal needs to be avoided and the inhibition of coke deposition needs to be achieved.

Several studies in which the addition of a second or third metal, to obtain a bimetallic catalyst, has been postulated to be a good way to effect reactivity and stability of more conventional monometallic catalyst through a synergistic effect, which results in one of more of the following: inhibition of the reduction of Au(III) to metallic gold, higher dispersion of Au on the catalyst surface, inhibition of formation of carbonaceous deposits or, lastly, enhanced absorption of the reactants. Examples include bimetallic systems, such as Au-Sr, [94] Au-Sn,[95] Au-Ba,[96] Au-Bi,[97] Au-Cs,[98] and Au-Cu,[99,100] but also trimetallic such as Au-Cs-Cu, [101] and Au-Cs-In,[99] and Au-Co-Cu .[102,103] However, the reaction conditions in which these catalytic system have been tested, usually have very low gas hourly space velocity (GHSV), which are not suitable to determine if these catalytic systems can be a valid alternative for an industrial application.

Catalysts which utilise a metal oxide in addition to the Au on an activated carbon support have also been investigated, for example ceria (CeO_2)[94] or titania (TiO_2)[104]. The choice of different support material than carbon has been investigated. Support materials are required, not only to be resistant to the harsh reaction conditions, but they must stabilise the high dispersion of metal chloride and prevent agglomeration and reduction of the active phase. Early studies utilised SiO_2 as a support material to aid in spectroscopy studies, but noted that the acidic groups caused polymerisation of the acetylene[26] also Al_2O_3 has been utilised as a support for a Au–Cu catalyst but suffered from deactivation caused by carbon deposition.[98] However, in all the cases reported above activities and selectivities of those systems are not high enough to results in a competitive catalytic material compared to Au/C catalyst made with *aqua regia*. Unfortunately, the stability of gold-based catalysts is not the only issue, several are the disadvantages which make the industrial application of this class of catalyst practically ineffective. The use of *aqua regia* in the catalyst preparation represent a significant concern both from an economic and a technical point of view in term of its handling/recycling/disposal.

Attempts at using alternative solvents lead to ineffective catalysts.[34] More recently, Zhao *et al*.[105] employed new ‘‘organicus liquor regius’’ prepared by adding organic compounds to $SOCl_2$, also named Organic Aqua Regia (OAR),[106] for the preparation of active Au/AC catalysts for the hydrochlorination of acetylene. However, at this stage, it does not provide a real alternative to more commonly used *aqua regia* preparation methods. Finally, the price of gold in the last three years fluctuated around a value of *ca.* 40 000 USD per kg.[107] Because of this, a low Au metal loading (<0.25 wt%) is desirable. Unfortunately, is not possible to use Au loadings of Au/C catalysts prepared from *aqua regia* below ca. 0.3% without experiencing difficulties with the catalyst activation. [12, 108]

In the last few years, interest has moved towards the possible use of different gold precursors to the conventionally used $HAuCl_4$. Huang *et al*.[54] reported the application of a highly stable Au(III)/Schiff-based catalyst in acetylene hydrochlorination reaction, in which the 1,10-phenanthroline ligand seems

to partially inhibit the reduction of gold. More recently, Zhou *et al.* [109] reported an interesting low content Au catalyst for hydrochlorination of acetylene, made by incipient wetness impregnation of a Au-thiocyanate complex. This catalyst showed to be extremely stable and was also employed in a pilot experiment, in which it maintained high stability and activity for over 3000 h (Figure 1.27).

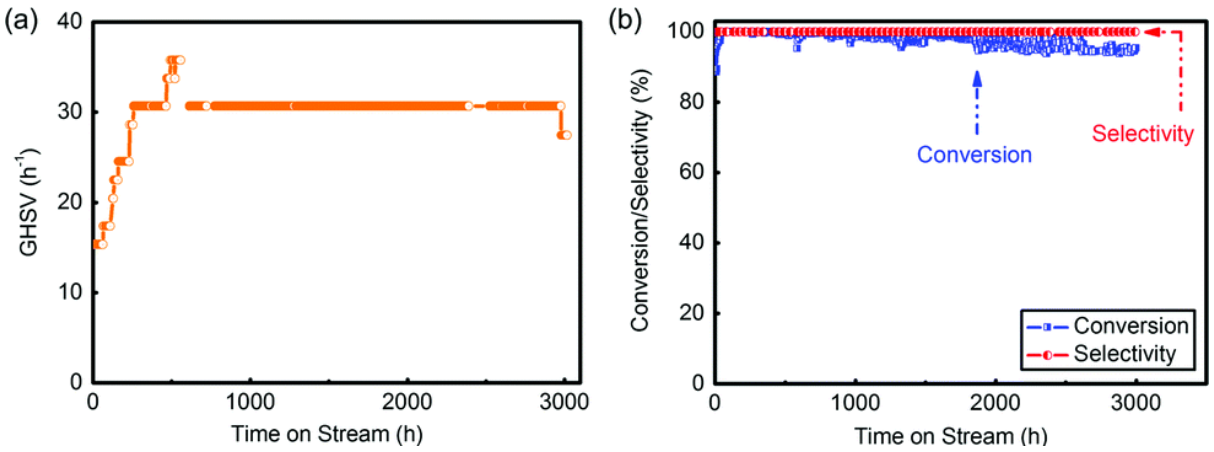

Figure 1.27 – (a) Gas Hourly Space Velocity (GHSV) during the evaluation of the pilot-trial analysis; (b) conversion and selectivity in this 3000 h evaluation.[109]

This catalyst exhibited a lower deactivation rate when compared to the tetrachloroaurate prepared catalysts. Although, the toxicity of the thiocyanate makes the industrial application of those class of catalyst unsustainable, the use of this kind of metal precursor, and in particular the use of alternative ligands, seems to be the right direction to obtain a real alternative catalyst to the one prepared by dissolving $HAuCl_4$ in *aqua regia*.

In 2007, Johnson Matthey started a project to develop an Au/C catalyst as a replacement of the $HgCl_2$/C catalysts operated in tubular fixed bed reactors in China.[12] Since the beginning, their aim was to identify a gold complex that could ensure stability of cationic gold under reaction condition. As to do so the stability constant for a selection of Au(I) and Au(III) complex has been investigated. It has been reported that complexes such us cyanides, thiourea, thiosulfate and thiocyanate are more stable, i.e. display a greater stability constant, than complexes containing halides, nitrogen or oxygen atoms.[12] Therefore, complexes with ligands containing soft donor atoms may display greater stability, and therefore activity, for this reaction over complexes with harder donor ligands. Based on this evidence, the performance in acetylene hydrochlorination of a series of sulphur-containing ligand catalyst have been evaluated and the results are showed in Table 1.3. Importantly, this new class of catalysts have been prepared by immobilisation of cationic gold complex on activated carbon from aqueous solution,[12,110] avoiding the use of *aqua regia*.

Au precursor complex	*Au (%)*	*Conversion[b] (%)*
$Au(CS(NH_2)_2)_2$	0.1	95
$Na_3Au(S_2O_3)_2$	0.1	86
$KAu(CN)_2$	0.1	85
$(NH_4)_3Au(S_2O_3)_2$	0.1	75
$KAu(SCN)_4$	0.1	74
$Ca_3[Au(S_2O_3)_2]_2$	0.1	74
$KAu(CN)_4$	0.1	69
$Au(NCNH_2)_2$	0.1	55
$HAuCl_4$ + *Aqua regia*	1.0	52
$HAu(C_3Cl_3N_3O_3)_3Cl$	1.0	52
$[Au(P(NCH_2CH_2OCH_2CH_2)_3)_2]NO_3$	1.0	33
$[(AuCl)_2dppe]$	1.0	14
$[Au(en)_2]Cl_3$	1.0	14
$HAuCl_4 + H_2O$	1.0	11
Blank Carbon extrudate (no Au)	0	7

Table 1.3 – Catalyst screening of Au/C catalysts prepared using different precursor complexes [a].[12]

[a] Test conditions: Catalyst: 5g; HCl flow: 60 mL/min, C_2H_2 flow: 50 mL/min. Reactor set point temperature = 130 °C. Total Gas Hourly Space Velocity (GHSV) = 500 h^{-1}.

[b] Conversion measured after 24 h reaction time on line

Moreover, the enhanced performance of these immobilised complexes allowed the Au loading to be decreased to the range of 0.15−0.6% Au, ensuring an obvious economic advantage still achieving satisfactory conversion values, Figure 1.28. Another advantage of using such a low metal loading is the minimisation of the reaction exotherm within the reactor, that even after long duration testing, lead to a minimal nanotube and carbon polymer build-up formation within the reactor. These catalysts were tested by Johnson Matthey in conjunction with a Chinese PVC producer in a pilot plant, which contained a full size single tube reactor of the same dimensions as a full scale commercial VCM reactor. Throughout the operation of the pilot plant, the catalyst conversion was >85%, and the catalyst selectivity was >99% (Figure 1.29).

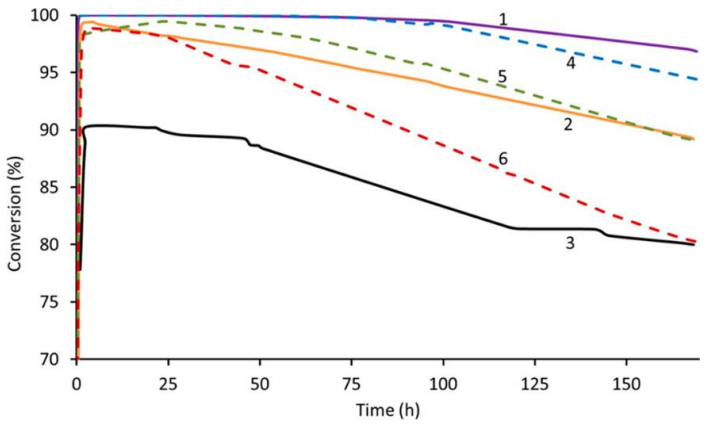

Figure 1.28 – Acetylene hydrochlorination over Au/C catalysts. Key: Line 1 (purple) = 0.6% Au/C, Line 2 (orange) = 0.3%, Line 3 (black) = 0.15% Au/C prepared from $[(NH_4)_3Au(S_2O_3)_2]$, Line 4 (blue) = 1% Au/C, Line 5 (green) = 0.75% Au/C, and Line 6 (red) = 0.5% Au/C prepared from $AuCl_3$/aqua regia. Catalyst = 12 g, reaction conditions: HCl flow = 137 mL/min, C_2H_2 flow = 114 mL/min. Reactor set point temperature = 180 °C. Gas Hourly Space Velocity (GHSV) = 500 h^{-1}.[12]

The new catalysts, prepared by supporting $Na_3Au(S_2O_3)_2$ on carbon extrudates, were significantly more stable than the mercuric chloride catalyst and subsequently a full-scale reactor trial was commissioned. The reactor was loaded with ca. 1.6 t of catalyst and was brought on line and operated under equivalent conditions for more than 4500 h time online. The catalyst was found to have excellent stability, the conversion was >90%, and the selectivity was >99% (Figure 1.26).[12] Following these outstanding results, Johnson Matthey has constructed a catalyst manufacturing plant at its Johnson Matthey Shanghai site for the production and supply of Au/C catalysts for the manufacture of VCM.

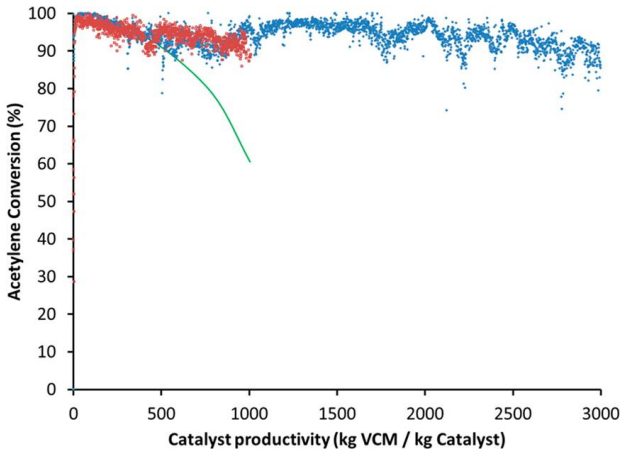

Figure 1.29 – Comparison of catalyst performance in a primary reactor for a 10% $HgCl_2$/C catalyst (green), pilot plant operation for 0.1_{wt}% Au/C to a yield of 3000 kg VCM/kg catalyst (blue), full scale commercial reactor for 0.1_{wt}% Au/C to a yield of 1000 kg VCM/kg catalyst (red). Catalyst = 0.1_{wt}% Au/C prepared by supporting $Na_3Au(S_2O_3)_2$ on carbon extrudates. Typical yield for 10% $HgCl_2$/C catalyst = *ca*. 1000 kg VCM/kg catalyst.[12]

1.4 – Thesis Aims

The aims of this thesis are outlined below:

1. Although the use of Au/C for the acetylene hydrochlorination reaction is a promising development with a full-scale pilot plant in production, the exact nature of the active form of the catalyst and the catalytic cycle are still uncertain. The different hypothesis regarding the active form of the catalyst arise mainly from ambiguous results obtained from *ex situ* characterisations. For this reason, it seems clear that better understanding of the active species could be achieved by in situ characterisation. This work will ascertain the changes in Au speciation during the initial induction phase, understand the active state of Au during catalysis and aim to determine the redox cycle which is currently proposed. Investigation concerning the nature of the active site will be carried out *via* an *in situ* X-ray absorption spectroscopy (XAS) characterisation.
2. The deactivation pathway for Au/C catalysts during the acetylene hydrochlorination reaction has been attributed to the reduction of active cationic gold to inactive metallic gold. The detrimental effect of acetylene has been suggested to be responsible both for this reduction and for the formation of carbonaceous species blocking the active site during the time on-line. Moreover, the role of the individual reactant has been studied in a sequential flow experiment has been carried out *in situ*. Both deactivation pathways will be studied in detail and the role of the single reactant will investigated in particular in term of their impact on the Au speciation.
3. Ligands play a major role in the final activity and selectivity for this class of catalysts. Unfortunately, very few are the studies in which their nature is investigated under operating conditions. An *in situ* K-edge XAS characterisation of gold on carbon catalyst for the hydrochlorination of acetylene will be performed to understand chlorine and sulphur speciation in the catalyst under operating conditions.

1.5 – References

1. https://goldbook.iupac.org/html/C/C00876.html

2. I. Chorkendorff and J.W. Niemantsverdriet, *Concepts of modern catalysis and kinetics*, John Wiley & Sons, Weinheim, **2006**.

3. https://ihsmarkit.com/products/vinyl-chloride-monomer-chemical-economics-handbook.html

4. D. W. Davies, *Manufacture and processing of PVC*, ed. R. H. Burgess, Applied Science Publishers, London, **1981**, 275.

5. D. Braun, *J. Polym. Sci., Part A: Polym. Chem.*, **2004**, *47*, 578–586.

6. J. G. Speight, *Chemical and Process Design Handbook*, McGraw-Hill, New York, **2002**, 2.542

7. S. Lakshmi and A. Jayakrishnan, *Artif. Organs*, **1998**, *22*, 222–229.

8. L. Ciacci, F. Passarini and I. Vassura, *Resour. Conserv. Recycl.*, **2017**, *123*, 108–116.

9. Polyvinyl Chloride (PVC) – Market Study|Ceresana, http://www.ceresana.com/en/marketstudies/plastics/polyvinyl-chloride/.

10. A. J. Magistro and J. A. Cowfer, *J. Chem. Educ.*, **1986**, *63*, 1056-1058.

11. M. Conte and G. J. Hutchings, *Modern Gold Catalyzed Synthesis*, F. D. Toste and A. S. K. Hashmi, Wiley-VCH Verlag GmbH, **2011**.

12. P. Johnston, N. Carthey and G. J. Hutchings, *J. Am. Chem. Soc.*, **2015**, *137*, 14548–14557.

13. G. J. Hutchings and D. T. Grady, *Appl. Catal.*, **1985**, *16*, 411-415.

14. G. J. Hutchings and D. T. Grady, *Appl. Catal.*, **1985**, *17*, 155-160.

15. J. B. Agnew and H. S. Shankar, *Ind. Eng. Chem. Prod. Res. Dev.*, **1986**, *25*, 19–22.

16. H. Bremer and H. Lieske, *Appl. Catal.*, **1985**, *18*, 191–203.

17. W. Ren, L. Duan, Z. Zhu, W. Du, Z. An, L. Xu, C. Zhang, Y. Zhuo and C. Chen, *Environ. Sci. Technol.*, **2014**, *48*, 2321–2327.

18. X. Xu, H. He, J. Zhao, B. Wang, S. Gu and X. Li, *Chin. J. of Chem. Eng.*, **2017**, *25*, 1217–1221.

19. Minamata Convention on Mercury, http://www.mercuryconvention.org/

20. J. P. Wibaut and J. van Dalfsen, *Recl. Trav. Chim. Pays-Bas*, **2010**, *51*, 636–640.

21. A.I. Gel'bshtein, M.I. Siling, G.A. Sergeeva and G.G. Shcheglova, *Kinet. Katal.*, **1963**, *4*, 149-155.

22. A.I. Gel'bshtein and M. I. Siling, *Kinet. Katal.*, **1963**, *4*, 303-306.

23. A.I. Gel'bshtein, G.A. Sergeeva and A.A. Khomenko, *Kinet. Katal.*, **1964**, *4*, 625-634.

24. D. M. Smith, P. M. Walsh and T. L. Slager, *J. Catal.*, **1968**, *11*, 113–130.

25. K. Shinoda, *Chem. Lett.*, **1975**, 219–220.

26. G. J. Hutchings, *J. Catal.*, **1985**, *96*, 292–295.

27. B. Nkosi, N. J. Coville and G. J. Hutchings, *Appl. Catal.*, **1988**, *43*, 33-39.

28. B. Nkosi, N. J. Coville, G. J. Hutchings, M. D. Adams, J. Friedl and F. E. Wagner, J. Catal., **1991**, *128*, 366-377.

29. B. Nkosi, N. J. Coville, G. J. Hutchings, *J. Chem. Soc., Chem. Commun*. **1988**, *0*, 71-72.

30. M. Conte, A. F. Carley and G. J. Hutchings, *Catal. Lett.*, **2008**, *124*, 165-167.

31. G.J. Hutchings, *Gold Bull.*, **2009**, *42*, 260-266

32. M. Conte, A. F. Carley, G. Attard, A. A. Herzing, C. J. Kiely and G. J. Hutchings, *J. Catal.*, **2008**, *257*, 190-198.

33. U. Belluco, R. Bertani, R.A. Michelin and M. Mozzon, *J. Organomet. Chem.*, **2000**, *6000*, 37-55.

34. X. Liu, M. Conte, D. Elias, L. Lu, D. J. Morgan, S. J. Freakley, P. Johnston, C. J. Kiely and G. J. Hutchings, *Catal. Sci. Technol.*, **2016**, *6*, 5144–5153.

35. J. J. Lingane, *J. Electroanal. Chem.*, **1962**, *4*, 332–342.

36. G. Beamson and D. Briggs, *High Resolution XPS of Organic Polymers*, Wiley, **1992**.

37. NIST X-ray Photoelectron Spectroscopy Database Version 4.1 (National Institute of Standards and Technology, Gaithersburg, 2012), http://srdata.nist.gov/xps/.

38. M. Haruta, T. Kobayashi, H. Sano and N. Yamada, *Chem. Lett.*, **1987**, *16*, 405-408.

39. M. Haruta, N. Yamada, T. Kobayashi, S. Iijima, *J. Catal.*, **1989**, *115*, 301-309.

40. G. C. Bond, C. Louis and D. T. Thompson, G. J. Hutchings Ed., *Catalysis by Gold*, Imperial College Press, **2006**.

41. A. S. K. Hashmi, G. J. Hutchings, *Angew. Chem., Int. Ed*., **2006**, *45*, 7896.

42. G. C. Bond, D. T. Thompson, *Catal. Rev.: Sci. Eng.*, **1999**, *41*, 319-388.

43. A. Corma, H. Garcia, *Chem. Soc. Rev.*, **2008**, *37*, 2096-2126.

44. B. Nkosi, M. D. Adams, N. J. Coville, and G. J. Hutchings, *J. Catal.*, **1991**, *128*, 378-386.

45. G. Malta, S. J. Freakley, S. A. Kondrat and G. J. Hutchings, *Chem. Commun.*, **2017**, *53*, 11733-11746

46. N. A. Carthey, P. Johnston, M. L. Smidt, *Improvements in Catalytic Processes*. WO 2010/055341A3, **2010**.

47. M. Conte, A. F. Carley, G. J. Hutchings, *Catal. Lett.*, **2008**, *124*, 165–167.

48. X. Tian, G. Hong, B. Jiang, F. Lu, Z. Liao, J. Wang and Y. Yang, *RSC Adv.*, **2015**, *5*, 46366-46371.

49. G. Hong, X. Tian, B. Jiang, Z. Liao, J. Wang, Y. Yang and J. Zheng, *RSC Adv.*, **2016**, *6*, 3806–3814.

50. X.-X. Di, J. Zhao, Y. Yu, X.-L. Xu, S.-C. Gu, H.-H. He, T.-T. Zhang and X.-N. Li, *Chin. Chem. Lett.*, **2016**, *27*, 1567–1571.

51. M. Conte, C. J. Davies, D. J. Morgan, T. E. Davies, D. J. Elias, A. F. Carley, P. Johnston and G. J. Hutchings, *J. Catal.*, **2013**, *297*, 128–136.

52. M. Conte, C. J. Davies, D. J. Morgan, A. F. Carley, P. Johnston and G. J. Hutchings, *Catal. Lett.*, **2014**, *144*, 1–8.

53. M. Conte, C. J. Davies, D. J. Morgan, T. E. Davies, A. F. Carley, P. Johnston and G. J. Hutchings, *Catal. Sci. Technol.*, **2013**, *3*, 128–134.

54. C. Huang, M. Zhu, L. Kang and B. Dai, *Catal. Commun.*, **2014**, *54*, 61–65.

55. S. L. Chao, Q. X. Guan and W. Li, *J. Catal.*, **2015**, *330*, 273–279.

56. Y. Wang, M. Zhu, L. Kang and B. Dai, *RSC Adv.*, **2014**, *4*, 38466–38473.

57. M. Conte, A. F. Carley, C. Heirene, D. J. Willock, P. Johnston, A. A. Herzing, C. J. Kiely and G. J. Hutchings, *J. Catal.*, **2007**, 250, 231–239.

58. K. Zhou, W. Wang, Z. Zhao, G. Luo, J. T. Miller, M. S. Wong and F. Wei, *ACS Catal.*, **2014**, *4*, 3112–3116.

59. B. Dai, Q. Wang, F. Yu and M. Zhu, *Sci. Rep.*, **2015**, *5*, 10553.

60. Y.-Y. Fong, B. R. Visser, J. R. Gascooke, B. C. C. Cowie, L. Thomsen, G. F. Metha, M. A. Buntine and H. H. Harris, *Langmuir*, **2011**, *27*, 8099–8104.

61. E. Ozkaraoglu, I. Tunc and S. Suzer, *Surf. Coat. Technol.*, **2007**, *201*, 8202–8204.

62. E. Ozkaraoglu, I. Tunc and S. Suzer, *Polymer*, **2009**, *50*, 462–466.

63. F. Karadas, G. Ertas, E. Ozkaraoglu and S. Suzer, *Langmuir*, **2005**, *21*, 437–442.

64. B. M. Weckhuysen, *Chem. Commun.*, **2002**, 97–110.

65. U. Bentrup, *Chem. Soc. Rev.*, **2010**, *39*, 4718–4730.

66. J. Singh, C. Lamberti and J. A. van Bokhoven, *Chem. Soc. Rev.*, **2010**, *39*, 4754–4766.

67. S. Carrettin, M. C. Blanco, A. Corma and A. S. K. Hashmi, *Adv. Synth. Catal.*, **2006**, *348*, 1283–1288.

68. A. S. K. Hashmi and G. J. Hutchings, *Angew. Chem., Int. Ed.*,**2006**, *45*, 7896 – 7936.

69. M. C. Blanco Jaimes, F. Rominger, M. M. Pereira, R. M. B. Carrilho, S. A. C. Carabineiro and A. S. K. Hashmi, *Chem. Commun.*, **2014**, *50*, 4937–4940.

70. Y. Ito, M. Sawamura and T. Hayashi, *J. Am. Chem. Soc.*, **1986**, *108*, 6405-6406.

71. M. Garcia-Mota, N. Cabello, F. Maseras, A. M. Echavarren, J. Perez-Ramirez and N. Lopez, *Chemphyschem*, **2008**, *9*, 1624-1629.

72. A. S. K. Hashmi, *Gold Bull.*, **2003**, *36*, 3-9.

73. D. A. Plattner, Y. Li and K. N. Houk in *Modern Acetylene Chemistry*, Eds.: P. J. Stang and F. Diederich, VCH, Weinheim, **1995**, pp 1

74. J. P. Collman, L. S. Hegedus, J. R. Norton and R. G. Finke, *Principles and Applications of Organotransition Metal Chemistry*, University Science Books, Mill Valley, California, **1987**, 42-156

75. G. G. Melikyan and K. M. Nicholas in Modern Acetylene Chemistry, Eds.: P. J. Stang and F. Diederich, VCH, Weinheim, **1995**, 99

76. H. Schmidbaur, A. Grohmann and M.E. Olmos, *Gold: Progress in Chemistry, Biochemistry and Technology*, Ed. H. Schmidbaur, J. Wiley and Sons, Inc., New York, **1999**, 647

77. D.M.P. Mingos, J. Yan, S. Menor and D.J. Williams, *Angew. Chem. Int. Ed.*, **1995**, *34*, 1894-1895.

78. Y. Fukuda and K. Utimoto, *J. Org. Chem.*, **1991**, *56*, 3729 – 3731.

79. J. H. Teles, S. Brode and M. Chabanas, *Angew. Chem. Int. Ed.*, **1998**, *37*, 1415 – 1418.

80. A. S. K. Hashmi, L. Schwarz, J.-H. Choi and T. M. Frost, *Angew. Chem. Int. Ed.*, **2000**, *39*, 2285 – 2288.

81. C. Gonzalez-Arellano, A. Corma, M. Iglesias and F. Sanchez, *Chem. Commun.*, **2005**, *0*, 3451-3453.

82. P. Roembke, H. Schmidbaur, S. Cronje and H. Raubenheimer, *J. Mol. Catal. A: Chem.*, **2004**, *212*, 35-42.

83. A. Arcadi, *Chem. Rev.*, **2008**, *108*, 3266-3325.

84. B. C. Gorske, C. T. Mbofana and S. J. Miller, *Org. Lett.*, **2009**, *11*, 4318-4321.

85. R. O. C. Norman, W. J. E. Parr and C. B. Thomas, *Chem. Soc., Perkin Trans. 1*, **1976**, *0*, 1983-1987.

86. M. Garcia-Mota, N. Cabello, F. Maseras, A. M. Echavarren, J. Perez-Ramirez and N. Lopez, *Chemphyschem*, **2008**, *9*, 1624-1629.

87. G. J. Hutchings, *Gold Bull.*, **1996**, 29, 123-130.

88. M. Perpointner, and A.S.K. Hashmi, *J. Chem. Theory Comput.*, **2009**, *5*, 2717-2725.

89. V. A. Rassolov, M. A. Ratner, J. A. Pople, P. C., Redfern and L. A. Curtiss, *J. Comput. Chem.*, **2001**, *22*, 976-984.

90. H. Stoll, D. Figgen, G. Rauhut and M. Dolg, *Chem. Phys.*, **2005**, *311*, 227-244.

91. S. A. Mitchenko, E. V. Khomutov, A. A. Shubin and Y. M. Shul'ga, *J. Mol. Catal. A: Chem.*, **2004**, *212*, 345–352.

92. T. V. Krasnyakova, I. V. Zhikharev, R. S. Mitchenko, V. I. Burkhovetski, A.M. Korduban, T. V. Kryshchuk and S. A. Mitchenko, *J. Catal.*, **2012**, *288*, 33–43.

93. S. Wang, B. Shen and Q. Song, *Catal. Lett.*, **2010**, *134*, 102–109.

94. G. B. Li, W. Li and J. L. Zhang, *Catal. Sci. Technol.*, **2016**, 1821–1828.

95. Y. Z. Dong, H. Y. Zhang, W. Li, M. X. Sun, C. L. Guo and J. L. Zhang, *J. Ind. Eng. Chem.*, **2016**, *35*, 177–184.

96. H. Y. Zhang, W. Li, X. Q. Li, W. Zhao, J. J. Gu, X. Y. Qi, Y. Z. Dong, B. Dai and J. L. Zhang, *Catal. Sci. Technol.*, **2015**, *5*, 1870–1877.

97. K. Zhou, W. Wang, Z. Zhao, G. H. Luo, J. T. Miller, M. S. Wong and F. Wei, *ACS Catal.*, **2014**, *4*, 3112–3116.

98. J. G. Zhao, J. J. Zeng, X. G. Cheng, L. Wang, H. H. Yang and B. X. Shen, *RSC Adv.*, **2015**, *5*, 16727–16734.

99. J. Zhao, J. T. Xu, J. H. Xu, J. Ni, T. T. Zhang, X. L. Xu and X. N. Li, *ChemPlusChem*, **2015**, *80*, 196–201.

100. J. M. Ma, S. J. Wang and B. X. Shen, *React. Kinet. Mech. Cat.*, **2013**, *110*, 177–186.

101. J. Zhao, S. C. Gu, X. L. Xu, T. T. Zhang, X. X. Di, Z. Y. Pan and X. N. Li, *RSC Adv.*, **2015**, *5*, 101427–101436.

102. H. Y. Zhang, B. Dai, W. Li, X. G. Wang, J. L. Zhang, M. Y. Zhu and J. J. Gu, *J. Catal.*, **2014**, *316*, 141–148.

103. M. Zhu, Q. Wang, K. Chen, Y. Wang, C. Huang, H. Dai, F. Yu, L. Kang and B. Dai, *ACS Catal.*, **2015**, *5*, 5306–5316

104. C. F. Huang, M. Y. Zhu, L. H. Kang, X. Y. Li and B. Dai, *Chem. Eng. J.*, **2014**, *242*, 69–75.

105. J. Zhao, B. Wang, X. Xu, Y. Yu, S. Di, H. Xu, Y. Zhai, H. He, L. Guo, Z. Pan and X. Li, *J. Catal.*, **2017**, *350*, 149–158.

106. W. Lin, R.-W. Zhang, S.-S. Jang, C.-P. Wong and J.-I. Hong, *Angew. Chem., Int. Ed.*, **2010**, *49*, 7929–7932.

107. Gold Price, http://goldprice.org/

108. P. T. Bishop and N. A. Carthey, WO Patent 2013008004A2, **2013**.

109. K. Zhou, J. Jia, C. Li, H. Xu, J. Zhou, G. Luo and F. Wei, *Green Chem.*, **2015**, *17*, 356–364.

110. P. T. Bishop, N. A. Carthey and P. Johnston, US Pat., WO 2013008004 A3, **2013**.

Chapter 2

Experimental

2.1 – Introduction

This chapter will provide details of the preparation methods employed in catalyst synthesis, the procedures followed in catalyst testing and both theoretical and practical aspects of the characterisation techniques applied.

2.2 – Catalysts preparation

2.2.1 – Gold on activated carbon catalysts prepared by impregnation

Impregnation is a technique frequently employed to prepare supported metal catalysts.[1] To obtain a well-controlled and highly dispersed distribution of the metal species, impregnation by soaking or with an excess of precursor solution[2] is commonly used. In this technique, the excess solvent is removed by evaporation or filtration to obtain the catalyst material. Monometallic gold catalysts were prepared by impregnating the support with an excess of $HAuCl_4$ solutions. The catalysts contained a nominal metal loading of 1_{wt}% unless otherwise stated.

A typical preparation for 2 g of 1_{wt}% Au/C was carried out according to the following procedure, which has been previously reported (Scheme 2.1).[3] The gold precursor $HAuCl_4 \cdot 3H_2O$ (Alfa Aesar, 99.9% (metals basis), Au 49%, 40 mg) was dissolved in 5.4 mL of solvent: namely (i) aqua regia (3 parts by

volume [HCl (Fisher, 32 wt.%)]: 1 part by volume [HNO_3 (Fisher, 70 wt. %)]); or (ii) deionised water. The gold precursor solution was then added drop-wise to the activated carbon (1.98 g) under vigorous stirring at ambient temperature for 1 hour, or, in the case of preparation with *aqua regia*, until NO_x production subsided. The solid was then dried for 16 h at 140 ºC under nitrogen flow to obtain the catalyst. Catalysts prepared using *aqua regia* or deionised water as solvents were labelled as 1_{wt}% Au/C-AR and 1_{wt}% Au/C-H_2O respectively.

As reported in Chapter 1, a gold on carbon catalyst has been recently validated for commercial application, based on a Au-thiosulphate precursors.[4] A different procedure was employed for the preparation of this catalyst: an aqueous $HAuCl_4 \cdot 3H_2O$ solution was mixed with an aqueous solution of sodium thiosulfate, $Na_2S_2O_3$ (Au : $Na_2S_2O_3$ molar ratio of 1:4), in order to obtain a $NaAuS_2O_3$ complex (dark yellow). The mixture obtained was added slowly in aliquots to the support while stirring manually with glass rod. The product was then dried at 110 °C overnight under a nitrogen flow. The 1_{wt}% Au/C-S_2O_3 tested and characterised in this thesis has been provided directly by Dr Peter Johnston, Johnson Matthey (JM).

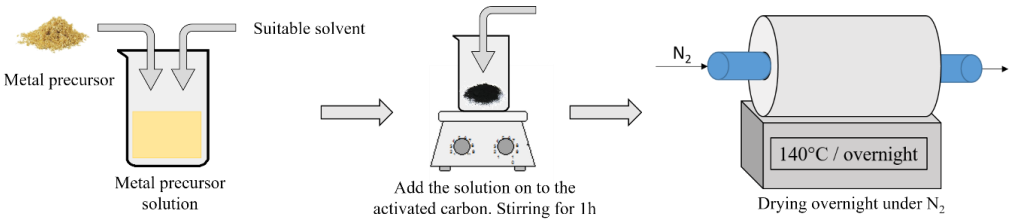

Scheme 2.1 – Schematic of the catalysts preparation.

In all cases the carbon support used is a Norit ROX 0.8, an activated carbon extrudate of 0.8 mm diameter, provided by Johnson Matthey, which was ground to obtain a fine powder and then sieved to 100-140 mesh. From Brunauer–Emmett–Teller (BET) and Raman spectroscopy analysis provided by JM and shown in figure 2.1, the activated carbon has a high surface area of 1482 m^2 g^{-1}, pore size diameter of 1.3 nm and it is characterised by amorphous and graphitic domains.

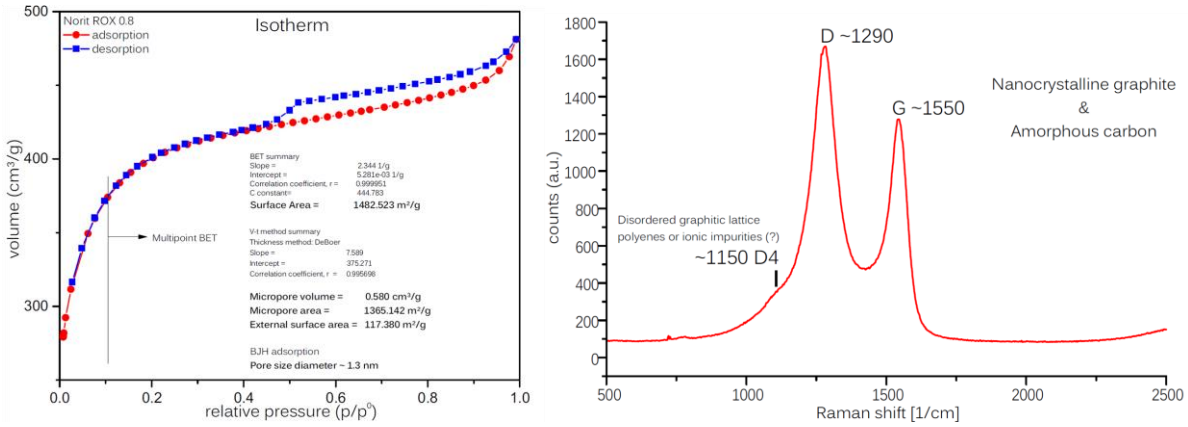

Figure 2.1 – (left) BET analysis and (right) Raman spectrum of the Norit ROX activated carbon.

2.3 – Catalysts Testing

The catalytic tests reported in this thesis have been carried out at the Diamond Light Source, the UK national synchrotron facility based at the Harwell Science & Innovation Campus or at the European Synchrotron Radiation Facility (ESRF) based in Grenoble (France). Preliminary tests and optimisation of the reaction conditions have been performed at Cardiff University.

2.3.1 – Cardiff University

2.3.1.1 – Reactor Design

A schematic diagram of the reactor set-up used is shown in figure 2.2, with a photograph in figure 2.3. The reactor was constructed using stainless steel (SS) tubing and Swagelok connections that had an internal diameter of 1/8 inch.

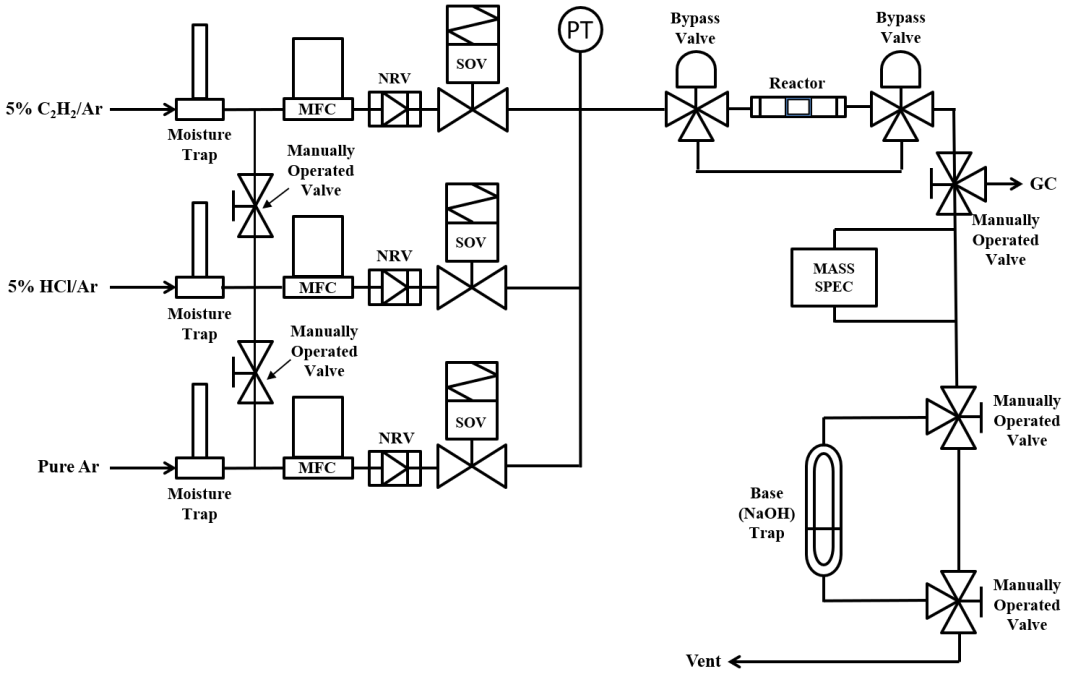

Figure 2.2 – Schematic diagram of the reaction set-up. *Key;* MFC – mass flow controller, NRV – non-return valve, SOV – solenoid valve, PT – pressure transducer, GC – gas chromatograph.

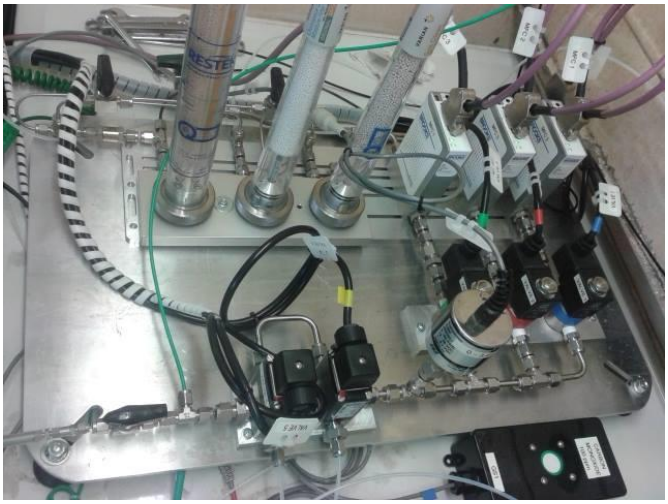

Figure 2.3 – Photograph of the reactor set-up used for acetylene hydrochlorination.

To perform the tests *in situ* at the synchrotron facilities the reactor set-up was fully automated. All the components of the system were connected via a Process Interface (PI) unit (IGI Systems 4 Ltd)[5] equipped with a Eurotherm 3216 temperature controller and 230V AC solid state relay to power the heater block, a 16-bit analogue to digital convertor to acquire signal from the pressure transducer (to act as an over-pressure interlock for the gas flows) and an 8-channel electromechanical relay module to actuate each individual 2- and 3-way solenoid valve. The PI unit also supplied 24V DC power and RS485 communication to the MFCs (Brooks Instrument GF40). The rig also contains gas sensors for acetylene and HCl connected to the PI unit. All reaction parameter set points could be controlled and adjusted remotely via LAB Interface software (IGI Systems Ltd)[6] which also acts as process parameter monitor and data logger (figure 2.4). High temperature, high pressure and gas alarm interlocks were also in place: which when triggered cause the system to shutdown leaving only a flow of inert gas in the system.

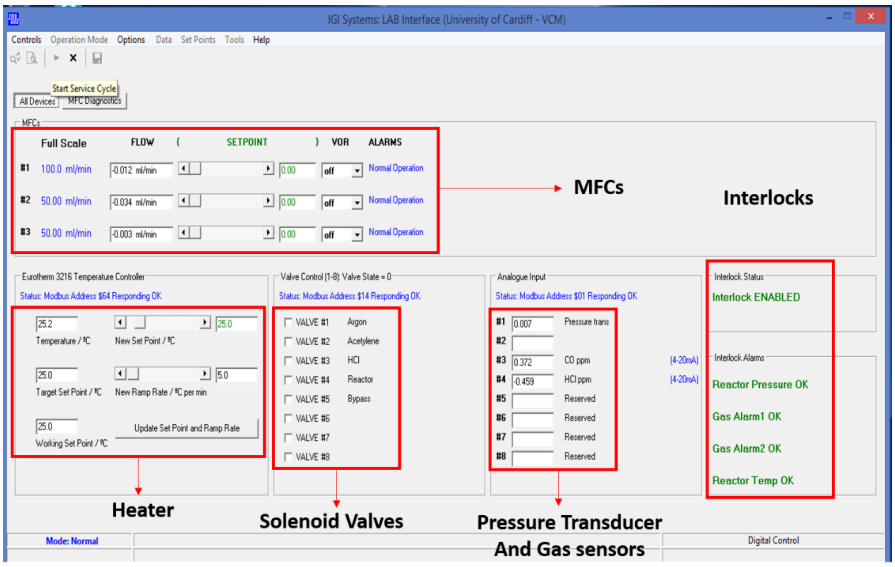

Figure 2.4 – LAB Interface software (IGI Systems Ltd).[6]

The catalyst bed is contained in a fixed-bed polyimide (Kapton) microreactor (O.D. 6 mm, length 20 cm). Typically, 90 mg of catalyst was packed into the microreactor between two pieces of quartz wool; moreover, two PTFE cylindrical fittings have been placed at the extremity of the microreactor to ensure a good seal with the Ultra-torr Swagelok fitting. Kapton possesses a unique combination of desirable physical properties, such as high chemical resistance, that are retained over a wide temperature range, and does not give rise to significant X-ray attenuation. The heating block was heated using heater cartridges and the temperature was controlled with the Eurotherm controller described above with a type K thermocouple positioned in the centre of the heater block. The heater block was modified to allow the incident X-rays from the synchrotron to pass through the catalyst bed (Figure 2.5).

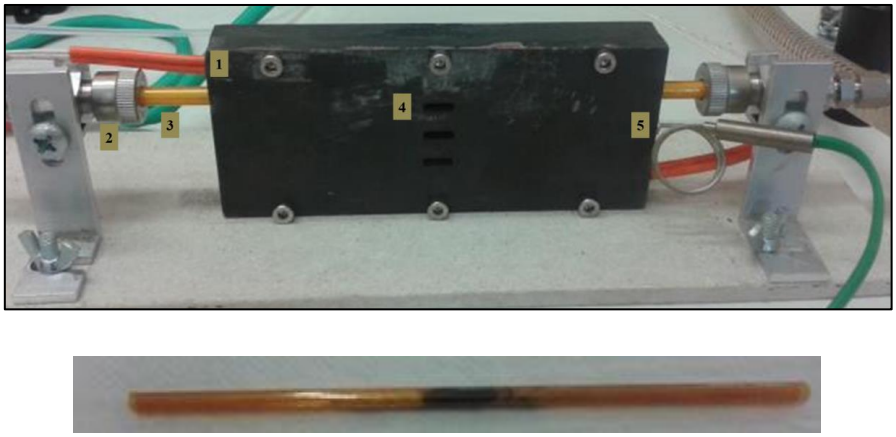

Figure 2.5 – (top) Picture of the modified heater block containing the Kapton microreactor. *Key;* 1 – heater cartridge, 2 – Ultra-torr fitting, 3 – Kapton microreactor, 4 – opening in the heating block to allow the passage of the X-ray beam, 5 – Thermocouple. (bottom) Kapton microreactor containing the catalyst, quartz wool and PTFE fittings.

2.3.1.2 – On-line Gases Analysis

2.3.1.2.1 – Gas Chromatography (GC)

Chromatography is a technique used to separate substances present in complex liquid or gaseous mixtures, which exploits the portioning of the components between two phases, a stationary phase and the mobile phase: the separated components are determined qualitatively and quantitatively using suitable detectors.[7] Gas Chromatography (GC) is one of the most used techniques for the analysis of gas mixtures. In GC the mobile phase is a gas and the stationary phase is a solid.[8] The mechanism of separation of the mixture is determined by the stationary phase since the mobile phase only works as a carrier. A GC analysis starts with the introduction of a sample of the mixture to be analysed into a mobile phase, the carrier gas (an inert gas, such as helium), which continuously flows through the system. The carrier gas containing the mixture is then passed through a sample loop with calibrated volume and it is injected into a column containing the stationary phase, which is held at a specific

temperature by an oven. The sample is injected using a heated 6 port valve, i.e. Valco 6 port valve, in which the calibrated loop (10-100 μL) is filled before injection.[9] Once the mobile phase containing the sample is introduced into the column, the components of the mixture are separated by the strength of their interactions with the stationary phase: if a component has a strong interaction with the column it will remain in the column for longer than a component that has a weak interaction. Thus, the components will leave the column and enter the detector at different times. The time at which a component is detected is known as its retention time, t_r.

There is a range of detectors that may be used with GC, two of the most commonly used are: thermal conductivity detectors (TCDs) and flame ionisation detectors (FIDs). For analysis of the acetylene hydrochlorination reaction, a flame ionisation detector (FID) is used. A FID works burning the components to be detected in a flame generated by a mixture of hydrogen in air, with a typical 1:10 ratio, which is positioned between two electrodes. This combustion involves an ionisation process, thus, the current between the electrodes changes. These changes in current are detected and quantified, in particular there is a proportional relationship between the number of carbon atoms in the flame and the number of ions produced (output signal).[8,10] When a component is detected it appears as a peak in the chromatogram; the area under the peak is proportional to the amount of the component present and so can be used for quantitative analysis. A schematic of a typical gas chromatography system is shown in figure 2.6.

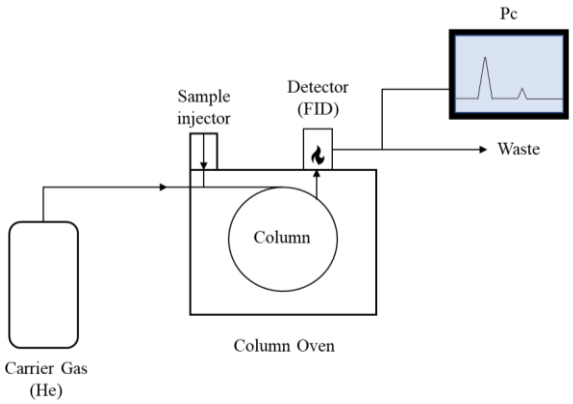

Figure 2.6 – Schematic of a typical gas chromatography system.

The analysis of the acetylene hydrochlorination reaction was done by time-on-line gas chromatography, using a Varian 450GC equipped with a FID. Chromatographic separation was carried out using a Porapak N packed column (6 ft × 1/8″ stainless steel). An isothermal temperature programme was used, at an oven temperature of 130 °C. Helium was used as a carrier gas, at a column pressure of 18.9 psi. Only two major components were observed in the GC trace, acetylene (t_r ~ 1.2 minutes) and VCM (t_r ~ 10 minutes), Figure 2.7.

Calibration allows quantification of the results obtained during reaction. Acetylene calibrations where repeated every month and every time a cylinder was replaced. As an example, an acetylene calibration curve is shown in Figure 2.7. To obtain the area values for each concentration, chromatograms were recorded until a stable value was achieved (usually 5 runs were necessary). Before reaction, the gas mixture was allowed to flow into the system bypassing the reactor and analysed by GC in order to have stable concentration (usually 30 min). The catalytic activity is described in terms of percentage acetylene conversion (see equation 2.1).

$$Acetylene\ Conversion\ (\%) = \frac{Area\ under\ C_2H_2\ peak\ from\ reaction}{Area\ under\ C_2H_2\ peak\ from\ calibration} \cdot 100 \qquad (2.1)$$

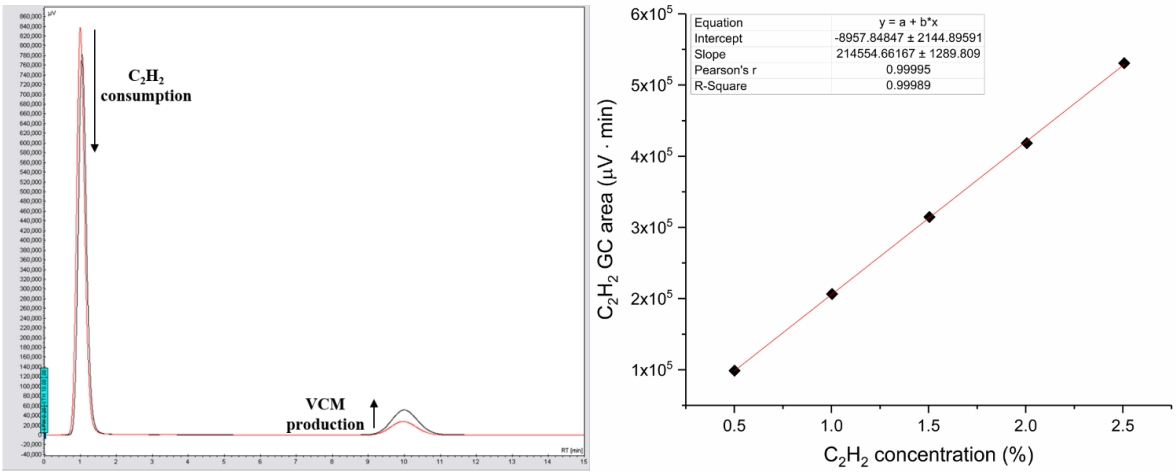

Figure 2.7 – (left) Typical chromatogram acquired during reaction and (right) C_2H_2 GC calibration curve.

2.3.1.2.2 – Mass Spectrometry (MS)

Mass spectrometry is an analytical technique allowing structural identification based on the ionisation of a molecule and on its subsequent fragmentation into ions of different ratio mass/charge (m/z).
A typical MS analysis works as follow:

- the ionisation of molecules in gas phase, a molecule is ionised by ejection of an electron;
- the partial fragmentation of the radical cation formed (molecular ion), generating cations and/or cation radicals (fragment ions);
- the molecular ion and the various ions that originate by fragmentation are distinguished based on their mass/charge ratio, typically through static or oscillating magnetic field;
- the products of the fragmentation are revealed by a detector.

MS has many advantages over GC, for example it is possible to run continuous detection of components simultaneously, with uninterrupted quantification and any leaks are easily detected. Unlike other spectroscopic techniques, however, this is a method of destructive analysis.

The analysis of the acetylene hydrochlorination reaction was done by time-on-line mass spectrometry using an Hiden QGA equipped with a quartz inert capillary, which enabled both qualitative and quantitative analyses by scanning fixed mass fragments according to selected mass-to-charge ratios (m/z). The Hiden QGA quantitative gas analysis system is configured for continuous analysis of gases and vapours at pressures near atmosphere. The QGA system has a mass range of 200 amu and a detection capability from 100% to less than 100ppb.

The sample is injected via a quartz inert capillary (QIC), typically operating at 200 °C. The capillary inlet is flexible, with a length of *ca*. 2 meters and provides fast response times, less than 300ms. Once the gas mixture is introduced in the MS, the molecules are ionised through a *Soft Ionisation* system, which allows to selectively ionise different gases by setting the ionisation energy for a particular mass. The ionisation energy can be altered from 4 to 150 eV, in 0.1 eV increments, standard operation is at 70 eV. The MS is associated with a QGA Professional Software for quantitative gas analysis providing real time continuous analysis of up to 32 species with concentrations measured in the range 0.1ppm to 100%, in which is possible to set up methods in which only the specific component of interest can be analysed. The MS is fitted with a vacuum system, to ensure the ions generated a free path through the ionisation chamber without any collisions with air molecules. Usually the system works at less than 10^{-7} mbar.
Once the ions are generated via soft ionisation, the mass are selected via a quadrupole mass analyser, which separates the atoms according to their mass/charge ratio. The basic principles of operation are as follows: the positive ions are accelerated so that they all reach the same kinetic energy and are then deflected under a strong magnetic field according to their mass. Lighter ions deflect more, with the degree of deflection also dependant on the number of positive charges on the ion.

Finally, the ions are detected with an Electron Multiplier detector, with a detection range from 100 % to 0.1 ppm. The main role of this kind of detector is to be amplifying the very weak current generated by ions that have passed the analyser. The signals obtained are transmitted to a computer able, with the appropriate software, to represent the abundance of each ion as a function of its mass.

The catalyst activity determined by MS is shown in terms of productivity towards vinyl chloride monomer (VCM). VCM production was calculated and normalised to catalyst mass considering the reaction being 100% selective towards VCM and in term of acetylene consumption to give a productivity value which is presented as $mol_{C2H2consumed}\ h^{-1}\ kg_{cat}^{-1}$ (equation 2.2). Acetylene calibration

where repeated every month and every time a cylinder was replaced. As an example, an acetylene calibration curve is shown in Figure 2.8.

$$Productivity = \frac{(mol\ C_2H_2\ consumed)}{Catalyst\ mass\ (kg) \cdot Reaction\ time\ (h)} \quad (2.2)$$

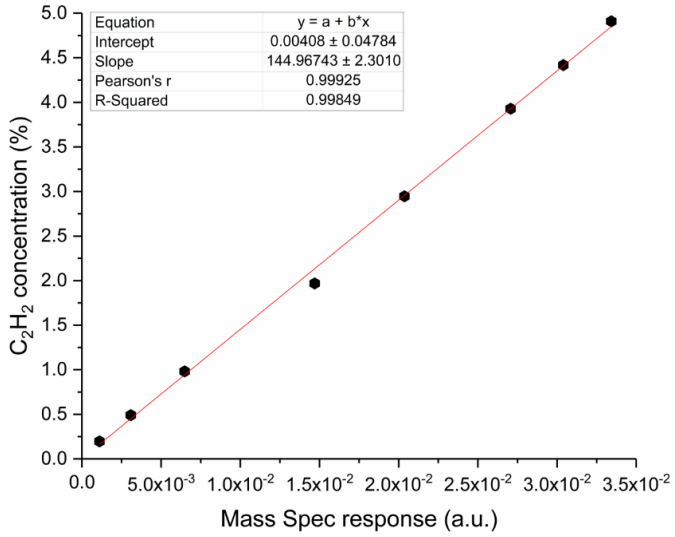

Figure 2.8 – C_2H_2 MS calibration curve.

2.3.1.3 – Reaction Conditions

Acetylene is an extremely flammable gas and potentially explosive[11] while HCl is highly toxic and corrosive.[12] For safety reasons, dilute gas mixtures were used C_2H_2/Ar (4.91% balanced in Ar, BOC) and HCl/Ar (5.00% balanced in Ar, BOC). The gases were dried, using moisture traps, prior to introduction to the reactor. In all cases, the reactor was purged with Ar (99.99 % BIP, Air Products) prior to admitting the hydrochlorination reaction mixture.

The reactor was heated to 200 °C at a ramp rate of 5 °C min^{-1} and held at temperature for 30 min under a flow of Ar (50 mL min^{-1}). The reaction gas mixture of C_2H_2/Ar (24 mL min^{-1}), HCl/Ar (24 mL min^{-1}) and additional Ar (2 mL min^{-1}) were introduced into the heated reactor chamber containing catalyst at a total gas hourly space velocity (GHSV, equation 2.3) of ~14 000 h^{-1}, keeping the C_2H_2:HCl ratio at a constant value of 1:1.02.

This residence time was chosen to test catalysts under mild conditions aiming for low conversion values in order to deliberately extend the catalyst induction period usually observed for gold on carbon catalyst for the acetylene hydrochlorination reaction (Figure 2.9).[13]

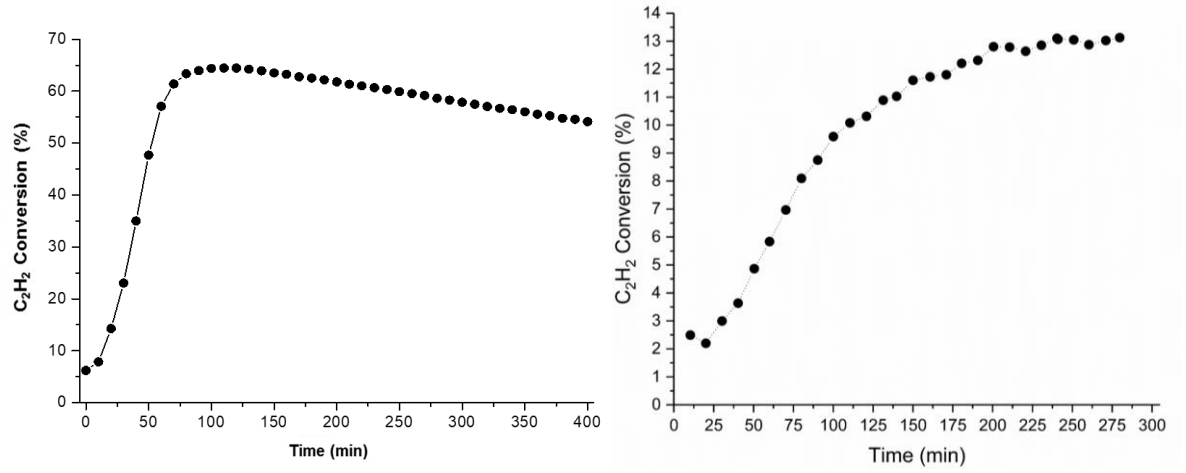

Figure 2.9 – Activity of a 1_{wt}% Au/C-AR catalysts at different reaction conditions: (Left) Reaction conditions: 1_{wt}% Au/C-AR (150 mg), 185 °C, C_2H_2 = 5mL min^{-1}, HCl= 6mL min^{-1}, N_2 = 10 mL min^{-1}, GHSV = 740 h^{-1}; [13] (bottom) Reaction conditions: 1_{wt}% Au/C-AR (90 mg), 200 °C, C_2H_2 = 24 mL min^{-1}, HCl = 24 mL min^{-1}, Ar = 2 mL min^{-1}, GHSV = 14 000 h^{-1}

Slightly different conditions were used for testing the Au/C-S_2O_3 material due to the different particle mesh size (>150 μm) of this catalyst, to avoid back pressure in the system. In this case, C_2H_2 (17.5 mL min^{-1}) and HCl (17.5 mL min^{-1}) were mixed via calibrated mass flow controllers into the heated reactor containing the catalyst, to give a total flow rate of 35 mL min^{-1} and a GHSV of ~11 000 h^{-1}.

$$Gas\ Hourly\ Space\ Velocity\ (GHSV) = \frac{Total\ flow\ (cm^3 h^{-1})}{Volume\ of\ catalyst\ bed\ (cm^3)} \quad (2.3)$$

Even though the maximum concentration of HCl allowed in the system is never greater than 5%, to avoid any possible damage due to the corrosion, after every reaction the whole system was purged with argon (*ca.* 50 ml min^{-1}) for several hours. As shown in the schematic diagram of the reactor in figure 2.2 a by-pass line, starting after the argon moisture trap, equipped with manual 2-way valves allowed the argon to flow through all the lines. Because of the corrosive nature of the HCl the mass flow controller was calibrated every month, example of the HCl MFC calibration curve is shown in Figure 2.10. The measured value is obtained using a PerkinElmer digital bubble flow meter.

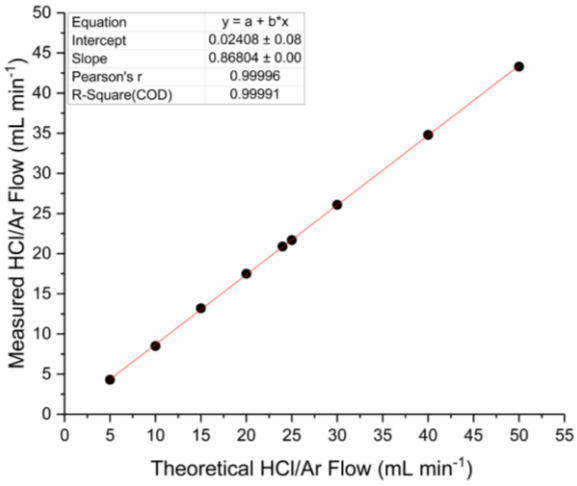

Figure 2.10 – HCl MFC calibration curve.

The outlet gas was passed through a bubbler containing aqueous sodium hydroxide solution in order to neutralise the unreacted hydrogen chloride including exit gases from the GC and MS analysis. Before reaction, the reaction mixture was let flow in the system bypassing the reactor and analysed by GC in order to have a stable on fixed concentration (usually 30 min).

2.3.2 – B18 – Diamond Light Source

The acetylene hydrochlorination reaction experiments reported in Chapter 3 and 4 of this thesis were carried out at the beam line B18 of the Diamond Light Source, the UK's national synchrotron, using the same reactor-set up and reaction conditions described in the previous section while recording X-ray absorption fine structure (XAFS) spectra at the Au L_3-edge (Figure 2.11), as it will describe later on in this chapter. The on-line analysis of the reaction mixture before and after reaction had been performed with the MS only.

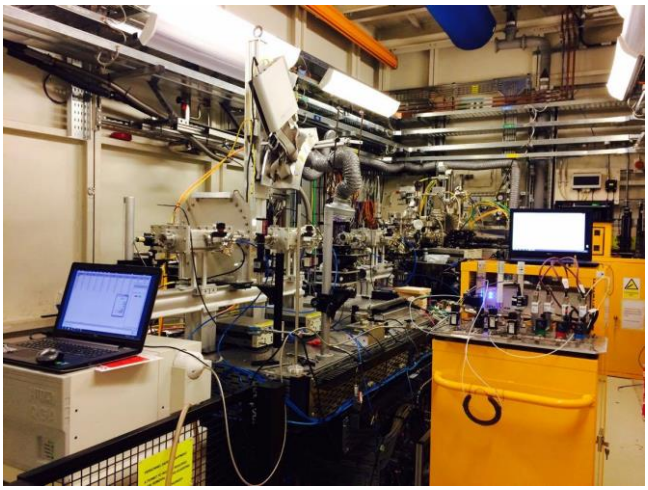

Figure 2.11 – Reactor-set up during the *in situ* synchrotron experiment at B18.

2.3.3 – BM28 – European Synchrotron Radiation Facility (ESRF)

The acetylene hydrochlorination reaction experiments reported in Chapter 5 of this thesis were carried out at Beamline BM28 (XMaS) at the European Synchrotron Radiation Facility (ESRF) based in Grenoble (France) (Figure 2.12). In this case, the reactions were performed while recording *in situ* the ligand K-edge X-ray absorption near edge structure (XANES). Donor K-edge XANES spectroscopy studies are preferably performed either under vacuum or in pure helium, to minimise absorption and scattering from the atmosphere (due to the low energies involved). For this reason, the microreactor needed to be located inside an environmental chamber or vacuum vessel, that allow a vacuum or a helium atmosphere. Thus, a different microreactor, or flow cell, and different reaction conditions have been used for this set of experiments. The set-up (vacuum vessel and cell) used have been developed by Thomson and Newton and it is widely described elsewhere in the literature.[14] Figure 2.12 shows the schematic of the environmental chamber, while in figure 2.13 the schematic and picture of the flow cell designed for soft X-ray studies. The flow cell is placed in the core of the environmental chamber.

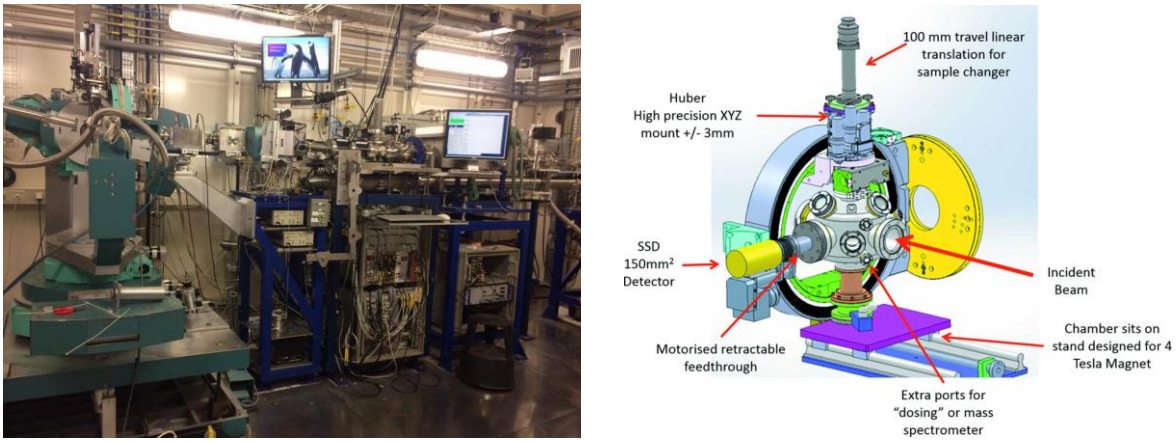

Figure 2.12 – (left) Picture of the experimental hutch of the beam line BM28. (right) Schematic of the environmental chamber designed and used for low-energy spectroscopic studies at BM28.[14]

Within this setup the dedicated space for the catalyst bed is very limited and the amount of catalyst used was 10 mg. For this reason, the total flow has been reduced to 5 ml min^{-1}: C_2H_2/He (2,5 mL min^{-1}) HCl/Ar (2,5 mL min^{-1}). Finally, the make-up gas was helium instead of argon. Dilute gas mixtures were used C_2H_2/He (4.97% balanced in He, Air Liquide) and HCl/He (5.00% balanced in He, Air Liquide). The gases were dried, using moisture traps, prior to introduction to the reactor setup. In all cases, the reactor was purged with He (99.99 %, Air Liquide), heated to 200 °C at a ramp rate of 2.5 °C min^{-1} and held at temperature for 30 min, all under a flow of He (5 mL min^{-1}), prior to admitting the hydrochlorination reaction mixture.

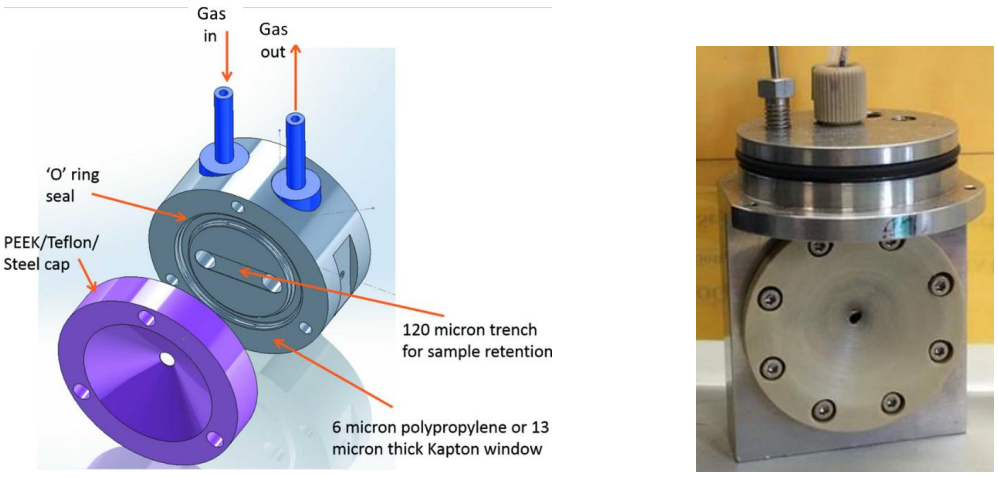

Figure 2.13 – (left) Schematic and (right) picture of the flow cell designed for soft X-ray studies at BM28.[14]

The same fully automated system previously described has been used for these experiments and the on-line analysis of the reaction mixture before and after reaction had been performed with the MS only.

2.4 – Catalysts Characterisation

2.4.1 – X-ray Diffraction (XRD)

X-ray diffraction (XRD) is a non-destructive technique widely employed in heterogeneous catalysis to gain information of the crystallographic structure of a material. In general, more than the 90% of materials are crystalline in nature, a crystal is a solid structure consisting of atoms, molecules or ions, having a regular geometrical arrangement, which is repeated indefinitely in the three dimensions (crystal lattice or Bravais lattice). Since the wavelength of X-ray radiation is comparable to the periodic spacings in a crystal lattice, diffraction occurs as the X-rays are reflected by the crystal planes, producing an interference pattern providing structural information about the sample.[15] Bragg's Law gives the conditions required for constructive interference of the waves reflected, i.e. diffraction, to occur (Equation 2.4). The law relates the wavelength of electromagnetic radiation (λ), to the diffraction angle (theta, θ) and the lattice spacing in a crystalline sample (d). Figure 2.14 shows that the beam diffracted from the lower surface travels further than that from the upper surface, when the path difference is equal to some integral multiple of the wavelength, constructive interference ensues ($AB + BC = n\lambda$). A schematic of Bragg scattering can be seen in Figure 2.14.

$$n\lambda = 2d_{hkl}\, sin\theta \qquad (2.4)$$

Where n= An integer, λ= Incident wavelength, dhkl = Atomic plane spacing of the planes (hkl), θ= Angle between the incident radiation and the scattering planes.[16]

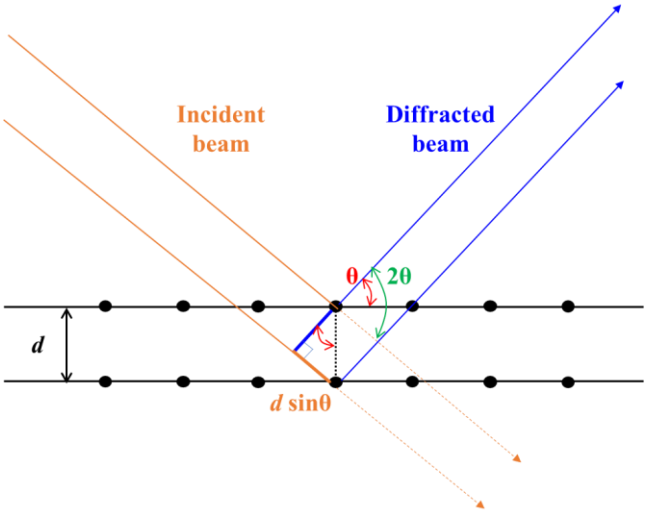

Figure 2.14 – Schematic representation of diffracted beams in crystal lattice. Where *d* is the lattice spacing and θ is the angle between incident and normal to the plane.

XRD may be carried out on single crystals or powders. Of these, powder XRD (p-XRD) is the most commonly used in the study of heterogeneous catalysts. In general, p-XRD analysis is carried out by exposing the sample to a monochromatic X-ray source and detecting the resulting diffracted X-rays. The X-rays are typically produced by bombarding a metal target with high energy electrons generated from a hot tungsten filament and accelerated with a high voltage. When electrons have sufficient energy to eject the inner shell electrons of the target metal, X-rays are produced. These X-rays pass through a monochromator, only a monochromatic X-ray, typically only the Kα radiation will be selected. As these X-rays hit the sample they are scattered as previously described. By maintaining a stationary X-ray source and using a movable detector to measure the angle at which constructive interference occurs (θ) it is possible to calculate the lattice spacing of the crystallite using the Bragg relationship (equation 2.4). In p-XRD the sample is also rotated, to increase the probability that the reflected X-rays are detected. The sample will be scanned through a range of 2θ angles. A schematic diagram of the XRD instrumentation is shown in figure 2.15. Each different crystalline solid has a unique diffraction pattern (diffractogram), which can be considered as a fingerprint for that material; e.g. reflections due to metallic gold are expected to be present at 2θ angles of 38°, 44°, 64° and 78°, corresponding to the Au set of planes {111}, {200}, {220} and {311} respectively.

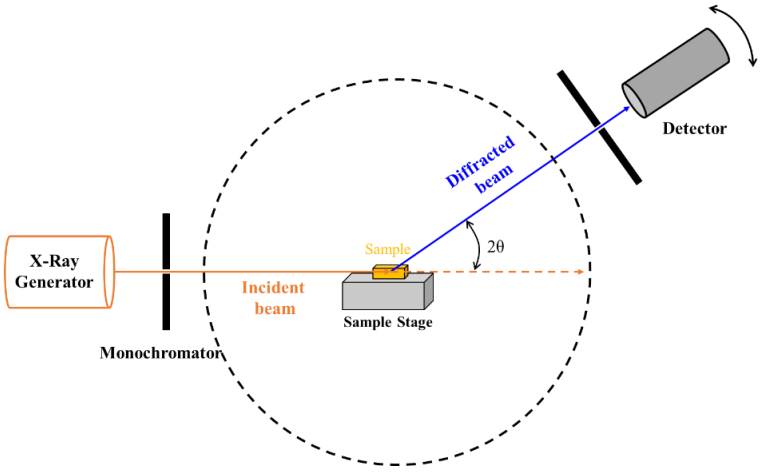

Figure 2.15 – Simplified XRD instrumentation schematic (diffractometer): X-ray source, sample stage and detector.

A very important tool that this technique can provide is to measure the size and shape of crystallites (coherently scattering domains). XRD reflections of perfect crystals are usually very sharp but when the crystallite size decrease (<100 nm) line broadening can occur. This is because large crystallites have more lattice place than small crystallites. The broadening can be used to give an estimate of the particle size; using the Full Width at Half Maximum (FWHM) value, after a background has been subtracted and a Gaussian peak fitted, the average particle size can be estimated using the Scherrer equation. (equation 2.5).[17] However, XRD has a detection limit of around 5_{wt}% and cannot detect crystallite phases of a size less than 5 nm.[17]

$$n = \frac{K\lambda}{\beta cos\theta} \qquad (2.5)$$

Where: n is crystallite size, λ is the x-ray wavelength of the X-ray radiation, β is the line broadening at half of the maximum intensity (FWHM), θ diffraction angle and K is a dimensionless shape factor (normally between 0.9-1) which is related to the shape of the crystallite.

p-XRD analysis was performed on a (θ-θ) PANalytical X'pert Pro powder diffractometer using a Cu Kα radiation source operating at 40 keV and 40 mA. Standard analysis was performed using a 40 min scan between 2θ values of 10-80° with the samples supported on an amorphous silicon wafer. Analyses of the spectra were carried out using X'Pert High Score Plus software. Diffraction patterns of phases were identified using the ICDD data base. The crystallite size of the metallic gold nanoparticles, where possible, were determined using the Scherrer equation assuming a spherical particles shape and a K factor of 0.9 at the reflection arising from the set of {111} Au planes, at 2θ = 38°.

2.4.1.1 – *In situ* Powder X-ray Diffraction (p-XRD)

In situ p-XRD allows the study of the sample continuously as this is heated. Investigation of the thermal stability of the catalysts was carried out using an X'pert Pro XRD fitted with an Anton-Parr XRK900 in-situ cell (internal volume of 0.5 L) with XRD patterns recorded between 10-80° 2θ. A flow of N_2 (50 ml min^{-1}) was passed through the sample bed whilst the cell was heated to 350 °C (5 °C min^{-1}). Patterns were identified using the ICDD database and crystallite sizes were determined using the Scherrer equation.

2.4.2 – Transmission Electron Microscopy (TEM)

Transmission Electron Microscopy (TEM) is a microscopy technique used to imaging samples on the nanometre scale, or even at atomic level resolution, widely used in heterogeneous catalysis. TEM applies the use of high energy electrons to provide morphological, compositional and crystallographic information of catalyst particles at the atomic scale.[18] Typically, a TEM image is acquired as follows:
(i) An electron gun at the top of the microscope emits a source of monochromatic electrons, which are accelerated under vacuum through the column. Varying the voltage of the gun alters the speed of the electrons and hence EM wavelength, the final image acquired can be adjusted: the shorter the wavelength, the faster the electrons move, and the clearer the image but the more likely the sample will be damaged.
(ii) Electromagnetic lenses are used to focus the electrons into a very thin beam. The beam is restricted by the condenser aperture, which eliminates high angle electrons.
(iii) The beam travels through the ultra-thin sample specimen (< 2000 Å). Depending on the density of the material being sampled.
(iv) Some of the electrons can be scattered, depending on the density of the material, while the non-scattered electrons hit a fluorescent screen at the bottom of the microscope, where electrons are converted to light to create an image of the specimen. Different darkness corresponds to change in density, with the lighter areas corresponding to a greater passage of electrons through the sample.

The majority of samples were analysed using bright field imaging that is generated by detecting the electrons which pass straight through and are therefore unaffected by the sample, as described above and as shown in figure 2.16. However, also dark field images can be obtained by the diffracted electron beam which is detected slightly off angle to the incident beam. The diffracted electrons can only be detected when the electron beam passes through a crystalline species. By detecting at even higher angles electrons scattered by the presence of heavy elements, this is known as high angle annular dark field, HAADF imaging. This method is highly sensitive to the atomic number, Z, of the scattering atoms with

heavier elements scattering more electrons. Therefore, heavier elements appear as bright regions in an image in contrast to bright field imaging where they are characterised by dark regions.

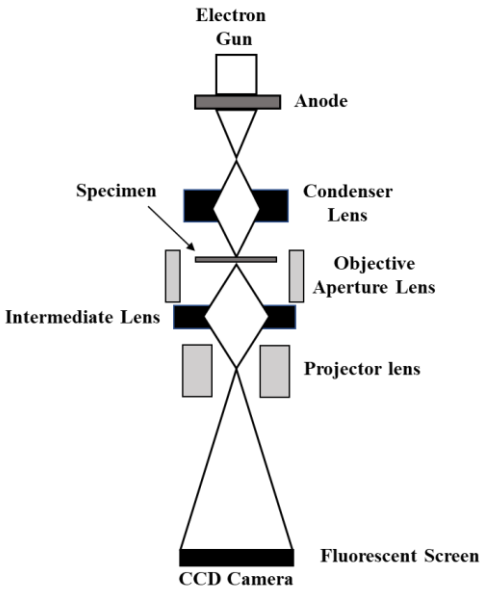

Figure 2.16 – Schematic setup of a BF-TEM with various components

To acquire Z-contrast annular dark-field imaging the use of Scanning Transmission Electron Microscope (STEM) is required. This is a type of TEM, in which electron beam is focused to a finest spot, typically 0.05 - 0.2 nm, which is then scanned over the sample in a raster STEM images presented in this thesis was acquired by Dr Li Lu within the Prof. Chris Kiley's group at Lehigh University. Materials for examination by STEM were dry dispersed onto a holey carbon TEM grid. These supported fragments were examined using atomic-resolution BF- and HAADF-STEM imaging mode in an aberration corrected JEOL ARM-200CF scanning transmission electron microscope operating at 200kV.[19] Aberration correctors are applied to the objective lens, improving the resolution limits to the atomic level. This microscope was also equipped with a Centurio silicon drift detector (SDD) system for X-ray energy dispersive spectroscopy (XEDS) analysis.

2.4.3 – X-ray Absorption Fine Structure (XAFS) Spectroscopy

2.4.3.1 – Introduction

X-ray Absorption Fine Structure (XAFS) spectroscopy is widely used in homogeneous and heterogeneous catalysis[20,21] to obtain information on chemical composition and local structure of materials without any long rang order, by studying X-ray absorption as a function of the incident radiation energy, at energies near and above the core-level binding energies of that specific atom/element. Therefore, XAFS is an element specific technique. An edge results when a core electron absorbs energy equal to or greater than its binding energy. These absorption edges are labelled according to the shell the core electron originates from. In a XAFS spectrum the energies involved are in a range from a few hundred eVs (soft X-rays) to several thousands of eVs (hard X-rays).

Figure 2.17 details a typical XAFS spectrum of metallic gold.

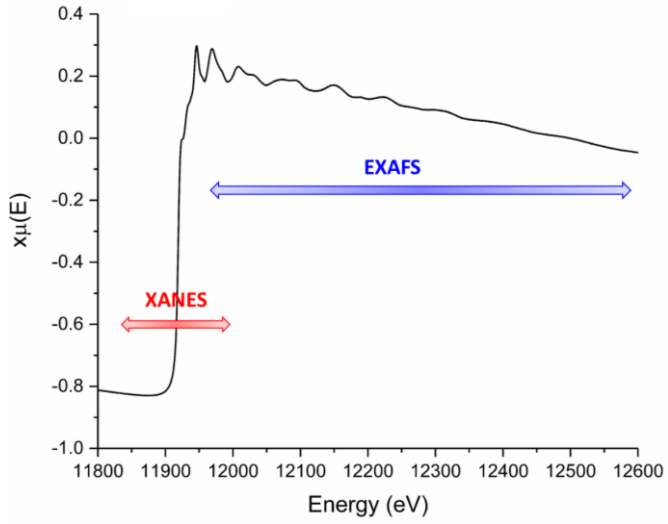

Figure 2.17 – XAFS spectrum of metallic Au. A XAFS spectrum consists of two main major regions: XANES and EXAFS, with descriptions to follow.

There are two main regions of XAFS spectra:

(i) X-ray absorption near edge structure (XANES): the energy of the photon is enough to excite a core electron to unfilled orbitals. This region is set within ~50 eV of the absorption edge.

(ii) Extended X-ray absorption fine structure (EXAFS): the oscillatory structure after the electron has been ejected, it can be >1000 eV past the edge.

In this study XAFS has been used to characterise the gold and its ligands to gain information on the structure, oxidation state, coordination number and bond length of the catalytic species. Unlike

surface specific techniques, e.g. X-ray photoelectron spectroscopy (XPS), XAS provides an "atom average", therefore probing all environments, both surface and bulk equally and providing an average signal. Since it is necessary to change the radiation energy continuously over a wide range, and since the useful signal is typically one thousandth of the total signal, a high-brightness X-ray source is required over a large energy band, i.e. synchrotron radiation.

2.4.3.2 – X-rays Generation at Synchrotron

The synchrotron is a cyclic particle, usually electrons, accelerator. Most synchrotrons are used to produce highly collimated and monochromatic X-rays, called synchrotron radiation or synchrotron light. Synchrotron radiation is generated by charged particles that travel at speeds close to the speed of light and are forced by a magnetic field to move along a curved path.
The generation of this high intensity radiation involve 5 main sections of a synchrotron (Figure 2.18):

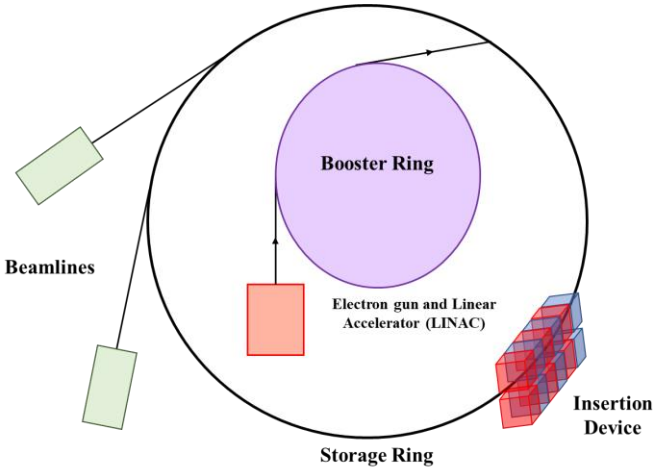

Figure 2.18 – General schematic of electron beam generation, storage and generation of X-rays at a synchrotron.

1) The electron gun: In this section the electrons are generated through a process called thermionic emission; the electrons are generated by a high voltage cathode, typically a tungsten oxide, heated under vacuum causing the ejection of electrons from the surface. By applying a positive voltage to the anode, a strong electric field is generated, the electrons are attracted away from the cathode. The electrons acquire a kinetic energy that is equal to the work done by the electric field in attracting them away from the cathode (equation 2.6).

$$^1/_2\, mv^2 = eV \qquad (2.6)$$

Where: m = the electron mass; v = its velocity as it leaves the gun; e = the charge of the electron; V = the Voltage on the anode.

The electrons then leave the electron gun and enter in the linear accelerator (LINAC)

2) Linear Accelerator (LINAC): In this section, the electrons are further accelerated to close to the speed of light be passing through a series of microwave radio frequency fields, more specifically a series of chambers with electric fields that alternate as the electrons pass through. This way the electrons always see a positive field ahead of them, which they accelerate towards. At very high energies the electrons approach the speed of light. The electrons travel within a vacuum, with a pressure lower than 10^{-11} torr.

   The electrons at such speed are then injected into the booster ring, with energy usually around 0.1 GeV.

3) Booster ring: In this section, the electrons follow a trajectory with two straight sections joined with semi-circular curves, an "athletics track" shaped trajectory. Several dipoles bending magnets are used to curve the electrons around the bends and a radio frequency voltage source accelerates the electrons along the straight sections. The magnetic field produced by the bending magnets is increased as the electron energy rises up to a final extraction energy up to few GeV, to maintain a fixed radius of curvature. So, in the booster ring the electrons are further accelerated before been injected into the storage ring.

4) Storage ring: The storage ring is maintained under vacuum to minimise electrons scattering off air molecules. The storage ring is a polygon comprised of straight sections angled together with bending/dipole magnets, which direct the electrons around the ring. As the electrons pass through each magnet, the direction of their flow is altered, causing them to give up their energy in the form of light. This synchrotron light generated is then directed to the different beamlines. However, it is possible to further tailor the intensity of the synchrotron radiation produced to the requirements of the experiment using insertion devices placed in the straight sections of the storage ring: namely wigglers and undulators. The wigglers cause the light to be produced in a wide cone; the broad spectrum of X-rays generated are typically used in beamlines where very high energy X-rays are required (up to 100 keV). The undulators, are more commonly used, and produce a very bright light in a very narrow beam over a continuous frequency range. In general, undulators are used for soft X-ray experiments.

5) Beamline: The beamline is where the sample is placed in the X-ray beam. Each beamline is optimised for its specific use; however, every beamline has four major sections:

- *Front end*; where the synchrotron light comes from the storage ring.

- *Optics hutch*; where the synchrotron radiation is modified for use. Specialised mirrors and crystal optics are in place to focus the beam, and to select the energy required for the experiment. Slits define the beam size and remove scatter, whilst mirrors focus the beam and remove higher energy.
- *Experimental hutch*; where the experiment takes place. Many beamlines allowed several different sample environments, including open to air, heated, cooled by liquid nitrogen, under pressure, and in liquid cells. The sample can also be analysed under in situ analysis monitoring XAFS while performing a specific reaction. The sample workspace may include motors that position the sample very precisely with respect to the beam (figure 2.18). To collect data for analysis, detectors are in place around the sample for either transmission or fluorescence modes.
- *Control cabin*; where the users monitors and controls every aspect of the experiment and takes data.

2.4.3.3 – Principles of XAFS

XAFS spectroscopy is based on the photoelectric effect, in which as X-rays pass through a material, there is a reduction in their intensity as they are absorbed. In particular, at certain energies electrons (photoelectrons) can be exited into higher energy electron orbitals that are unoccupied, or into the continuum where the electron is no longer associated with the atom, generating core holes. This process occurs at energies which are specific to the absorbing atom, therefore providing an element specific technique.

In order to return to the ground state, the core hole is filled by an electron from a higher energy orbital, this transition is accompanied by a release of energy that can be in the form of:[22]

- fluorescence radiation; which occurs when an electron from a higher-energy orbital fills the core hole by releasing an X-ray having energy equal to the difference in the energies of the two orbitals.
- Auger electron production; An electron from a higher-energy orbital fills a core hole, losing its energy by the emission of another electron (Auger electron) from the same or a different atomic shell.

The loss in intensity of the incoming X-ray is proportional to the incident intensity of the X-rays and the path length, as described in the Beer-Lambert equation (Equation 2.7):

$$I_t = I_0\, e^{-\mu(E)x} \qquad (2.7)$$

Where: I_t = the intensity of the X-ray beam transmitted through the sample, I_0 = the initial intensity of the X-rays, μ = absorption coefficient and x = the path length.

The X-ray absorption coefficient (μ) is the probability for an X-ray to be absorbed by a sample and is a function of the incident X-ray energy. In particular, the probability for absorption increases sharply when the incident X-ray energy equals the energy required to excite an electron to an unoccupied electron orbital (figure 2.17). These steps in the absorption coefficient are named absorption edges.

The energy of a specific edge increases as the atomic number of the element increases. This is because elements with greater atomic numbers have more positively charged nuclei from a greater number of protons, and therefore, they have a greater binding energy of an electron in a given atomic orbital. Each element has a specific set of absorption edges at the binding energies of its electrons.

The absorption edges are named depending on which core electron is excited: the principal quantum numbers n = 1, 2, and 3, correspond to the K-, L-, and M-edges, respectively; e.g. if a 1s electron is excited, this corresponds to the K-edge. Table 2.1 shows the relationship between the principal quantum number, the corresponding edge/orbital and the spin state j.

n	**Edge**	**Orbital**	**j**
1	K	1s	
2	L_1	2s	
2	L_2	2p	1/2
2	L_3	2p	3/2
3	M_1	3s	
3	M_2	3p	1/2
3	M_3	3p	3/2
4	M_4	3d	3/2
4	M_5	3d	5/2

Table 2.1 – List of edges with corresponding orbital and spin state j.

The dipole selection rules for transitions determination are:

$\Delta l = +/- 1$, $\Delta j = +/- 1$, $\Delta s = 0$

Where: l= total orbital angular momentum, j = total angular momentum, s=total spin; with examples being s→p and p→d (K→L and L→M).

To conclude, XAFS measures the energy dependence of the X-ray absorption coefficient, μ(E), at and above the absorption edge of a selected element. A typical X-ray absorption spectrum is collected from approximately 200 eV below an absorption edge of interest to approximately 1000 eV above the edge.

2.4.3.4 – Extended X-ray Absorption Fine Structure (EXFAS)

Above the absorption edge, the energy of the X-ray is used to excite an electron into the continuum, and the remaining energy is given to the photoelectron in the form of kinetic energy (E_k). The E_k of the photoelectron is equal to the difference between the incident X-ray energy and the electron binding energy of the photoelectron (E_0) (Equation 2.8):

$$E_k = h\upsilon - E_0 \qquad (2.8)$$

Where: E_k = the kinetic energy of a photo emitted electron; hν = the energy of the X-rays and E_0 = the binding energy of the electron.

The ejection of a photoelectron in a completely isolated atom results in the photoelectron propagating as an unperturbed isotropic wave. However, more realistically the absorber atom is surrounded by neighbours. The outgoing photoelectron behaves as a wave with a wavelength (λ), which is related to its momentum (*p*) by the de Broglie equation (2.9):

$$\lambda = \frac{h}{p} \qquad (2.9)$$

Where: *h* = is Planck's constant

The momentum (p) is also related to the *photo-electron wave vector*, *k*, by $p = \hbar k$, with $\hbar = h/2\pi$.
Since E_k and *p* are defined as $E = \frac{1}{2}mv^2$ and $p = m_e v$, it is possible to obtain the following relationships for an electron of mass m_e: $2Em_e = p^2$ and thus $\hbar k = \sqrt{(2Em_e)}$.
Thus, at a particular X-ray photon energy *E* above the threshold energy E_o, the photoelectron wave vector will be given by (equation 2.10):

$$k = \sqrt{\left(\frac{2m_e(E - E_0)}{\hbar^2}\right)} \qquad (2.10)$$

As the photoelectron wave leaves the atom, it will become back-scattered by the surrounding atoms (Figure 2.19).

The effect of constructive and destructive interference will cause an increase or decrease in the absorption coefficient respectively, represents the process contributing to the EXAFS region, resulting in the oscillations in the spectrum which starts approximately 50 eV after the edge (up to 1000 eV), as showed in figure 2.17.

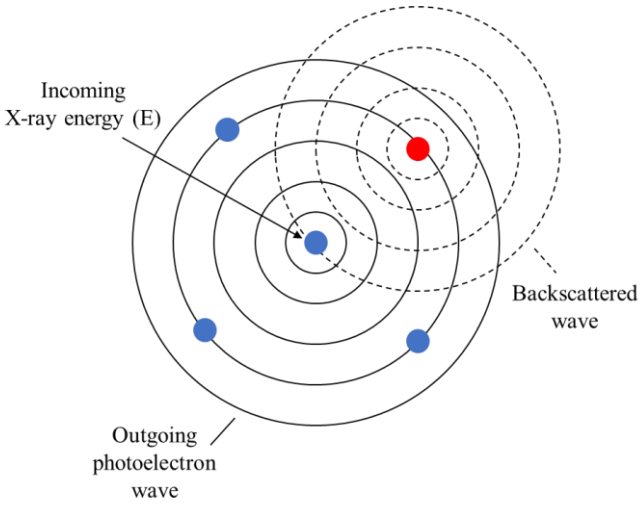

Figure 2.19 – Schematic representation of the interference pattern between outgoing and back scattered electrons, where blue is the absorber and red is the scatterer atom.

The electron scattering process is influenced by several factors, including the following:

- The atomic number of the scatterer: heavier atoms will scatter more than lighter ones.
- The distance between the absorber and the scatterer, which have a pronounced effect on the phase of the scattered electron and frequency of the oscillations.
- Thermal effects and the De-bye Waller factor: temperature reduces the oscillations in the EXAFS region.
- The energy of the scattered electron.

For all that said, EXAFS is based upon fractional changes in absorption as a function of k, $\chi(k)$. The EXAFS signal, $\chi(k)$ can be therefore described as a function of the wave factor k, as describe in equation 2.11:

$$\chi(k) = \frac{(\mu - \mu_0)}{\mu_0} \qquad (2.11)$$

Where: μ= The observed absorption coefficient, and μ_0= The absorption observed in the absence of EXAFS effects, i.e. a smooth background function representing the absorption of an isolated atom. The subtracted μ_0 represents removal of the background, and the division by μ_0 represents the normalisation of the function, to represent the average structure surrounding the central absorber atom. Since μ_0 cannot be directly measured, it is approximated, by fitting a smooth spline function through the data; these matters will be resumed in the section dedicated to the *data reduction*.

The EXAFS equation (2.13),[27,23] relates the EXAFS signal to structural parameters and allowed to obtain information from the EXAFS experimental spectra.

The equation is derived from the local scattering model proposed by Stern.[24,25] The model was based upon a single scattering process, in which the photoelectron is considered as being scattered back from one atom, i.e. the photoelectron is only scattered once before returning to the central atom. It is however well known that multiple scattering occurs for many systems. The EXAFS equation results as a summation of the sine waves produced by the outgoing photoelectron wave function and the back-scattered wave function from each coordination shell (equation 2.12, 2.13) in which the photo-electron visits two or more atoms before its return to the central atom.

$$\chi(k) = \sum_j \chi_j(k) \qquad (2.12)$$

$$\chi(k) = \sum_j S_o^2 \boldsymbol{N}_j \frac{|f_{effj}(k)|}{k\boldsymbol{R}_j^2} \sin\left(2kR_j + \delta_j(k)\right) e^{-\frac{2R_j}{\lambda(k)}} e^{-2k^2\boldsymbol{\sigma}_j^2} \qquad (2.13)$$

Where:

j = coordination shell;

$S_o^2 \boldsymbol{N}_j$ = terms that modify the amplitude of the EXAFS signal and do not have a *k*-dependence. In particular, for single scattering, Nj is number of coordinating atoms within a particular shell (coordination number) and S_0^2 is the amplitude reduction factor, accounting for relaxation of the absorbing atom due to the presence of the empty core level and multi-electron excitations (typically between 0.7 and 1.1)[26]. S_0^2 is different for different elements, but the value is generally transferable between different species from the same element and the same edge;

$f_{effj}(k)$ = term that accounts for the element sensitivity of EXAFS. This term is the effective photoelectron (back-) scattering amplitude. For a single scattering path, it is the atomic scattering factor used in X-ray diffraction. In general, atoms with more electrons scatter photoelectrons more strongly at higher wavenumbers. Because this factor depends on the number of electrons, it is similar between elements with nearly the same number of electrons, e.g. chlorine and sulphur, that can rarely be distinguished on the basis of their scattering amplitude alone.

Rj = average interatomic distance absorber-scatter.

$\sin\left(2kR_j + \delta_j(k)\right)$ = term account for the oscillations in the EXAFS signal with a phase given by $2kR_j + \delta_j(k)$. The path of the photoelectron is described by 2Rj which is multiplied by its

wavenumber (k) to determine the phase. $\delta_j(k)$ is a phase shift of the photoelectron caused by the interaction of the photoelectron with the nuclei of the absorber atom and the interaction with the nuclei of the coordinating atoms of the photoelectron path. Because the photoelectron has a negative charge and the nucleus is positively charged, the photoelectron loses energy and its wavelength lengthens as it interacts with the coordinating atoms and the absorber atom.
As it will be described later in this chapter, this term makes the Fourier transform (FT) of the XAFS signal resulting in peaks at distances related to Rj. The peak is not precisely at Ri due to the phase shift $\delta_j(k)$, which causes a shift in distance of approximately −0.5 Å.

$e^{-2k^2\sigma_j^2}$ = term as the EXAFS isotropic or effective Debye–Waller factor, which represents the decay of the signal with increasing thermal or static disorder. The effect of thermal or static disorder causes fluctuations in the positions of the atoms from their equilibrium atomic positions. As we go further out from the absorber, the effects will become greater, hence a reducing of the EXAFS signal further out in k, as a result of the mean squared disorder term σ^2.

$e^{-\frac{2R_j}{\lambda(k)}}$ = exponential term that depends on λ(k), the mean free path of the photoelectron (mfp). This term that causes the EXAFS signal to be dominated by the scattering contributions from atoms within approximately 10 Å of the absorber atom and makes EXAFS a local structural probe.

In summary, extended X-ray absorption fine structure (EXAFS) is an oscillatory modulation in the X-ray absorption coefficient, occurring at higher energies of the absorption edge. The EXAFS equation is used to extract information on the number and types of atoms in the immediate environment of the absorbing atom, as well as accurate absorber-neighbour distances.[27,28,29] However, the equation breaks down at low k (XANES region), as the $1/k$ term increases, and the single particle scattering is no longer a good approximation. Moreover, the term Rj^2 causes the expression to decrease exponentially over large values of Rj (larger distances between absorbing and scattering atoms), making EXAFS much weaker over long-distances (up to 4-5 Å) as opposed to short ranged neighbouring atoms.

2.4.3.5 – X-ray Absorption Near Edge (XANES)

The region of the XAS spectra within ~50 eV of the absorption edge is called X-ray Absorption Near Edge (XANES), mainly originating from electronic transitions from the core levels of the element being studied to higher levels either unfilled or partially filled, e.g. s → p, or p → d, following the dipole selection rules already mentioned. It strongly depends on local geometry (coordination number and ligand symmetry), with the absorption edge position and shape providing information on the oxidation state of the absorber.[30]

Three features can appear in the XANES region:

1) The absorption Edge, E_o: The absorption edge is the most prominent feature in the XANES spectrum and defines the onset of continuum states. The energy of the edge is specific to the element analysed (E_0 for the gold L_3-edge is 11919 eV). E_0 is a function of the absorber oxidation state, it may also increase by several eV per oxidation unit, and binding geometry. However, practically, it can be defined as the first inflection point in the XANES region, or the steepest inflection point, a point half way up the edge or it may be taken from a table. These ways of defining E_0 typically result in values that differ from each other by several electron volts. In certain XANES spectra, as in the case of L_3-edge of transition metal, i.e. gold, there is an intense initial peak at the top of the absorption edge. This peak historically called a 'white line' as it was first detected in early experiments on photographic plates which showed up as a white line due to the strong absorption. The term "white line" comes from the days when X-ray spectra were collected on film. Strong absorption at a given energy left the photographic negative unexposed, creating a literal white line.

2) The pre-edge: (not to be confused with the pre-edge region) The pre-edge occurs at a lower energy than the rising edge and is a result of electronic transitions to empty bound states near the Fermi energy. The final state is usually not atomic-like and may have hybridisation with other orbitals. Pre-edges provide information about absorber local geometry and electronic state around the absorber. This region can be used to estimate the ligand-field.

3) Post-edge: The post edge is reliant on multiple scattering features. The analysis of the post-edge provides information regarding the local atomic structure and geometry.

The advantages of XANES analysis are outlined below:

- Element Specific
- Provides a good fingerprint for quick analysis
- Quicker to measure than the whole EXAFS spectra.
- Weak temperature dependence (Debye Waller effect), so measurement can be performed in situ
- Simpler spectrum to measure than EXAFS. The absorption edge is usually very intense.

Although XANES benefits from the above advantages, it can be very complicated to analyse, since features are dominated by multiple scattering resonances of the photoelectrons ejected at low kinetic energy. As previously told, the EXAFS equation breaks down at low k, due to the $1/k$ term and the increase in the mean free path at very low k. This complicates the XANES interpretation significantly,

and as a consequence, the majority of XANES analysis is limited to a semi-quantitative interpretation. For this reason, XANES was used for determination of oxidation state by comparison with standards and through the use of linear combination fittings (LCF's), as it will describe in chapter 4. Here, linear combinations of known spectra from reference compounds are able to quantify ratios of valence states and phases within unknown compounds. The fits can be done using normalised μ(E) spectra or $\chi(k)$ spectra and using ATHENA software to carry out this analysis as it will also describe below.

2.4.3.6 – Acquisition modes

There are two common modes to measure XAFS spectra: transmission and fluorescence. Both modes will yield absorption spectra, but a choice of which is most appropriate depends on the sample being studied.

2.4.3.6.1 – Transmission

XAFS measurement in transmission measures the X-ray flux transmitted through a sample. When possible, transmission mode is considered the best way of acquiring XAFS data due to relatively high quality of data (signal to noise ratio) as well as the speeds at which the spectra can be recorded.
The intensity of the X-ray beam is measured before and after the sample and the absorbance (μx) is calculated using the Beer Lambert law (equation 2.14). The intensity of the X-ray beam is typically measured using ionisation detectors.

$$I_t = I_0 e^{-\mu t} \qquad (2.14)$$

Where I_o= Initial X-ray energy and I_t= Transmitted X-ray energy, t= Sample thickness.

The X-ray absorption coefficient is determined by rearranging equation 2.14 (equation 2.15):

$$\mu t = ln\left(\frac{I_0}{I_t}\right) \qquad (2.15)$$

For an ideal sample, between 50 and 90 % of the X-ray beam intensity is absorbed, details about the possible acquisition mode are described later on in this chapter. Typically, the ion chambers measure the initial intensity (I_0), the intensity after passing through the sample (I_t) and intensity after passing through a reference foil (I_f). Measuring I_t and I_f allows for the calculation of the absorption spectra over the reference foil. This is useful as it can act as an internal calibration as it is measured at the same time as the sample and can be used, for example, to align spectra. This is very useful to compare spectra of

the same sample recorded at different times or beamlines, where small shifts in energy can be observed. The basic principle of the ionisation chamber is that it measures the charge created through the direct ionisation of a gas from the X-rays.[31] The chamber consists of a gas-filled unit, with two metal plates, a cathode and an anode, with a voltage applied to stimulate an electric field in the fill gas. Each ion chamber is filled with a mixture of inert gasses; depending on the X-ray flux the gas composition will be set accordingly. Gas between the electrodes becomes ionised by the incoming radiation, creating ion pairs. Positive ions will quickly diffuse to the cathode, whilst the electrons produced will attract to the anode under the influence of the electric field. This results in an ionisation current, measured by an electrometer. Each ion pair created deposits or removes a small electric charge to or from the electrode. The accumulated charge is proportional to the number of ion pairs created in the process, this will therefore indicate the X-ray dose.

2.4.3.6.2 – Fluorescence

Fluorescence mode can be used if the sample is not able to be run in transmission due to an unsuitable concentration (dilute systems down to ppm levels) or a high absorption matrix or thick samples.
The absorbance of the sample is measured by monitoring the intensity of the X-ray fluorescence produced, when higher-shell electrons relax and refill the deep core hole left by the photoelectron. The energy difference between the outer shell and the inner shell is emitted as fluorescent radiation characteristic of the target element. In particular, because core hole production and consequent relaxation processes are proportional to absorption, the absorption coefficient can also be derived from the number of fluorescence X-rays (I_f) as follow (equation 2.16):

$$\mu x \propto \frac{I_f}{I_0} \qquad 2.16$$

The standard geometry for fluorescence detection is designed to optimise the fluorescence signal, by placing the detector away from the X-ray path (at 45˚ to the sample).
However, there are several draw-backs to fluorescence including poor data quality (signal to noise ratio) especially at high *k* values and often measurements can be time consuming which can be a problem when synchrotron time is limited.

2.4.3.6.3 – Measurements at B18

B18 is a general purpose XAS beamline located in Zone 1 at the Diamond Light Source. Diamond light source produces an electron beam with 3 GeV of energy. B18 can access energies in the range of 2-35 keV. In the optics hutch three main optical elements are in place: a collimating mirror, a double crystal monochromator and a double toroidal focusing mirror, for the lower energy range it is also possible to exploit harmonic rejection mirrors. B18 allowed detection both in transmission, using ionisation

chambers, and in fluorescence, using a high rate fluorescence 9 element Ge solid state detector system. In particular, the monochromatic beam generated in optics hutch passes through an ion chamber that monitors the beam intensity, I_0, by absorbing part of it (~20%) (Figure 2.20). The energy of the beam depends on the monochromator used: the Si (111) gives a range of 2.1-20.2 keV, whilst the Si (311) gives an energy range of 4-35 keV, which is primarily used for high energy, but also at low energy for improved edge resolution. The monochromator can operate in both step-scan and continuous (QEXAFS) scan modes. The beam then passes through the sample, and the X-rays intensity, I_t, is monitored by the second ionisation chamber. Finally, the beam passes through the reference foil, I_r measures the intensity of X-rays after passing through the sample and a reference foil. Figure 2.20 details about the XAS setup, the sample stage and the schematic of the reactor and the heater modified to allowed measurements in transmission mode.

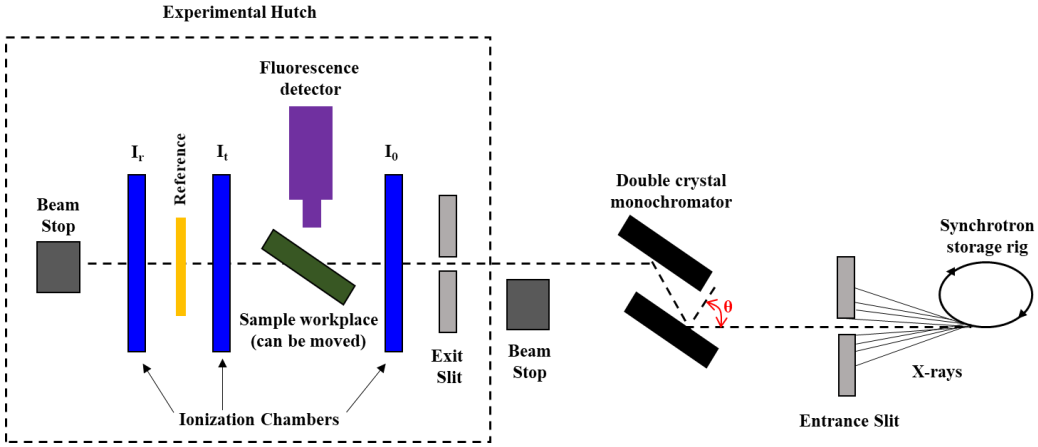

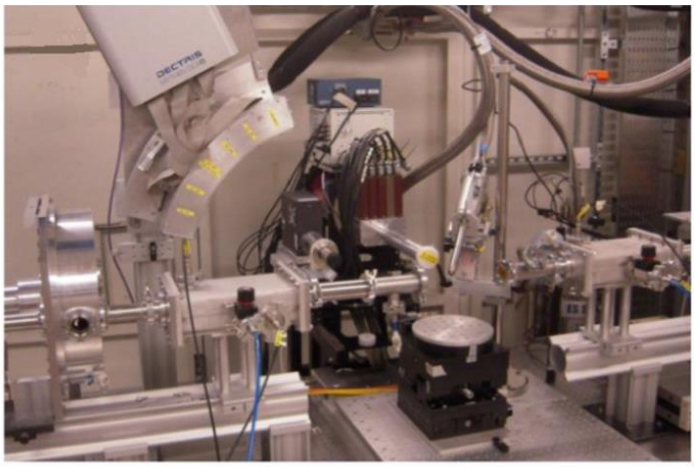

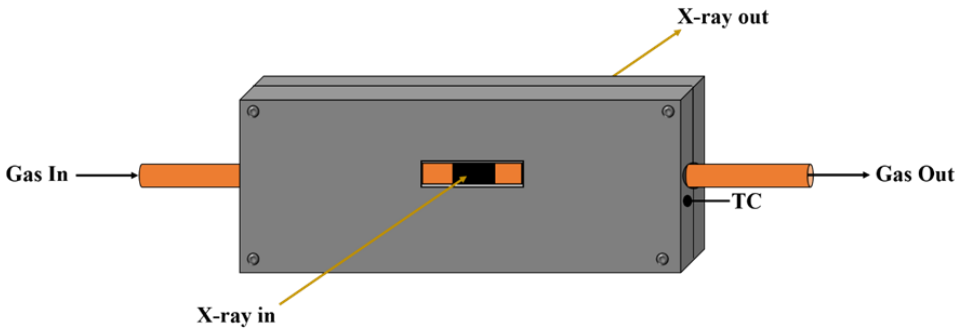

Figure 2.20 – (top) Example of XAFS set up, (centre) picture of sample workspace and (bottom) schematic of the modified heater to allow the measurement in transmission mode.

X-ray absorption fine structure (XAFS) spectra for all the Au/C samples were recorded at the Au L_3-absorption edge, in transmission mode, under reaction conditions, at the B18 beamline of Diamond Light Source, Harwell, UK. The measurements were performed using a QEXAFS setup with a fast-scanning Si (111) double crystal monochromator. For the *in situ* measurements the time resolution of the data acquisition was 20s/ spectrum. All transmission XAFS spectra were acquired concurrently with a Au foil placed between *It* and *Iref*.

2.4.3.6.4 – Measurements at BM28

The BM28 - XMaS beamline is sited on the soft end of dipole 28 (critical energy 9.8 keV) is located at the ESRF. The ESRF consists of an 844 m circumference storage ring fed from a 300 m circumference 6 GeV booster synchrotron and a LINAC pre-injector. BM28 has been designed to perform experiments over an energy range of 2.4 to 15 keV continuously tuneable.

The ligand K-edge XANES spectra recorded and shown in Chapter 6 where recorded in fluorescence mode. The fluorescent signal was detected using a silicon drift diodes detector. A schematic of the experimental hutch is shown in figure 2.21.

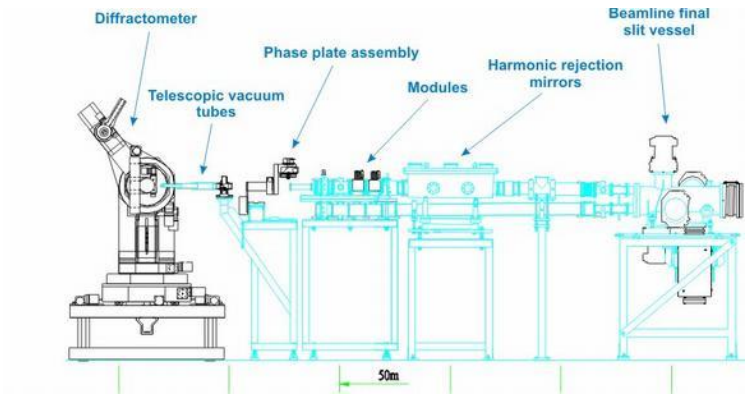

Figure 2.21 – Physical layout of the equipment in the experimental hutch in BM28.[32]

At the BM28 it is possible to run a so-called XESCAN.MAC – Extended Escan: Variable point density. In particular, it is possible to perform energy scan for multiple consecutive energy regions, with equal or different step (variable point density), full details are reported in Chapter 6.

2.4.3.6.5 – Samples preparation

To perform an XAFS experiment a sample must be uniform and homogeneous. Moreover, the amount of sample used in the experiment is a key factor that is influenced by both the experimental mode used (transmission or fluorescence) and the edge chosen. The edge used should not have an energy greater than 40 keV. In general, the binding energy increase with the increase of the atomic number, thus for small atomic number it may be possible to use the K-edge, while for greater atomic numbers a greater edge such as the L- or M-edge may be required (Figure 2.22).

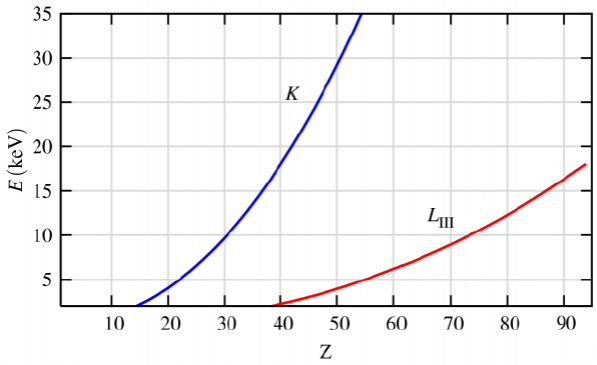

Figure 2.22 – Plot of the Atomic number, Z, versus Energy/eV. Hard X-ray region: 4-40 keV Soft X-ray region: 0.2-4 keV.[33]

Once the edge has been chosen it is possible to calculate the XAS absorption coefficient, μ, for each element in the sample to analyse and thus the total absorption of the sample. (Equation 2.26).

$$\mu = \sigma\rho \qquad (2.26)$$

Where: μ = absorption coefficient, σ= Cross section, which depends on the edge energy and can be obtained online from various XAS related sites and ρ = Density.

To conduct experiments in transmission mode the element must be concentrated enough in order to give an edge step of >0.1, reasonably concentrated elements would be >3-5 w/t %. The thickness must be adjusted so that the total absorption is <2.5 absorption lengths, ideally giving an edge step of approximately 1. This is because, if the concentration of the target element is too dilute not enough X-rays will be absorbed and there will be a poor signal to noise ratio, while, if the sample is too

concentrated then it is possible that there will be too much X-ray absorption for clean data. Moreover, if the absorption of the sample is too high this could induce self-absorption, resulting in errors in the determination of co-ordination numbers in EXAFS analysis. When the total absorption is higher the data must be collected in fluorescence mode or diluting the sample with cellulose or boron nitride must be considered.

2.4.3.7 – Data Reduction

Data reduction is possible through the use of IFEFFIT, which is a combination of programs for XAFS analysis, including Hephaestus, Athena and Artemis. Athena is the software specifically designed for the XANES part of the analysis, whilst Artemis is the software primarily used for EXAFS investigations. The software enables the user to do a multitude of tasks including the following:

- Read/Write ASCII data files.
- Data manipulation.
- Data plotting.
- XAS pre and post edge removal, normalisation and E_o determination.
- EXAFS Fourier Transform (Hanning, Kaiser-Bessel, and Sine Window Functions).
- Simultaneous refinement of multiple data sets.
- Apply constraints and restraints to the fit.

Data reduction involves several steps:

1) The measured intensities are converted to absorption μ(E), and plotted against energy (eV)
2) A smooth pre-edge function is subtracted from μ(E), to remove the baseline from the EXAFS. This accounts for any instrumental background, and absorption from other edges.
3) A post-edge function is subtracted. Post-edge background subtraction involves drawing a smooth background through the oscillatory part of the XAFS and extracting χ(k).
4) E_0 is defined. This is usually performed taking the maximum of the first derivative of μ(E) or a point half way up the edge or it may be taken from a table (E_o for the Au L_3-edge is 11919 eV).
5) The data is normalised between 0 and 1, i.e. so that the edge jump is equal to 1. This allows the user to compare between data sets, as well as the comparison of data with theory.
6) A conversion is performed from χ(E) to χ(k), i.e. isolation of the XAFS χ(k). *k*-weighting of the XAFS is performed (weighting between k^1- k^3). This can then be Fourier transformed to give a radial distribution plot in R-Space. A FT is a mathematical transform which converts one mathematical function into another. In XAFS, the FT essentially acts as a frequency filter transforming into frequency space, which results in a radial distribution function where peaks

correspond to the most likely distances of the nearest-neighbours. The FT can therefore take a signal which is delocalised in *k*-space and transform it so that it is localised in R space (See Figure 2.22 C and D). In other words, FT's can break down a *k*-space signal into its different constituent frequencies. The IFFEFIT package enables the user to perform FT's quickly and easily, with the ability to do both forward FT's and reverse. It must be noted that, for many systems, the following approximation in possible: $\delta j(k) \approx -2\alpha 0k$, where $\alpha 0$ is the Bohr radius. Causing peaks for a particular shell in the Fourier transform of $\chi(k)$ to be shifted ~ 0.5 Å below the actual interatomic distance.

All these steps are described in figure 2.22.

Once the data has been processed and normalised in Athena it can be transferred to Artemis and a fit generated for determination of coordination number, R distance, Debye Waller factor and R factor (measure of how close the fit is) for a given sample. The first step in Artemis is to calculate the amplitude reduction factor for a given element by fitting the foil for the appropriate element with a cif file and used as a fixed input parameter. Once this is done the cif file/files containing the scattering path/paths to be fitted needs to be imported. With all the parameters set up the software can generate a fit with the calculated values for coordination number, R distance, Debye Waller factor and R factor. To improve the quality of the fit it is sometimes necessary feed the calculated values back in to the software and refit in an iteration process.

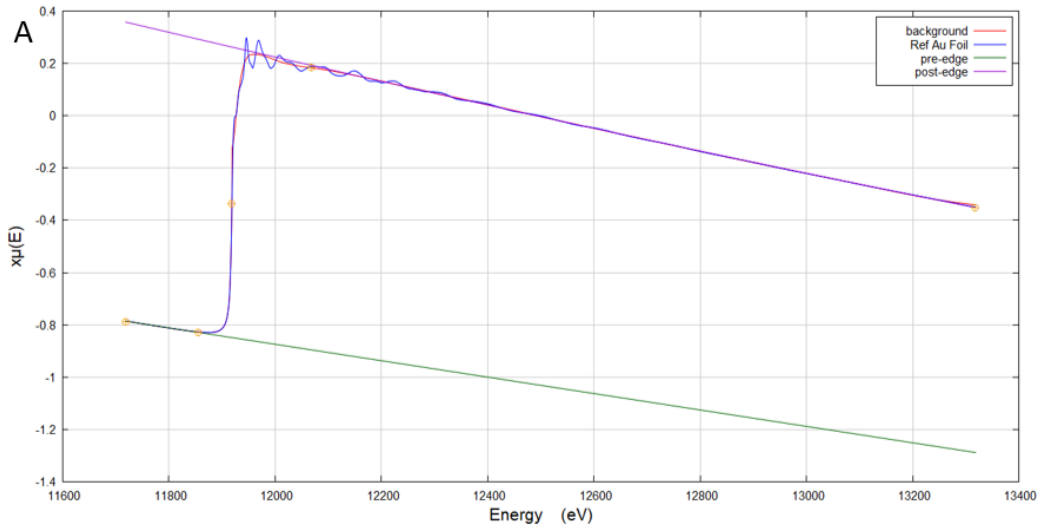

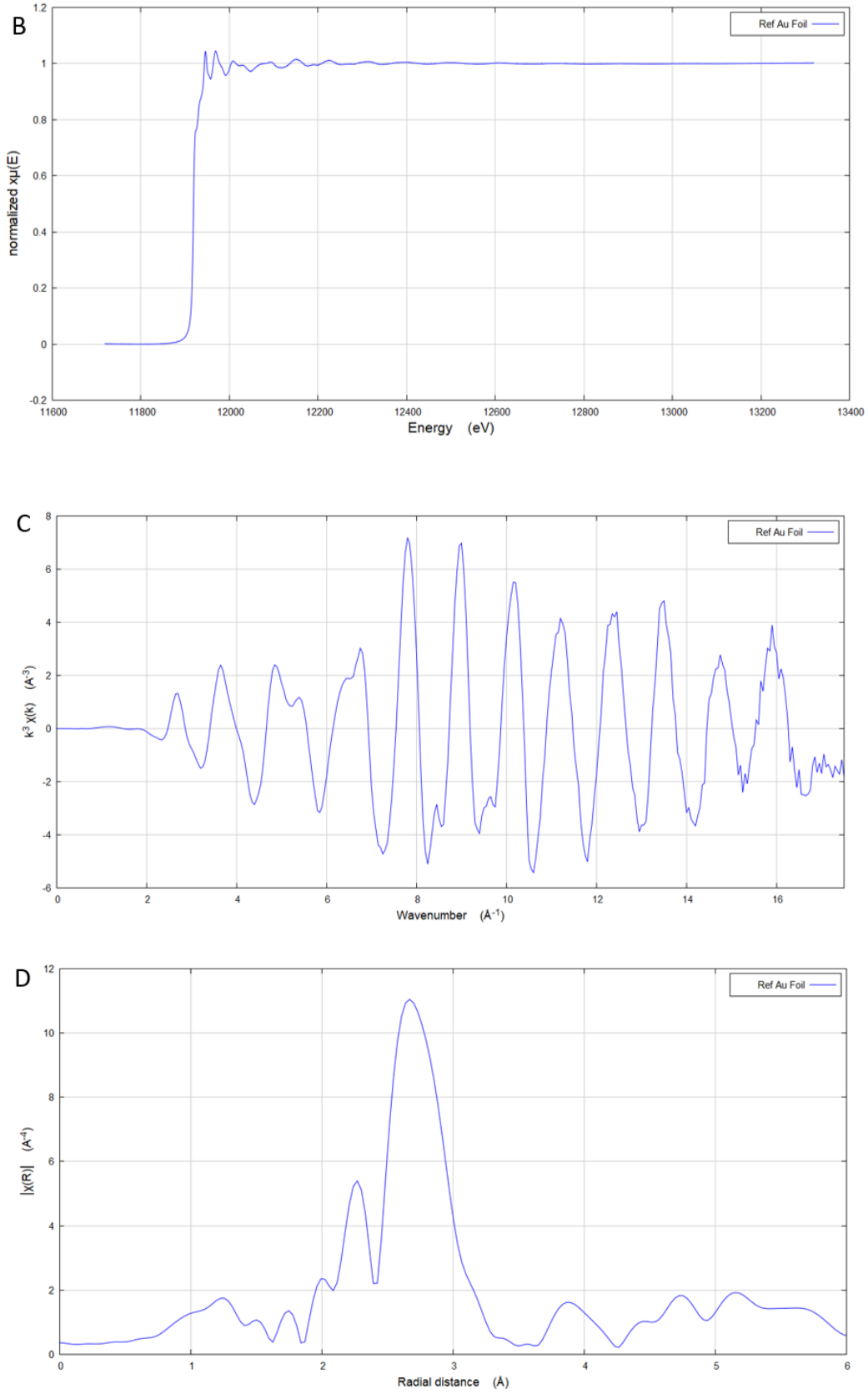

Figure 2.22 – Au L_3 edge (A) Raw data including absorption (xμ), background (bkg), post and pre-edge lines, (B) normalised absorption, (C) removal of background (χ) and (D) radial distance produced by a Fourier Transform of χ.

2.4.4 – Inelastic Neutron Scattering (INS)

Neutron spectroscopy measures the atomic and magnetic motions of atoms. Inelastic neutron scattering (INS) measures the change in the energy of the neutron as it scatters from a sample, which can be used to probe a wide variety of different physical phenomenon: diffusional or hopping motions of atoms, the rotational modes of molecules, sound modes and, or like in the case showed in chapter 6, molecular vibrations. INS data have been acquired at the ISIS Neutron and Muon Source, based at the STFC Rutherford Appleton Laboratory in Oxfordshire, UK.

In ISIS neutrons are produced via a spallation process, in which a heavy atom is invested by a high-energy particle that causes the emission of nucleons with a consequent reduction of the mass. The heavy metal destroyed in the process produces a certain number of hot neutrons for each impact, in addition to lighter residual atoms, thermal energy and highly energetic fermions. The neutrons are collected and sent to the instruments. In particular, INS spectra presented in Chapter 6 were recorded with the MERLIN[34] spectrometer (Figure 2.23).

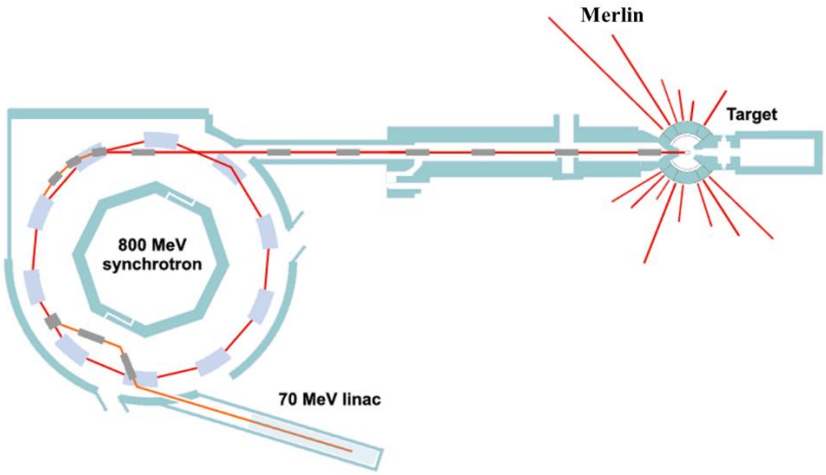

Figure 2.23 – Schematic diagram of the pulsed source at ISIS.[35]

~10 g of 2wt% Au/C-AR, Au/C-HNO_3 and Au/C-H_2O was loaded into an in wire sealed flat plate Al can and the spectra were recorded at <20 K to minimise the Debye-Waller factor (figure 2.24 - B). All the samples will be measured using incident energies of 600, 250 and 100 meV to observe the C–H/O–H stretch, in-plane C–C stretches/C–H bends and the out-of-plane deformations respectively ~ 10 g 2% Au/C-AR catalyst was loaded into a Conflat sealed stainless steel cell[36] and dried at 200 °C under vacuum (figure 2.24 - A). The catalyst was then dosed with C_2H_2(5%)/He at 200 °C. After measurement of the spectra, the catalyst was then dosed with 100% C_2H_2 at 200 °C and the spectra measured using the same incident energies mentioned above.

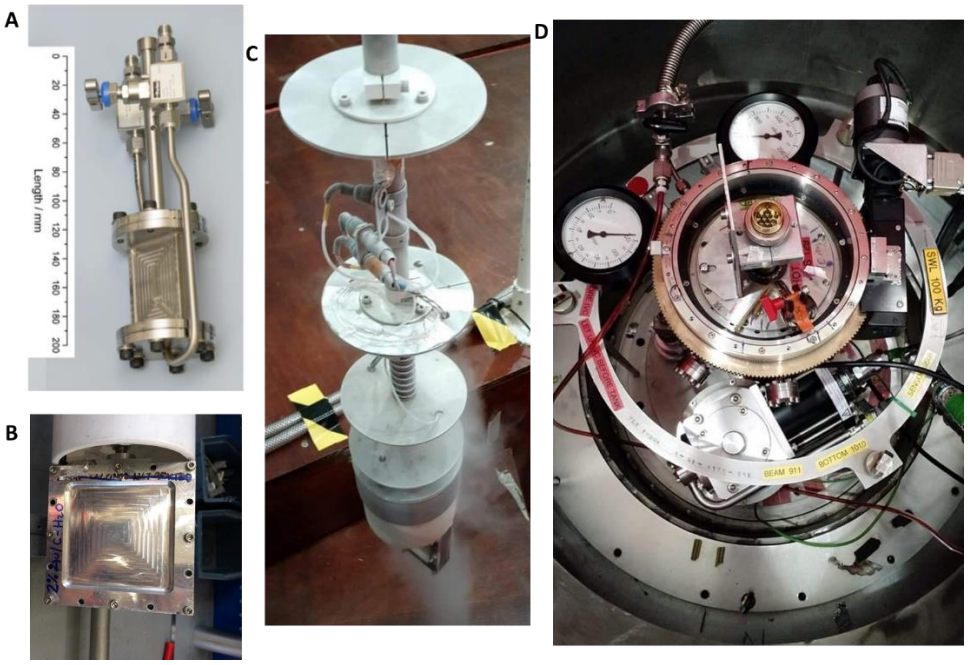

Figure 2.24 – (A) Conflat sealed stainless steel cell, (B) wire sealed flat plate Al can, (C) cell or plate are mounted to the Merlin setup and cool down to <20 K and (D) the reactor is then placed in the ground for measurement.

2.4.5 – Computational Studies

Computational work showed in Chapter 4 has been performed by Dr A. Thetford within the group of Prof. R. Catlow. To investigate the role of cationic gold, i.e. Au(I), in the reaction mechanism a Density Functional Theory (DFT) study of the interaction of HCl with supported Au species have been performed using the CASTEP code.[37,38,39] The investigation was focused on the study of AuCl species on a graphite surface. The model used for the surface is from the work of Willock *et al*..[40] More detail about this study are reported elsewhere in literature.[41]

2.5 – References

1. J. Haber, J. H. Block and B. Delmon, *Pure Appl. Chem.*, **1995**, *67*, 1257–1306.

2. J. P. Brunelle, in *Preparation of Catalysts*, II, Eds.: B. Delmon, P. Grange, P. A. Jacobs, G. Poncelet, Elsevier Science, Amsterdam, **1979**, 211.

3. X. Liu, M. Conte, D. Elias, L. Lu, D. J. Morgan, S. J. Freakley, P. Johnston, C. J. Kiely and G. J. Hutchings, *Catal. Sci. Technol.*, **2016**, *6*, 5144–5153.

4. P. Johnston, N. Carthey and G. J. Hutchings, *J. Am. Chem. Soc.*, **2015**, *137*, 14548–14557

5. http://www.igisystems.co.uk/process-interface.html

6. http://www.igisystems.co.uk/LAB-Interface.html

7. G. Schwedt, *Essential Guide To Analytical Chemistry*, Wiley and Sons, **1997**, 142-173.

8. D. A. Skoog, D. M. West, F. J. Holler and S. R. Crouch, Fundamentals of Analytical Chemistry, 8th edn., Thomson Learning, **2004**.

9. https://www.vici.com/support/app/app11j.php

10. L. Szepesy, *Gas Chromatography*, Iliffe Books Ltd., **1970**.

11. https://www.boconline.co.uk/internet.lg.lg.gbr/en/images/tg-8364-acetylene410_39655.pdf?v=6.0

12.https://www.boconline.co.uk/internet.lg.lg.gbr/en/images/sg-069-hydrogen-chloride-v1.4410_39634.pdf?v=3.0

13. C. Davies, *Gold Catalysts for the Hydrochlorination of Acetylene* (Doctoral dissertation), **2012.**

14. P. B. J. Thompson, B. N. Nguyen, R. Nicholls, R. A. Bourne, J. B. Brazier, K. R. J. Lovelock, S. D. Brown, D. Wermeille, O. Bikondoa, C. A. Lucas, T. P. A. Hasee and M. A. Newton, *J. Synchrotron Rad.*, **2015**, *22*, 1426-1439

15. J. Pickworth Glusker and K. N. Trueblood, Crystal Structure Analysis, 3rd edn., Oxford University Press, **2010**.

16. W. L. Bragg, Proc. R. soc. Lond. Ser. A-Contain. Pap. Math. Phys. Character, **1913**, *89*, 248-277.

17. J. W. Niemantsverdriet, *Spectroscopy in Catalysis 3rd Edition*, Wiley, **2007**.

18. S. Amelinckx, D. V. Dyck and J. V. Landuyt, *Handbook of Microscopy – Applications in Materials Science, Solid State Physics and Chemistry Methods II*. **1997**.

19. http://www.lehigh.edu/~inmicro/200cf.html

20. S. Bordiga, E. Groppo, G. Agostini, J. A. Van Bokhoven and C. Lamberti, *Chem. Rev.*, **2013**, *113*, 1736–1850.

21. G. J. Sherborne and B. N Nguyen, *Chem. Cent. J.*, **2015**, *9*, 37

22 B. K. Teo, EXAFS spectroscopy: Basic principles and data analysis. Springer-Verlag, New York, 1986.

23. F. Lytle, D. Sayers and E. Stern, *Physical Review B*, **1975**, *11*, 4825.

24. E. A. Stern, *Contemp. Phys*., **1978**, *19*, 239–310

25. E. A. Stern and S.M. Heald, *Basic principles and applications of EXAFS*, In Handbook of synchrotron radiation Vol. 10, Ed.: E.E. Koch, North-Holland, Amsterdam. **1983**, 995–1014

26. G.G. Li, F. Bridges and C.H. Booth, *Phys. Rev. B*, **1995**, *52*, 6332–6348.

27. S. Kelly, D. Hesterberg and B. Ravel, *Methods of soil analysis. Part 5*, **2008**, *5*, 387-464.

28. G. Bunker, *Introduction to XAFS – A Practical Guide to X-ray Absorption Fine Structure Spectroscopy*, Cambridge University Press, **2010**.

29. J. Evans, *X-ray Absorption Spectroscopy for the Chemical and Materials Sciences*, Wiley, **2018.**

30. J. J. Rehr and A. Ankudinov, *Coord. Chem. Rev.*, **2005**, *249*, 131-140.

31. R. Pettifer, M. Borowski, and P. Loeffen, J. Synchrot. Radiat., **1999**, *6*, 217-219.

32. https://warwick.ac.uk/fac/cross_fac/xmas/xmasbeamline/description/equipment/experimentalhutch

33. M. Newville, *Fundamentals of XAFS*, Consortium for Advanced Radiation Sources, University of Chicago, Chicago, **2004**.

34. R. I. Bewley, T. Guidi, S. M. Bennington, Notiziario Neutroni e Luce di Sincrotrone, **2009**, 1422-1427

35. http://pd.chem.ucl.ac.uk/pdnn/inst3/pulsed.htm

36. R. Warringham, D. Bellaire, S. F. Parker, J. Taylor, C. M. Goodway, M. Kibble, S. R. Wakefield, M. Jura, M. P. Dudman, R. P. Tooze, P. B. Webb and D. Lennon, *J. Phys. Conf. Ser.*, **2014**, *554*, 012005.

37. S. J. Clark, M. D. Segall, C. J. Pickard, P. J. Hasnip, M. J. Probert, K. Refson and M. C. Payne, *Z. Kristallogr.*, **2005**, *220*, 567-570.

38. N. Govind, M. Petersen, G. Fitzgerald, D. King-Smith, J. Andzelm, *Comput. Mater. Sci.*, **2003**, *28*, 250–258.

39. E. R. McNellis, J. Meyer and K. Reuter, *Phys. Rev. B*, **2009**, *80*, 205414.

40. R. Burgess, C. Buono, P. R. Davies, R. J. Davies, T. Legge, A. Lai, R. Lewis, D. J. Morgan, N. Robinson and D. J. Willock, *J. Catal.*, **2015**, *323*, 10–18.

41. G. Malta, S. A. Kondrat, S. J. Freakley, C. J. Davies, L. Lu, S. Dawson, A. Thetford, E. K. Gibson, D. J. Morgan, W. Jones, P. P. Wells, P. Johnston, C. R. A. Catlow, C. J. Kiely and G. J. Hutchings, *Science*, **2017**, 355, 1399–1403.

Chapter 3

Investigation into the nature of the active site in gold catalysts for acetylene hydrochlorination

3.1 – Introduction

The prediction that gold could be an active catalyst for the hydrochlorination of acetylene to produce vinyl chloride monomer (VCM) dates back to 1985,[1] the recent validation of a Au/C catalyst at industrial scale has increased the need to understand the nature of the active form of the catalyst and the catalytic cycle which is still being investigated and debated. Early studies regarding Au/C catalysts, used an impregnation method from *aqua regia* as a solvent to guarantee the gold dissolution.[2,3,4] Already at this stage, the considerably high activity of these class of catalysts was postulated to be due to the presence of oxidised gold species in the final material.

A Mössbauer spectroscopy study by Nkosi,[4] provides some of the earliest evidence for cationic Au being the catalytically active species in the acetylene hydrochlorination reaction. Following this, other works have suggested the presence of Au(III) is important for high activity to be observed.[5] However, *ex situ* spectroscopy and electron microscopy studies showed that gold nanoparticles are predominantly present in the catalytic material and the active site could be cationic gold associated with the periphery of these nanoparticles.[4,6,7,8] However, the observation of Au(0) in these studies has led some researchers to suggest that metallic Au nanoparticles are themselves the active site.[6,8] Recent work from Hutchings and co-workers reported the use of various acids (HNO_3, HCl) for the dissolution of

the metal precursor ($HAuCl_4$) which affected both the dispersion and the nature of the Au species present on the catalyst. [9] These catalysts, and especially the most active, which was shown to be prepared from an *aqua regia* solution, were initially inactive and characterised by a pronounced induction period. This induction phase was hypothesised to be associated with development of the active gold species. It was proposed that the active sites were comprised of metallic nanoparticles partially oxidised at the surface and that Au(I)/Au(III) couple was formed *in situ* by reaction with both reactants.

From these general consensuses that the active site could be cationic Au, P. Johnston *et al.* concluded that catalysts prepared from complexes containing soft donor ligands, like sulphur, may display considerable activity by stabilising Au on the carbon support in high oxidation states (Au(I) and Au(III)).[10,11] However, this hypothesis was based largely on the characterisation and comparison of fresh and used catalysts. To draw accurate structure-function relationship these changes in Au speciation need to be observed *in situ*, and X-ray absorption fine structure (XAFS) spectroscopy is the ideal technique to provide these insights. XAFS has been extensively applied to study heterogeneous and homogeneous catalysts,[12,13] providing information on the electronic and structural properties[14,15] of catalysts while working at real reaction conditions.

This chapter investigates the evolution of Au speciation in Au/C catalysts during the acetylene hydrochlorination reaction measuring the Au L_3-edge XAFS spectra under reaction conditions. This work aims to determine the changes in Au speciation during the initial induction period and the active state of Au during the catalysis. The role of the solvents used in the catalysts preparation will be investigated and the activity will be compared with the recently industrially validated catalyst.[10,11]

3.2 – Results and discussion

3.2.1 – Experimental

In this chapter, two sets of Au/C catalysts (1_{wt}% Au/C-AR and 1_{wt}% Au/C-H_2O) were prepared by the wet impregnation methods described in Chapter 2 using tetrachloroauric acid as metal precursor. Moreover, a 1_{wt}% Au/C-S_2O_3 provided by Johnson Matthey[16] was characterised and tested. The catalytic tests were carried out according to the testing procedures described in Chapter 2. A summary of the testing conditions is given below.

3.2.1.1 – Reaction conditions for the catalytic test of Au/C-AR and Au/C-H_2O

The reaction gas mixture of 5% C_2H_2/Ar (24 mL min^{-1}), 5% HCl/Ar (24 mL min^{-1}) and additional Ar (2 mL min^{-1}) was introduced into the heated reactor chamber containing the catalyst (90 mg) to give a

total flow of 50 mL min^{-1} at a total gas hourly space velocity (GHSV) of ~14,000 h^{-1}, keeping the C_2H_2 : HCl ratio at a constant value of 1 : 1.02.

3.2.1.2 – Reaction conditions for the catalytic test of Au/C-S_2O_3

C_2H_2 (17.5 mL min^{-1}) and HCl (17.5 mL min^{-1}) were mixed via calibrated mass flow controllers into the heated reactor containing the catalyst (90 mg), to give a total flow rate of 35 mL min^{-1} and a GHSV of ~11,000 h^{-1}, keeping the C_2H_2 : HCl ratio at a constant value of 1 : 1.02.

3.2.2 – Investigation of the active site in Au/C-AR catalyst

3.2.2.1 – *Ex situ* characterisation of the freshly prepared Au/C-AR catalyst

A Au/C catalyst was prepared according the method previously reported in the literature,[9] using activated carbon as support and *aqua regia* as solvent (1_{wt}%Au/C-AR). The freshly prepared 1_{wt}% Au/C-AR catalyst was characterised *ex situ* to gain information about structure and morphology of the material after drying at 110 °C for 16 h under an N_2 atmosphere. Figure 3.1 shows representative high-angle annular dark-field (HAADF) - scanning transmission electron microscopy (STEM) images of the freshly prepared catalyst, acquired by our collaborators at Lehigh University in the group of Prof. C. Kiely. The HAADF-STEM figures were acquired by rastering an ultra-fine electron beam over the specimen under conditions optimised to prevent damage to the sample by over exposure of the electron beam. The HAADF-STEM images shown in figure 3.1, reveal the presence of highly dispersed isolated Au species with limited presence of sub-nanometer clusters. Contrary to previous reports,[9] no beam damage has been observed upon extended electron beam irradiation.

HAADF-STEM analysis also allowed the detection of a small population of possible dimeric Au species (Figure 3.1). Acquiring a STEM image, it is not possible to have certainty of the relative position of two neighbouring atoms; but if the two neighbouring atoms are both in good focus, chances are they are at similar heights in the sample. In the fresh catalyst sample, where atomic Au could be observed as the predominant species, Au-Au atomic pairs with a distance below 0.34 nm were also detected (with an error in distance measurement of ±0.024 nm). Considering the Au-Au distance in $AuCl_3$ is 0.32-0.34 nm, the possible formation of dimers was also distinguished in this sample. However, the presence of those dimeric species was a negligible component compared to the isolated monomeric Au species.

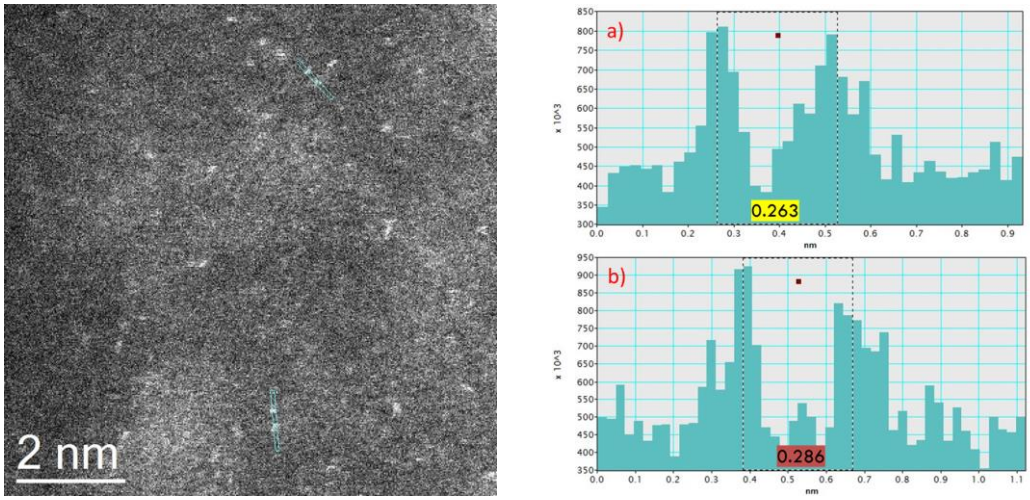

Figure 3.1 – (Left) Representative HAADF-STEM images of a freshly prepared 1_{wt}% Au/C-AR catalyst. (right) Evidence of dimeric Au species.

With the aim of excluding the presence of Au nanoparticles in the freshly prepared material, powder X-ray diffraction (p-XRD) patterns were acquired (Fig. 3.2). Reflections due to gold are expected at 38, 44, 64 and 78° 2θ. However, the p-XRD pattern for the sample is comparable to that of the carbon support alone, with the absence of any degree of long range order. The carbon support comprises of amorphous and graphitic domains, the latter of which give rise to the broad diffraction peak at $2\theta \approx 43°$.

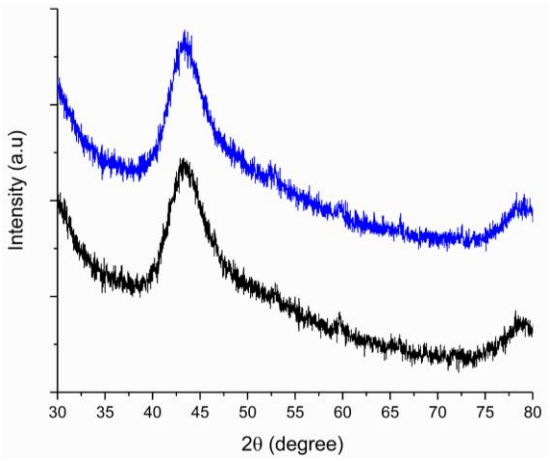

Figure 3.2 – p-XRD data of a 1_{wt}% Au/C-AR catalyst (blue solid line – top) and the bare carbon support (black solid line – bottom).

The same material was characterised *ex situ* by X-ray absorption fine structure (XAFS) spectroscopy at the Au L_3-edge to obtain information the electronic state of the gold by the analysis of the X-ray absorption near edge structure (XANES) and about the local structural model by analysing the extended X-ray absorption fine structure (EXAFS). The spectra were acquired on the B18 beamline in transmission mode, as described in Chapter 2.

The analysis of the XANES region of the XAFS spectrum have been performed by focusing on the changes in absorption intensity and energy position of the so called "white line". The white line intensity indicates the occupancy of the metal d-band, i.e. Au species with high oxidation states have strong white line adsorption features. Analysis of the sample spectra, when compared to appropriate standards,[17,18] can provide information about the photoabsorber oxidation state. To allow this to be determined, the XAFS spectra of a Au(III) standard has been recorded together with the reference, gold foil. As for the Au(I) standard, due to the high instability of the AuCl compound, an $[AuCl_2]^-$ standard obtained from difference spectra calculated in previously reported work was used from the raw data supplied by the authors of the study.[17] Figure 3.3 shows the XANES spectra for cationic Au standards of Au(III) ($KAuCl_4$/$[AuCl_4]^-$), Au(I) ($[AuCl_2]^-$) and the reference material (gold foil). In the XANES region of the Au(III) standard spectrum a very prominent feature on the absorption edge is observed and this is attributed to the Au $2p_{3/2} \rightarrow 5d$ transition. The intensity of this peak is reduced in the Au(I) standard and is absent for the gold foil where a typical absorption edge shape is observed. The normalised white line height value for the cationic Au standards, Au(III) and Au(I), are 1.1 and 0.6 respectively. More details about data elaboration and interpretation are reported in Chapter 2.

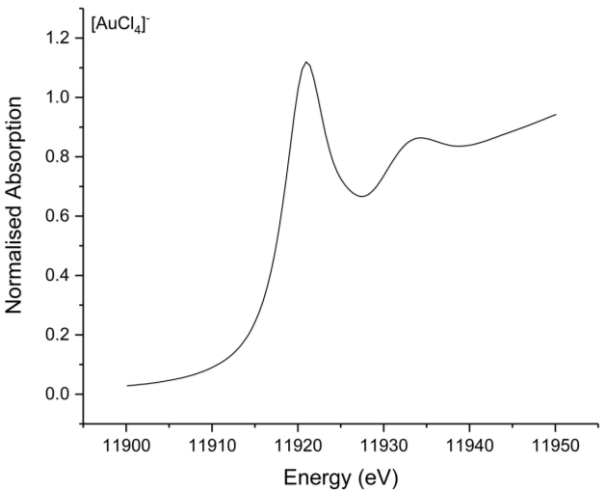

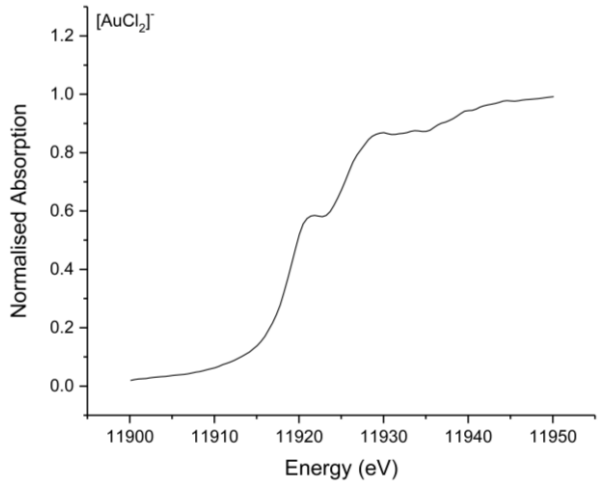

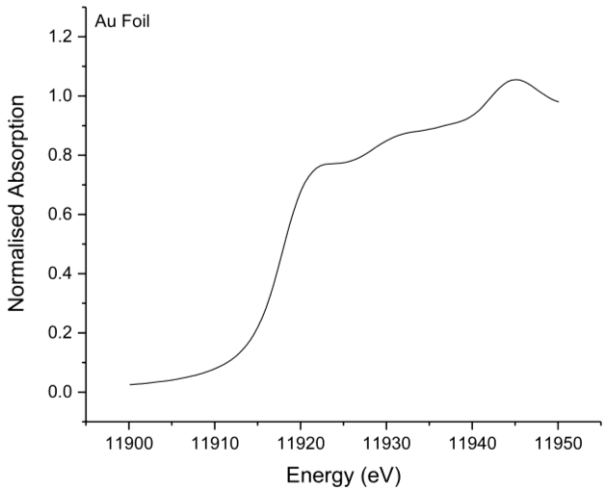

Figure 3.3 – Au L_3-edge XANES region for the Au standards used: (top) Au(III) $[AuCl_4]^-$, (centre) Au(I) $[AuCl_2]^-$ and (bottom) Au(0), gold foil. For the two cationic Au standards, the white line intensity values are 1.1 and 0.6 respectively.

Figure 3.4 shows the Au L_3-edge XANES of the fresh 1_{wt}% Au/C-AR catalyst compared with the reference material, gold foil. The white line normalised intensity of the sample was 0.78. Considering the value of the standards [(e.g., $KAuCl_4$/$[AuCl_4]^-$) and Au(I) (e.g., $[AuCl_2]^-$) are 1.1 and 0.6], a value of 0.78 indicates a noticeably oxidised Au speciation. More importantly, the direct comparison with the spectrum of the gold foil underlines the considerable difference between this reference material and the sample. Considering XAFS as a global averaging technique, we can consider the average oxidation state of the Au atoms in the freshly prepared as cationic. The Athena software package provides the capability of fitting a linear combination (LCF) of standard spectra to the sample spectra to determine the species and quantities of standards in the heterogeneous sample. In particular, the acquisition of good quality Au standards makes possible to perform a LCF-XANES to have a numerical value of the contribution by weight of the different Au speciation present in the catalytic material. Figure 3.4 show the results obtained from the LCF-XANES of the freshly prepared catalyst Specifically, no contribution from Au(0) (within fitting error) has been observed, while 56% of the sample was comprised of Au(I) and 44% of Au(III).

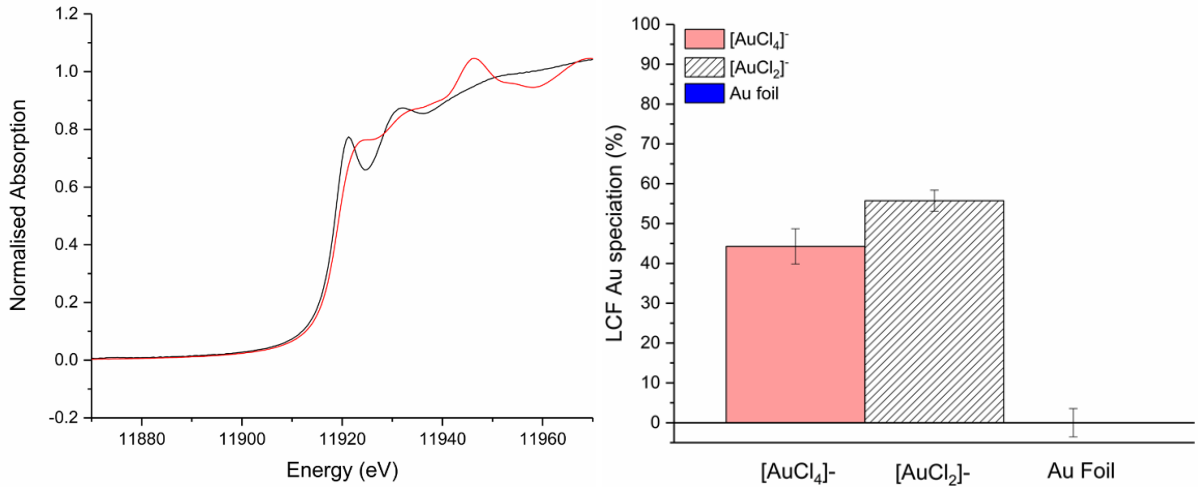

Figure 3.4 – (left) *Ex situ* Au L_3 edge–normalised XANES spectra of the 1_{wt}% Au/C-AR (black solid line) and a gold-foil reference material (red solid line) and (right) relative LCF-XANES results.

The EXAFS region of the freshly prepared sample has also been analysed. The k^3-weighted EXAFS data and corresponding Fourier transform for the sample has been compared with that of Au(III) and Au(0) standards (Figures 3.5). The k^3-weighted data of the freshly prepared material showed similar phasing and amplitude of the $[AuCl_4]^-$ standard. The data generated are in good agreement with the findings from the XANES analysis. The scattering path for EXAFS was dominated by low-Z scatterers (i.e. chlorides). In particular, the EXAFS-Fourier Transform (FT-EXAFS) of the sample, examined in comparison with the $[AuCl_4]^-$ standard and the gold foil, showed no Au-Au characteristic distances, while the only observed contribution was consistent with the presence of Au-Cl entities. This result supported also the lack of long-range order in the XRD with the major contribution at low values of R in the Fourier transform associated with a short Au-Cl distance.

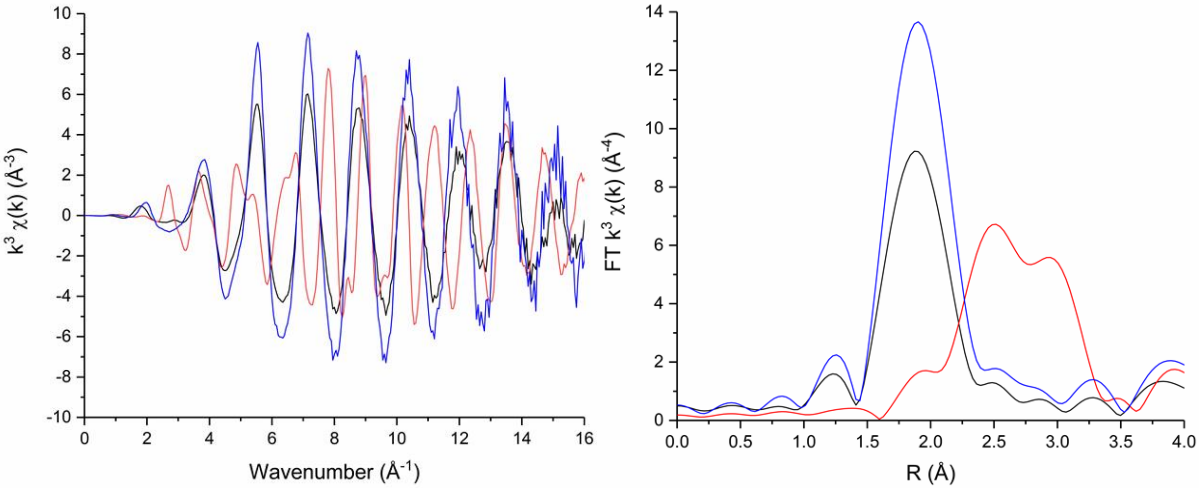

Figure 3.5 – Experimental k^3-weighted EXAFS data (left) and corresponding Fourier transform (right) for the gold foil (red solid line), Au(III) standard (blue solid line) and the 1_{wt}% Au/C-AR (black solid line).

In conclusion, it is possible to confirm that the preparation method used lead to the formation of a near atomically dispersed cationic Au on carbon material. In particular, the different intensity registered for the 1_{wt}% Au/C-AR sample, when compared with the pure Au(III) standard, reaffirm the mixed oxidation state (Au(III)/Au(I)) Au speciation of which the catalytic material was comprised.

3.2.2.2 – *In situ* Au L_3-edge XAFS study of Au/C-AR catalyst

The *in situ* experiment started by recording the Au L_3-edge XAFS of the 1_{wt}%Au/C-AR catalyst upon heating to reaction temperature (200 °C) under an inert atmosphere (Ar flow = 50 mL min^{-1}), before the addition of the reactants. As reported in Chapter 2, all reaction parameters were controlled remotely via LAB Interface software (IGI Systems Ltd). The interface works also as process parameter monitor and data logger allowing the correlation between the information obtained spectroscopically with the changes in temperature. Figure 3.6 shows that on heating, a decrease in white line intensity from 0.78 at 25 °C to 0.68 at 200 °C was observed. This behaviour suggested a change from a mixed Au(III)/Au(I) chloride speciation to predominantly Au(I) chloride-like species, which correlates well with the decomposition temperature of $AuCl_3$ to AuCl that occurs at ~160 °C.[19] Also in Figure 3.6 the corresponding LCF-XANES performed at three specific points of the heating ramp (25, 110, 200 °C) is reported. The trend observed in the changes in white line height during the heating ramp matched well with the LCF-XANES Au speciation values obtained.

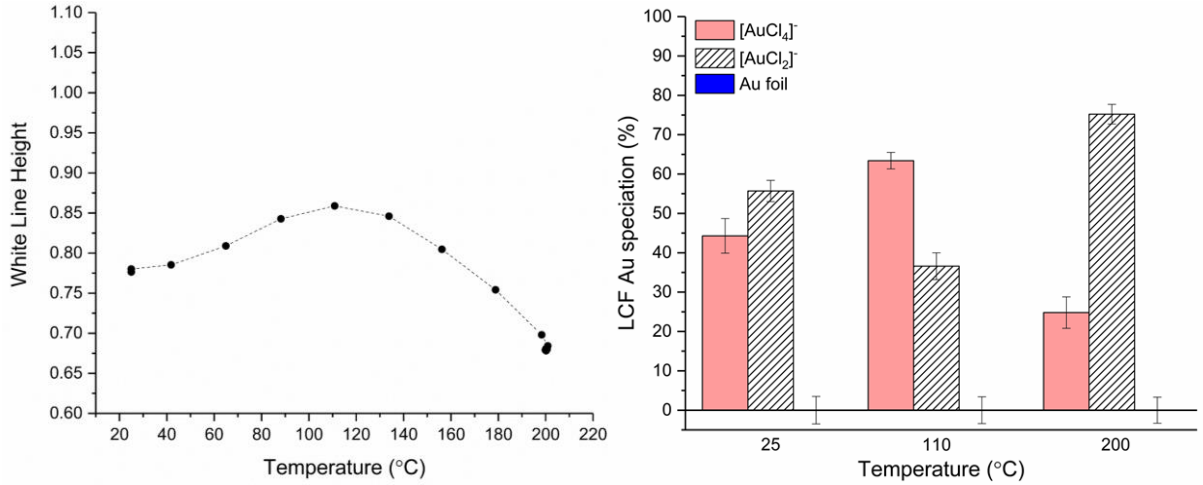

Figure 3.6 – (Left) Changes in white line height for the 1_{wt}% Au/C-AR catalyst during heating to reaction temperature under Ar at 5 °C min^{-1}. (right) relative LCF-XANES for the 1% Au/C-AR catalyst at three different temperature ((25, 110, 200 °C) while heating to reaction temperature under Ar at 5 °C min^{-1}.

Figure 3.7 shows the comparison of the XANES and EXAFS spectra recorded at room temperature and once 200 °C was reached. The continued absence of any detectable Au-Au distances in the catalyst indicates that the Au remained in a highly dispersed state, moreover the decrease in intensity observed in the EXAFS signal is another proof of the change in the oxidation state of the Au absorber that is now surrounded by less Cl atoms.

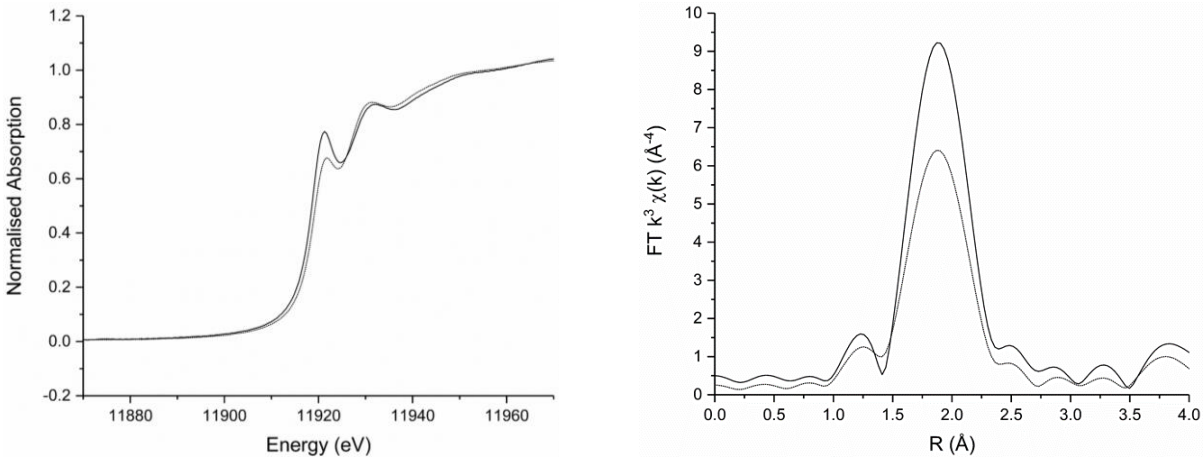

Figure 3.7 – XANES spectra (left) and FT-EXAFS (right) data recorded at room temperature (black solid line) and once reached 200 °C (black dotted line).

The white line intensity was stable at 0.68 during the 30 min isotherm at 200 °C, before the addition of reactant gases. Figure 3.8 shows the direct comparison of the white line changes and the VCM productivity recorded during the time-on-line. In particular, immediately after the introduction of the reactants the normalised white line height increased. The maximum value of white line height, 0.94, was reached after 20 min of reaction corresponding to a productivity towards VCM of *ca*. 0.5 (mol kg^{-1} h^{-1}). During the following 180 minutes of reaction, the white line intensity progressively decreased to a stable value of 0.72 corresponding to a productivity increase to *ca*. 2.75 (mol kg^{-1} h^{-1}). The most plausible interpretation of this behaviour is that Au(I)-Cl species of which the catalytic material was initially comprised, were oxidised to predominantly Au(III)-Cl species by reaction with both acetylene and hydrogen chloride during the first 20 min. After this initial perturbation of the system due to the introduction of the reactants, the average oxidation state of the gold speciation steadily recovered a similar initial value.

To have a more precise idea of the contribution of the gold species in this induction period LCF-XANES analysis have been performed. LCF-XANES spectral data with $[AuCl_4]^-$, $[AuCl_2]^-$ and Au-foil standard spectra showed a trend supporting the hypothesis proposed from the white line intensity examination (Figure 3.9). Table 3.1 shows the LCF-XANES results of the catalysts freshly prepared and at three moments of the reaction, i.e. at the beginning of the reaction (time zero), after *ca*. 25 min (maximum of white line height) and at steady state conditions.

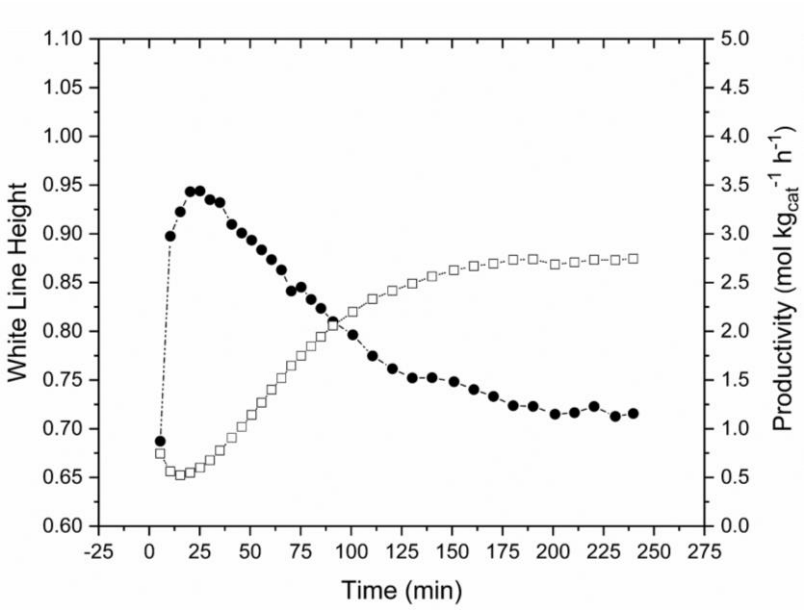

Figure 3.8 – Catalytic performance as a function of time-on-line (empty squares) and the change in normalised white-line intensity (full black circles) as a function of reaction time. Reaction conditions: 5% C_2H_2/Ar = 24 mL min^{-1}, 5% HCl/Ar = 24 mL min^{-1}, Ar = 2 mL min^{-1}, catalyst amount = 90, GHSV ~14,000 h^{-1}, temperature = 200 °C.

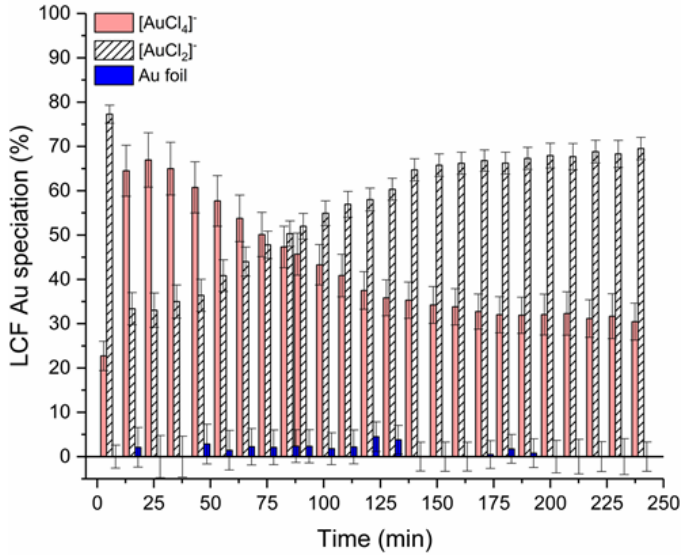

Figure 3.9 – (right) LCF- XANES for the 1$_{wt}$% Au/C-AR catalyst during reaction. Reaction conditions: 5% C_2H_2/Ar = 24 mL min^{-1}, 5% HCl/Ar = 24 mL min^{-1}, Ar = 2 mL min^{-1}, catalyst amount = 90, GHSV ~14,000 h^{-1}, temperature = 200 °C.

		Quantification (%)		
		Au(0)	Au(I)	Au(III)
1_{wt}% Au/C-AR	Freshly prepared	0 (3.5)	55.7 (2.7)	44.3 (4.4)
	Time zero	0 (3.3)	75.2 (2.5)	24.8 (4.0)
	Maximum of the white line intensity	0 (4.8)	33.1 (3.9)	66.9 (6.1)
	Steady state	0 (4.05)	68.3 (3.1)	31.7 (5.1)

Table 3.1 – LCF-XANES results of the catalyst freshly prepared and at three moments of the reaction.

Figure 3.10 shows the results of the data fitting for the spectrum acquired at the steady state (after 240 minutes of reaction). The fit does not match exactly with the XANES spectrum of the sample at the steady state, this could mean that the interpretation of the XANES spectral changes being exclusively associated with changes in the relative concentrations of $[AuCl_4]^-$ and $[AuCl_2]^-$ could be a simplification. Several factors can influence the XANES spectra of a sample, especially when recorded *in situ* under reaction conditions. For example, it must be considered the possible hybridisation of substrate/reactant molecules and metal d-band orbitals [20,21] or the changes in metal-speciation geometry through interaction with the support.[22] In this specific case, both complications are plausible.

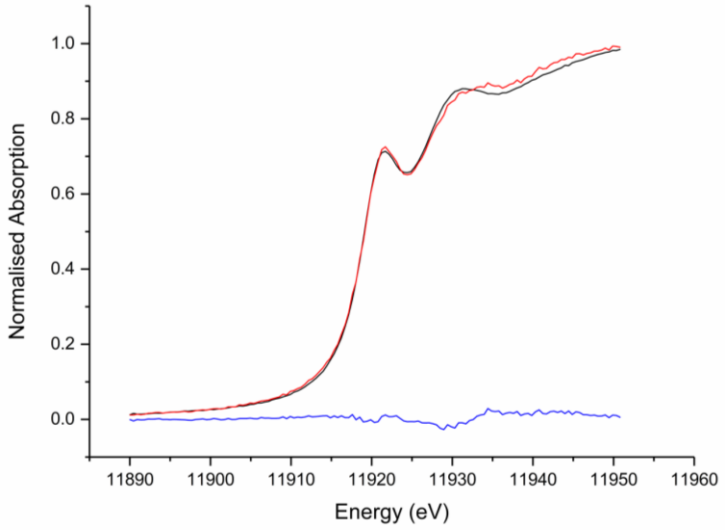

Figure 3.10 – XANES data fitting for the 1_{wt}% Au/C-AR catalyst under reaction conditions at steady state. Key: black line (experimental data); red line (fit); blue line (residual). Reaction conditions: 5% C_2H_2/Ar = 24 mL min^{-1}, 5% HCl/Ar = 24 mL min^{-1}, Ar = 2 mL min^{-1}, catalyst amount = 90, GHSV ~14,000 h^{-1}, temperature = 200 °C.

In order to clarify this point, an important tool is the calculation of the coordination number (N) associated with the photo absorber. Using Artemis, as outlined in Chapter 2, it is possible to calculate N of the 1st shell of the Au in the sample. Table 3.2 shows the EXAFS modelling for the Au L_3-edge of the $KAuCl_4$ standard and 1_{wt}% Au/C-AR sample, freshly prepared and *in situ* at different times-on-line, i.e. at the beginning of the reaction (time zero), after *ca*. 25 min (maximum of white line height) and at steady state conditions. To fit the data, the $KAuCl_4$ standard was fitted with a fixed CN of 4 and used to determine the Debye-Waller factor for samples at 25 ˚C and also the amplitude reduction factor for all other fittings (S_0^2 = 0.75(3)). Fitting a first coordination shell for Au-Cl gave, for the freshly prepared sample, an average N of 2.6. This value changed at the different stages selected during the time-on-line in good agreement with the change in contribution of the gold speciation observed in the analysis of the XANES. For example, after 20 minutes of reaction, when it was observed the maximum value of white line recorded during the *in situ* experiment, the higher value of N has been also calculated (*ca*. 3.3). Confirming that at this stage the catalyst was comprised of a high percentage of Au(III)-chloride like speciation (*ca*. 70%). The bond distance, R(Å), remained almost stable, implying the scattering path for EXAFS was dominated by low-Z scatterers at every stage of the reaction.

Sample	Scattering Path	N	R (Å)	$2\sigma^2$ (Å^2)	E_f (eV)	R_{factor}
$KAuCl_4$ (Au(III) standard)	Au-Cl 1	4*	2.284(3)	0.001	2.9(5)	0.014
1_{wt}%Au/C-AR Freshly prepared	Au-Cl 1	2.58(8)	2.273(4)		2.8(7)	0.006
1_{wt}%Au/C-AR Time zero	Au-Cl 1	2.39(9)	2.268(6)		1(1)	0.008
1_{wt}%Au/C-AR^ Maximum of the white line intensity	Au-Cl 1	2.78(46)	2.297(18)	0.0037#	1(1)	0.005
	Au-Cl 2	0.54(37)	2.171(76)			0.005
	Combined	3.32(83)	2.277(5)			-
1_{wt}%Au/C-AR Steady state	Au-Cl 1	2.46(9)	2.275(6)		1.2(9)	0.006

Table 3.2 – EXAFS fitting parameters for the Au L_3-edge of the $KAuCl_4$ standard and 1_{wt}% Au/C-AR (fresh and *in situ*). Where N= coordination number, R= Bond distance of the absorber-scatterer, $2\sigma^2$= mean squared disorder term or Debye Waller factor, E_f= E^0, R_{Factor} = statistic of the fit, which is a way of visualising how the misfit is distributed over the fitting range. A R_{factor} value below 0.05 generally means an acceptable fit.

* $KAuCl_4$ standard was fitted with a fixed CN of 4 and used to determine the Debye-Waller factor (for samples at 25 ˚C) and also the amplitude reduction factor for all other fittings.

Debye-Waller factor at 200 ˚C was calculated from literature values and the value calculated at 25 ˚C.
^ For the Au/C-AR catalyst after 20 min reaction time, two distinct Au-Cl scattering paths were observed.

Finally, it was possible to obtain a linear correlation between white line normalised intensity and the EXAFS-derived Au-Cl N at different reaction times (figure 3.11), which supports the interpretation of the white line intensity as being directly associated with changes in the Au-Cl speciation. Analysis of the used catalyst by HAADF-STEM imaging confirmed the prevalence of atomically dispersed Au species as well as some occasional sub-nanometre clusters, but there was a total absence of any metallic Au nanoparticles (figure 3.12).

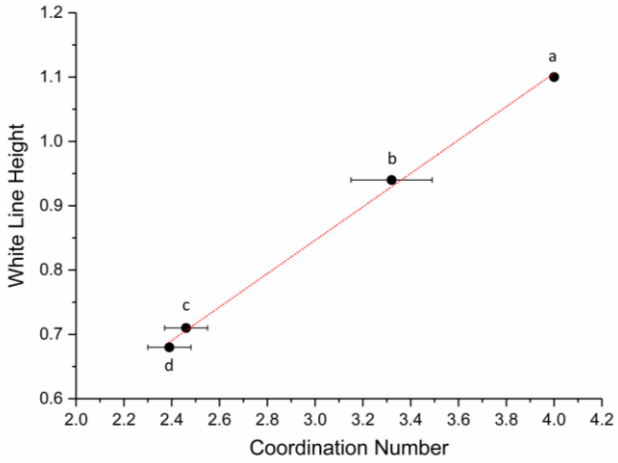

Figure 3.11 – Correlation of relative white line intensity with the EXAFS-derived coordination number for the 1_{wt}% Au/C-AR catalyst under reaction conditions: (a) the Au(III) ($KAuCl_4$) standard, (b) at the maximum of the white line intensity, after *ca*. 25 min of reaction, (c) at steady state, after 240 min of reaction and (d) at time zero (beginning of reaction).

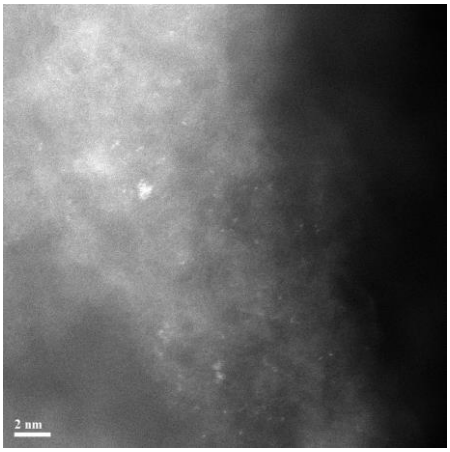

Figure 3.12 – Representative STEM-HAADF image of the 1_{wt}% Au/C-AR catalyst in the used state showing the presence of occasional Au clusters as well as atomically dispersed Au species.

Notably, no characteristic Au-Au distances were measurable by EXAFS while the catalyst was producing VCM during the entire reaction period (figure 3.13). These results underline the high stability of the cationic Au speciation on the carbon support during the reaction time-on-line.

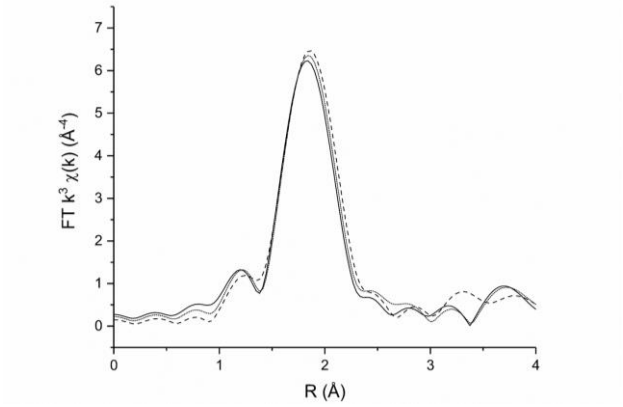

Figure 3.13 – FT-EXAFS for the 1_{wt}% Au/C-AR, at different times-on-line: time zero (black solid line) after *ca*. 25 min of reaction (black dashed line) and at the steady state (black dotted line).

3.2.3 – Investigation of the active site in Au/C-H_2O catalyst

3.2.3.1 – *Ex situ* characterisation of the freshly prepared Au/C-H_2O catalyst

In order to ascertain the role and influence of the choice of the solvent used the catalyst preparation on the catalytic activity, an Au/C catalyst was prepared according the method previously reported in the literature,[9] using activated carbon as support and water as solvent (namely 1_{wt}% Au/C-H_2O). The freshly prepared 1_{wt}% Au/C-H_2O catalyst was characterised *ex situ* after drying at 140 °C for 16 hours. Figure 3.14 shows the p-XRD of the freshly prepared material. The catalyst was composed predominantly of metallic-Au nanoparticles. Reflections due to gold are present at 38, 44, 64 and 78° 2θ. The crystallite size of the metallic gold nanoparticles was determined using the Scherrer equation, as described in Chapter 2, obtaining an estimated crystallite size of *ca*. 17 nm.

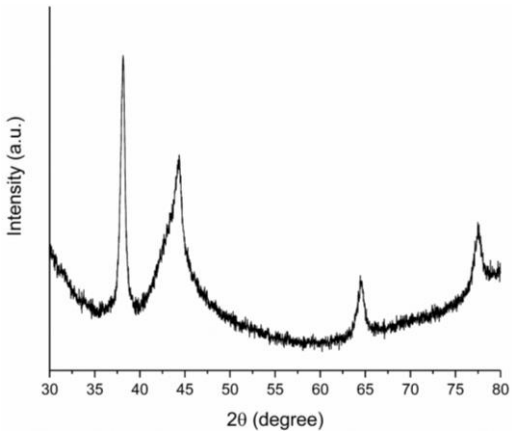

Figure 3.14 – p-XRD pattern of the freshly prepared 1_{wt}% Au/C-H_2O catalyst.

Figure 3.15 shows the STEM images of the freshly prepared material. Prior to use this catalyst consist entirely of supported gold nanoparticles in the 5-100 nm size range. In addition, it was possible to detect areas of the carbon support totally lacking any atomically dispersed Au species. It is possible to assume that the use of water as a solvent does not provide the functionalisation on the carbon material needed to immobilise or to stabilise Au speciation in a cationic form, but instead led to the aggregation of the Au atoms and formation of metallic nanoparticles.

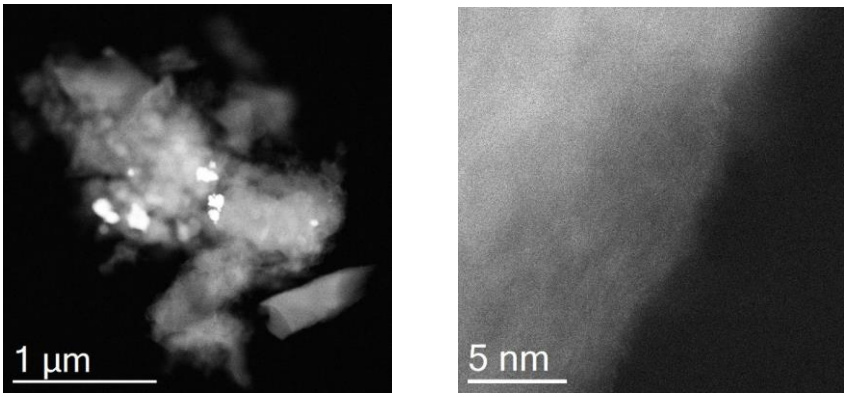

Figure 3.15 – STEM of the freshly prepared 1_{wt}% Au/C-H_2O catalyst. (left) shows the presence of gold nanoparticles (right) shows just the carbon support.

Ex situ Au L_3-edge XANES spectra and FT-EXAFS data are shown in figure 3.16. In the XANES spectrum no white line was observed, re-confirming the predominant presence of Au(0) in the sample. However, it is not possible to totally exclude a very low concentrations of dispersed Au species. Indeed, this catalyst had obvious Au-Au scattering paths in the FT-EXAFS data and showed no characteristic Au-Cl distances. The *ex situ* characterisation of this catalytic material is distinctly different to that acquired for the Au/C-AR catalyst, showing how the use of a different solvent for the dissolution of the metal precursor in the catalyst preparation lead to a completely different catalytic material.

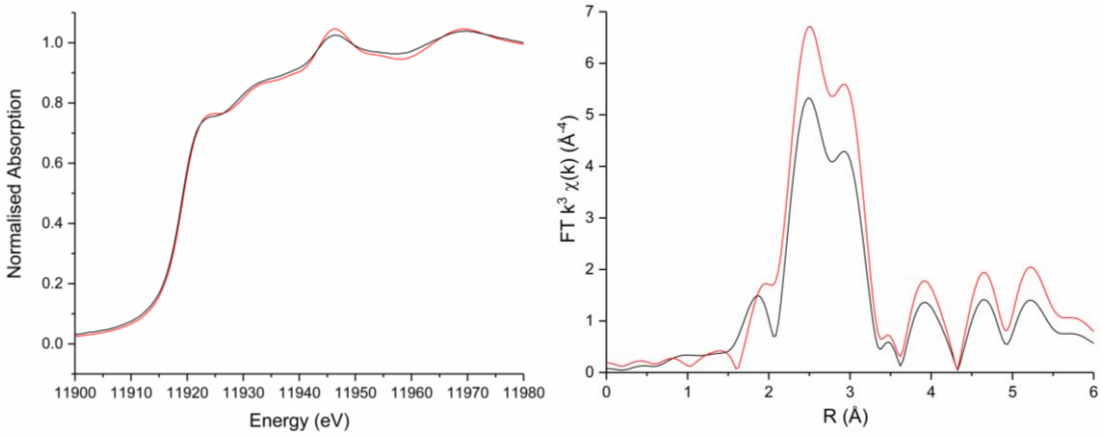

Figure 3.16 – XANES spectra (left) and FT-EXAFS (right) data of the freshly prepared 1_{wt}% Au/C-H_2O catalyst recorded at room temperature (black solid line) and the gold foil (red solid line).

3.2.3.2 – *In situ* Au L_3-edge XAFS study of Au/C-H_2O catalyst

As reported in the introduction to this chapter, previous work claimed the active site to be associated with the presence of gold nanoparticle. In particular, it was hypothesised the possible formation of Au(III)/Au(I) cationic speciation on the surface of those metallic nanoparticles were responsible for activity. To verify this assumption, an *in situ* XAFS experiment during the acetylene hydrochlorination reaction has been performed also for this catalytic material. Figure 3.17 the catalytic behaviour of the 1_{wt}%Au/C-H_2O catalyst in term of VCM productivity during the time-on-line is reported. The catalytic activity recorded was negligible, *ca*. 0.15 mol kg^{-1} h^{-1} at the steady state, an order of magnitude lower than the 1_{wt}% Au/C-AR catalyst, with no improvement observed during the time-on-line. This result definitively demonstrates that a catalytic material mainly comprised of Au(0) nanoparticles is almost inactive for the acetylene hydrochlorination reaction.

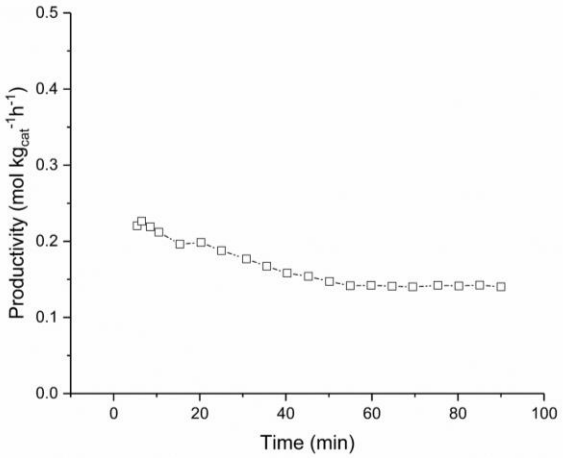

Figure 3.17 – Productivity of the 1_{wt}% Au/C-H_2O catalyst during the time-on-line. Reaction conditions: 5% C_2H_2/Ar = 24 mL min^{-1}, 5% HCl/Ar = 24 mL min^{-1}, Ar = 2 mL min^{-1}, catalyst amount = 90, GHSV ~14,000 h^{-1}, temperature = 200 °C.

Under reaction conditions, virtually no change was observed in the *in situ* XANES and EXAFS spectra, as shows in Figure 3.18. In the XANES region, apart from a slight change recorded upon introduction of the reactants, most likely because of the changes in the environment around photo absorber, no variation was observed at any stage during the time-on-line. Most importantly, it was not possible to identify a white line in this catalyst as it remained similar to bulk gold metal. The same considerations can be made while examining the FT-EXAFS data of the sample recorded during the time-on-line, in which it is possible to observe only a Au-Au contribution.

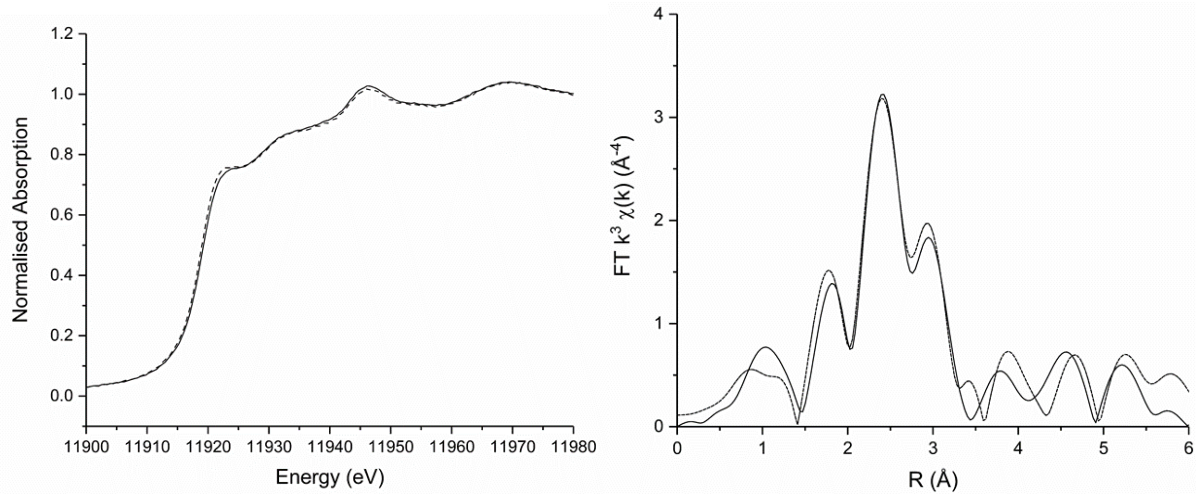

Figure 3.18 – XANES spectra (left) and FT-EXAFS (right) data of the 1_{wt}% Au/C-H_2O catalyst recorded under reaction conditions at different times-on-line. Time zero (black solid line), after *ca*. 20 min of reaction (black dashed line) and at the steady state (black dotted line).

However, the HAADF-STEM images acquired after used (figure 3.19) showed that together with 5-100 nm particles still present in the sample there was also evidence of some very occasional atomically dispersed Au entities in the carbon support. It might be possible that these species were formed, upon introduction of the reactants, but not at the surface of the metal nanoparticle. XAFS analysis did not show the formation or the presence of those entities as they are low in concentration compared to the Au(0) species. However, the HAADF-STEM evidence of the presence of cationic entities, could justify the low levels of activity in this catalytic material. These results underlined the importance of a concerted use of different characterisation techniques.

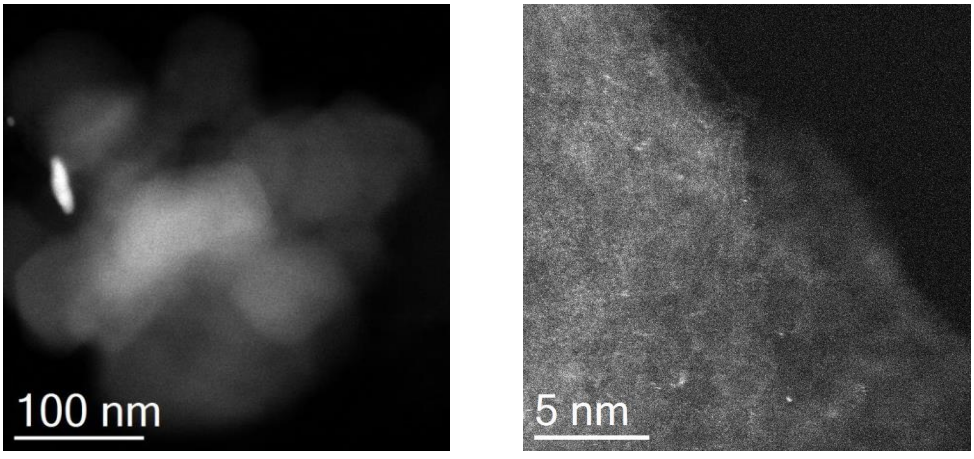

Figure 3.19 – STEM of the freshly prepared catalyst. (left) shows the presence of gold nanoparticles (right) completely bare carbon. After use the 5-100 nm particles were still evident (left), but now there was evidence of some very occasional atomically dispersed Au entities in the carbon support (right).

3.2.4 – Investigation of the active site in Au/C-S_2O_3 catalyst

3.2.4.1 – *Ex situ* characterisation of the freshly prepared Au/C-S_2O_3 catalyst

A Au/C catalyst prepared by using Au(I)-thiosulfate complex as metal precursor (designated as 1_{wt}% Au/C-S_2O_3), has been provided by Johnson Matthey in order to have a direct comparison of our best catalysts made with *aqua regia* and the recently commercially validated catalyst for the acetylene hydrochlorination reaction.[10] Figure 3.20 shows the p-XRD of the freshly prepared material. No distinct gold reflections were observed in the 1_{wt}% Au/C-S_2O_3 catalyst. Several reflections observed in the catalyst can be attributed to the presence of impurities in the carbon support used, as suggested by the industrial collaborators. However, the composition of the carbon support used for this catalyst preparation must be considered equal to the carbon material used for the preparation of the other catalysts analysed previously. The carbon used is also in this case a Norit ROX 0.8. This material was tested for the acetylene hydrochlorination reaction showing no activity. Moreover, the same material was used to prepare a 1_{wt}% Au/C-AR catalyst, following the same preparation method previously described, which was tested for the acetylene hydrochlorination reaction showing the usual catalytic performances. For these reasons, differences in these catalytic materials, 1_{wt}% Au/C-AR and 1wt% Au/C-S_2O_3, and their activity, must be attribute exclusively to the catalyst preparation itself and not to be attributed to the impurities present on the carbon support.

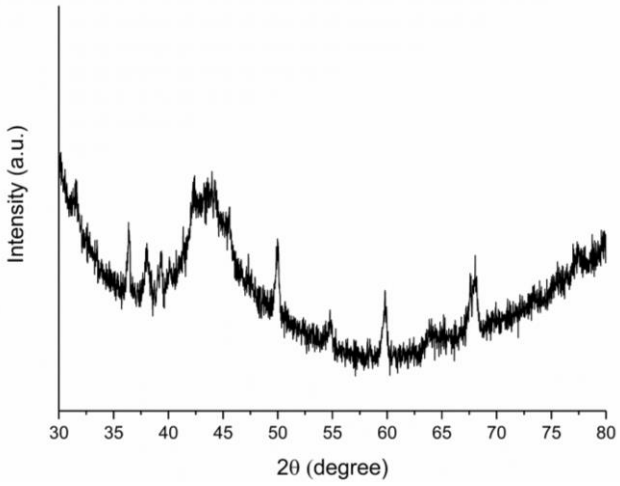

Figure 3.20 – X-ray powder diffraction patterns of the $1_{wt.}$% Au/C-S_2O_3 catalyst materials before use.

Figure 3.21 shows representative STEM- HAADF images of the freshly prepared material. In the unused material, the Au consisted primarily of atomically dispersed Au species along with some minority cluster species.

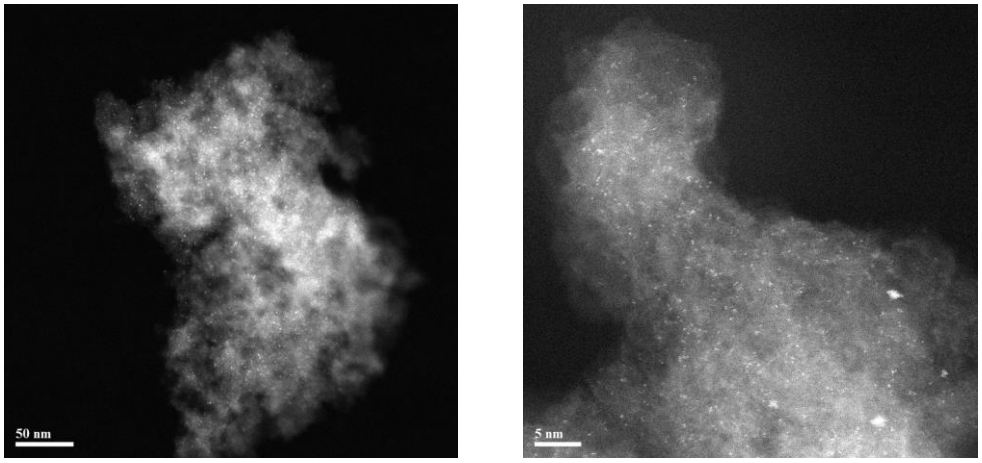

Figure 3.21 - Representative STEM-HAADF images of the freshly prepared 1_{wt}% Au/C-S_2O_3 catalyst.

As with the 1_{wt}% Au/C-AR and 1_{wt}%Au/C-H_2O materials, the unused catalyst was characterised *ex situ* by XAFS. The analysis of the XANES region (figure 3.22) showed a white line high of *ca*. 0.68, meaning that the average of the gold speciation in the unused catalyst was mostly in an Au(I) oxidation state. LCF-XANES performed on this spectrum (figure 3.22) showed the 23% of the sample was comprised of $[AuCl_4]^-$ and 72% of $[AuCl_2]^-$.

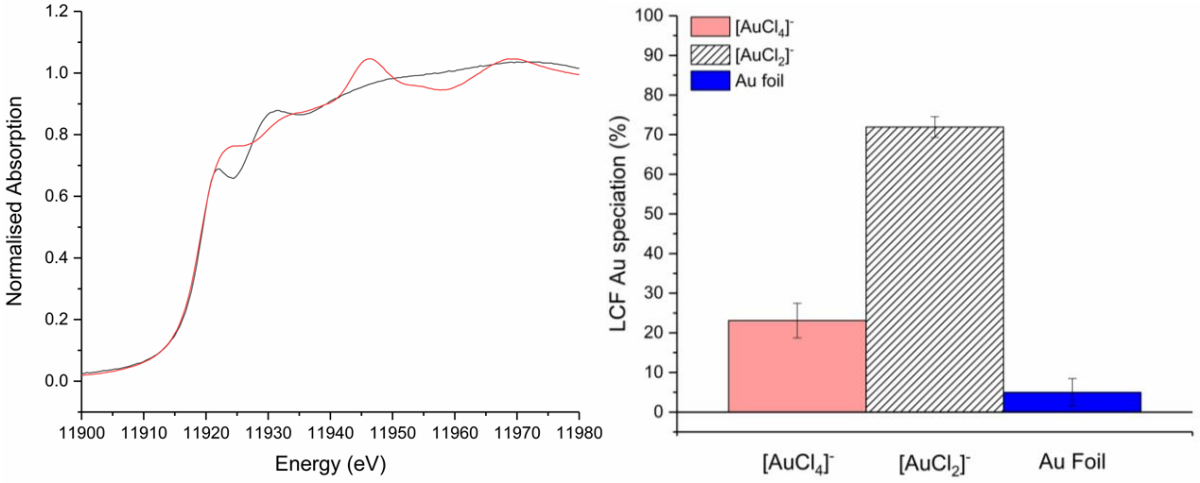

Figure 3.22 - (left) Au L_3-edge XANES spectra of the freshly prepared 1_{wt}% Au/C-S_2O_3 catalyst (black solid line) and gold foil (red solid line) and (right) relative LCF-XANES.

The FT-EXAFS analysis showed no Au-Au contribution, while the only feature observed was attributable to Au scattering path with a low–atomic number neighbour (figure 3.23). Unfortunately, Cl and S have comparable nature from an EXAFS perspective. Moreover, it is reported that Au thiosulphate complexes have almost undistinguishable molecular geometry compared to $[AuCl_2]^-$ having two Au–S bonds with an angle near 180°,[23] it was not possible to distinguish between Au-Cl

and Au-S scattering paths. However, by fitting the EXAFS data (table 3.3) gave a CN of 2.0 (±0.1), this result is consistent with a Au bisthiosulfate complex.[23]

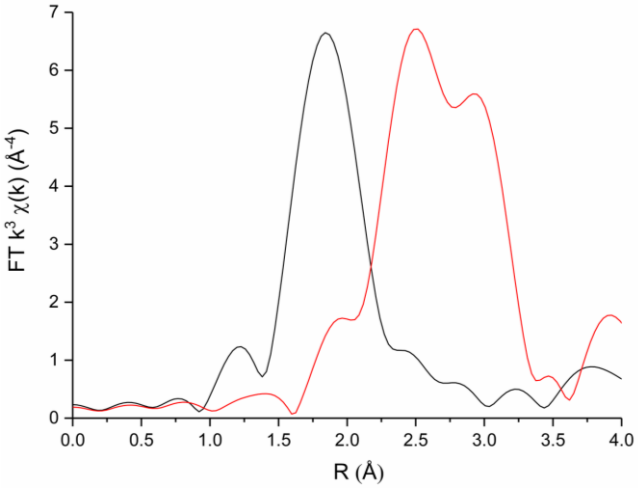

Figure 3.23 – Au L_3-edge FT-EXAFS data of the freshly prepared 1_{wt}% Au/C-S_2O_3 catalyst (black solid line) and gold foil (red solid line).

Sample	Scattering Path	N	R (Å)	$2\sigma^2$ (Å^2)	E_f (eV)	R_{factor}
1wt%Au/C-S_2O_3 Freshly prepared	Au-S(Cl)$^{\$}$	1.97(8)	2.269(5)	0.001	1.7(9)	0.010

Table 3.3 – EXAFS fitting parameters of the 1_{wt}% Au/C-S_2O_3 unused sample.
Where N= Coordination number, R= Bond distance of the absorber-scatterer, $2\sigma^2$= Mean squared disorder term or Debye Waller factor, E_f= E^0, R_{Factor}= A statistic of the fit, which is a way of visualising how the misfit is distributed over the fitting range. A R_{factor} value below 0.05 generally means an acceptable fit.
$ Due to comparable Z numbers, S and Cl are indistinguishable via EXAFS analysis.

3.2.4.2 – *In situ* Au L_3-edge XAFS study of Au/C-S_2O_3 catalyst

The 1_{wt}%Au/C-S_2O_3 catalyst has been analysed *in situ* during the acetylene hydrochlorination reaction. During the first 30 minutes of reaction, this catalyst also showed a short induction period. Through this initial phase, it was possible to observe a slight increase in white line intensity from 0.68 to 0.78, indicating the possible oxidation of some of the Au species from Au(I) to Au(III) (figure 3.24). Notably, the increase in white line intensity was far less pronounced than that with the 1_{wt}% Au/C-AR catalyst, indicating a higher stability of the Au speciation in this catalyst. In Figure 3.24 the catalytic activity of

1_{wt}% Au/C-S_2O_3 is compared with the change in white line height recorded. Interestingly, after the initial modification observed, the relative white-line intensity at steady state was the same as for the 1_{wt}% Au/C-AR catalyst at similar activity. As expected, this Au/C-S_2O_3 catalyst was more stable and active under reaction conditions than those made with the $HAuCl_4$ precursor.[10,24] LCF-XANES performed on three selected moment during the time-on-line, confirmed the stability of the Au speciation in during the time-on-line, in which the main contribution was predominantly from Au(I) species (Figure 3.24).

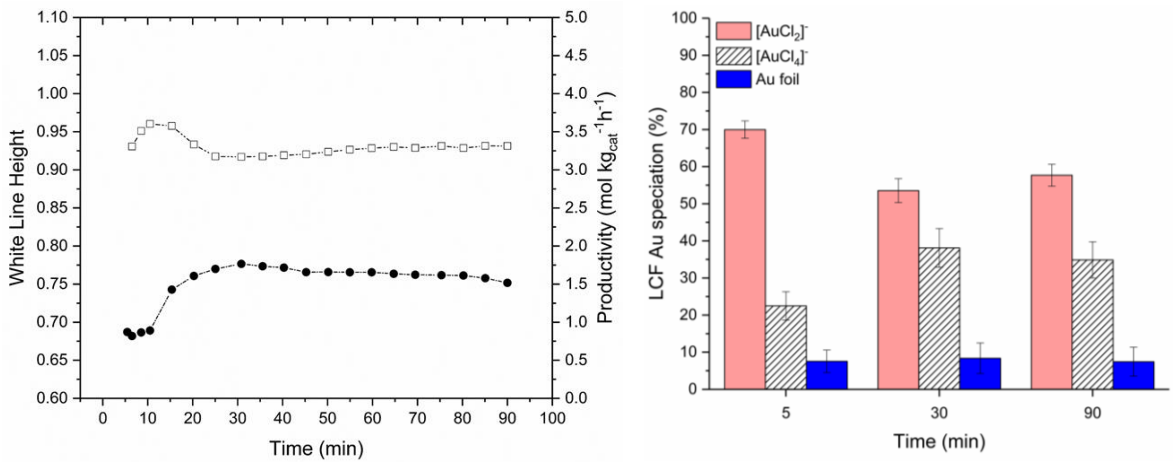

Figure 3.24 – (left) Catalytic performance of the 1_{wt}% Au/C-S_2O_3 catalyst (empty squares) and the change in normalised white line intensity (black circles) as a function of reaction time. (right) LCF-XANES for the 1_{wt}% Au/C-S_2O_3 catalyst at three moments during the time-on-line.

As showed in table 3.4, the system was actually perturbed during the catalysis. The EXAFS fitting of the first coordination shell showed that upon the addition of the reactant gases, together with the slight increase in white line intensity to 0.78 recorded in the XANES region, a concomitant change in N from 2.0 to 2.6 was observed. This indicated also from the EXAFS perspective the oxidation of some of the Au(I) species. In particular, this increase in N could be attributed to the possible coordination of Cl to the Au-thiosulphate complex.

A representative STEM-HAADF image of the 1_{wt}%Au/C-S_2O_3 catalyst showed in figure 3.25, reports that the Au was almost entirely in an atomically dispersed form (with only a few dimeric species) on the C support after the *in situ* experiments.

Sample	Scattering Path	N	R (Å)	$2\sigma^2$ (Å^2)	E_f (eV)	R_{factor}
1wt%Au/C- S_2O_3 Freshly prepared	Au-S(Cl)$^{\$}$	1.97(8)	2.269(5)	0.001	1.7(9)	0.010
1wt%Au/C- S_2O_3 Time zero	Au-S(Cl)$^{\$}$	2.23(6)	2.264(7)	0.0037$^{\#}$	1.3(6)	0.005
1wt%Au/C-AR^ After 30 min of reaction	Au-S(Cl)$^{\$}$	2.61(9)	2.277(5)		2.0(8)	0.007

Table 3.4 – EXAFS fitting parameters of the 1_{wt}% Au/C-S_2O_3 unused sample, at the beginning of the reaction (time zero) and after 30 minutes of reaction. Where N= Coordination number, R= Bond distance of the absorber-scatterer, $2\sigma^2$= Mean squared disorder term or Debye Waller factor, Ef= E^0, R_{Factor}= A statistic of the fit, which is a way of visualising how the misfit is distributed over the fitting range. $ Due to comparable Z numbers, S and Cl are indistinguishable via EXAFS analysis.

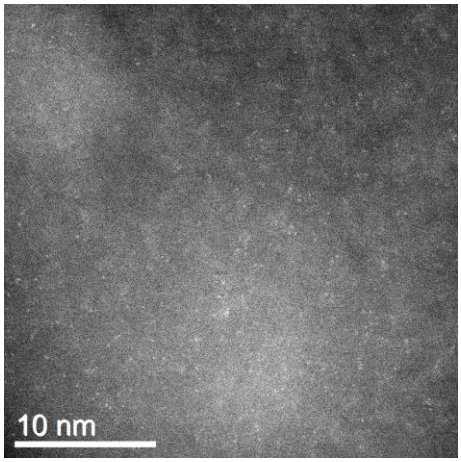

Figure 3.25 – Representative HAADF-STEM images of the 1_{wt}% Au/C-S_2O_3 catalyst in used states showing the Au was almost entirely atomically dispersed.

3.2.5 – Evidence of the active site and proposed reaction mechanism

The structure-activity correlation showed previously in this chapter for the two active catalysts tested (1_{wt}% Au/C-AR and 1_{wt}%Au/C-S_2O_3) and the similar white line height value recorded at the steady state suggested that a correlation could be made between the Au L_3-edge white line intensity and VCM production of those two catalysts during the time-on-line. Figure 3.26 shows that a linear correlation could be obtained, reaffirming the original consideration that the high activity of this class of catalysts could be attributed to the presence of oxidised gold species in the final material. Specifically, the contemporary presence of a population of highly dispersed Au(I) and Au(III) entities is demonstrated

to be crucial in order to observe high activity. In particular, high productivity values can be correlated with white line normalised intensity of *ca*. 0.75 corresponding to a Au(I)/Au(III) ratio of *ca*. 1.5.

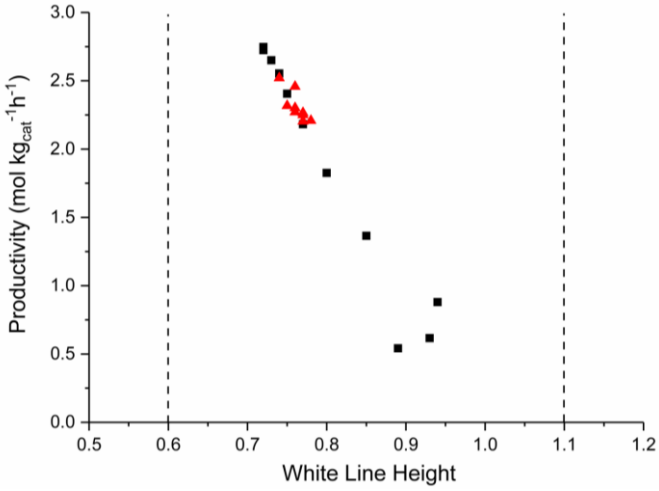

Figure 3.26 – Linear correlation between VCM productivity and white line height for the 1_{wt}% Au/C-AR catalyst (black full squares) and the 1_{wt}%Au/C-S_2O_3 catalyst (red full triangles). Dashed lines represent the white-line intensities of the Au(I) $[AuCl_2]^-$ standard (value of 0.6) and the Au(III) $[AuCl_4]^-$ standard (value of 1.1).

The results obtained experimentally could suggest a possible reaction mechanism in which the Au(I)/Au(III) redox couple is involved. Until now the role of Au(I) was not considered because of lack of experimental evidence. On the other hand, it was not possible yet to obtain a catalytic material containing only Au(I) or Au(III) species. In order to clarify the character of the Au speciation in the reaction mechanism a density functional theory (DFT) study has been undertaken by our collaborator Adam Thetford, within the group of Prof C.R.A. Catlow. Figure 3.27 shows the proposed reaction mechanism, that generally consists in the transformation of Au(I)Cl to $AuCl_2H$ and formation of VCM regenerating Au(I)Cl. The likelihood of each step is showed in term binding energies for each energy minima and the Hirshfeld charge on each Au atom. In particular, the energies are given with reference to the geometry-optimised configuration of AuCl on the carbon support and gas phase acetylene and HCl. In particular, the HCl is added across the AuCl forming $AuCl_2H$. This species shows a Hirshfeld charge of 0.37e corresponding to a pronounced Au(III) character. This first step demonstrates the possible oxidative addiction of the HCl to the Au(I)Cl speciation present on the carbon support as first step of the reaction mechanism. At this stage, the dissociation of the HCl is inhibited by hydrogen-bonding interactions. Once this species is formed, the following step consist in the addiction of an acetylene molecule, leading to the generation of VCM via $AuCl_2(C_2H_3)$, with a binding energy of –224 kJ mol^{-1}. VCM then is further stabilised with a binding energy of –269 kJ mol^{-1}, but this can be displaced by the introduction of a second HCl. In conclusion, the reaction could be hypothesised to

proceed through the oxidative addition of HCl to Au chloride, followed by the insertion of acetylene and reductive elimination of VCM through an Au(I)-Au(III) redox couple.

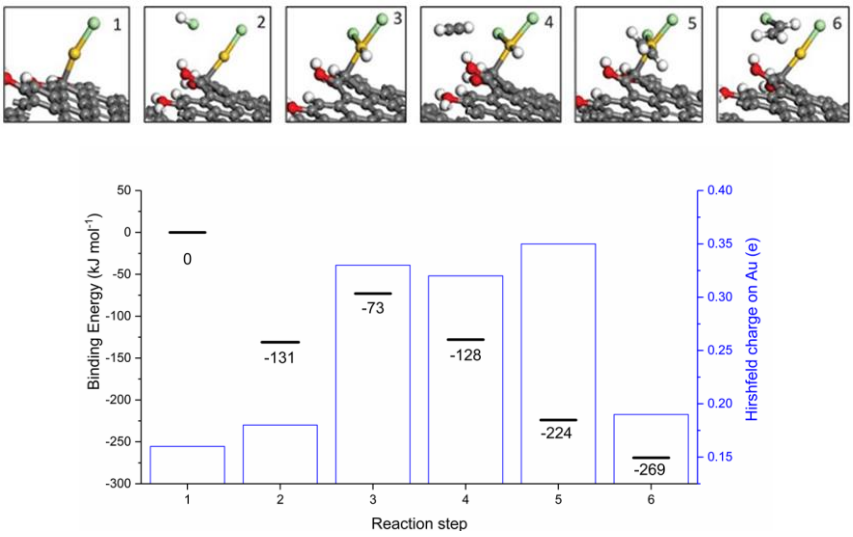

Figure 3.27 – Proposed mechanism for the transformation of AuCl to $AuCl_2H$ and formation of VCM reproducing AuCl. Au atoms (gold), Cl atoms (green), H atoms (white), C atoms (gray), and O atoms (red). The bar chart shows binding energies for each energy minima and the Hirshfeld charge on each Au atom. Energies are given with reference to the geometry-optimised configuration of AuCl on the carbon support and gas phase acetylene and HCl.

3.3 – Conclusions

The acetylene hydrochlorination reaction represent one of the first heterogeneous gold-catalysed reactions that after more than 30 years is now moving towards industrial application. The work utilised the combination of common characterisation techniques together with more challenging *in situ* XAFS experiments under acetylene hydrochlorination reaction conditions to gain information about the catalytically active site for Au/C catalysts and to propose a reaction mechanism supported by computational modelling. This study led to the conclusion that highly active catalysts comprise of single-site cationic Au entities whose activity correlates with the ratio of Au(I):Au(III) present. In this perspective, given also the proposed mechanism based on a redox couple of Au(I)/Au(III) species, the active form of these catalysts can be thought of as analogous to the homogenous single site Au cations.

Single gold cations have been previously employed in heterogeneous catalysts,[25,26,27,28] but, contrary to what has been reported previously in this chapter, these materials either deactivate rapidly or undergoes drastic nuclearity modification during the reaction. Further insight into the possible deactivation mechanism and the role of the ligand in the high stability of those catalytic material will be further analysed in Chapter 4 and Chapter 5.

3.4 – References

1. G. J. Hutchings, *J. Catal.*, **1985**, *96*, 292–295.

2. B. Nkosi, N. J. Coville and G. J. Hutchings, *Appl. Catal.*, **1988**, *43*, 33–39.

3. B. Nkosi, M. D. Adams, N. J. Coville and G. J. Hutchings, J. Catal., **1991**, *128*, 378–386.

4. B. Nkosi, N. J. Coville, G. J. Hutchings, M. D. Adams, J. Friedl and F. E. Wagner, J. Catal., **1991**, *128*, 366–377.

5. M. Conte, A. F. Carley, C. Heirene, D. J. Willock, P. Johnston, A. A. Herzing, C. J. Kiely and G. J. Hutchings, *J. Catal.*, **2007**, *250*, 231–239.

6. G. Hong, X. Tian, B. Jiang, Z. Liao, J. Wang, Y. Yang and J. Zheng, *RSC Adv.*, **2016**, *6*, 3806–3814.

7. M. Zhu, Q. Wang, K. Chen, Y. Wang, C. Huang, H. Dai, F. Yu, L. Kang and B. Dai, *ACS Catal*., **2015**, *5*, 5306–5316

8. X. Tian, G. Hong, B. Jiang, F. Lu, Z. Liao, J. Wang and Y. Yang, *RSC Adv.*, **2015**, *5*, 46366-46371.

9. X. Liu, M. Conte, D. Elias, L. Lu, D. J. Morgan, S. J. Freakley, P. Johnston, C. J. Kiely and G. J. Hutchings, *Catal. Sci. Technol.*, **2016**, *6*, 5144–5153.

10. P. Johnston, N. Carthey and G. J. Hutchings, J. Am. Chem. Soc., **2015**, *137*, 14548–14557.

11. R. Ciriminna, E. Falletta, C. Della Pina, J. H. Teles and M. Pagliaro, *Angew. Chem., Int. Ed.*, **2016**, *55*, 14210–14217.

12. S. Bordiga, E. Groppo, G. Agostini, J. A. Van Bokhoven and C. Lamberti, *Chem. Rev.*, **2013**, *113*, 1736–1850.

13. G.J. Sherborne and B. N. Nguyen, *Chem. Cent. J.*, **2015**, *9*, 37

14. C. Garino, E. Borfecchia, R. Gobetto, J. A. van Bokhoven and C. Lamberti, *Coord. Chem. Rev.*, **2014**, 277–278, 130–186.

15. A. S. K. Hashmi, C. Lothschütz, M. Ackermann, R. Doepp, S. Anantharaman, B. Marchetti, H. Bertagnolli and F. Rominger, *Chem. – Eur. J.*, **2010**, *16*, 8012–8019.

16. Johnson Matthey PRICAT catalysts, total and selective hydrogenation duties, http://www.jmprotech.com/pricat-johnson-matthey

17. S.-Y. Chang, A. Uehara, S. G. Booth, K. Ignatyev, J. F. W. Mosselmans, R. A. W. Dryfe and S.L. M. Schroeder, *RSC Advances* **2015**, *5*, 6912–6918.

18. A. Pantelouris, G. Kueper, J. Hormes, C. Feldmann, M. Jansen, *J. Am. Chem. Soc.*, **1995**, *117*, 11749–11753.

19. O. Glemser and H. Sauer, *Handbook of Preparative Inorganic Chemistry*, Ed.: G. Brauer, Academic Press, *2*, 1056.

20. P. Hu, P. N. Duchesne, Y. Song, P. Zhang andS. Chen, *Langmuir*, **2015**, *31*, 522–528.

21. N. Weiher, A. M. Beesley, N. Tsapatsaris, L. Delannoy, C. Louis, J. A. van Bokhoven and S. L. M. Schroeder, *J. Am. Chem. Soc*., **2007**, *129*, 2240–2241.

22. M. Fernández-García, *Catal. Rev., Sci. Eng.*, **2002**, *44*, 59–12.

23. R. A. Bryce, J. M. Charnock, R. A. D. Pattrick and A. R. Lennie, *J. Phys. Chem. A*, **2003**, *107*, 2516–2523.

24. P. T. Bishop, N. A. Carthey, P. Johnston, **2013**, U.S. Patent, WO 2013008004 A3.

25. M. Flytzani-Stephanopoulos, *Acc. Chem. Res.*, **2014**, *47*, 783–792.

26. W. Deng, A. I. Frenkel, R. Si and M. Flytzani-Stephanopoulos, *J. Phys. Chem. C*, **2008**, *112*, 12834–12840.

27. J. C. Fierro-Gonzalez and B. C. Gates, *J. Phys. Chem. B*, **2004**, *108*, 16999–17002.

28. J. Lu, C. Aydin, N. D. Browning, B. C. Gates, *Angew. Chem. Int. Ed. Engl.*, **2012**, *51*, 5842–5846.

Chapter 4

In situ study of the deactivation of Au/C-Aqua Regia catalysts for the acetylene hydrochlorination reaction

4.1 – Introduction

In Chapter 3 a detailed *in situ* X-ray absorption fine structure (XAFS) spectroscopy study describing the behaviour of Au/C catalysts during acetylene hydrochlorination reaction has been reported. XAFS analysis showed that, under operating conditions, the most active catalysts comprise atomically dispersed cationic species, in both Au(III) and Au(I) oxidation states. Although these results give details of the nature of the active catalyst, a study of the deactivation of the catalyst will provide a deeper understanding of the catalytic behaviour and the reaction mechanism. Preliminary studies on the deactivation of gold on carbon catalysts during acetylene hydrochlorination were based on the investigation of the effect of the reaction temperature on the deactivation rate.[1] In this study two deactivation mechanisms have been identified:

1) The formation of oligomers on the catalyst surface (with consequent site blocking);
2) The reduction of active cationic gold to inactive metallic Au.

At temperatures between 100–120 °C the catalyst deactivation could be attributed to build-up of carbonaceous residues on the catalyst surface. Recently, P. Johnston *et al*. reported TEM images of a

gold on carbon catalyst that had been operated in industrial conditions for several months.[2] This TEM analysis showed the formation of nanotubes, arising from the acetylene polymerisation, on the catalyst surface most likely generated from gold nanoparticles, found at the tip of those carbon nanotubes. Moreover, the formation of those polymeric compounds is believed to occur *via* an acid catalysed polymerisation reaction at the strong acid sites introduced on the catalysts surface from the preparation using *aqua regia*.[2,3] At a temperature range between 120–180 °C, the loss in activity observed was attributed to the reduction of cationic gold to metallic Au. Post reaction Mössbauer spectroscopy, *ex situ* XRD and XPS studies all shown the deactivated catalysts to be mostly comprise of Au(0) nanoparticles.[1,4,5,6]

In Chapter 3 it was also postulated, based on the combination of *in situ* XAFS and DFT studies, that the reaction mechanism for Au catalysed acetylene hydrochlorination might proceeds *via* an oxidative addition-reductive elimination process to generate VCM. Given the postulated reaction and deactivation mechanisms previously described, it can be expected that exposure to the full reaction mixture or each individual reactant gas would affect the Au speciation.[7,8] A detailed investigation into the mechanism of the reaction, including the study of the effects of the individual reactants on the catalyst has been performed previously. In this study by Conte *et al.*,[8] Au/C catalysts collected after exposure to different combinations of reactants were analysed by *ex situ* XPS showing that: exposure to HCl lead to an increase of Au(III) and Au(I) concentration at the expense of Au(0), whilst the treatment with C_2H_2 resulted in a reduction of Au(III) causing the deactivation of the catalyst.

Despite the importance of this XPS study, this did not yet provide details of the reaction mechanism. Furthermore, carrying out these experiments *ex situ* might have caused changes in the Au speciation due to the exposure to air and moisture once the catalyst was removed from the reactor to perform the analysis. Finally, as already mentioned in Chapter 1, the over representation of Au(0), that appears as the dominant signal in XPS analysis, possibly due to the to the significant photo-reduction of gold chlorides during the characterisation, might have led to misinterpretation of the changes in Au(III) and Au(I) species, which signals appear minor in comparison the Au(0).

In this chapter, the role of the individual reactants is correlated with the observed changes in Au speciation during an *in situ* gas switching experiment performed while recording the Au L_3-edge XAFS. These results have been used to further elucidate the reaction mechanism. The formation of polymeric organic species on the catalyst surface is investigated via an inelastic neutron scattering (INS) study. Finally, the formation of Au(0) is directly correlated with a decrease in VCM productivity when under reaction conditions.

4.2 – Results and discussion

4.2.1 – Experimental

In this chapter, a 1_{wt}% Au/C-AR was prepared by the impregnation methods described in Chapter 2 using tetrachloroauric acid as metal precursor. *Ex situ* characterisations of the freshly prepared 1_{wt}% Au/C-AR catalyst performed via XRD, STEM and XAFS are reported in Chapter 3. A 2_{wt}% gold supported on activated carbon catalysts was prepared using the same impregnation method but on a larger scale (~10g batch). The metal loading was increased by keeping the support/solvent ratio constant and increasing the amount of metal precursor for the desired loading. The catalytic tests were carried out according to the testing procedures described in Chapter 2. A summary of the testing conditions is given below.

4.2.1.1 – Reaction conditions for the catalytic test of Au/C-AR

The reaction gas mixture of 5% C_2H_2/Ar (24 mL/min), 5% HCl/Ar (24 mL/min) and additional Ar (2 mL/min) was introduced into the heated reactor chamber containing the catalyst (90 mg) to give a total flow of 50 mL/min at a total gas hourly space velocity (GHSV) of ~14,000 h^{-1}, keeping the C_2H_2 : HCl ratio at a constant value of 1 : 1.02. The sequential flow experiment (reaction sequence) was performed using the 1_{wt}% Au/C-AR catalyst while recording simultaneously the Au L_3-edge XAFS and catalytic activity.

Reaction sequence:
step (1) = HCl+C_2H_2/Ar, step (2) = HCl/Ar, step (3) = HCl+C_2H_2/Ar, step (4) = C_2H_2/Ar and step (5) = HCl+C_2H_2/Ar.

The duration of each step was not the same; the gas composition during the experiment was changed only when no variation in the XAFS spectra recorded online was observed. For this reason, the duration of each step is different, step (1) = 240 min, step (2) = 75 min, step (3) = 120 min, step (4)= 70 min and step (5) = 90 min

4.2.1.2 – Determination of orders of reaction with respect to the reactant gases

The reactions were performed using the same reactor setup described in Chapter 2. The reaction mixture, before and after reaction were analysed by gas chromatography, the results are shown in terms of acetylene conversion (%).

Reaction conditions: Mass of catalyst: 45 mg; Temperature: 200 °C; Total flow of gases: 50 mL/min; Gas make-up: 5% C_2H_2/Ar, 5% HCl/Ar, Ar; Initial gas concentrations: 2.4% C_2H_2/Ar, 2.5% HCl/Ar.

The concentration of C_2H_2/Ar was then altered (% C_2H_2/Ar = 2.5 – 2 – 1.5) maintaining constant the concentration of HCl/Ar (2.5%) or the concentration of HCl/Ar was changed (% HCl/Ar = 2 – 2.5 – 3) maintaining constant the concentration of C_2H_2/Ar (2.0%). In all cases, values were not obtained in sequence.

4.2.1.3 – *In situ* X-ray Absorption Fine Structure (XAFS) experiment

X-ray absorption fine structure (XAFS) spectra were recorded in transmission mode at the Au L_3 absorption edge, at the B18 beamline of Diamond Light Source, Harwell, UK. The measurements were performed using a QEXAFS setup with a fast-scanning Si (111) double crystal monochromator. For the in-situ measurements, the time resolution of the data acquisition was 20 s/spectrum. X-ray absorption near-edge structure (XANES) analysis was mainly focused on the understanding of the white line detectable at an absorption energy of ~11920 eV and corresponding to the Au $2p_{3/2} \rightarrow 5d$ primary transition. Three different Au standards were used to perform the linear combination fitting (LCF) analysis of the Au L_3-edge XANES: Au(III) (e.g., $KAuCl_4$/$[AuCl_4]^-$), Au(I) (e.g., $[AuCl_2]^-$), and Au-foil standard spectra. The normalised white line intensity values observed the $[AuCl_4]^-$ and $[AuCl_2]^-$ are 1.1 and 0.6, respectively, details of this are reported in Chapter 3.

The extended X-ray absorption fine structure (EXAFS) data analysis was performed by using IFEFFIT with the Demeter software package (Athena and Artemis). 1st Shell Au paths were fitted at all k weighted χ data, using a k space window of 3-11 and an R window of 1.25-2.6. Debye-Waller ($2\sigma^2$) and the amplitude reduction factor (S_o^2) were fixed during fitting of data at 0.0037 Å and 0.75 respectively. These values were determined from fitting of $KAuCl_4$ at a known temperature and with a fixed coordination number (N) of 4, as reported in Chapter 3.

4.2.2 – Thermal stability: *in situ* p-XRD

In Chapter 3 it was demonstrated that highly active catalysts for the acetylene hydrochlorination reaction, prepared by the impregnation of the Au precursor from a solution of *aqua regia*, consist of atomically dispersed cationic Au. To test the thermal stability of these highly dispersed Au species, an *in situ* p-XRD experiment was carried out. The catalyst was heated to 350 °C (5 °C min^{-1}) under an inert atmosphere of nitrogen, in order to avoid the combustion of the carbon support while being characterised *in situ* (Figure 4.1). The atomically dispersed Au(III)/Au(I) species in 1_{wt}% Au/C-AR showed high thermal stability from ambient temperature up to 250 ºC, with no distinct face centred cubic (FCC) metallic Au reflections being observed over this temperature range. On reaching 300 °C, reflections corresponding to the {111}, {200}, {220} and {310} Au lattice planes were clearly visible demonstrating the presence of metallic Au crystallites. The crystallite size of the metallic gold

nanoparticles was determined using the Scherrer equation, as described in Chapter 2, giving an average crystallite size of *ca*. 29 nm. Increasing the temperature up to 350 °C the nanoparticles size increases accordingly, giving a calculated crystallite size of *ca*. 31 nm. Moreover, given the increased magnitude of the Au metal diffraction at 350 °C it is possible to affirm that a greater amount of Au in the sample is in a crystalline state.

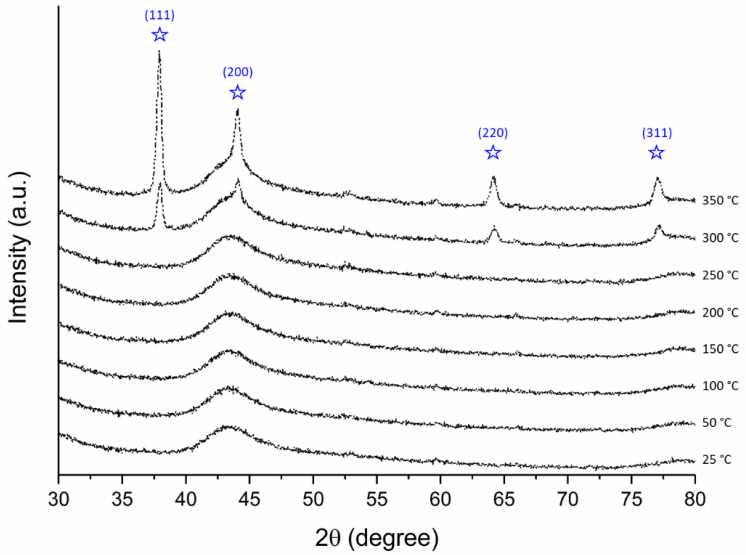

Figure 4.1 – *In situ* p-XRD characterisation of 1_{wt}% Au/C-AR recorded increasing temperature up to 350 °C (5 °C min^{-1}) under an inert atmosphere of nitrogen.

This analysis demonstrates that the 1_{wt}% Au/C-AR is thermally stable up to 300 °C under an inert atmosphere; however, the Au oxidation state is affected by the increase of the temperature. In particular, while heating the catalyst to reaction temperature (200 °C) under Ar, the XAFS analysis showed in Chapter 3, showed that the Au(III)/Au(I) ratio significantly changed due to the decomposition of Au(III) chloride to Au(I) chloride. In particular from LCF-XANES analysis already performed in Chapter 3, once reached the reaction temperature, the catalyst was comprised for the 28% of Au(III) and 76% by Au(I) (Figure 3.7, Chapter 3).

4.2.3 – Sequential flow experiment and investigation of the reaction mechanism

To elucidate the influence of each single reactant on the gold speciation in a 1_{wt}% Au/C-AR catalyst under reaction condition, a sequential flow experiment was performed *in situ* while recording the Au L_3-edge XAFS. Figure 4.2 shows a plot of the VCM productivity with respect to the reaction time and the relative changes in the normalised white line intensity during the whole sequential experiment. The

catalytic behaviour of the 1_{wt}% Au/C-AR catalyst for the first 240 min of reaction (step (1), Figure 4.3) shows the same trend already described in Chapter 3. In particular, during the induction period (*ca*. 180 min) the normalised Au L_3-edge white line increased to *ca*. 0.94 and after reaching this maximum slowly decrease to a value of *ca*. 0.70 reaching the steady state conditions (Figure 4.3). This change in white line is associated with the rapid formation of Au(III) chloride like species followed by its gradual reduction to one mainly containing Au(I) chloride, LCF-XANES values at the steady state are *ca.* 30% Au(III) and *ca.* 70% Au(I).

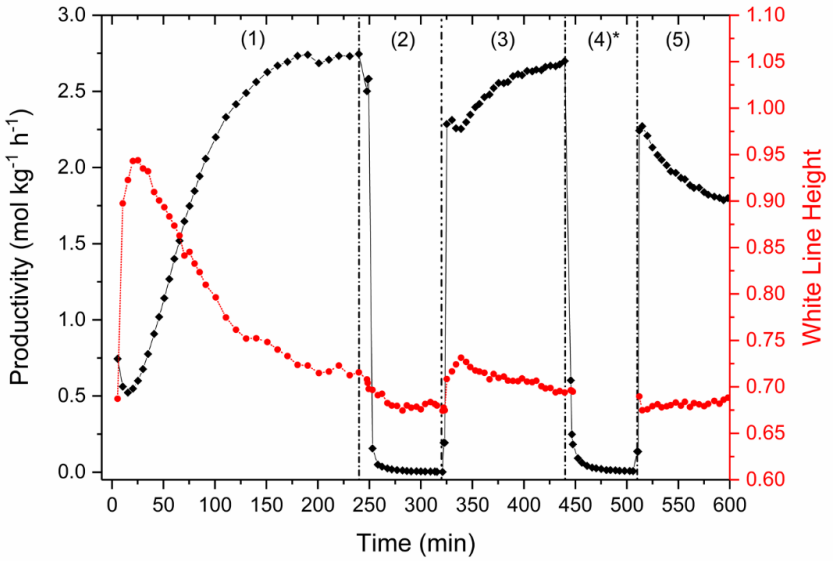

Figure 4.2 – VCM production (black diamonds) as a function of time-on-line during sequential gas experiment with simultaneously recorded XANES data showed in term of normalised white line (red circles); where (1) HCl+C_2H_2/Ar, (2) HCl/Ar, (3) 2nd HCl+C_2H_2/Ar, (4)* C_2H_2/Ar and (5) 3rd HCl+C_2H_2/Ar.

* During step 4 no white line was detected.

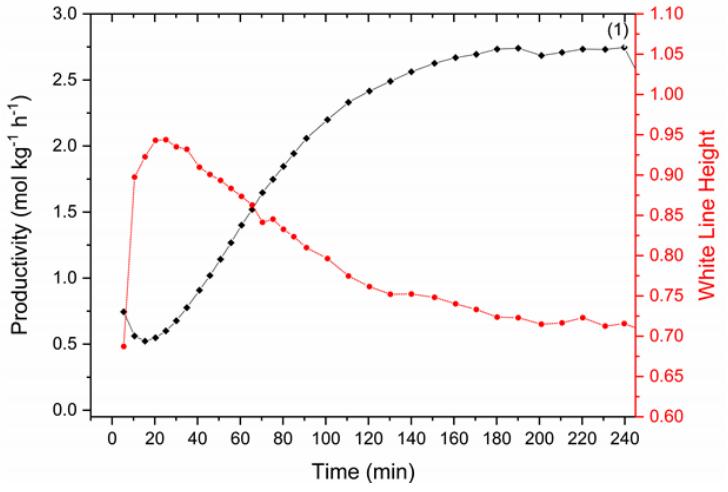

Figure 4.3 – VCM production (black diamonds) and simultaneously recorded XANES data showed in term of normalised white line (red circles); as a function of time-on-line during step(1) = HCl+C_2H_2/Ar.

Once at steady state conditions, after 240 min of reaction, the catalyst was exposed to only HCl diluted in argon for *ca.* 70 min (step (2), Figure 4.4), at a flow corresponding to the total flow of the reaction mixture (50 ml min^{-1}).

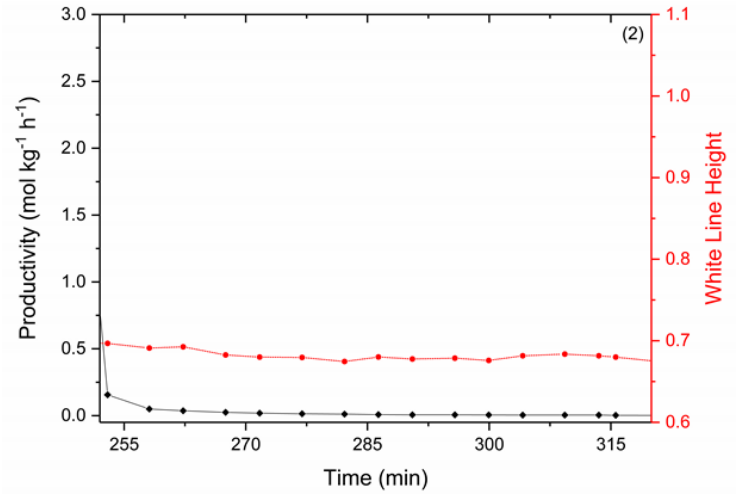

Figure 4.4 – VCM production (black diamonds) and simultaneously recorded XANES data showed in term of normalised white line (red circles); as a function of time-on-line during step(2) = HCl /Ar.

Figure 4.5 shows the changes in the XANES region during step 2, in which is possible to observe a decrease in the normalised white line height from 0.70 to 0.68. This slight change in the XANES spectra is not enough to be attributed to a potential Au reduction, is it then possible to affirm that almost no change in the Au oxidation state was observed at this stage. However, this result seems to be in contradiction with the previous postulation reported in Chapter 3, in which during the first step of the reaction mechanism proposed, HCl was considered as an oxidant within the reaction.

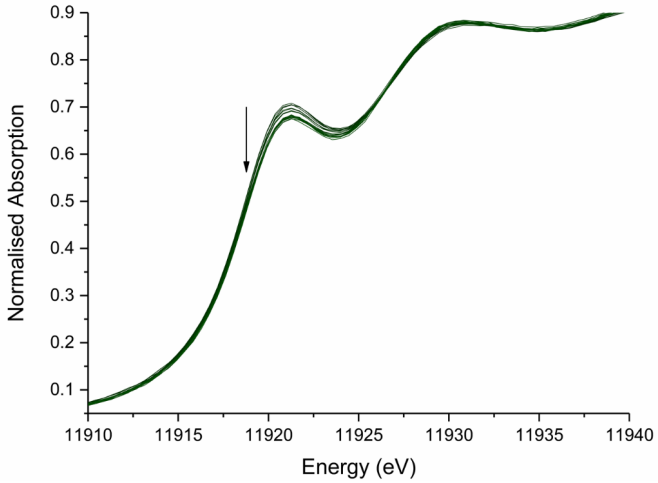

Figure 4.5 – Evolution of XANES spectra recorded during step (2) of the sequential flow experiment.

The slight reduction observed could be attributed to the thermal decomposition of Au(III)Cl species at reaction temperature to Au(I) chloride species, in the same way as was shown during the heating ramp in Chapter 3. Another possible explanation could be ascribed to the significant low concentration of HCl, i.e. 2.5% of the total gas composition, that could limit the oxidation potential of the reaction environment, differently from previously reported results in which a higher HCl concentration was used.[4,6] While flowing HCl/Ar only, no vinyl chloride monomer (VCM) formation was observed.

After 70 min of HCl/Ar treatment, when no variation in the intensity of the white line was observed, the reaction mixture was reintroduced (step (3), figure 4.6). In this step, an almost immediate return of VCM production was observed together with a short induction period. The initial productivity of 2.28 mol $kg^{-1}h^{-1}$ gradually increased until reaching a steady state productivity value of 2.70 mol $kg^{-1}h^{-1}$ after *ca.* 115 min. During this step, in the same fashion reported in step (1), the normalised white line decreased while the activity increase. This result can lead to the conclusion that C_2H_2 must assist in the oxidative addition of HCl in the first step of the reaction mechanism. Thus, it is possible to speculate a concerted HCl and C_2H_2 addition to the Au(I)Cl species. This assumption changes the proposed mechanism in Chapter 3, in which the oxidative addition of HCl was then followed by C_2H_2 addition and the reductive elimination of VCM.

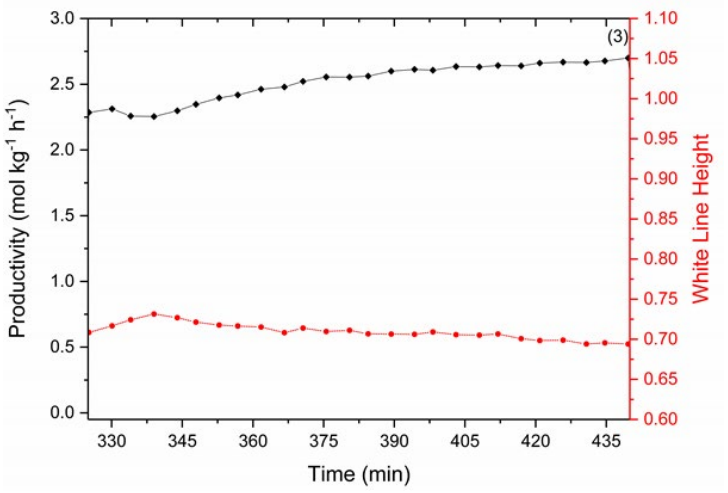

Figure 4.6 – VCM production (black diamonds) and simultaneously recorded XANES data showed in term of normalised white line (red circles); as a function of time-on-line during step(3) = HCl+C_2H_2/Ar.

Further evidence to support this theory could be obtained by studying the order of reaction with respect to HCl and C_2H_2. If Au(I)Cl oxidation results from a concerted addition of HCl and C_2H_2, as suggested from XANES data, and this step is rate limiting, the reaction rate should be first order with respect to each reactant. Figure 4.7 shown the linear dependence of both HCl and C_2H_2 reaction rate and demonstrates 1st order dependence for each reactant, i.e. 2nd order overall. The combined evidence from the *in situ* XANES and the 1st order dependence for each reactant provides evidence for a concerted

HCl and C_2H_2 addition to the Au(I)Cl active site. The results shown in figure 4.7 were not obtained during *in situ* measurements and the tests were performed as described in Chapter 2.

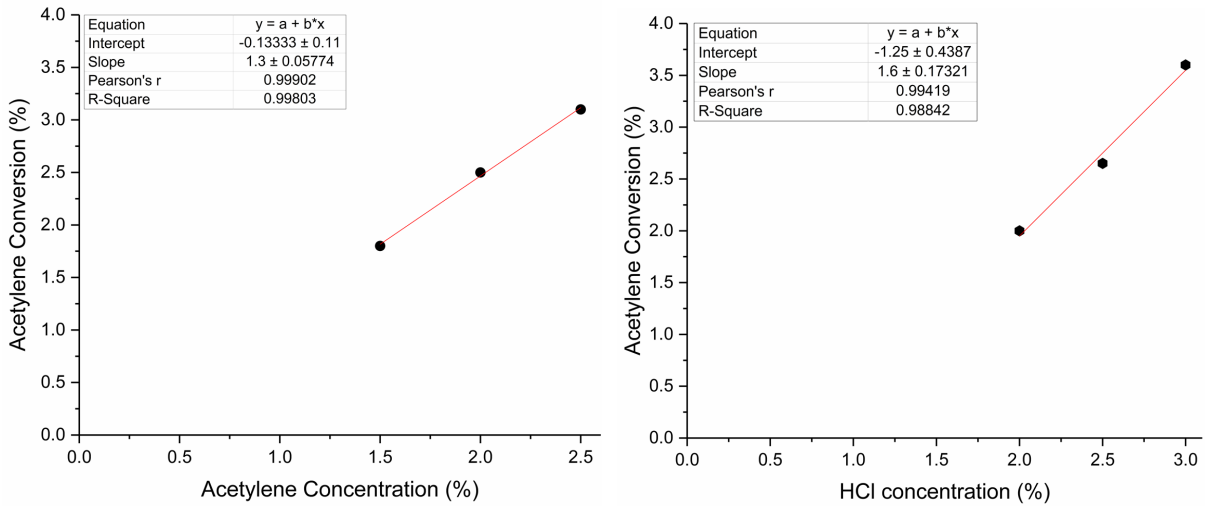

Figure 4.7 – Determination of orders of reaction with respect to the reactant gases. Reaction conditions: Mass of catalyst: 90 mg; Temperature: 200 °C; Total flow of gases: 50 mL min^{-1}. In all cases, values were not obtained in sequence. (top) Order of reaction; Reaction conditions: 1_{wt}% Au/C-AR (45 mg), 200 °C, [C_2H_2] = 2,5 – 2.0 – 1.5%, [HCl] = 2.5%). (bottom) Reaction conditions: 1_{wt}% Au/C-AR (45 mg), 200 °C, [C_2H_2] = 2.0 %, [HCl] = 2.0 - 2.5 – 3.0%).

After step 3, once the steady state activity was regained, the catalyst was exposed to dilute acetylene [C_2H_2/Ar] only (step (4), figure 4.8). As shown in figure 4.9, during this step, the XANES spectra recorded look significantly different from anything previously observed. In particular, a gradual loss of the white line feature at 11921 eV and a post edge feature at 11931 eV, and the simultaneous appearance of a new feature at 11923 eV with an absorption edge shift to higher energy.

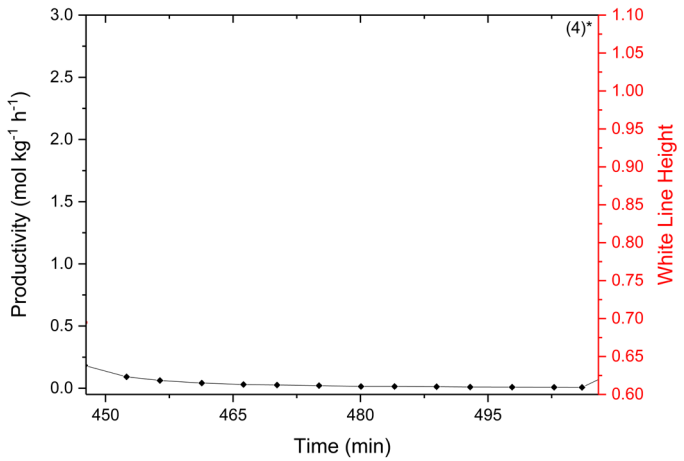

Figure 4.8 – VCM production (black diamonds) and simultaneously recorded XANES data showed in term of normalised white line (red circles); as a function of time-on-line during step(4) = C_2H_2/Ar.
* During step 4 no white line was detected.

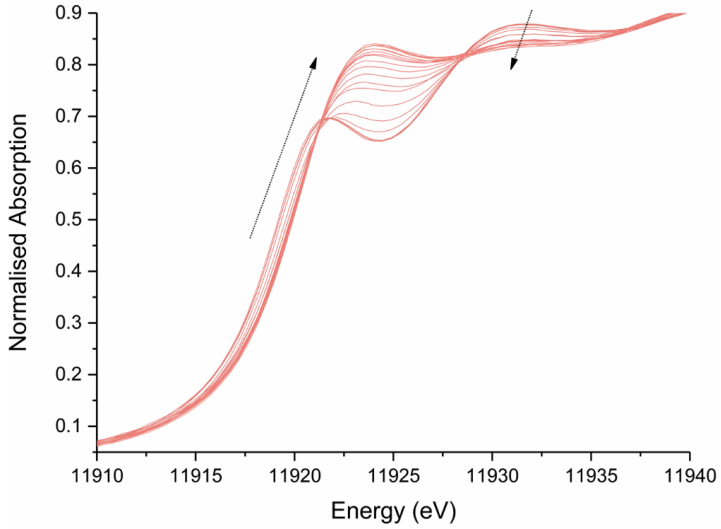

Figure 4.9 – Evolution of XANES spectra during step (4)**.**

Unfortunately, as shown in figure 4.10, in which a C_2H_2/Ar XANES spectrum is compared with the Au(III), Au(I) and Au(0) standards, this new feature was not clearly attributable to either Au(III) or Au(I) like chloride like speciation. A slight similarity to Au (0) can be observed, although the absorption edge positions are notably different. Given that exposure of Au catalysts to acetylene without an excess of HCl is known to result in catalyst deactivation,[2] the observed changes in XANES spectra is evidence of a strong Au-C_2H_2 interaction that is potentially detrimental to the catalytic performance. As in step 2, also in this case no VCM was produced while flowing C_2H_2/Ar only.

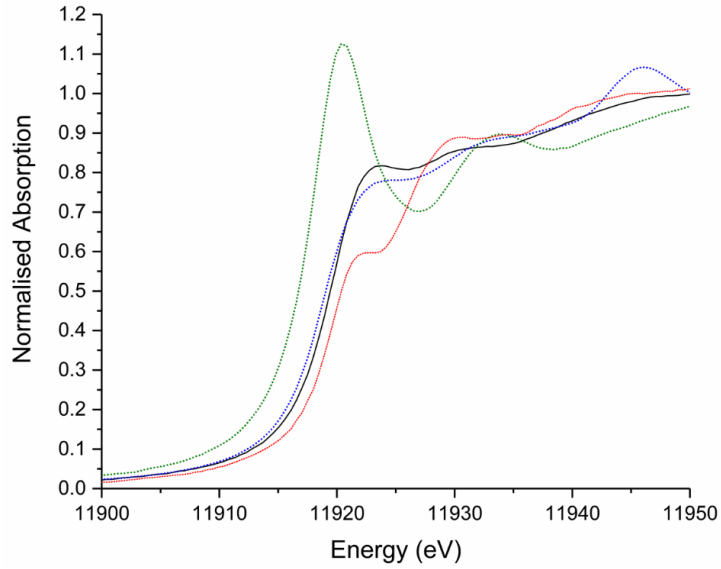

Figure 4.10 – Comparison of Au L_3-edge XANES of 1_{wt}% Au/C-AR catalyst under C_2H_2/AR atmosphere (Black solid line) and Au (III) standard $[AuCl_4]^{-1}$(green short-dotted line), Au(I) standard $[AuCl_2]^-$ (red short-dashed line) and Au(0) foil (blue short-dashed line).

Re-introduction of reactant gases to the 1_{wt}%Au/C-AR catalyst after C_2H_2/Ar treatment resulted in VCM productivity returning (step (5), figure 4.11). However, unlike the original induction period or after HCl/Ar treatment, over 90 minutes of reaction a decrease in VCM productivity from 2.24 mol kg^{-1} h^{-1} to 1.79 mol kg^{-1} h^{-1} was observed, providing evidence that the Au acetylene interaction observed under C_2H_2/Ar deactivated the catalyst. On reintroduction of the reaction mixture (HCl+C_2H_2/Ar) the XANES of the catalyst returned to the more recognisable spectra of an Au(I)/Au(III) spectrum seen in previous reaction steps.

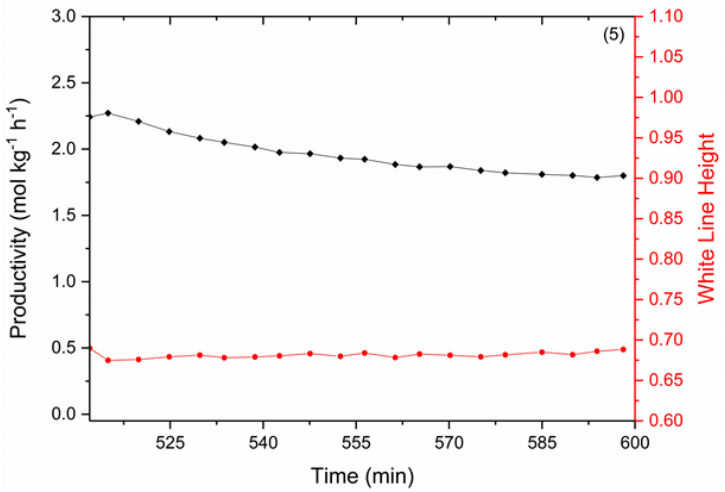

Figure 4.11 – VCM production (black diamonds) and simultaneously recorded XANES data showed in term of normalised white line (red circles); as a function of time-on-line during step(5) = HCl +C_2H_2/Ar.

Figure 4.12 shown the correlations between the normalised white line height and the VCM productivity during step (1), (3) and (5) respectively. The strongest linear correlation, with a Pearson's correlation coefficient (r) value of -0.9994, can be observed for the step (1), with an observed gradient of 0.104 (±0.002). A good correlation could be also obtained for step (3), although, plotting the normalised white line height versus VCM productivity it is possible to observe a shift in the trend towards lower normalised white line values. Moreover, the gradient of the trend line in this case has changed to lower values: 0.057 (±0.007). When performing the same correlation for step (5 the gradient decreases considerably to a value of only 0.009 (±0.005), indicating that trend between productivity and normalised white height is now almost invariant.

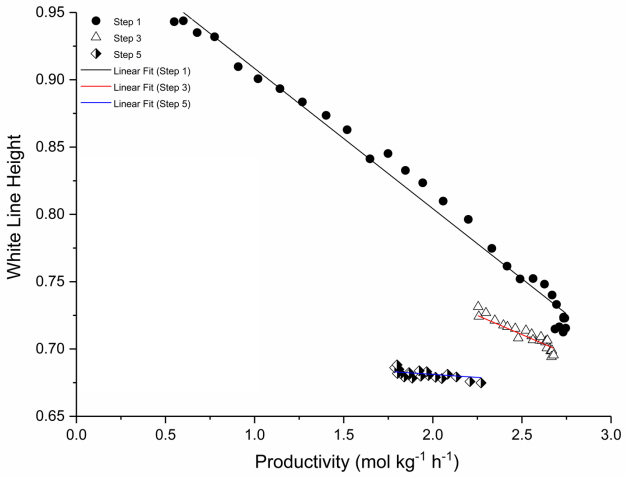

Figure 4.12 – Comparison of white line height and VCM productivity of 1_{wt}% Au/C-AR catalyst under HCl/C_2H_2 reaction gas after different single reactant gas treatments. Solid black circles; catalyst during first induction period (productivity and white line data from step 1, Figure 4.3), open triangles; catalyst after HCl/Ar treatment (productivity and white line data from step 3, Figure 4.6) and half-filled diamonds; catalyst after C_2H_2/Ar treatment (productivity and white line data from step 5, Figure 4.11).

A possible reason for the loss of correlation is that one or more additional spectator species, which contribute to the XANES spectra in the region of the Au(I)/Au(III) white line, might be present after treatment with HCl/Ar and in a larger extent after C_2H_2/Ar. In fact, figure 4.13 shows the comparison of the XANES spectra of the catalyst at steady state for each reaction period (step (1), (3) and (5)), in which it is possible to observe a shift in the position of the white line of ~1eV between the initial and finial steady state spectra (end of step (1) and end of step (5)), demonstrating a notable change in Au species.

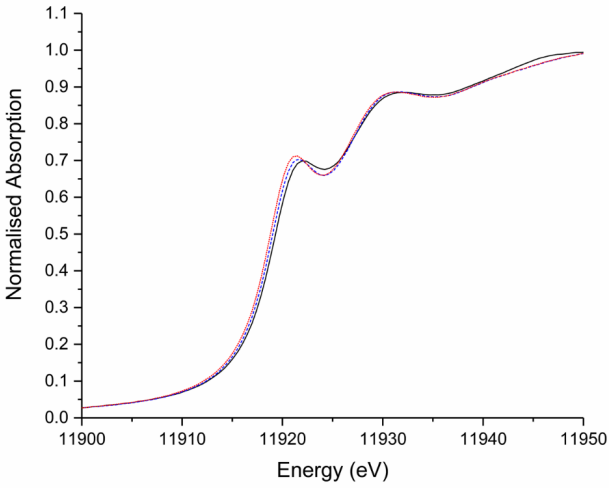

Figure 4.13 – XANES spectra of 1_{wt}% Au/C-AR catalyst at steady acetylene hydrochlorination after different sequential gas treatments. Red dotted; 1st reaction (step (1)), blue dotted line; 2nd reaction (step (3)- after HCl/Ar treatment) and black solid 3rd (step (5)- after C_2H_2 /Ar treatment).

A LCF-XANES analysis (Figure 4.14) has been performed to obtain the Au contribution values at the end of each step, to try to understand if the changes observed in the XANES spectra could be attributed to the presence of metallic gold that could explain the loss in correlation between white line and VCM productivity. The catalyst during the first reaction period (step (1)), under HCl/Ar (step (2)) and during the second reaction period (step (3)) were comparable with similar ratios of Au(III) and Au(I), although a small amount of metallic Au was calculated to be present in catalyst at the end of the step 3, *ca.* 4%; concentration comparable with the estimated error. Unfortunately, the LCF-XANES of the catalyst during step (4), under C_2H_2/Ar was not successful, meaning that no acceptable fit was found with the three standards chosen, highlighting a strong interaction between C_2H_2 and the gold species present on the catalyst. The results obtained after step (5), in which a clear evidence of metallic Au (*ca.* 21%) was found are significantly different to the other spectra. Metallic Au is catalytically inactive for acetylene hydrochlorination and this high concentration calculated in the used catalyst can be correlated with the loss in activity seen after C_2H_2/Ar treatment. Such a high amount of metallic Au can justify the observed reduction in white line previously observed, given that Au(0) has a normalised absorption value of *ca.* 0.6 at the energy of the Au(III) white line (11920 eV). This influence in the normalised absorption intensity together with the possible residual amounts of the unknown species generated under the C_2H_2/Ar treatment, can also explain the loss in correlation between normalised white line height and VCM productivity shown in figure 4.12.

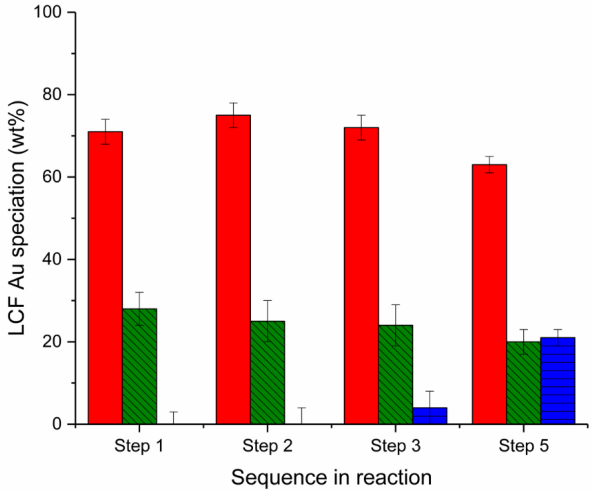

Figure 4.14 – LCF-XANES of 1_{wt}% Au/C-AR catalyst at the end of each sequence of gas switching (excluding step 4- C_2H_2/Ar). Percentage Au associated with; Au(I) chloride (standard $[AuCl_2]^-$) in red, Au(III) chloride (standard $[AuCl_4]^-$) in green, and Au(0) (standard Au foil) in blue. Reaction sequence; step (1) = HCl+C_2H_2/Ar, step (2) = HCl/Ar, step (3) = HCl+C_2H_2/Ar, step (4) = C_2H_2/Ar and step (5) = HCl+C_2H_2/Ar.

Additional information to clarify this interpretation could be obtained by analysing the EXAFS region of the XAFS spectrum. Figure 4.15 shows FT-EXAFS data of the catalyst at three points in the reaction

profile (step (1), (3) and (5)). In all three samples is possible to observe a predominant feature that can be attributed to the 1st shell Au-Cl interactions with multiple Au-Cl scattering events beyond 3 Å. But in step (5) a feature associated with Au-Au interactions between 2.5 and 3 Å become notable (although the FT magnitude is small) confirming the observation from the LCF-XANES that metallic Au nanoparticles are present at this point during the reaction profile.

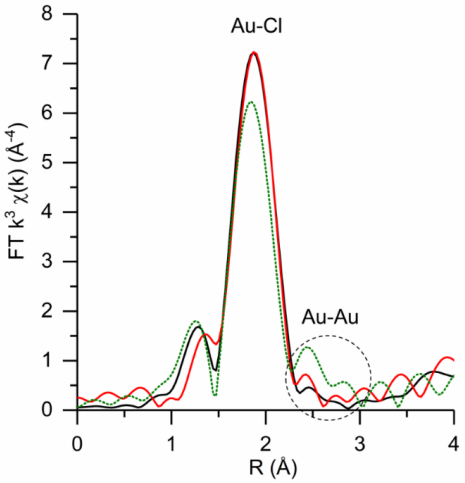

Figure 4.15 – FT-EXAFS of 1_{wt}% Au/C-AR catalyst under steady state reaction conditions. Black solid line; in step 1, red line; in step 3, green short dotted line; in step 5.

EXAFS analysis can also provide further information on the nature of the Au speciation, especially while the catalyst was under C_2H_2/Ar only. Even if the Au L_3-edge XANES of this species was clearly different to Au chloride (figure 4.9), the FT-EXAFS shows that Au-Cl interactions are still present in the C_2H_2 treated sample. Figure 4.16 shows that the magnitude of this scattering in the FT-EXAFS analysis was significantly lower than the catalyst in the presence of both reactants (figure 4.15). Moreover, no additional interactions associated with Au-C or Au-Au were observed in the C_2H_2 treated sample, showing no clear evidence of either Au-C_2H_2 complex or Au(0) nanoparticle formation.

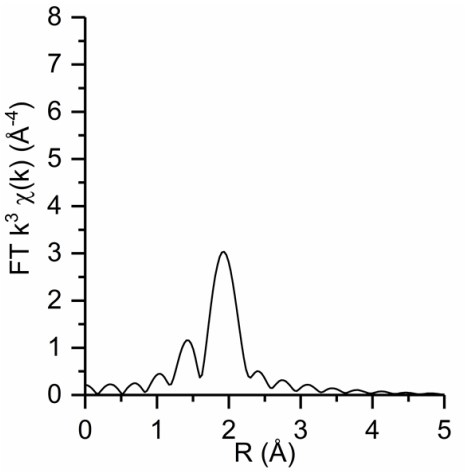

Figure 4.16 – FT-EXAFS of 1_{wt}% Au/C-AR catalyst during treatment with C_2H_2/Ar (step 4).

4.2.4 – Inelastic Neutron Scattering (INS)

To clarify the effect of the C_2H_2 treatment on the gold speciation, as shown in step 4 in the previous section, vibrational spectroscopy had been used. Unfortunately, the carbon support limits the choice of characterisation techniques, for example the use of infrared radiation due to the high absorption coefficient of carbon. For this reason, inelastic neutron scattering (INS) spectroscopy has been chosen to observe hydrogen speciation in the C_2H_2/Ar treated sample and thus to understand the nature of the complexes. The INS experiment was performed at the ISIS Neutron and Muon Source, based at the STFC Rutherford Appleton Laboratory in Oxfordshire, UK. This characterisation has been performed in collaboration with Dr Stewart Parker using a MERLIN spectrometer[9]: incident energies of 600, 250 and 100 meV have been used to observe the C–H/O–H stretch, in-plane C–C stretches/C–H bends and the out-of-plane deformations respectively, as described in Chapter 2. Unfortunately, this technique intrinsically suffers from low signal to noise. Hence, a 2_{wt}% Au/C-AR catalyst has been prepared to increase the concentration of Au species for acetylene to interact with in the sample. The freshly prepared 2_{wt}%Au/C-AR catalyst has been characterised *ex situ* via p-XRD, XAFS and STEM. In figure 4.17, the p-XRD pattern for the sample shows the absence of any degree of long range order and the representative HAADF-STEM image of the freshly prepared catalyst (figure 4.17), acquired by our collaborators at Lehigh University in the group of Prof. C. Kiely, also shows for this high loaded catalyst the presence of highly dispersed isolated Au species with limited presence of sub-nanometer clusters.

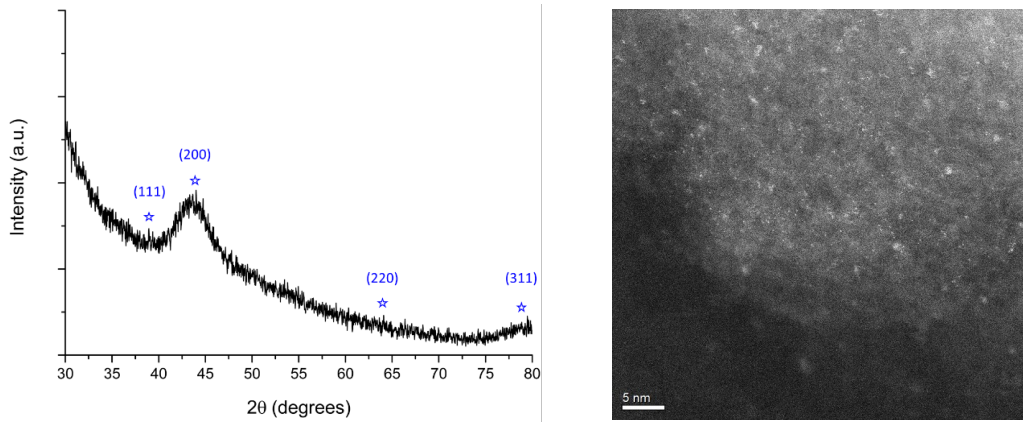

Figure 4.17 – (left) *Ex situ* p-XRD (and) representative STEM-HAADF image of the freshly prepared 2_{wt}% Au/C-AR catalyst.

Figure 4.18 shows the *ex situ* XAFS characterisation of the material. In particular, the Au L_3-edge XANES of the fresh 2_{wt}%Au/C-AR catalyst compared with the reference material, gold foil, shows a white line normalised intensity of the sample of *ca*. 1.1, indicating a noticeably oxidised Au speciation. (Considering the value of the standards [(e.g., $KAuCl_4$/$[AuCl_4]^-$) and Au(I) (e.g., $[AuCl_2]^-$) are 1.1 and

0.6 respectively). The k^3-weighted FT-EXAFS for the sample shows no Au-Au characteristic distances, while the only observed contribution was consistent with the presence of Au-Cl entities. This result also supported the lack of long-range order in the XRD with the major contribution at low values of R in the FT associated with a short Au-Cl distance.

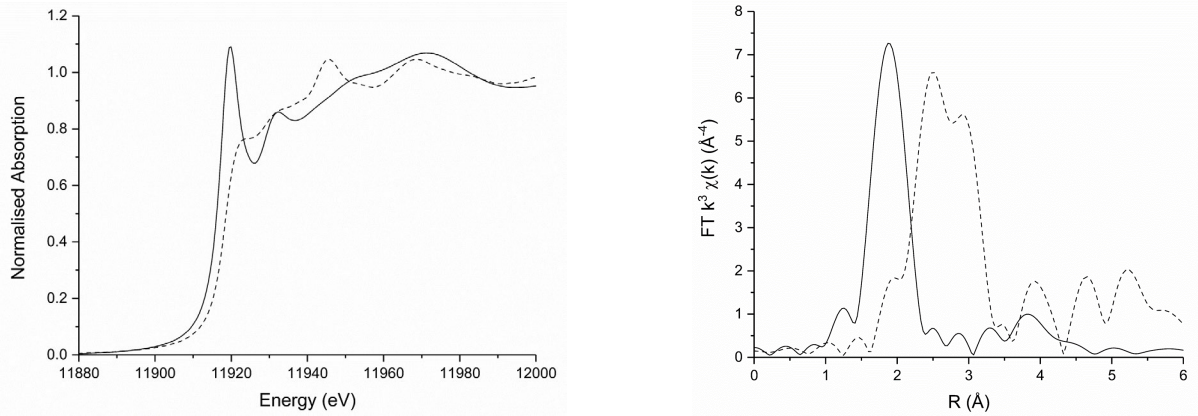

Figure 4.18 – (left) Au L_3-edge XANES of 2_{wt}%Au/C-AR catalyst (black line) and a gold foil reference material (black dashed line) and (right) FT-EXAFS of the sample (black line) and the gold foil (black dashed line) recorded at room temperature.

The 2_{wt}% Au/C-AR catalyst was sequentially treated under helium (He), dilute acetylene gas mixture (5% C_2H_2/He) or concentrated acetylene (100% C_2H_2) in a reaction cell for *ca*. 30 minutes at 200 ˚C. Between each step the sample was cooled, and the cell flushed with helium prior to spectra acquisition. This experiment was performed with the aim of obtaining spectra providing details of acetylene species while the catalyst is exposed to an excess of acetylene. Figure 4.19 shows the spectrum of the 2_{wt}% Au/C-AR prior to acetylene treatment, 2_{wt}% Au/C-AR after treatment in 5% C_2H_2/He and 100% C_2H_2. To gain some useful information from the spectra recorded, the spectrum of the 2_{wt}% Au/C-AR prior to acetylene treatment was used as a background spectrum and subtracted from the other two.

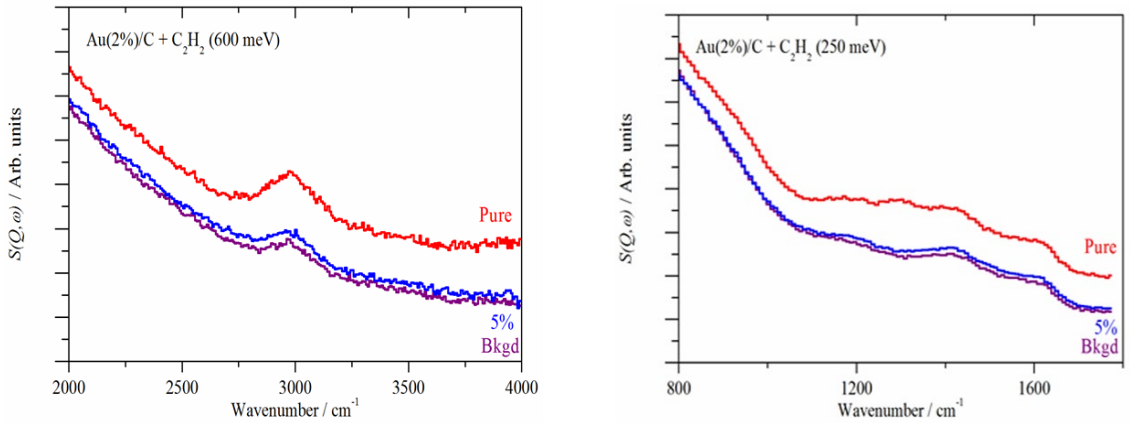

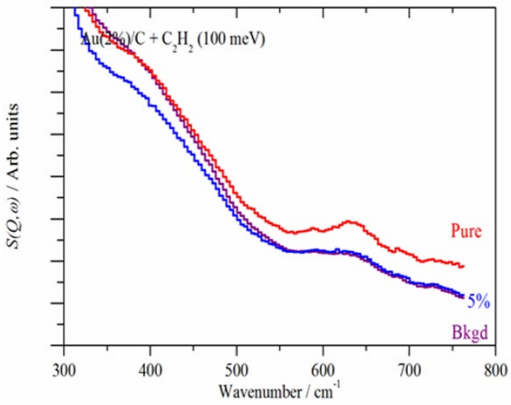

Figure 4.19 – INS spectra of 2_{wt}% Au/C-AR catalyst. (top left) Spectra in C–H/O–H stretch region. (top right) spectra the C–H in-plane bend and C–C stretch region. (bottom) C–H out-of-plane bend region. Purple line: background spectra of catalyst, blue line: after treatment with 5% C_2H_2 in Ar, red line: treatment in pure C_2H_2.

The difference spectra are shown in figure 4.20. The reaction with the 5% C_2H_2/He mixture resulted in no observable changes in the spectra, while in contrast reaction with 100% C_2H_2 results in bands at 2990, 1295, 961, 700 and 640 (and possibly 400) cm^{-1}.

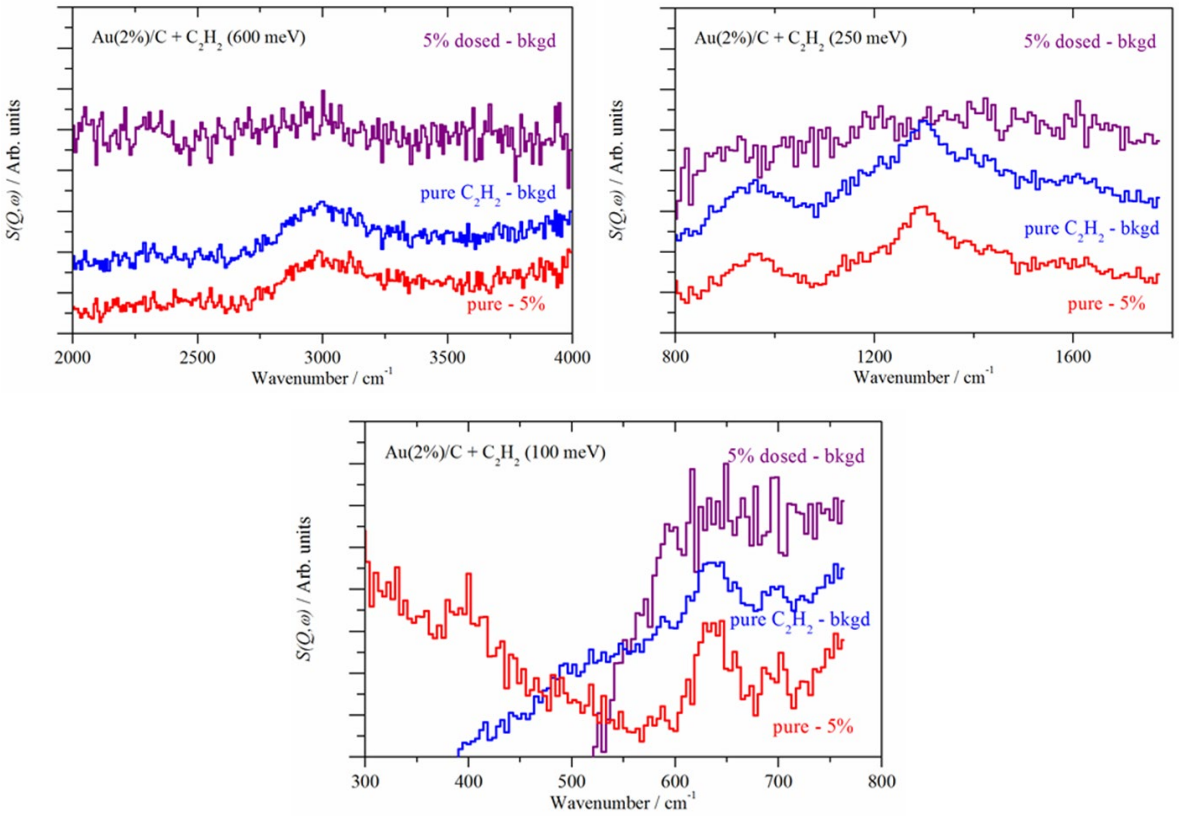

Figure 4.20 – INS difference spectra of 2_{wt}% Au/C-AR catalyst (with background subtraction) in: (top left) the C–H/O–H stretch region; (top right) the C–H in-plane bend and C–C stretch region and (bottom) the C–H out-of-plane bend region.

The bands seen in the difference spectra of 100% C_2H_2, i.e. after the background subtraction, could be assignment to oligomerised acetylene species. In fact, figure 4.21 shows the INS spectrum of polyacetylene, which exhibits bands at similar energies to those seen on the 2_{wt}% Au/C-AR catalyst after the C_2H_2 treatment.[10] However, it must be noted that there are several modes absent in the 2_{wt}% Au/C-AR catalyst after C_2H_2 treatment, compared to polyacetylene. These absent modes could be potentially associated with shorter oligomeric species on the catalyst surface. To test this possibility, an *all-trans*-1,3,5,7-octatetraene (Figure 4.21 – inset) was used as a model for a short chain acetylene oligomer. Figure 4.21 compares the experimental and calculated spectra with good agreement, particularly regarding the 1295 cm^{-1} mode that is clearly present.

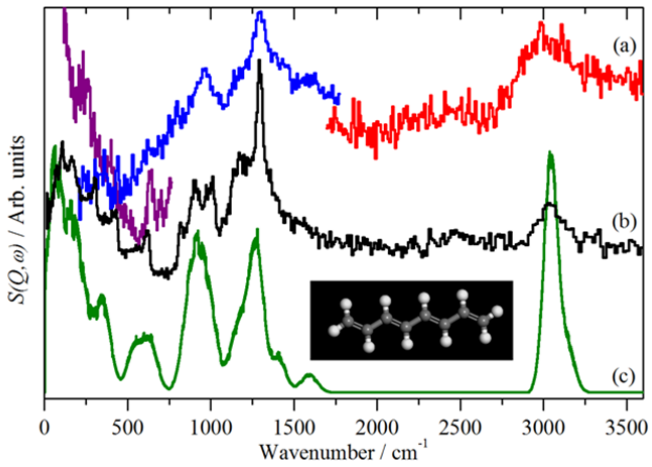

Figure 4.21 – Comparison of INS spectrum of: (a) (C_2H_2 100% dosed – C_2H_2 5% dosed) with (b) polyacetylene recorded on a TOSCA-like INS spectrometer and (c) that calculated for all-trans-1,3,5,7-octatetraene. The inset shows the structure of all-trans-1,3,5,7-octatetraene.

The used catalyst after the INS experiment was then analysed *ex situ* by XAFS and STEM. Figure 4.22 shows that the XANES spectrum recorded after the INS experiment is almost identical the one obtained for the 1_{wt}% Au/C-AR catalyst during the step (4) (C_2H_2/Ar) of the sequential flow experiment. Moreover, also in this case, the Au-Cl intensity in the FT-EXAFS after the INS experiment is decreased compared to the spectrum of the freshly prepared catalyst (figure 4.23). STEM image show that the gold is still atomically dispersed on the carbon support (figure 4.24). The INS data showed the presence of oligomeric acetylene species, while the Au XANES showed a clearly altered Au species after C_2H_2 treatment. Unfortunately, there is no clear evidence that these two species are connected, as no evidence of Au-acetylene bonding was found from either XANES or INS. However, it is possible to conclude that the significant surface acetylene species formed on exposure of a C_2H_2 are detrimental to catalytic activity.

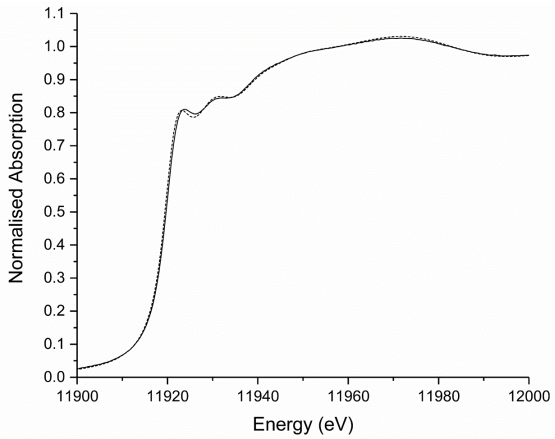

Figure 4.22 –XANES spectra of 2_{wt}%Au/C-AR catalyst after the INS experiment (black dashed line) and the spectrum recorded *in situ* during step (4) of the sequential flow experiment (black solid line).

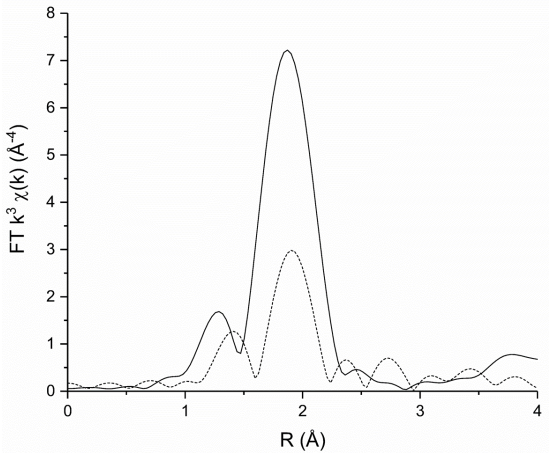

Figure 4.23 – FT-EXAFS of freshly prepared catalyst (black line) and after the INS experiment (black dashed line).

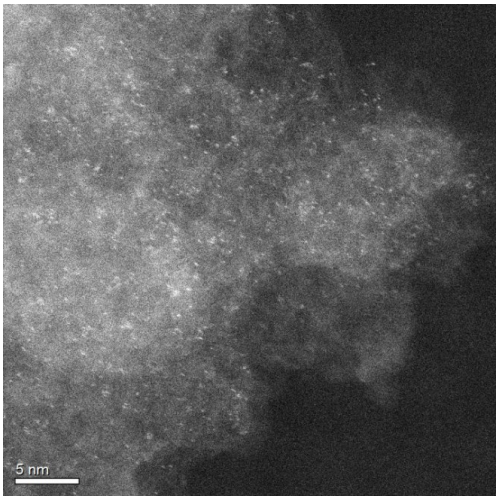

Figure 4.24 –Representative STEM image of the 2_{wt}% Au/C-AR catalyst after the INS experiment.

4.2.5 – *In situ* study of the deactivation of 2_{wt}% Au/C-AR

The sequential flow experiment discussed previously, provided interesting information about the catalyst deactivation associated with Au(0) formation, which caused a loss of correlation between white line height and VCM productivity. Unfortunately, the catalyst deactivation period, with a constant gas composition, would be too slow to be studied *in situ* while recording XAFS spectra over a single beamtime experiment. It has been shown that the 2_{wt}% Au/C-AR catalyst used for INS studies possesses a comparable initial dispersion of $AuCl_x$ species. However, due to the higher concentration of Au that might facilitate agglomeration, this catalyst can be expected to undergo a more rapid deactivation associated with Au(0) particle formation.

The 2_{wt}% Au/C-AR catalyst was initially heated under argon (5°C min^{-1}) up to the reaction temperature (200 °C) and, as observed for the lower metal loading catalyst, a decrease in normalised white line height was recorded, moving from 1.07 at room temperature to 0.68 at 200 °C (Figure 4.25). A LCF-XSNES analysis of the 2_{wt}% catalyst confirmed the absence of Au(0) in the fresh catalyst and a negligible content of metallic gold at 200 °C (0.6±3) (figure 4.25).

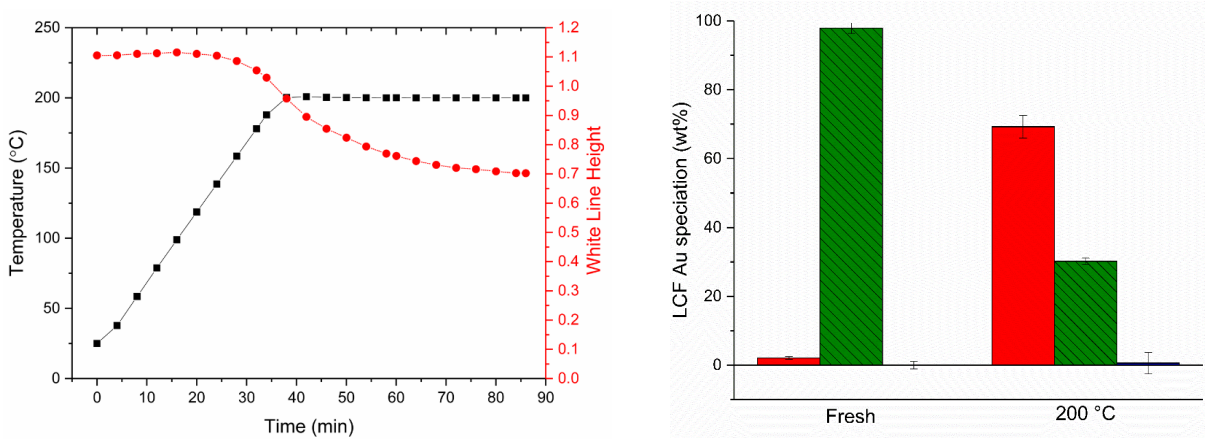

Figure 4.25 – (left) Au L_3-edge XANES for the 2_{wt}% Au/C-AR catalyst during heating to reaction temperature 200 °C under Ar (5 °C min^{-1}). (rigth) LCF-XANES for the freshly prepared 2_{wt}%Au/C-AR catalyst at room temperature and 200 °C under Ar. Percentage Au associated with; Au(I) chloride (standard $[AuCl_2]^-$) in red, Au(III) chloride (standard $[AuCl_4]^-$) in green and Au(0) (standard Au foil) in blue.

Once introduced to the reaction mixture the initial behaviour of the 2_{wt}% Au/C-AR catalyst is comparable with the observed behaviour for the 1_{wt}% catalyst. Figure 4.26 shows that the normalised white line almost immediately increased from 0.68 to 0.85 and then began to decrease over a 20 min period, with a corresponding increase in VCM productivity. However, after *ca*. 40 min of reaction, it is possible to observe a gradual and continued loss in activity, with VCM productivity dropping by 40% between 40 and 200 min of reaction.

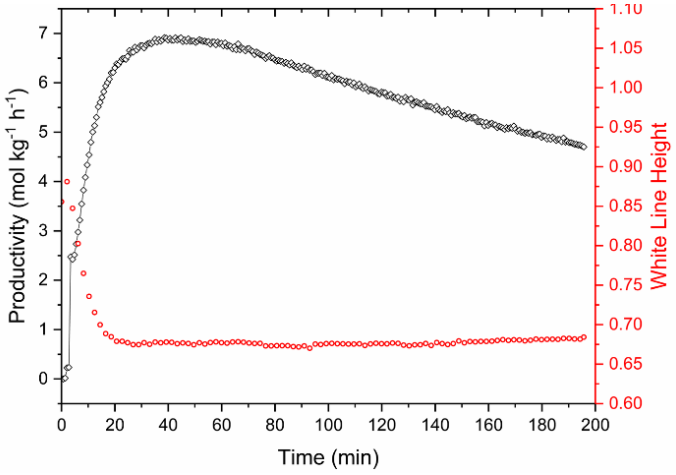

Figure 4.26 – VCM productivity of 2_{wt}% Au/C-AR catalyst during the first 200 min of reaction combined with *in situ* Au L_3-edge XANES. VCM production (black open squares) as a function of time-on-line and simultaneously normalised white line (red open circles).

Noticeably, during the deactivation period observed, the normalised white line height remained relatively constant, possibly implying a loss of correlation between the normalised white line height and VCM productivity as observed during the sequential flow experiment. The LCF-XANES performed at the end of the reaction showed that the catalyst contained considerable amounts of metallic Au (*ca.* 22.5 %) (Figure 4.27).

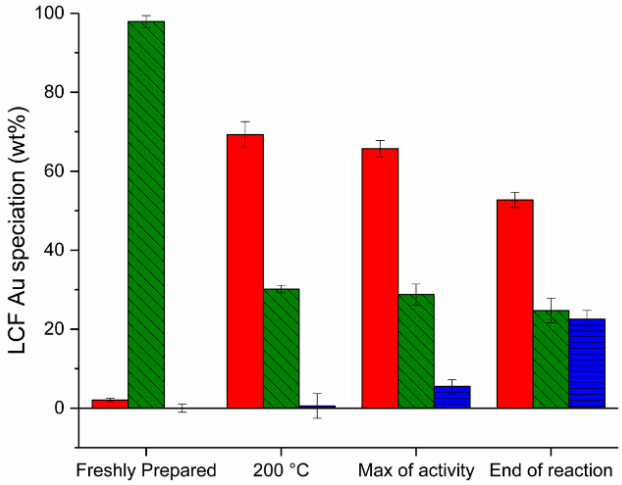

Figure 4.27 –LCF-XANES for the fresh 2_{wt}%Au/C-AR catalyst as prepared at room temperature, once reached 200 °C under Ar and at the end of the reaction (after 200 min). Percentage Au associated with; Au(I) chloride (standard $[AuCl_2]^-$) in red, Au(III) chloride (standard $[AuCl_4]^-$) in green and Au(0) (standard Au foil) in blue.

Also, the FT-EXAFS analysis (Figure 4.28) shown a notable feature associated with Au-Au interactions between 2.5 and 3 Å confirming the observation from the LCF-XANES.

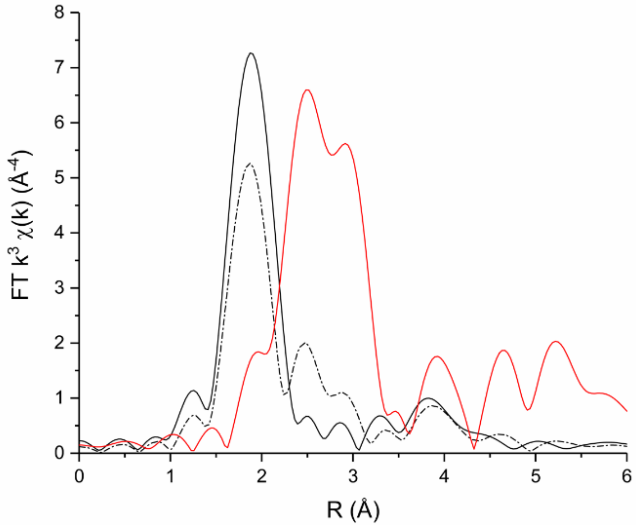

4.28 – FT-EXAFS of 2_{wt}% Au/C-AR catalyst as prepared and after 200 min of reaction. Black line; FT of the fresh catalyst, black dash-dotted line; FT of catalyst after 200 min of reaction, red line; FT of reference material Au foil.

Figure 4.29 shows two representative STEM images of the used 2_{wt}%Au/C-AR catalyst, in which together with areas still comprising of high concentrations of atomically dispersed gold it was possible to detect the presence of large particles of Au. Interestingly, the observed Au particle sizes were predominantly above 200 nm, suggesting that once the $AuCl_x$ species is reduced to Au(0), sintering occurred rapidly under reaction conditions.

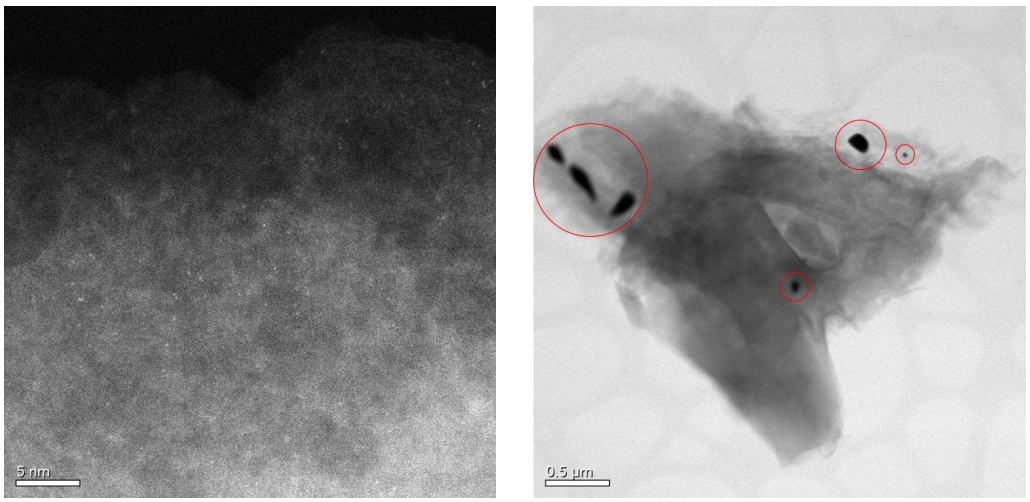

Figure 4.29 – Representative STEM images of the used 2_{wt}% Au/C-AR catalyst.

Au atom number density calculation was also performed, by our collaborator on the 2_{wt}%Au/C-AR catalyst before and after use (Table 4.1). Although, the measurements vary considerably between different images of the same sample, a definite trend was observed with dispersed Au atom density

dropped to *ca*. 1/3rd of its original value after use further suggesting that the reduction and agglomeration of Au species is an important deactivation mechanism.

2_{wt}% Au/C-AR before reaction				2_{wt}% Au/C-AR post reaction			
Image	**Atoms counted**	**Area (nm^2)**	**Area density (atoms nm^{-2})**	**Image**	**Atoms counted**	**Area (nm^2)**	**Area density (atoms nm^{-2})**
1	146	338.26	0.432	a	84	247.46	0.339
2	105	314.24	0.334	b	102	821.91	0.124
3	130	378.42	0.344	c	52	312.86	0.166
4	41	142.54	0.288	d	28	348.76	0.080
5	104	94.60	1.099	e	46	294.32	0.156
6	193	262.80	0.734				
Total	719	1530.86	0.470	Total	312	2025.32	0.154

Table 4.1 – Atom density calculation from sets of STEM images of 2_{wt}% Au/C-AR catalyst before and after acetylene hydrochlorination reaction.

4.3 – Conclusions

In this chapter atomically dispersed Au/C catalysts, prepared by impregnation of an Au *aqua regia* solution, were studied by XAFS and INS under various reactant gas compositions to gain a greater understanding of the reaction mechanism and catalyst deactivation. The sequential flow experiments performed have provided insights into the reaction mechanism leading to the postulation that HCl, in the absence of C_2H_2 cannot re-oxidise Au(I) chloride species under reaction conditions; thus, the oxidative addition of HCl across the Au(I) chloride species requires the concerted addition with C_2H_2. Exposure to C_2H_2 only drastically changes the Au speciation, as clearly shown in the analysis of the XANES region which did not resemble Au(III), Au(I) chlorides or Au(0). INS studies of the catalyst exposed to C_2H_2 showed the formation of oligomeric acetylene species on the catalyst surface, which ultimately lead to the catalyst deactivation. The catalyst deactivation, both after C_2H_2 treatment and time-on-line studies with higher Au loadings, was found to be associated with the formation of metallic Au particles, which significantly affected the strong correlation between normalised white line height and VCM usually observed in the active catalyst.

4.4 – References

1. B. Nkosi, N. J. Coville, G. J. Hutchings, M. D. Adams, J. Friedl and F. E. Wagner, *J. Catal.*, **1991**, 128, 366-377.

2. P. Johnston, N. Carthey and G. J. Hutchings, *J. Am. Chem. Soc.*, **2015**, 137, 14548–14557

3. N. A. Carthey, P. Johnston, M. L. Smidt, Improvements in Catalytic Processes. WO 2010/055341A3, **2010**.

4. B. Nkosi, M. D. Adams, N. J. Coville, G. J. Hutchings, *J. Catal.*, **1991**, 128, 378–386.

5. B. Dai, Q. Wang, F. Yu, M. Zhu, *Scientific Reports*, **2015**, 5, 10553.

6. B. Nkosi, N. J. Coville, G. J. Hutchings, *J. Chem. Soc. Chem. Commun*. **1988**, *0*, 71-72.

7. M. Conte and G. J. Hutchings, *Modern Gold Catalyzed Synthesis*, Eds.: F. D. Toste and A. S. K. Hashmi, Wiley, **2011**.

8. M. Conte, A. F. Carley, C. Heirene, D. Willock, J. P. Johnston, A. A. Herzing, C. J. Kiely, G. J. Hutchings, *J. Catal.*, **2007**, *250*, 231–239.

9. R. I. Bewley, R. S. Eccleston, K. A. McEwen, S. M. Hayden, M. T. Dove, S. M. Bennington, J. R. Treadgold and R. L. S. Coleman, *Phys. B Condens. Matter* **2006**, 385–386, 1029–1031.

10. S. Hirata, H. Torii, Y. Furukawa, M. Tasumi, J. Tomkinson, *Chem. Phys. Lett*., **1996**, 261, 241–245.

Chapter 5

In situ K-edge XAFS study of ligands present in Au/C catalysts for the acetylene hydrochlorination reaction

5.1 – Introduction

In the previous Chapters the performances of gold on carbon catalysts during the acetylene hydrochlorination reaction have been correlated with *in situ* Au L_3-edge X-ray absorption fine structure (XAFS) spectroscopy studies. Under operating conditions, the active catalysts were shown to be comprised of atomically dispersed cationic Au species, with changes in activity correlating with the changing Au(I)/Au(III) ratio. Thus, these materials can be classed as a "single atom catalysts" (SACs).[1,2] By definition, these materials contain isolated metal atoms dispersed on supports, with maximised atom efficiency. In addition to the metal nuclearity and metal oxidation state, the nature of the ligands, including the support, needs to be considered and investigated in these systems. Ligand-metal interactions[3,4] are essential aspects to be considered in being able to maintain high dispersion and stability of the active site and can greatly affect the catalytic activity and the selectivity of the catalysed reaction.[5] The choice of an appropriate ligand to stabilise SACs can therefore play a major role in catalyst.

Despite the established high activity of the Au/C catalyst made with *aqua regia*[6] there are several disadvantages which made its industrial application uneconomical: the use *aqua regia* as a

solvent in the catalysts preparation represents a major concern in both an economic and technical point of view due to the NO_x formation during the catalyst preparation together with the impossibility to decrease the Au loadings below *ca*. 0.3% without experiencing difficulties with the catalyst activation and, lastly, the choice of the chloride ligands, usually too labile and easily dissociated/disproportionated during the synthesis and use of the catalyst.[7]

Johnston and collaborators[7,8] realised the use of soft donor atoms, i.e. sulphur containing ligands, instead of hard ligands, i.e. chloride, could produce a class of more stable catalysts due to the increased stability constants of the Au-S species compared to the Au-Cl.

In Chapter 3, these two classes of gold on carbon catalysts have been compared; the first made with a $HAuCl_4$ precursor and *aqua regia* as solvent (1_{wt}% Au/C-AR), the second made using a Au-thiosulfate precursor and water as solvent (1_{wt}% Au/C-S_2O_3), both preparations are described in Chapter 2. A structure/activity correlation can be made for the two catalysts, as described in Chapter 3, throughout their induction periods and at steady state condition, suggesting interesting similarities in these two catalytic systems.

In this chapter these two catalysts will be compared from the ligands perspective *via* an *in situ* donor K-edge XANES study. Studies that employ soft X-ray in the field of catalysis and under operating conditions are limited.[9,10,11,12,13,14,15] This is due to the technical challenges associated with *in situ* experiments performed at the soft X-ray energy range, e.g. low absorption energies. Typically, the K-edge energies of most common ligand elements are in a range of *ca*. 2–30 keV and are often found close to other absorption edges, e.g. the L_3-edges of elements >Cs; sometimes limiting the XAFS acquisition to the XANES region only. Increased scattering and absorption events occur at lower-energy, that result in a much-reduced ability to penetrate matter. Moreover, to be able to discern changes in the electronic structure of the element under investigation, high-quality data with good resolution is required, implying longer acquisitions time and, again, limited to the XANES region only. When elements like Cl and S are present in the same chemical system with 5d transition metal elements as ligand, is it possible to obtain information about these lower Z elements from the study of the higher energy metal K-edge XAFS. However, this route does not provide direct evidence about speciation and electronic structure of the ligands. On the other hand, the choice of other characterisation techniques that could provide information about structure and speciation of elements such as Cl and S, e.g. NMR, IR and Raman spectroscopy, also have their limitations, both in sensitivity and operation, for example the challenge to work at high temperatures, limiting their application for *in situ* studies.

Previous work has tried to understand the role of the chloride ligand in gold on carbon catalysts for the acetylene hydrochlorination reaction, for example using *ex situ* XPS, identifying multiple Cl environments, which are seen to change through the course of the induction period.[6] While, due to the novelty of this sulphur-ligand containing gold on carbon material and the difficulties in the spectroscopic characterisation of sulphur, no extensive studies can be found in this field.[7,16]

In this chapter, *in situ* donor K-edge XANES characterisation of gold on carbon catalysts during the hydrochlorination of acetylene will be performed, and the effect of the catalysts preparation in the final material will be study also via INS.

5.2 – Results and discussion

5.2.1 – Experimental

In this chapter, 1_{wt}% Au/C-AR was prepared by the impregnation method described in Chapter 2 using tetrachloroauric acid as metal precursor. A 1_{wt}% Au/C-S_2O_3 provided by Johnson Matthey was also characterised and tested. *Ex situ* characterisation of the freshly prepared 1_{wt}% Au/C-AR and 1_{wt}% Au/C-S_2O_3 catalysts performed via XRD, STEM and XAS are reported in Chapter 3. 2_{wt}% gold supported on activated carbon catalysts was prepared using the same impregnation method but on a larger scale, ~10 g batch. The metal loading was increased by keeping the support/solvent ratio constant and increasing the amount of metal precursor for the desired loading.

The bare carbon material has been modified *via* a "washing step", which reproduced the conventional catalyst preparation method without using the metal precursor. In particular, *ca.* 2 g of carbon, previously ground, were mixed with *ca*. 5mL of solvent under vigorous stirring at ambient temperature for 1 h. The carbon was then dried overnight at 140 °C under a flow of nitrogen. The solvents used were *aqua regia* and water and the carbon materials obtained were named C-AR and C-H_2O respectively.

5.2.1.1 – *In situ* ligand K-edge XANES experiment at BM28

In situ XANES experiments have been carried out at the BM28 (XMaS) beamline at the European Synchrotron Radiation Facility (ESRF) is situated on the soft end of an ESRF dipole magnet as described in Chapter 2. At the BM28 it is possible to run a so-called XESCAN.MAC – Extended Escan: Variable point density. In particular, it is possible to perform energy scan for multiple consecutive energy regions, with equal or different step (variable point density).

For the analysis of the Cl K-edge two XEscan has been used:

1) Short scans (60 points from 2.8 to 2.850 keV, with a counting time of 2 seconds per point) (Table 5.1).

Energy (keV)		Points
Start	**End**	
2.8	2.819	5
2.819	2.823	20
2.823	2.835	22
2.835	2.850	12

Table 5.1 – Cl K-edge short XEscan.

2) Long scan (296 points from 2.75 to 2.9 keV, with a counting time of 5 seconds per point) (Table 5.2).

Energy (keV)		Points
Start	**End**	
2.75	2.81	15
2.81	2.815	5
2.815	2.85	225
2.85	2.90	50

Table 5.2 – Cl K-edge long XEscan.

The long scan has been used for *ex situ* acquisition or *in situ* when no change in the XANES spectrum has been observed to acquire even better-quality data, for example at the end of an heating ramp or before switching of a reaction.

For the analysis of the S K-edge a two XEscan has been used:

1) Short scans (83 points from 2.46 to 2.507 keV, with a counting time of 2 seconds per point) (Table 5.3).

Energy (keV)		Points
Start	**End**	
2.460	2.471	6
2.471	2.476	20
2.476	2.480	8
2.480	2.487	28
2.487	2.507	20

Table 5.3 – S K-edge short XEscan.

2) Long scan (216 points from 2.450 to 2.52 keV, with a counting time of 10 seconds per point) (Table 5.4).

Energy (keV)		Points
Start	**End**	
2.450	2.465	10
2.465	2.49	180
2.49	2.52	25

Table 5.4 – S K-edge long XEscan.

Also in this case, long scans have been used for *ex situ* acquisition or *in situ* when no change in the XANES spectrum has been observed to acquire better-quality data, for example at the end of an heating ramp or before switching to the reaction gases. The sample chamber was purged with helium for at least an hour after the sample introduction to remove air introduced during sample loading. The beam upstream of the sample chamber is contained within a helium-filled tube to minimise X-ray absorption by the air. The fluorescent signal was detected using a silicon drift diodes detector. The XANES region is generally used without further manipulation, apart from the data reduction steps reported in Chapter 2. All spectra have been acquired in fluorescence mode.

5.2.1.2 – Reaction conditions for the catalytic tests at BM28

The catalytic tests were carried out according to the testing procedures described in Chapter 2. A summary of the testing conditions is given below.

Dedicated space for the catalyst bed within the reaction cell was very limited and the amount of catalysts used was typically 10 mg. For this reason, the total flow has been reduced to 5 ml min^{-1}: C_2H_2/He (2.5 mL min^{-1}) HCl/Ar (2.5 mL min^{-1}). The make-up gas used was helium instead of argon which is typically used in our reactor systems. Dilute gas mixtures were used C_2H_2/He (4.97% balanced in He, Air Liquide) and HCl/He (5.00% balanced in He, Air Liquide). The gases were dried, using moisture traps, prior to introduction to the reactor setup. In all cases, the reactor was purged with He (99.99 %, Air Liquide, 5 mL min^{-1}), heated to 200 °C at a ramp rate of 2.5 °C min^{-1} and held at temperature for 30 min, under a flow of He, prior to admitting the hydrochlorination reaction mixture. The same fully automated system described in Chapter 2 has been used for these experiments and the on-line analysis of the reaction mixture had been performed with the MS only.

5.2.2 – Study of the effect of the catalyst preparation method

5.2.2.1 – Cl K-edge XANES

Figure 5.1 shows the Cl K-edge XANES spectrum of the bare carbon support in comparison with the spectrum of a standard material, NaCl, in which it is possible to observe an absorption peak at *ca.* 2828.16 eV (A). The presence of this feature confirmed that the bare activated carbon contained Cl species, as shown in previously *ex situ* XPS study.[6] In particular, the comparison with the NaCl standard might suggest the feature rising in the bare carbon XANES spectrum (feature A in figure 5.1) to be associated with Cl atoms bonded with inorganic species, i.e. like in the case of the NaCl standard, although the small shoulder on the main feature (feature B in figure 5.1) might suggest also the presence of some C-Cl functionality.[17]

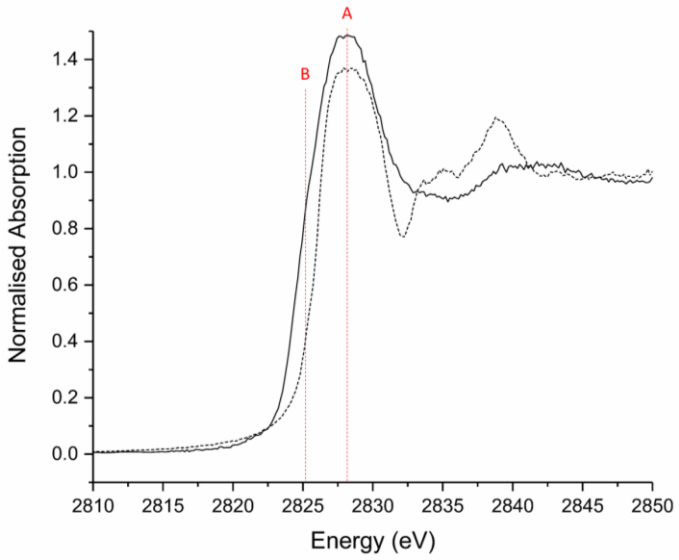

Figure 5.1 – Cl K-edge XANES of bare carbon (black solid line) and NaCl, reference material (black dotted line).

It has been previously reported that the catalyst preparation method, i.e. the choice of the solvent, when using a chlorinated metal precursor such as $HAuCl_4$ or $AuCl_3$, leads to catalytic materials with varying activity.[6] It is possible to expect different types of solvents could lead to the formation of diverse Cl speciation on the support that disperse and stabilise the cationic gold to differing degrees. Figure 5.2 shows the Cl K-edge XANES normalised absorption spectra of the carbon support washed with water (C-H_2O) and *aqua regia* (C-AR) together with the XANES spectrum of the bare carbon support.

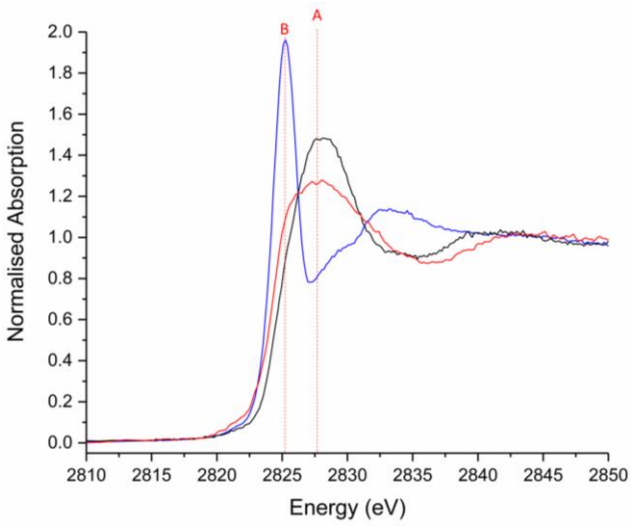

Figure 5.2 – Effect of the solvent on the Cl speciation. Cl K-edge XANES spectra of the bare carbon (black solid line), washed with water, C-H_2O (red solid line) and washed with *aqua regia*, C-AR (blue solid line).

The Cl K-edge XANES spectrum of the C-H_2O, compared to the bare carbon also showed the feature at 2828.16 eV, but the peak is broader and less intense. The reduction in the relative intensity in this feature might suggests that some of the Cl, initially present in the bare carbon material, has been washed away after treatment with water consistent with inorganic chlorides such as NaCl. In the XANES of the C-AR material, it is possible to observe a sharp absorption edge at *ca*. 2825.26 eV (B) and the edge-peak at 2828.16 eV is not detected.

As expected, the effect of the choice of different solvent on the support is evident. It is possible that washing the carbon support with water led to the removal of some of the inorganic species responsible for the formation of feature A, hence broadening the band. While treating the carbon with *aqua regia* increased the C-Cl population, increasing the intensity of the feature at *ca*. 2825 eV.

When a ligand is involved in a bond with a metal, also a new orbital becomes available for the excitation of the 1s electron: the unoccupied molecular orbital that is formed from the interaction of the metal d-orbitals with the ligand 3p orbitals. The excitation from the 1s to this "molecular orbital" gives rise to the so-called pre-edge feature, characterised by absorption energy below the absorption edge (in the case of chlorine < 2822 eV). From the analysis of the pre-edge, energy position, intensity and shape, it is possible to obtain information about oxidation state, coordination geometry and character of the bond.[18,19] Figure 5.3 shows the *ex situ* XANES spectra of 1_{wt}%Au/C-AR and a 1_{wt}%Au/C-H_2O. The introduction of the gold leads to the formation of a pre-edge at *ca.* 2821.29 eV (feature C, figure 5.3). The intensity of the pre-edge is pronounced in the 1_{wt}% Au/C-AR catalyst while is almost negligible in

the 1_{wt}% Au/C-H_2O. This might be due to a general low amount of Cl in the system, but also because most of the gold in this sample is metallic, as reported in Chapter 3.

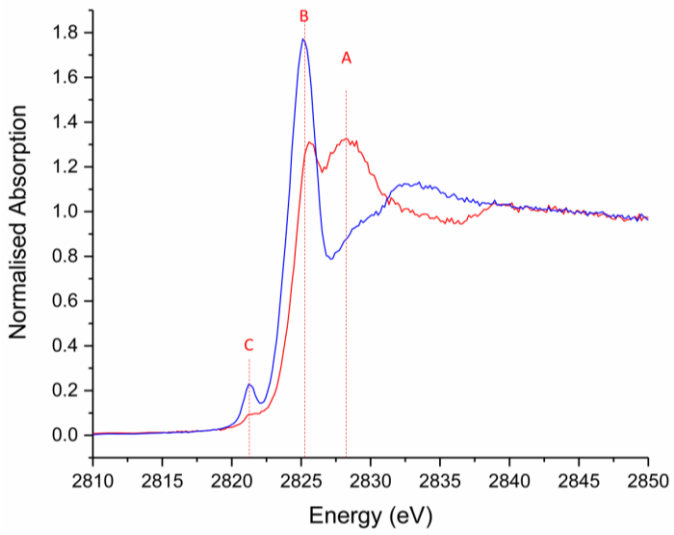

Figure 5.3 –XANES spectra comparison between a 1_{wt}%Au/C-AR (blue solid line) and a 1_{wt}% Au/C-H_2O (red solid line).

Comparing the XANES normalised absorption of the 1_{wt}% Au/C-H_2O and the C-H_2O it is possible to observe the formation of a feature at *ca*. 2825 eV (feature B, figure 5.4), as observed in the 1_{wt}% Au/C-AR catalyst, implying that also in this case, part of the chlorine introduced in the system during the catalyst preparation led to the formation of C-Cl speciation. Comparing the XANES spectrum of the 1_{wt}% Au/C-AR catalyst with the one of the C-AR sample, it is possible to observe that a significant fraction of the total Cl, previously involved in the formation of feature B, is now bound directly to gold and involved in its stabilisation/dispersion in the catalytic system (feature C, figure 5.5).

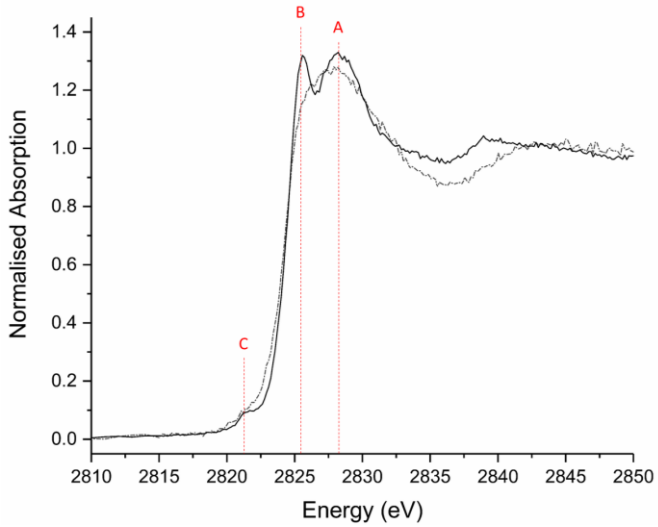

Figure 5.4 – Comparison between XANES normalised absorption spectra of a C-H_2O (black dash-dotted line) and a 1_{wt}% Au/C-H_2O (black solid line).

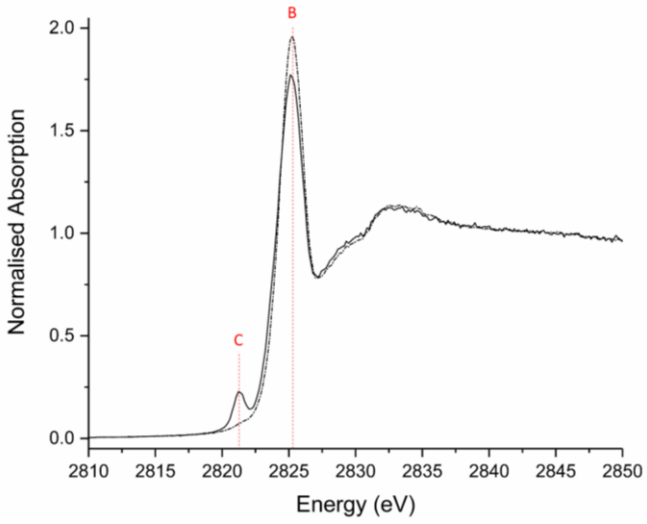

Figure 5.5 – Comparison between XANES normalised absorption spectra of the C-AR (black dash-dotted line) and a 1_{wt}% Au/C-AR (black solid line).

The intense band at *ca*. 2825 eV (feature B) reported for Cl-C- bonds [24] had been shown to be similar to the distinct feature of the H-Cl σ bond due to the Cl 1s→3p transition.[20] For this reason, the Cl K-edge XANES spectrum of the 1_{wt}% Au/C-AR catalyst has been compared with XANES spectrum of gaseous HCl (5%HCl/He, 40 mL min^{-1}) as shown in figure 5.6. Based on the comparison between the two spectra, we can consider the main feature at *ca*. 2825 eV observed in the C-AR and 1_{wt}% Au/C-AR samples, and less pronounced in the 1_{wt}% Au/C-H_2O, to arise from the $Cl_{1s} \rightarrow Cl_{3p}$ transition due to the presence of C-Cl speciation.

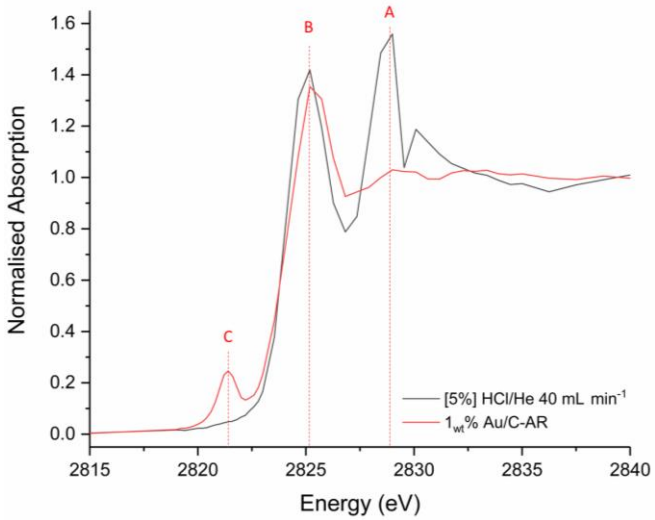

Figure 5.6 – Cl K-edge XANES spectra of the 1wt%Au/C-AR catalysts (black solid line and gaseous 5%HCl/He 40 mL min^{-1} (red solid line).

5.2.2.2 – Inelastic Neutron Scattering (INS)

To clarify the effect of the catalyst preparation on the carbon support a vibrational spectroscopy experiment using inelastic neutron scattering (INS) spectroscopy was performed. As already mentioned in Chapter 4, the carbon support limits the choice of characterisation techniques, making INS spectroscopy the most suitable tool for this purpose. The INS experiment was performed at the ISIS Neutron and Muon Source, based at the STFC Rutherford Appleton Laboratory in Oxfordshire, UK. This characterisation has been performed in collaboration with Dr Stewart Parker using the MERLIN spectrometer.[21] Approximately 10 g of sample was loaded into an indium wire sealed aluminium can and the NS spectra were recorded with incident energies of 600, 250 and 100 meV have been used to observe the C–H/O–H stretch, in-plane C–C stretches/C–H bends and the out-of-plane deformations respectively, as described in Chapter 2 and 4.

The samples analysed were: bare carbon, C-AR, 2_{wt}%Au/C-AR and 2_{wt}%Au/C-H_2O. Characterisation of the 2_{wt}% Au/C-AR catalyst are reported in Chapter 4, while the 2_{wt}% Au/C-H_2O catalyst has been characterised via *ex situ* p-XRD. Figure 5.7 shown the catalyst was composed predominantly of metallic gold nanoparticles. Reflections due to gold are detectable at 38, 44, 64 and 78° 2θ. The crystallite size of the metallic gold nanoparticles was determined using the Scherrer equation, as reported in Chapter 2, and gave an estimated crystallite size of *ca*. 50 nm.

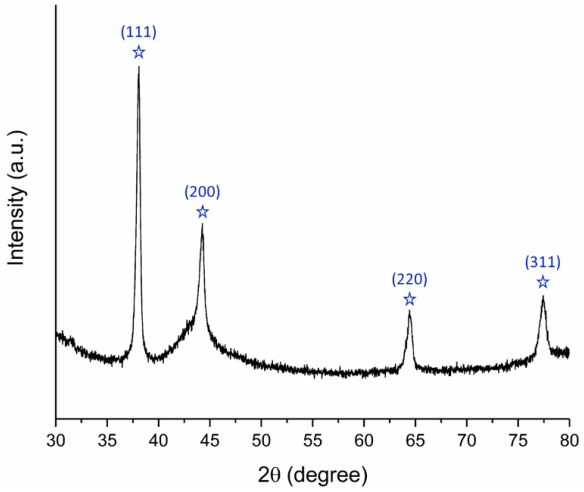

Figure 5.7 – *Ex situ* p-XRD of the freshly prepared 2_{wt}% Au/C-H_2O catalyst.

Figures 5.8-9-10 show the spectra in the three regions recorded for the four samples (bare carbon, C-AR, 2_{wt}%Au/C-AR and 2_{wt}%Au/C-H_2O).
The ordinate scale is the same for all the spectra within a figure, however, it differs between the figures. Thus, assuming the sample masses are the same in each case, the relative intensities within a figure are

comparable. The 2_{wt}% Au/C-H_2O only and the bare carbon support are very similar, showing the characteristic modes of activated carbon support materials: aromatic C–H stretchs at 3070 cm^{-1}, C–C stretchs at 1420 cm^{-1}, C–H in-plane bending modes at 1190 cm^{-1} and C–H out-of-plane bending modes at 870 cm^{-1} (Figure 5.7 and 5.8). There is no evidence for water or hydroxyl groups in these two samples. The other samples (2_{wt}% Au/C-AR and C-AR) all show the presence of an O–H stretch at 3500 cm^{-1} (Figure 5.8). This is especially pronounced for the 2_{wt}%Au/C-AR sample; in this case the water scissors mode at 1650 cm^{-1} and vibrational modes ~550 cm^{-1} are apparent in Figures 5.8 and 5.9 respectively. For the carbon support treated with aqua regia (C-AR) only the O–H stretch is clearly seen.

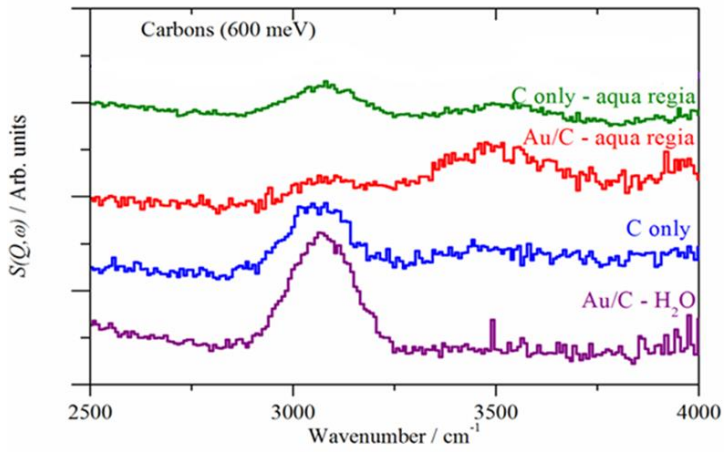

Figure 5.8 – INS spectra of treated carbons and catalysts in the C–H/O–H stretch region (incident energy 600 meV).

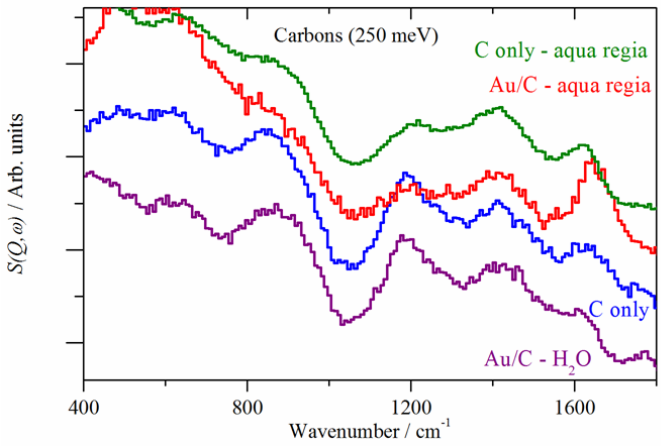

Figure 5.9 – INS spectra of treated carbons and catalysts in the C–H in-plane bend, C–C stretch and H–O–H scissors region (incident energy 250 meV).

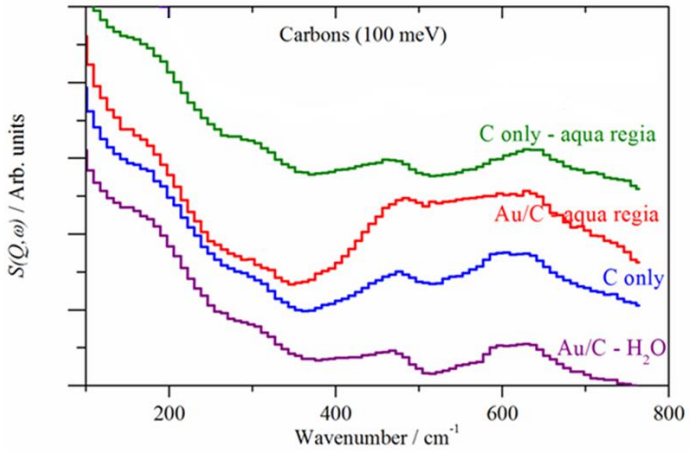

Figure 5.10 – INS spectra of treated carbons and catalysts in the water librational region ((incident energy 100 meV).

Combining the spectroscopic observations acquired from both XAFS and INS studies, it might be plausible that the pronounced feature at *ca*. 2825 eV observed in the Cl K-edge XANES spectra of the C-AR, 1_{wt}%Au/C-AR and 1_{wt}%Au/C-H_2O catalysts, rises from the Cl 1s→3p transition in a C-Cl bond. However, is not possible to exclude without doubt that some of the Cl species in the systems studied might be bonded to a hydroxy group via the hydrogen atom introduced on the carbon during the catalyst preparation.

5.2.3 – *In situ* Cl K-edge of the 1_{wt}%Au/C-AR during reaction

In Chapter 3 the changes in gold speciation in Au on carbon catalysts during the hydrochlorination of acetylene in a *in situ* study of the Au L_3-edge XAFS were described. In this chapter, a similar test was performed while recording the Cl K-edge XANES. Figure 5.11 shows the Cl K-edge XANES, and related normalised first derivative, of the 1_{wt}%Au/C-AR catalyst as prepared, recorded *ex situ* compared with one recorded *in situ* under helium flow and room temperature. No changes in the absorption edge positions were observed when comparing the two spectra. What does change is the intensity of those features, mainly of the main absorption edge at *ca*. 2825 eV. The low intensity observed in the *in situ* recorded spectrum could be attributed to experimental self-absorption, due to the inevitable difference in the sample preparation.[22] Nevertheless, we consider this phenomenon to effect negligibly the interpretation of the *in situ* recorded XANES spectra.

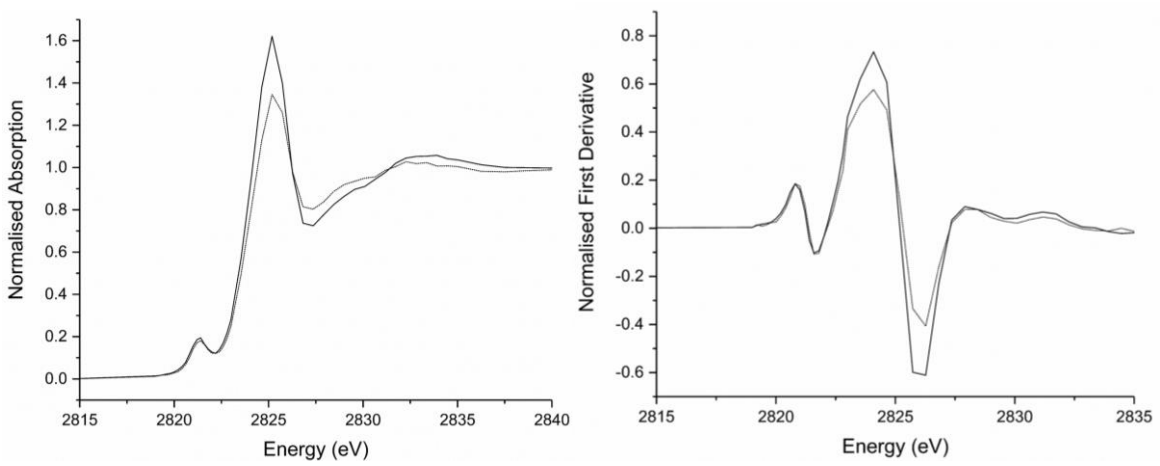

Figure 5.11 – Comparison between the Cl K-edge XANES spectra of a 1_{wt}%Au/C-AR catalyst acquired *ex situ* (black solid line) and *in situ* at room temperature under helium flow (5ml min^{-1}) (black short dotted black line). (left) Normalised XANES (right) Normalised first derivative.

Figure 5.12 shows all the XANES spectra acquired *in situ* at the Cl K-edge while heating the catalyst to the reaction temperature under helium flow (200 °C - 2.5 °C min^{-1}). It is possible to observe that, while the main absorption edge (2825.18 eV) does not change during the heating ramp, changes in the pre-edge (2821.30 eV) are evident.

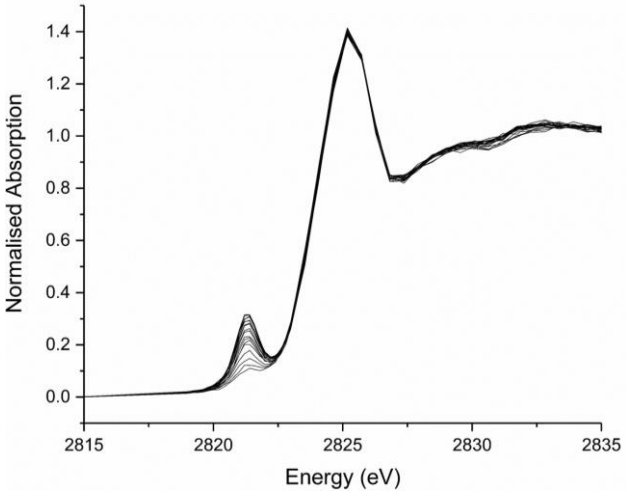

Figure 5.12 – *In situ* Cl K-edge XANES spectra of the 1_{wt}%Au/C-AR catalyst while heating to reaction temperature (200 °C).

Figure 5.13 shows the change in the pre-edge intensity as a function of temperature together with both the normalised XANES and the normalised first derivative recorded at three different points of the heating ramp. The pre-edge normalised intensity is *ca*. 0.21 at room temperature, after 20-25 minutes (between 80-100 °C) it reaches a maximum of intensity (0.31) and finally collapses to 0.09 once 200

°C is reached. It is reported that when the d-orbitals of the metal are fully occupied, as for Au(I), the pre-edge feature is absent from the absorption spectra,[23] this result is in agreement with the Au L_3-edge experiments (figure 3.7, Chapter 3) in which a decrease in white line intensity from 0.78 at 25 °C to 0.68 at 200 °C was observed and is attributed to a change from a mixed Au(III) and Au(I) chloride speciation to predominantly Au(I) chloride-like species, which was correlated with the thermal decomposition of $AuCl_3$ to AuCl.[24]

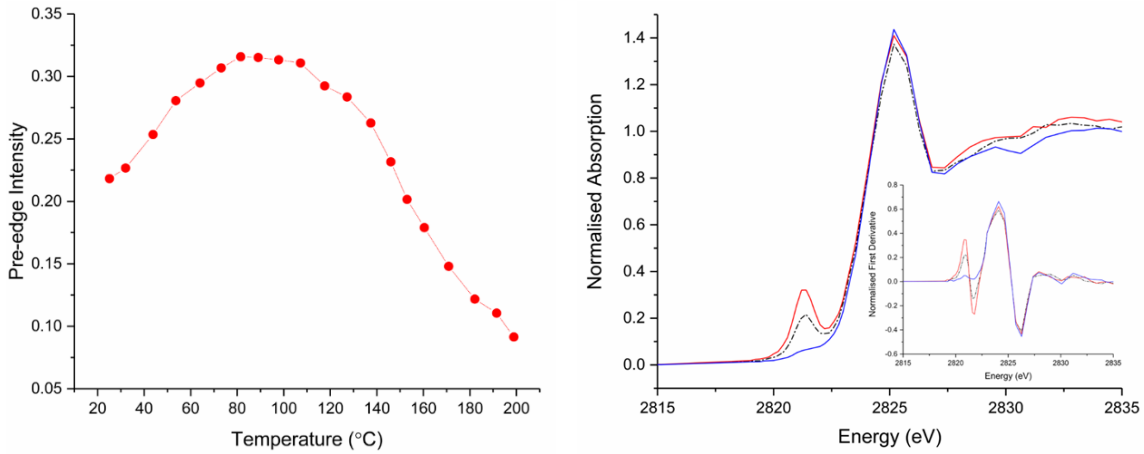

Figure 5.13 – (left) *In situ* recorded Cl K-edge changes in pre-edge intensity of the 1_{wt}%Au/C-AR catalyst while heating to reaction temperature. (right) Detail of under helium at room temperature (black dot-dashed line) at the maximum pre-edge intensity (red solid line) and at 200 °C (blue solid line) and the associated first derivative (insert).

At 200 °C the reaction mixture was introduced into the system. Figure 5.14 shows the normalised spectra acquired during the time-on-line through the induction period until steady state conditions. The changes observed in $Cl_{1s} \rightarrow Cl_{3p}$ edge are negligible (mainly fluctuating within the normal variations), while clear variations in the pre-edge were observed.

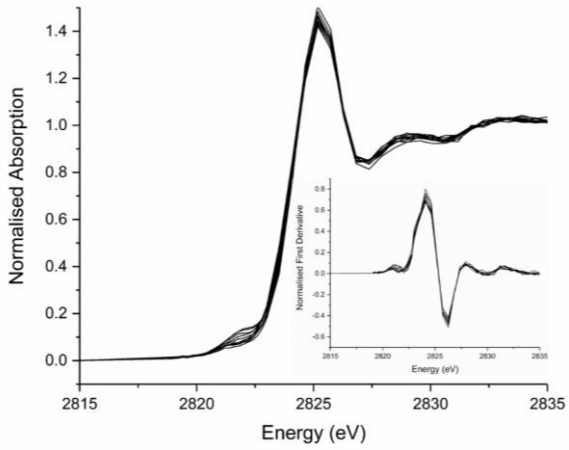

Figure 5.14 – *In situ* Cl K-edge XANES of 1_{wt}%Au/C-AR catalyst during the time-on-line. All Normalised XANES and normalised first derivative (insert) during of the reaction until the steady state.

Three XANES spectra recorded at different time during the time-on-line were selected together with the associated normalised derivative and are reported in figure 5.15. The pre-edge increased during the first 20 min of reaction and then started to decrease, reaching a similar initial intensity value at the steady state. Interestingly, a shift in energy is also observed, meaning that together with contribution of the Cl 3p to the metal-ligand molecular orbital also the geometry of the Au-Cl, e.g. bond length, is changing.[18] In particular, as already mentioned, the position of the ligand pre-edge peak reported to be dependent primarily on the d orbital energy (M oxidation state), and considering the results reported in Chapter 3, the change observed in the Cl pre-edge peak are in line with the changes in Au oxidation state obtained from the analysis of the XANES Au L_3-edge white line height.

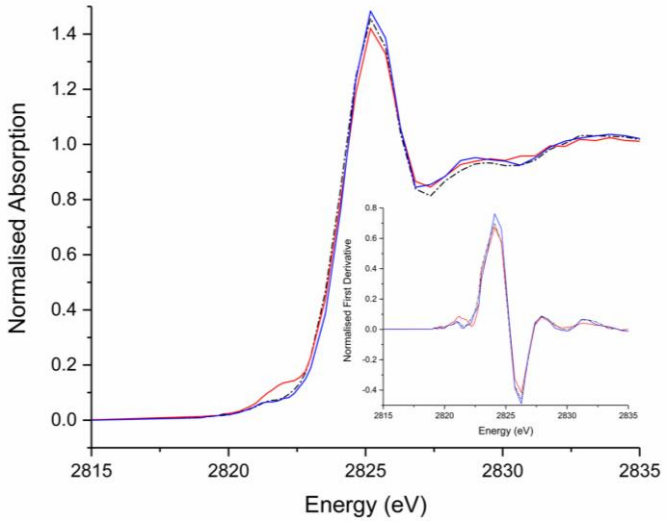

Figure 5.15 – Normalised XANES and normalised first derivative (insert) recorded at moments of reaction: beginning of the reaction (black dot-dashed line) max of pre-edge intensity (red solid line) and at steady state (blue solid line).

The *ex situ* XANES spectrum of three gold chloride standard materials were also recorded to gain a better understanding of the observed pre-edge (AuCl, red dotted line; $AuCl_3$, blue solid line and $KAuCl_4$, black dotted line) (Figure 5.16). It is well known that $AuCl_3$ has a thermodynamically favoured dimeric structure,[19] in which the Cl is involved in two different bonding environments with different bond lengths (terminal and bridged). This is reflected in a split XANES pre-edge in the $AuCl_3$ standard material. During the time-on-line we did not observe any splitting of the pre-edge peak, confirming also form the ligand perspective the catalysts consist in mainly atomically dispersed Au-Cl active species under reaction conditions.

Unfortunately, it was not possible to correlate the changes in the pre-edge with the VCM productivity precisely during the time on line. The new setup used, and the low flow rate required, did not allow

VCM production to be monitored at a reasonable time resolution. Even though we can report our productivity at steady state was 0.2 mol $kg^{-1}h^{-1}$.

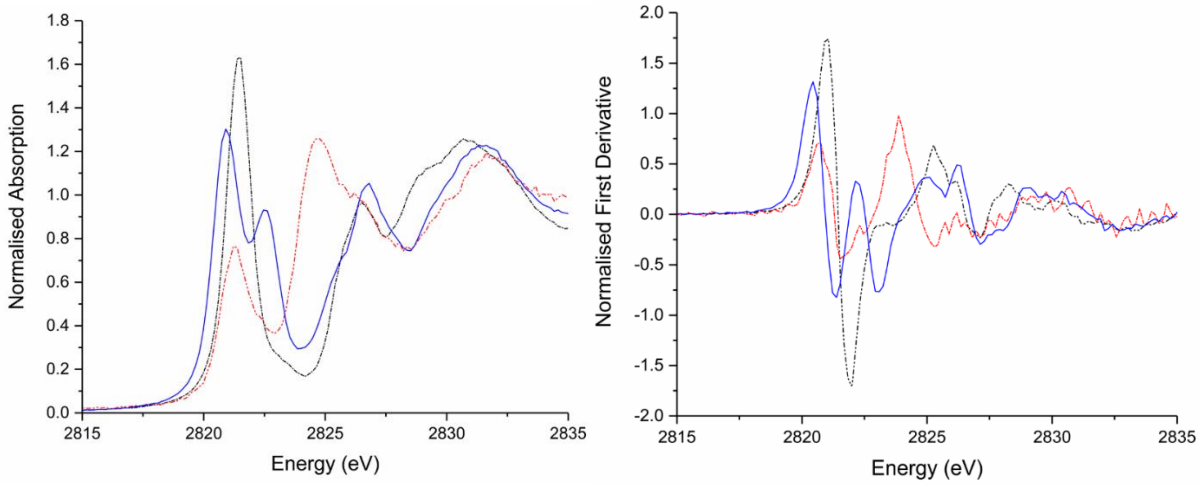

Figure 5.16 – (Left) Normalised XANES and (right) normalised first derivative three gold chloride standard materials. AuCl (red dotted line) $KAuCl_4$ (black dot-dashed line) and $AuCl_3$ (blue solid line).

5.2.4 – *In situ* Cl K-edge XANES of the 1_{wt}%Au/C-S_2O_3 during reaction

The same experiment reported in the previous paragraph has been performed on a 1_{wt}%Au/C-S_2O_3 catalyst, to understand if Cl is interacting with Au in this new class of catalysts based on Au-S compounds as in the case of the 1_{wt}% Au/C-AR material. Figure 5.17 shows the XANES normalised absorption and normalised derivative of the freshly prepared 1_{wt}% Au/C-S_2O_3 catalyst. The spectrum recorded is characterised by a broad absorption-edge at *ca*. 2828 eV, very similar to the broad main edge observed in the C-H_2O and 1wt% Au/C-H_2O samples (Figure 5.4). The analogies in the spectra of these different samples might arise from the similar preparation method, i.e. the use of water as solvent for the dissolution/deposition of the metal precursor. A pre-edge feature is detectable at *ca*. 2821 eV suggesting that in the fresh catalyst part of the chlorine, that comes mainly from the gold precursor used ($HAuCl_4$), is directly bounded to the cationic Au species. This is direct evidence that also in this catalyst, made with a gold-thiosulfate precursor, it is possible to detect $AuCl_x$ species. From the study of the normalised XANES spectrum (figure 5.17), it is possible to detect a shoulder in the main absorption edge (*ca*. 2825 eV). This feature might be attributed also in this case to the transition from the Cl 1s to the Cl 3p, associated to H-Cl or, more likely to C-Cl speciation present in the fresh carbon material.

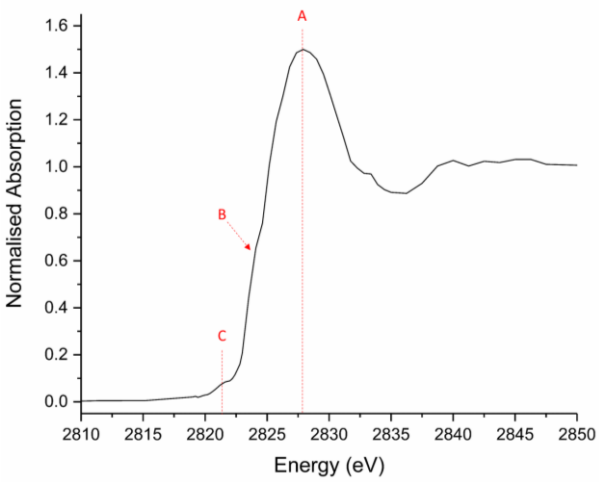

Figure 5.17 – Cl K-edge XANES the freshly prepared 1_{wt}% Au/C-S_2O_3 catalyst.

Figure 5.18 shown all the XANES spectra recorded during the heating ramp (2.5 °C min^{-1} up to 200 °C) and the spectra recorded at three different moments of the heating ramp, i.e. at beginning of the reaction (time zero), at the maximum of the pre-edge intensity and at 200 °C), together with the relative first derivative. The pre-edge changes in the same fashion previously observed for the 1_{wt}% Au/C-AR, starting from a normalised pre-edge intensity of ~ 0.09 it initially increased to ~0.13 and then decreased again to a pre-edge intensity of ~0.08. The interpretation of the changes in the main edge at ~ 2828 eV is difficult, and the shoulder did not follow a definitive trend. It seems like the increase of temperature greatly modifies the main absorption feature, possibly due to loss of some of the chlorine from the system, making difficult to monitor changes in the shoulder. However, it must be also taken in account that the preparation method for this catalyst, reported in Chapter 2, uses water as solvent and the absence of any additional source of Cl, apart from the metal precursor, lead to a quite negligible Cl content. This low chlorine content lead to difficulties in the XANES data reduction normalisation step, so that the changes observed might also been affected to the quality of the spectra recorded.

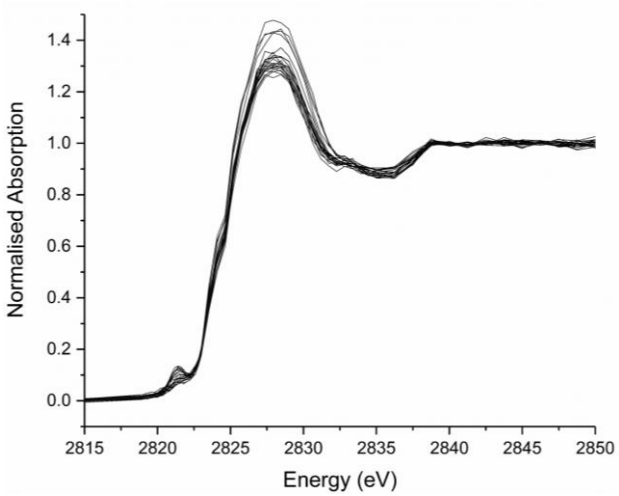

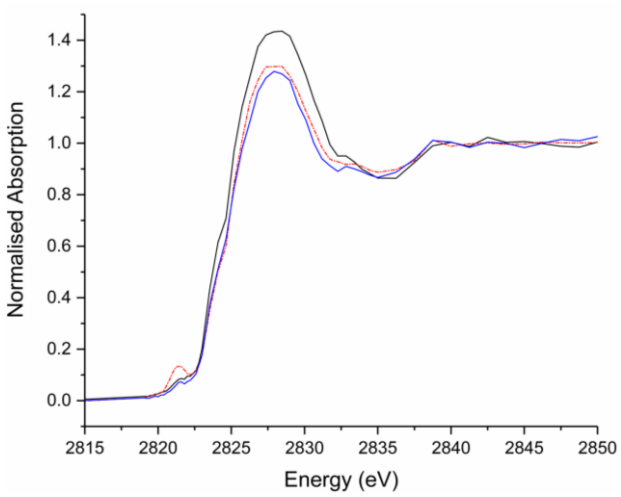

Figure 5.18 – *In situ* recorded Cl K-edge XANES spectra of the 1_{wt}%Au/C-S_2O_3 catalyst while heating to reaction temperature. (left) All XANES spectra and (right) Normalised XANES and normalised first derivative (insert) recorded at moments of the heating ramp: beginning (black solid line) max of pre-edge intensity (red dash-dotted line) and at 200 °C (blue solid line).

Once the reaction temperature was reached, the reaction mixture was introduced in the system. Once again, as showed in figure 5.19, changes in the pre-edge feature could be observed.

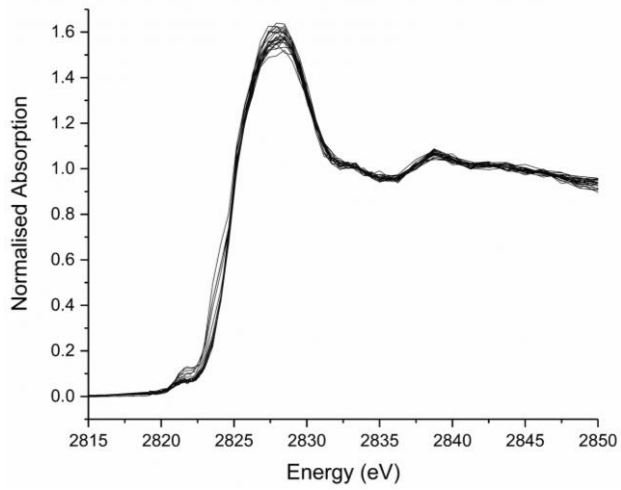

Figure 5.19 – *In situ* recorded Cl K-edge XANES spectra of the 1_{wt}%Au/C-S_2O_3 catalyst during reaction.

Figure 5.20 shows the XANES spectra recorded at three different moments during the reaction. Starting from a pre-edge intensity of *ca*. 0.08, it increased during the first 20 min of reaction to *ca*. 0.12 and then decreased to *ca*. 0.06 remaining stable until the steady state was reached. The changes observed in the pre-edge feature agreed with what observed from the Au L_3-edge changes in white line height reported in Chapter 3 (figure 3.25) for the 1_{wt}% Au/C-S_2O_3, confirming that the gold speciation involved in the

catalysis are directly bonded to Cl ($AuCl_x$ species) and the changes in the gold oxidation state could be observed also from the ligand K-edge perspective.

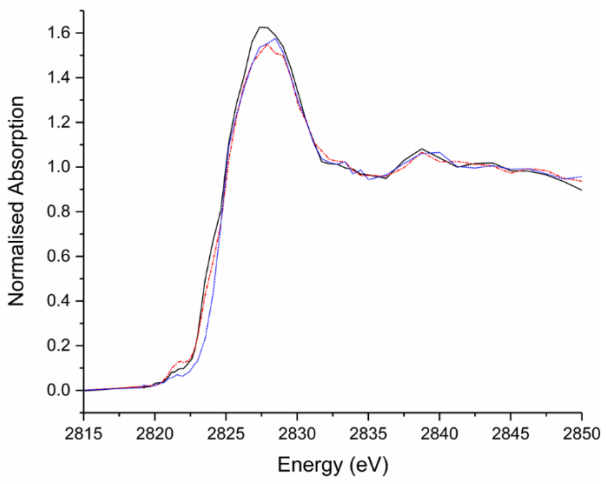

Figure 5.20 – *In situ* recorded Cl K-edge normalised XANES spectra of the 1_{wt}%Au/C-S_2O_3 catalyst at three moments during reaction. Beginning (black solid line) max of pre-edge intensity (red dash-dotted line) and at steady state (blue solid line).

Interestingly the shoulder in the main edge arising from the Cl 1s→ 3p transition disappeared once the steady state condition was reached, while in the case of the 1_{wt}% Au/C-AR the corresponding feature remained stable during the catalysis. It is possible that the corresponding Cl speciation in the case of the 1_{wt}% Au/C-AR are in part responsible for the stability of the $AuCl_x$ active species, while this is not the case for the 1_{wt}%Au/C-S_2O_3. For the latter the improved stability might be attribute to the sulphur speciation present in the catalytic material, this matter is further investigated in the following paragraph.

Even though the interpretation of the full XANES spectrum remains difficult, the general changes in the pre-edge observed agreed with the results obtained both from the 1_{wt}% Au/C-AR and the 1_{wt}%Au/C-S_2O_3 Au L_3-edge XAFS study reported in Chapter 3. This implies that in the 1_{wt}% Au/C-S_2O_3 catalyst some Cl is bounded directly to the gold and it is involved in the reaction re-affirming that $AuCl_x$ speciation are active site for the acetylene hydrochlorination reaction for both these catalytic systems.

5.2.5 – *In situ* S K-edge XANES of the 1_{wt}% Au/C-S_2O_3 catalyst during reaction

Even if more investigation is needed to have a full understanding of this new catalytic system from the Cl K-edge perspective, it is clear from the study of the pre-edge that $AuCl_x$ speciation are involved in the reaction mechanism also in this class of catalyst. In order to understand what is the actual role of

the sulphur in the 1_{wt}% Au/C-S_2O_3 catalyst, the same *in situ* experiment performed while recording the Cl K-edge XANES has been performed at S K-edge.

The absorption edges for sulphur occur at 2472 eV (K), 230.9 eV (L_1), 163.6 eV (L_2) and 162.5 eV (L_3), and correspond to the creation of a photoelectron from the 1s, 2s, $2p_{1/2}$ and $2p_{3/2}$ core levels, respectively.[25] In general, as the formal oxidation state of S increases the shielding of the nuclear charge is reduced, resulting in an increase of the binding energy of the core orbitals, meaning that the S-absorption edges are extremely sensitive to the sulphur oxidation state. In particular, in the S K-edge XANES region is it possible to observe an energy shift of *ca*. 15 eV going from S(-2) of sulphides and S(+6) of a sulphate.[26]

When sulphur is a donor element in complicated system such us oxyanions, it can show more than one oxidation state within the same compound. It has been reported that in case like this, it is possible to attribute the maximum position of the rising absorption edge as derived from electronic transitions from the core-level orbital 1s to the 3p (often called white line), as a function of the oxidation state. In particular following the Kunzl' rule, considering that the XANES actually shows the charge density of an atom in a molecule, the changes in atomic density are represented in a "chemical shift" of the absorption edge in the XANES region.[27] Moreover, when a sample contains a photo-absorber that occurs in various oxidation states, like in the case of oxyanion of sulphur, the spectrum originated will show all oxidation states of the element that are present in the sample (XANES spectra additivity).

As already mentioned, the main transition observed in the S K-edge XANES spectrum is the transition $S_{1s} \rightarrow S_{3p}$, in which energy and intensity changes indicate changes in oxidation state. It can be found in the literature that several types of sulphur compounds have a unique pattern of transitions on the absorption edge making the sulphur K-edge XANES suitable to qualitatively determine the speciation of sulphur compounds in samples with complex composition.[22] So, in contrast with analysis of the XANES spectra recorded at the Cl K-edge, in the case of sulphur we consider only one transition (1s to 3p) and the changes in the absorption energies (chemical shifts) as change in the occupancy of the orbital involved in the transition, i.e. changes in occupancy of the 3p orbital due to the change in oxidation state. More so in the case of oxyanions of sulphur, in which the strong electron withdrawing capability of the number of oxygen atoms attached to the sulphur, results in a large de-shielding effect on the sulphur.

Unfortunately, studies reported in literature shown that the interpretation of the S K-edge is more challenging. Debate exists about the actual oxidation state of the sulphur atoms in thiosulphate ions; for example, according to Vairavamurthy *et al*.,[27, 28] the two sulphur atoms of thiosulfate should exist in the oxidation state of sulphate (+6) and sulphide (−2), however, the results obtained based on XANES spectroscopy indicate that the two different sulphur atoms in thiosulfate have charge densities

corresponding to the oxidation states that were established for the outer and inner sulphur atoms of thiosulfate as −1 and +5, respectively. It must be also considered that, experimentally, the S-S bond is somewhere between a single bond and a double bond based on its length. Thus, it has been reported that: if an S=S double bond or an S-S bond of thiosulfate is cleaved homolytically, the resulting S oxidation states are 0 and +4, as reported in figure 5.21.[29]

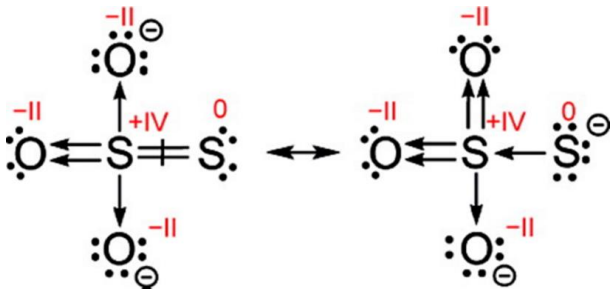

Figure 5.21 – Oxidation states in the thiosulphate ion.[29]

However, another study claims that bonds between two atoms of the same element are divided equally with no exceptions for formal charges. Thus, the oxidation states -1, +5 if the S-S bond is single and 0, +4 if the S=S bond is double are both possible.[30]

The S K-edge XANES spectrum of a $Na_2S_2O_3$ standard was recorded and Figure 5.22 shows the comparison in both normalised absorption XANES and normalised first derivative of the sodium thiosulfate standard recorded *ex situ* at BM28 with one reported in the ESRF database.[31] It is still possible to observe the thiosulfate spectrum contains two major peaks, which, according to the previous comments, can be attributed to the outer sulphur (S^{1-} or S^0) at *ca*. 2473 eV and inner sulphur (S^{+5} or S^{+4}) at *ca*. 2481 eV respectively.

Figure 5.23 shows the comparison between the reference material $Na_2S_2O_3$ and the 1_{wt}% Au/C-S_2O_3 catalyst freshly prepared. In the XANES spectrum of the 1_{wt}% Au/C-S_2O_3 sample the first feature corresponds to the outer S atom (S^{1-} or S^0) and the second main feature corresponds to the inner sulphur atom (S^{5+} or S^{4+}) are shifted towards higher absorption energies implying an increased oxidation state of both S atoms or alternatively a change in geometry, *i.e.* different bond lengths. Moreover, looking at the first absorption edge in the XANES spectrum of the freshly prepared catalyst (figure 5.23), it is possible to observe that this feature presents a shoulder (potentially a second peak).

This evidence suggests that the outer sulphur atom might be present in the sample in two different oxidation states, especially if this sulphur atom is involved in Au-S bond. In fact, as reported in Chapter 3, the fitting of the Au L_3-edge EXAFS data for the freshly prepared catalyst resulted in a N of 2 (±0.1), consistent with a gold bisthiosulfate complex.[32] However, for the Au L_3-edge EXAFS it was not possible to definitively distinguish between Au-Cl and Au-S scattering paths, in this case , the absence of a pre-edge does not allow us to determine without doubt if the outer sulphur is directly bound to the Au species.

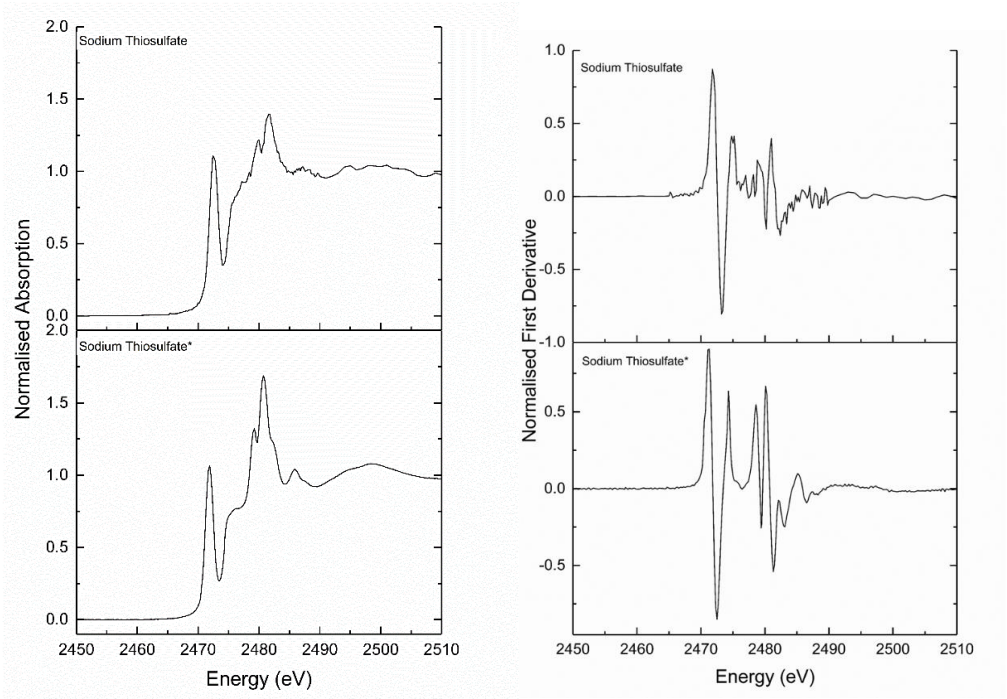

Figure 5.22 – Comparison between (left) normalised absorption and (right) normalised first derivative of the sodium thiosulfate standard acquired at BM28 (top) and the sodium thiosulfate from the data base (bottom(*)).[31]

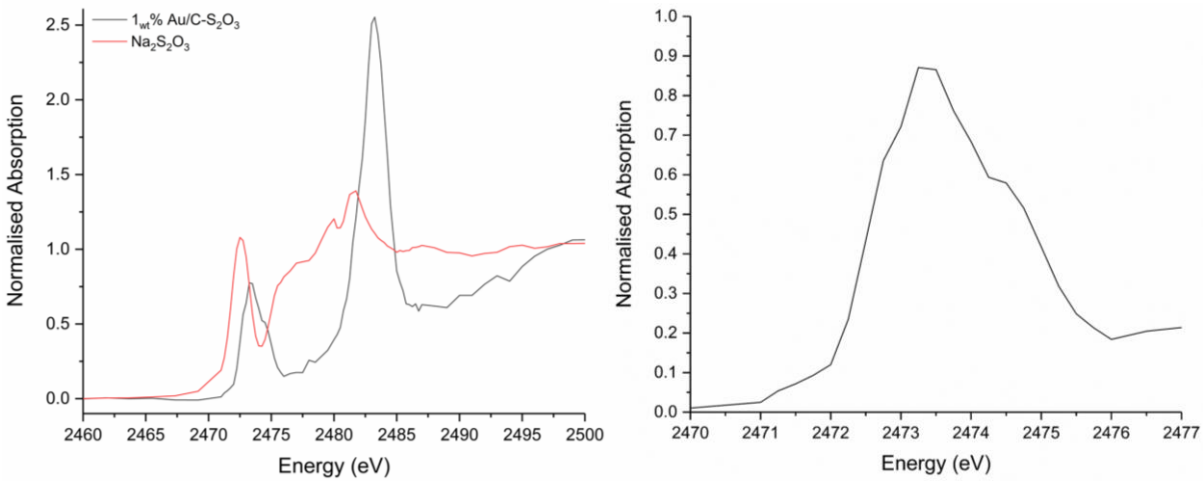

Figure 5.23 – (left) Comparison between the S K-edge XANES normalised absorption of the reference material $Na_2S_2O_3$ (red solid line) and the 1_{wt}% Au/C-S_2O_3 (black solid line). (right) Detail of S K-edge normalised absorption spectrum of the 1_{wt}% Au/C-S_2O_3 catalyst

Figure 5.24 shows that upon heating the catalysts to reaction temperature the two main absorption edges do not change, neither in intensity or energy position, in contrast with the behaviour of the Cl speciation observed for both the 1_{wt}%Au/C-S_2O_3 and 1_{wt}%Au/C-AR catalyst, in which the changes observed were

attributed to the thermal decomposition of $AuCl_3$ to AuCl.[24] Meaning that the S speciation in the 1_{wt}% Au/C-S_2O_3 catalyst are more thermally more stable than the Cl species.

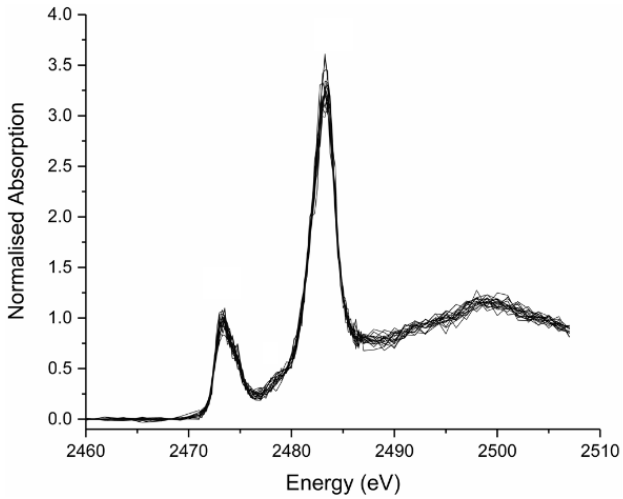

Figure 5.24 – *In situ* S K-edge XANES spectra of the 1%Au/C-S_2O_3 catalyst while heating to reaction temperature.

Once the reaction temperature was reached, the reaction mixture was introduced in the system. Figure 5.25 shows a shift in the absorption-edge energy of the outer S during the first 20 min of reaction while the inner S remains generally stable. Because of the absence of a pre-edge feature in the sulphur K-edge XANES, is not possible to determine without doubt if this shift can be correlated to a change in Au oxidation state recorded both from the Au L_3-edge and the Cl K-edge perspective. Moreover, due to the delay between the spectra acquisition and the MS response, due to the low flow used and the reactor setup itself (described in Chapter 2), a correlation of changes observed in the XANES region and VCM production was not possible. But assuming catalytic behaviour similar to the *in situ* XAFS experiment described in Chapter 3 (figure 3.24) it is possible to consider a possible interaction/bond between the cationic gold and the sulphur, resulting in a change in the electronic charge on the sulphur inner atom. As already mentioned, the edge rising from the inner S atom does not change during the heating ramp and the time on line. As predicted by Johnston *et al.*,[7] it might be speculated that the greater activity and stability of this catalyst is determined by the presence of sulphur moiety, i.e. the outer S atom, that remains anchored on the carbon support, preventing the sintering and reduction of the cationic gold.

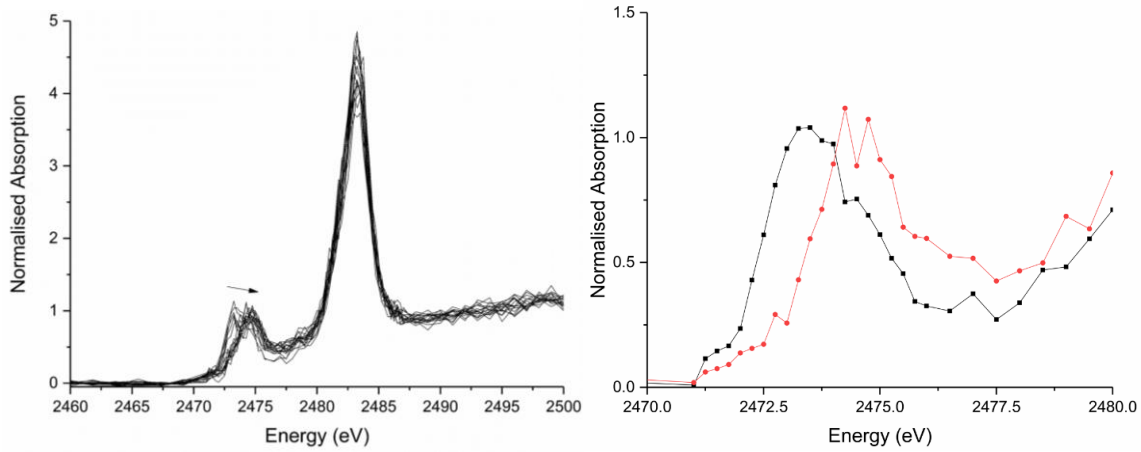

Figure 5.25 – *In situ* S K-edge XANES of the 1%Au/C-S_2O_3 catalyst during the time on line. (left) All S K-edge XANES spectra. (left) XANES normalised absorption spectra at two different moment of the time-on-line: (black) at the beginning of the reaction and (red) after 20 minutes of reaction.

5.3 – Conclusions

In the first section of this chapter the role of the solvent used in the catalyst preparation has been studied via Cl K-edge XANES and INS. It has been shown the choice of different solvents, i.e. aqua regia or water, when using a chlorinated metal precursor, $HAuCl_4$, modifies the Cl speciation in the final material. The treatment with *aqua regia*, leads to the formation of hydroxyl groups on the carbon support, as shown from INS analysis, while the use of water leads to a decrease in Cl amount without modifying the carbon support. The effect of gaseous HCl has been also investigated showing the possible formation of an H-Cl film on the carbon support. Combining this information, it is possible to speculate that the treatment with *aqua regia* lead to formation a Cl speciation bonded to a hydroxyl groups on carbon support, via the hydrogen atom, that ultimately stabilised the Au in a cationic form.

An *in situ* donor K-edge XANES characterisation of gold on carbon catalysts during the hydrochlorination of acetylene has also been performed, in order to understand the role of the ligand in the catalytic activity. The catalytic behaviour of a 1wt% Au/C-AR catalyst has been studied *in situ* while recording the Cl K-edge XANES. The results obtained were in agreement with what was observed during the *in situ* Au L_3-edge experiment described in Chapter 3, confirming also form the ligand perspective the catalysts consist in atomically dispersed $AuCl_x$ active species.

The study of the 1_{wt}% Au/C-S_2O_3 catalyst resulted in a difficult interpretation both from the Cl and the S K-edge XANES perspective and further investigation is needed. Possibly, X-ray Emission Spectroscopy (XES), which is a technique complementary to XAFS, might be a good way of solving this problem, providing valuable information with respect to the electronic structure as well as the nature

of the bound ligands. Even though the interpretation of the full XANES spectrum remains difficult, the general changes in the pre-edge observed in the Cl K-edge XANES region agreed with the results obtained from the 1_{wt}%Au/C-S_2O_3 Au L_3-edge. This implies that in the 1_{wt}% Au/C-S_2O_3 catalyst some Cl is bounded directly to the gold and it is directly involved in the reaction re-affirming that $AuCl_x$ speciation are active site for the acetylene hydrochlorination reaction for both these catalytic systems.

5.4 – References

1. H. Zhang, G. Liu, L. Shi and J. Ye, *Adv. Energy Mater.*, **2018**, *8*, 1701343.

2. X.-F. Yang, A. Wang, B. Qiao, J. Li, J. Liu and T. Zhang, *Acc. Chem. Res.*, **2013**, *46*, 1740–1748.

3. M. Behrens, F. Studt, I. Kasatkin, S. Kuhl, M. Havecker, F. Abild- Pedersen, S. Zander, F. Girgsdies, P. Kurr, B. L. Kniep, M. Tovar, R. W. Fischer, J. K. Norskov and R. Schlögl, *Science*, **2012**, *336*, 893–897.

4. M. Flytzani-Stephanopoulos and B. C. Gates, *Annu. Rev. Chem. Biomol. Eng.*, **2012**, *3*, 545–574.

5 A. Zecchina, S. Bordiga and E. Groppo, *The Structure and Reactivity of Single and Multiple Sites on Heterogeneous and Homogeneous Catalysts: Analogies, Differences, and Challenges for Characterization Methods*, in Selective Nanocatalysts and Nanoscience: Concepts for Heterogeneous and Homogeneous Catalysis, Eds: A. Zecchina, S. Bordiga and E. Groppo, Wiley, **2011**

6. X. Liu, M. Conte, D. Elias, L. Lu, D. J. Morgan, S. J. Freakley, P. Johnston, C. J. Kiely and G. J. Hutchings, *Catal. Sci. Technol.*, **2016**, *6*, 5144–5153.

7. P. Johnston, N. Carthey and G. J. Hutchings, *J. Am. Chem. Soc.*, **2015**, *137*, 14548–14557

8. P. T. Bishop, N. A. Carthey and P. Johnston, **2013**, WO 2013/008004A3.

9. P. B. J. Thompson, B. N. Nguyen, R. Nicholls, R. A. Bourne, J. B. Brazier, K. R. J. Lovelock, S. D. Brown, D. Wermeille, O. Bikondoa, C. A. Lucas, T. P. A. Hase and M. A. Newtone, *J. Synchrotron Rad.*, **2015**, *22*, 1426–1439

10. A. M. J. van der Eerden, J. A. van Bokhoven, A. D. Smith and D. C. Koningsberger, *Rev. Sci. Instrum.*, **2000**, *71*, 3260–3266.

11. C. E. Hayter, J. Evans, J. M. Corker, R. J. Oldman and B. P. Williams, *J. Mater. Chem.*, **2002**, *12*, 3172–3177.

12. H. Dathe, A. Jentys and J. A. Lercher, *J. Phys. Chem. B*, **2005**, *109*, 21842–21846.

13. G. Nurk, T. Huthwelker, A. Braun, C. Ludwig, E. Lust and R. P. W. J. Struis, *J. Power Sources*, **2013**, *240*, 448–457.

14. T. B. Bolin, T. Wu, N. Schweitzer, R. Lobo-Lapidus, A. J. Kropf, H. Wang, Y. Hu, J. T. Miller and S. M. Heald, *Catal. Today*, **2013**, *205*, 141–147.

15. C. F. J. König, P. Schuh, T. Huthwelker, G. Smolentsev, T. J. Schildhauer and M. Nachtegaal, *Catal. Today*, **2014**, *229*, 56–63.

16. K. Zhou, J. Jia, C. Li, H. Xu, J. Zhou, G. Luo and F. Wei, *Green Chem.*, **2015**, *17*, 356.

17. S. C. B. Myneni, *Science*, **2002**, *295*, 1039-1041.

18. S.E. Shadle, B. Hedman, K. O. Hodgson and E. I. Solomon, *J. Am. Chem. Soc.*, **1995**, *117*, 2259-2212.

19. T. Glaser, B. Hedman, K. O. Hodgson and E. I. Solomon, *Acc. Chem. Res.*, **2000,** *33*, 859-868.

20. J. L. Fulton and M. Balasubramanian, *J. Am. Chem. Soc*., **2010**, *132*, 12597–12604.

21. R. I. Bewley, R. S. Eccleston, K. A. McEwen, S. M. Hayden, M. T. Dove, S. M. Bennington, J. R. Treadgold, R. L. S. Coleman, *Phys. B Condens. Matter*, **2006**, *385–386*, 1029–1031.

22. F. Jalilehvand, *Chem. Soc. Rev.*, **2006**, *35*, 1256–1268

23. L. S. Kau, D. J. Spira-Solomon, J. E. Penner-Hahn, K. O. Hodgson, E. I. Solomon, *J. Am. Chem. Soc*., **1987**, *109*, 6433-6442.

24. O. Glemser and H. Sauer, *Handbook of Preparative Inorganic Chemistry*, Ed. G. Brauer, Academic Press, **1965**, *2*, 1056.

25. A. Thompson, I. Lindau, D. Attwood, P. Pianetta, E. Gullikson, A. Robinson, M. Howells, J. Scofield, K. Kim, J. Underwood, J. Kirz, D. Vaughan, J. Kortright, G. Williams and H. Winick, *X-ray data booklet*, Lawrence Berkeley National Laboratory, University of California, Berkeley, CA, **2001** – http://xdb.lbl.gov.

26. B. Hedman, P. Frank, J. E. Penner-Hahn, A. L. Roe, K. O. Hodgson, R. M. K. Carlson, G. Brown, J. Cerino, R. Hettel, T. Troxel, H. Winick and J. Yang, *Nucl. Instrum. Methods Phys. Res., Sect. A*, **1986**, *246*, 797–800.

27. A. Vairavamurthy, B. Manowitz, G. W. Luther III and Y. Jeon, *Geochimica et Cosmochimica Acta*, **1993**, *57, 1619-1623*

28. A. Vairavamurthy, *Spectrochimica Acta Part A: Molecular and Biomolecular Spectroscopy*, **1998,** *54*, 2009-2017.

29. H.-P. Loock, *J. Chem. Educ*., **2011**, *88*, 282-283.

30. P. Karen, P.McArdle and J. Takats, *Pure Appl. Chem.*, **2014**, *86*, 1017–108.

31.http://www.esrf.eu/home/UsersAndScience/Experiments/XNP/ID21/php/DatabaseSCompounds.html

32. R. A. Bryce, J. M. Charnock, R. A. D. Pattrick and A. R. Lennie, *J. Phys. Chem. A*, **2003**, *107*, 2516–2523.

Chapter 6

Conclusions and Future Work

The acetylene hydrochlorination reaction to form vinyl chloride monomer (VCM) represents one of the first heterogeneous gold-catalysed reactions that is now moving towards industrial application as a replacement of the currently used highly volatile and toxic mercuric chloride catalyst.[1] In 1985, while studying the activity of supported metal chloride catalysts for this reaction,[2] Graham Hutchings predicted that Au containing catalysts would have shown the best activity.[3] After almost 30 years, the strong drive to replace the current mercuric chloride catalyst used,[4] led to the development and commercialisation of a gold on carbon (Au/C) catalyst for this process.[5] Although the use of Au/C for the acetylene hydrochlorination reaction is a promising development, with a full-scale pilot plant in production, the exact nature of the active Au species and the catalytic cycle are still not fully understood.

As reported in chapter 1, the different hypothesis advanced regarding the active form of the catalysts arise mainly from results obtained from *ex situ* characterisation and comparison of the fresh and used catalyst. In their recent work X. Liu *et al*.[6] reported Au/C catalysts, prepared using different acid media, to be initially inactive and characterised by a pronounced induction period, which was hypothesised to be associated with development of the active oxidised gold species produced *in situ* at the periphery of gold nanoparticles by reaction with both reactants. However, the absence of *in situ/operando* studies of the acetylene hydrochlorination reaction with Au/C catalysts has hindered the understanding of these systems. Chapter 3 reports the investigation of the nature of the active site via an *in situ* X-ray absorption spectroscopy (XAS) characterisation and investigates the evolution of Au speciation in Au/C catalysts during the acetylene hydrochlorination reaction measuring the Au L_3-edge XAS spectra under reaction conditions. The activity of these Au/C catalysts, prepared using different

media, has been compared with the recently industrially validated catalyst.[5] The aim of the investigation was to understand the influence of the choice of solvent and metal precursor during the catalyst preparation in the activity of the final material, to identify the catalytically active site and to propose a reaction mechanism based on the combination of theoretical and experimental data. During the time online studies, distinct changes in the XANES, i.e. changes in the white line height, were observed, which could be explained as changes in the relative concentrations of Au(I) chloride and Au(III) chloride. In particular, the variations in the XANES region clearly correlate to the catalyst productivity through a linear correlation. The most active catalyst, before, during and after reaction shown to maintain a highly cationic gold dispersion, as also supported by STEM characterisation. This study led to the conclusion that highly active catalysts comprise of single-site cationic Au entities whose activity correlates with the ratio of Au(I)/Au(III) present. In this perspective, the active form of these catalysts can be likened to the homogenous single site Au catalysts,[7] while the mechanism has been hypothesised to proceed through the oxidative addition of HCl to Au chloride, followed by the insertion of acetylene and reductive elimination of VCM through a Au(I)/Au(III) redox couple.

Contrary to previously reported case of single site gold catalysts employed in heterogeneous catalysis, [8,9,10,11] which either deactivate rapidly or undergo radical modification during the reaction; in our conditions, the highly active catalysts remained atomically dispersed throughout the catalysis. However, it is important to have a full understanding of the possible deactivation mechanisms of these catalytic materials. Preliminary studies on the deactivation of gold on carbon catalysts during acetylene hydrochlorination identified two possible deactivation mechanisms:[12] the formation of oligomers on the catalyst surface at 100–120 °C[5,13] and the reduction of active cationic gold to inactive metallic Au at a temperature range between 120–180 °C. In particular, together with the effect of the reaction temperature used, the damaging effect of acetylene has been suggested to be responsible both for deactivation pathways. Thus, the investigation of the influence of the individual reactant seems to be essential to further elucidate both the reaction and deactivation mechanism. Based on the study of Conte *et al.*, [14] chapter 4 investigates the effects of the individual reactants on a Au/C catalyst via an *in situ* gas switching experiment while recording the XAS spectra at the Au L_3-edge.

The unexpected results obtained while flowing only HCl through the catalyst at reaction temperature, which, in the absence of C_2H_2, did not re-oxidise the Au(I) chloride species, lead to postulate that the oxidative addition of HCl across the Au(I) chloride species requires the concerted addition with C_2H_2, in partial modification of the reaction mechanism proposed in chapter 3. On the other hand, exposure of C_2H_2, in the absence of HCl, severely modifies the Au speciation, making difficult the interpretation of the XANES spectra recorded, which could not be associated to neither Au(III), Au(I) chlorides or Au(0). An inelastic neutron scattering (INS) study of the catalyst exposed to C_2H_2 showed the formation of oligomeric acetylene species on the catalyst surface, which, upon re-introduction of both reactants, led to significant catalyst deactivation associated with consequent formation of metallic Au nanoparticles. The formation of Au(0) has been directly correlated with a decrease in VCM productivity

when under reaction conditions also using an higher Au loading catalyst. Moreover, the formation of metallic Au particles greatly affected the strong correlation between normalised white line height and VCM productivity reported in chapter 3. In particular, the decrease in VCM production was invariant to the change in normalised white line height, i.e. loss of the linear correlation. Thus, monitoring the change in white line height might not be a useful tool in case of the study of complicated system in which spectator species, in this case Au(0) may be present.

DFT study are required to confirm the plausibility of the reaction mechanism proposed in chapter 4 and more information are needed, i.e. XANES modelling, to better understand the exact nature of Au speciation when the catalyst is expose to only acetylene in the absence of HCl.

As already pointed out in chapter 1, even though gold on carbon are the most active and selective catalyst for the reaction, in the perspective of an industrial application, their stability is still considered an issue. In particular, in spite of the established high activity of the Au/C catalyst made with *aqua regia*[6] there are several disadvantages which have inhibited its industrial application.[5] In this view, an important expect to consider is choice the ligands. This is even more valid considering the results obtained in chapter 3, in which Au/C catalysts have been found to contain isolated metal atoms individually dispersed on supports and, thus, can go under the classification of "single atom catalysts" (SACs). The recently validated Au/C catalyst by Johnson Matthey[5,15] is prepared by using a sulphur containing ligand and under industrial condition produced a class of catalysts more active and stable than the traditional Au/C catalyst made with aqua regia. In chapter 3, this two class of gold on carbon catalysts have been already compared from the gold perspective, i.e. *in situ* Au L_3-edge XANES experiment, underlying interesting similarity between these two catalytic systems.

Chapter 5 aims to further investigate the active site from a ligand perspective via an *in situ* ligand K-edge XANES characterisation of gold on carbon catalyst to elucidate the role of chlorine and sulphur speciation in the catalyst under operating conditions. Also in chapter 5, the effect of the catalysts preparation in the final material has been investigated via an INS experiment. Combining the results obtained from the Cl K-edge XANES and INS, the choice of the solvent, i.e. aqua regia or water, when using chlorinated metal precursor, modify the Cl speciation in the final material. In particular, via INS it was possible to observe that the use of *aqua regia* leads to the formation of hydroxyl group on the carbon support, causing the possible formation of an H-Cl film on the carbon support. Merging this information, it is possible to speculate that this H-Cl film formed onto the carbon support after treatment with *aqua regia*, raised from the bond of Cl species with the hydrogen atom of the hydroxyl group, might stabilised the Au in a cationic form. Even though, the interpretation of the full XANES spectrum was not possible, and further investigation is needed, the general changes in the pre-edge feature observed in the Cl K-edge XANES region for both the catalysts under study agreed with the results obtained from the Au L_3-edge. In particular, in both catalytic system some of the Cl is bounded directly to the gold and is directly involved in the reaction mechanism, re-affirming that $AuCl_x$ speciation are active site for the acetylene hydrochlorination reaction.

Unfortunately, the studies that employ soft X-ray in the field of catalysis under operating conditions are limited, making difficult the interpretation of the results obtained. In particular, the role of the sulphur in the recently commercially validated catalyst needs further investigation; possibly the acquisition of more sulphur standard for the analysis of the XANES region or even better, considering the sensitivity of the ligand K-edge XANES, the use of modelled XANES spectra might help the interpretation of the results obtained.

All the results obtained can be used to hypothesise a reaction mechanism based on a redox process (Au(I)/Au(III)) as reported in figure 6.1.

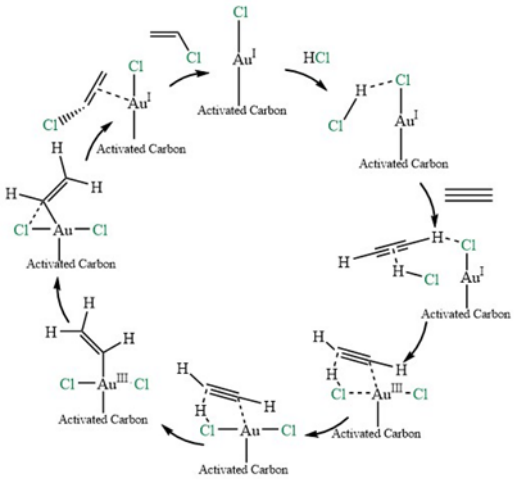

Figure 6.1 – Hypothesised reaction mechanism for the acetylene hydrochlorination reaction catalysed by Au/C catalysts based on a redox process.

It also possible to suppose, based on the results obtained in chapter 6 the Au to be bond to the carbon support via a Cl atom. However, in order to further elucidate the possible reaction mechanism for this Au catalysed reaction more kinetic studies needs to be performed. Also, X-ray Emission Spectroscopy (XES), which is a technique complementary to XAFS, might be a good way of solving this problem, providing valuable information with respect to the electronic structure as well as the nature of the bound ligands.

References

1. R. Ciriminna, E. Falletta, C. Della Pina, J. H. Teles and M. Pagliaro, *Angew. Chem. Int. Ed.*, **2016**, *55*, 14210 – 14217.

2. K. Shinoda, *Chem. Lett.*, **1975**, 219–220.

3. G. J. Hutchings, *J. Catal.*, **1985**, *96*, 292–295.

4. Minamata Convention on Mercury, http://www.mercuryconvention.org/

5. P. Johnston, N. Carthey and G. J. Hutchings, *J. Am. Chem. Soc.*, **2015**, *137*, 14548–14557.

6. X. Liu, M. Conte, D. Elias, L. Lu, D. J. Morgan, S. J. Freakley, P. Johnston, C. J. Kiely and G. J. Hutchings, *Catal. Sci. Technol.*, **2016**, *6*, 5144–5153.

7. A.S.K. Hashmi, *Gold Bull.*, **2003**, *36*, 3-9.

8. M. Flytzani-Stephanopoulos, *Acc. Chem. Res.*, **2014**, *47*, 783–792.

9. W. Deng, A. I. Frenkel, R. Si and M. Flytzani-Stephanopoulos, *J. Phys. Chem. C*, **2008**, *112*, 12834–12840.

10. J. C. Fierro-Gonzalez and B. C. Gates, *J. Phys. Chem. B*, **2004**, *108*, 16999–17002.

11. J. Lu, C. Aydin, N. D. Browning and B. C. Gates, *Angew. Chem. Int. Ed. Engl.*, **2012**, *51*, 5842–5846.

12. B. Nkosi, N. J. Coville, G. J. Hutchings, M. D. Adams, J. Friedl and F. E. Wagner, *J. Catal.*, **1991**, *128*, 366-377.

13. N. A. Carthey, P. Johnston and M. L. Smidt, **2010**, WO 2010/055341A3,

14. M. Conte, A. F. Carley, C. Heirene, D. J. Willock, P. Johnston, A. A. Herzing, C. J. Kiely and G. J. Hutchings, *J. Catal.*, **2007**, 250, 231–239.

15. P. T. Bishop, N. A. Carthey and P. Johnston, **2013**, WO 2013/008004A3.